The University Of Sheffield.

Preparation, Characterization, and Properties of Polymer Graphene Nanocomposites

By:

Zaid Ghanem Mohammadsalih

A thesis submitted in partial fulfilment of the requirements for the degree of Doctor of Philosophy

The University of Sheffield
Faculty of Engineering
The Department of Materials Science and Engineering

January 2018

Dedication

To…

My Lovely Parents … For their unforgettable sacrifices.

My wife and daughters … For their patience and valuable support.

Declaration

I declare that this thesis has not been submitted as an exercise for a degree at this or any other University and it is entirely my own work. I agree to deposit this thesis in the University's open access institutional repository or allow the library to do so on my behalf, subject to British Copyright Legislation and The University of Sheffield library conditions of use and acknowledgements.

Zaid Ghanem Mohammadsalih

October 2017

Abstract

The history of polymer composite materials can be traced back to the period of 1930s-1940s with the development of glass fibre reinforced composites. Since then several generations of this technology have evolved, each one marked by increasingly smaller scales of the reinforcement materials. Polymer nanocomposites, PNCs, are the most recent class which- by virtue of their remarkable thermal and mechanical properties- have attracted world-wide attention. These properties are ascribed to the presence of graphene as a reinforcing agent which has exceptional thermal conductivity, high electron mobility, and superior mechanical properties. Although the modulus of graphene oxide, GO, is only about 25% of that of a monolayer of graphene, it remains the preferred material for polymer reinforcement. This is due to the abundance of oxygenated functional groups in its basal plane and peripheries, which enables easier coupling interactions between the nanofillers and different polymer matrices. Furthermore, GO is the precursor of graphene production and can be synthesized in bulk. The structure of the polymer matrix and the low loadings of the nanofillers are the main attributes leading to improved nanocomposite performance. In the research described in this thesis, polystyrene PS and poly (styrene-co-acrylonitrile) SAN were selected as the polymer matrices and very low loadings of GO (1.0 wt. % and below) were incorporated into these materials. The resulting nanocomposites were then characterised in terms of their mechanical and thermal properties. Hummers' method was used to prepare GO, and a solution blending approach was adopted for preparing the nanocomposites. One important requirement in the fabrication of these nanocomposites is that the dispersion of the nanofillers in the polymer matrix should be homogenous so that the benefits of the improved material properties are consistent throughout the volume of material. Any local aggregation of the nanofillers would result in a loss of uniformity which will consequently affect the mechanical performance and the thermal stability of these materials.

Several techniques were employed to achieve homogeneity in nanofiller dispersion in the nanocomposites. A homogenous dispersion for GO in PS and SAN was achieved by adopting a combination of different dispersion techniques, bath sonication and shear mixing, for two different processing times, 0.5 and 1.0 hour respectively. The solvent used to prepare the nanocomposites was tetrahydrofuran THF rather than dimethyl formamide DMF due to the poor volatility and poor samples obtained by employing the latter.

In order to obtain information on material properties at the nanoscale, such as elasticity, adhesion, and surface forces, force curves were obtained by Atomic Force Microscopy AFM and Quantitative Nanomechanical Measurements QNM. This information are important in terms of achieving improvement for many kinds of applications such as computer industry and storage devices with high data density. Using this approach, the reduced modulus of elasticity for GO was found to be higher than that of PS as achieved by utilizing AFM/QNM and the Derjaguin-Muller-Toporov DMT formula. Furthermore, few authors investigated the nanomechanical behaviour at the cryogenically fractured surface. The topography for the latter was successfully imaged and the moduli for GO nanosheets and PS were successfully obtained.

To move towards achieving the outstanding properties of graphene when using GO, GO was reduced. Several reduction techniques are available, though some of these require the use of chemicals that can have a negative impact on the environment and this was an important consideration in this work. The more eco-friendly approach route was taken here based on low temperature reduction using a vacuum assisted technique. The applied temperatures for reducing GO, under the influence of vacuum, were 130, 165 and 200°C.

A successful reduction was obtained in the GO as indicated by different characterization techniques, and the resulting nanocomposites of PS reinforced with the reduced form of GO showed better mechanical and thermal improvement compared with the nanocomposites of PS reinforced with low loadings of the pristine form of GO.

The thermal reduction of GO played a major role in the production of graphene like materials that provide better mechanical and thermal performance when incorporated in the polymer matrix.

It was important to obtain a good understanding about the performance of other groups of nanocomposites based on one of the PS counterparts which was SAN. The employment of SAN in the work described in this thesis was based on its improved mechanical and thermal performance compared with PS beside its wide range of applications. The mechanical and thermal performance for SAN and its nanocomposites were improved when compared to those based on PS and its nanocomposites. The presence of the acrylonitrile, AN, monomer contributed in efficient intercalation of the copolymer in the gallery of GO. This led to stronger interfacial interaction of SAN with GO nanocomposites that resulted in better performance of SAN nanocomposites compared to PS nanocomposites.

To conclude, the current study describes the successful preparation of GO and nanocomposites and the results of numerous methods for characterising these materials. The mechanical, thermal, and thermomechanical properties for the nanocomposites were significantly improved over that of the neat polymers. The PNCs may find potential applications in medicine, military aspects, optoelectronics, aerospace engineering, safety issues, and many others.

Acknowledgements

All praise and thanks go to Allah the Almighty, The Most Gracious and The Most Merciful, who gave me the potential and knowledge to accomplish this challenging task.

Then, I would like to acknowledge and express my gratitude for all the people who helped me through the course of my Doctoral study. I would like first to thank my sponsor, The Ministry of Higher Education and Scientific Research in The Republic of Iraq, and the staff of The Iraqi Cultural Attaché in London, UK.

I would like to sincerely thank my respected supervisors, Professor Biqiong Chen and Professor Beverley J. Inkson for their supervision, guidance, and mentorship that made the completion of this thesis possible. Their exhaustive knowledge and thoughtful critique proved to be of invaluable assistance over the course of my study.

Also, I would like to thank Dr. Nicholas Mullin from the Department of Physics for his valuable role in performing the nanomechanical measurements. Also, I am sincerely grateful to Dr. Ihtesham-U-Rehman for providing invaluable help, resources and knowledge through the Polymer Chemistry module he was teaching. I would also like to extend my thanks to my respected tutors in English Language Teaching Centre (ELTC) for their role in improving my English language skills. Thanks are especially going to Susan Nurse, Sheridan Macinnes, Catherine Journeaux, Beverley Slater, Suzanne Priestley, and Lynne Newcombe. I want also to thank Dr. Kevin Byron for his dedicated efforts in proofreading my thesis.

I also would like to thank the staff of the Department of Materials Science and Engineering and The Library at The University of Sheffield for providing all the necessary facilities and scientific resources. I am thankful to the University accommodation / Endcliffe Village for the amazing services they provide. Special thanks go to the respected technicians Rob Hansen, Ben Palmer, Dawn Bussey, Christopher Hill, Le Ma, Dean Haylock, Beverley Lane, and Deborah Hammond for carrying out the samples tests and for sending the results in a timely manner, and also thanks to my respected colleague Rob Masters for providing the contact information of Dr.

Mullin. I want also to thank all the members of my research group for their kind help especially during the initial stages of my academic course. I would like to thank Ahmed Al-Zahrany, Ehssan Al-Bermany, Xiangshuai Geng, Yahui Wen, and Xing Su without forgetting all other respected members. I am grateful to respected colleagues Husein Meshreghi, Lawan Grema, Dilwar Hussain, Ahmad Faik, and Hamza Al-Tameemi for their valuable help and cooperation. I would like also to acknowledge the spiritual and valuable support of the Islamic community in Muslim Welfare House in Sheffield (MWHS) namely, Imam Mohammad Ismail the head of Muslim Chaplain in The University of Sheffield, Dr. Mohammad Nassar, Dr. Hashil Al-Saadi, and all other brothers in the community. Sincere thanks to my respected uncle Dr. Firas Al-Douri and his family with special thanks to my respected brother Ahmed Firas, for their support, encouragement, and dedicated efforts. Also, I would like to acknowledge the support and punctual pursuance of my employer, The University of Technology, Baghdad, Iraq that helped me pursue my Doctoral studies. I am greatly appreciative to Assistant Professor Qassim S. Qassim, the former head of the Department of Applied Sciences, for nominating me a Ph.D. candidate and also to Professor Ali Al-Zuhairy, the current head of the Department. Many thanks also to Dr. Mutaz Al-Azzawi, Dr. Buthaina A. Ibrahim, Dr. Mohammad Sa'aeed, Dr. Wala'a Eldin K. Sa'aeed, Mrs. Raghad Al-Janabi for their cooperation and help in providing the required official documents for my scholarship and ensuring its continuity.

I owe my family sincere thanks for their truthful help, encouragement, and support during the course of my study, particularly my parents, my sister Dr. Zainab Mohammadsalih and her husband Dr. Faris Arif, my brother Dr. Mohammad, my sister Ban, and other respected relatives and friends in Iraq, Jordan, UK, UAE, US, and Canada who were enthusiastically making supplications and showing encouragement. Finally, I owe my dearest wife Noor and my beloved daughters, Somaiya and Safiya, my hearty gratitude. I ask Allah the Almighty to reward them, grant them success in this life and in the hereafter, and to shower them with his mercy and grace.

Nomenclature

0D, 1D, 2D, 3D – Zero, one, two, three Dimensional

1, 2 DCB - Dichlorobenzene

ABS - Acrylonitrile Butadiene Styrene

AFM - Atomic Force Microscopy

AN - Acrylonitrile

BCP - Burnham Colton Pollock

CB - Carbon Black

CMG - Chemically Modified Graphene

CMNs - Ceramic Matrix Nanocomposites

CNF - Carbon Nano-Fibres

CNTs - Carbon Nanotubes

CRGO - Chemically Reduced Graphene Oxide

CS - Chitosan

CVD - Chemical Vapour Deposition

DCM - Dynamic Contact Module

DFT - Density Functional Theory

DMA - Dynamic Mechanical Analysis

DMAc - Dimethylacetamide

DMF - N, N Dimethyl Formamide

DMT - Derjaguin Muller Toporov

DSC - Differential Scanning Calorimetry

DTG - Derivative Thermogravimetric

EG - Expandable Graphite

F-D - Force-Distance

FET - Field Effect Transistors

FFM - Friction Force Microscopy

FGS - Functionalised Graphene Sheets

FLG - Few Layered Graphene

FTIR - Fourier Transform Infrared Spectroscopy

GNRs - Graphene Nanoribbons

GNS - Graphene Nanosheets

GO - Graphene Oxide

GPC - Gel Permeation Chromatography

HRGO - Highly Reduced Graphene Oxide

IHM - Improved Hummers' Method

JKR - Johnson Kindall Roberts

LBL - Layer By Layer

LCD – Liquid Crystal Devices

LIB - Lithium Ion Batteries

LPE - Liquid Phase Exfoliation

MD - Molecular Dynamics

MD - Maugis Dugdale

MEMS - Microelectromechanical Systems

MERGO - Microwave Exfoliated Reduced Graphene Oxide

MMNs - Metal Matrix Nanocomposites

MMT - Montmorillonite

MWCNT - Multi Walled Carbon Nanotube

MYD/HW - Muller –Yuscchenko- Derjaguin/ Hughes- White

NEMS - Nanoelectromechanical Systems

NMP - N-Methyl Pyrrolidone

NPs - Nanoparticles

OLED - Organic Light Emitting Diodes

OM - Optical Microscopy

P3HT - poly (3-hexylthiophene)

PA6 - Polyimide

PANI - Polyaniline

PBI - Polyisobutylene

PBT - Poly (butylene terephthalate)

PC - Polycarbonate

PCL - Polycaprolactone

PDMS - Poly (dimethyl siloxane)

PEDOT: PSS - poly (3, 4 ethyencdioxy thiophene) poly (styrenesulphonate)

PEEK – Polyether ether Ketone

PEI - Poly (ethyleneimine)

PEO - Poly (ethylene oxide)

PET - Polyethylene Terephthalate

PGNs - Polymer Graphene Nanocomposites

PMC - Polymer based Matrix Composites

PMMA - Poly (Methyl Methacrylate)

PNC - Polymer Nanocomposites

PP - Polypropylene

PPS – Polyphenylene Sulfone

PPy - Polypyrrole

PS - Polystyrene

PSF - Polysulfone

PTFE - Poly (tetrafluoroethylene)

PU - Polyurethane

PVA - Poly (vinyl alcohol)

PVC - Poly (vinyl chloride)

PVDF - polyvinylidene fluoride

QNM - Quantitative Nanomechanical Measurements

rGO, RGO - reduced Graphene oxide

RLB - Rechargeable Lithium Batteries

RPM - Rotation Per Minute

RT - Room Temperature

SAN - Poly (styrene-co-acrylonitrile)

SBR - Styrene Butadiene Rubber

SDS - Sodium Dodecyl Sulphate

SEBS - styrene (ethylene-co-butylene)

SEM - Scanning Electron Microscopy

SFA - Surface Force Apparatus

SI-ATRP - Surface Initiated- Atom Transfer Radical Polymerization

SiC - Silicone Carbide

SLG - Single Layered Graphene

sPS – Syndiotactic Polystyrene

SRGO - Sulfonated Reduced Graphene Oxide

SSNMR – Solid State Nuclear Magnetic Resonance

STM - Scanning Tunnelling Microscope

SWCNT - Single Walled Carbon Nanotube

T_d, $T_{d\ max.}$, T_d Peak - Degradation Temperature

TEM - Transmission Electron Microscopy

T_g - Glass Transition Temperature

TGA - Thermal Gravimetric Analysis

THF - Tetrahydrofuran

TOM - Transmission Optical Microscopy

TPEE - Thermoplastic Polyester Elastomer

TPO - Thermoplastic Polyolefin

TPU - Thermoplastic Polyurethane

TRG - Thermally Reduced Graphene

TRGO - Thermally Reduced Graphene (graphite) Oxide

T.S – Tensile Strength

XGnP - Exfoliated Graphene Nanoplatelets

XPS - X ray Photoelectron Spectroscopy

XRD - X Ray Diffraction

C - Carbon

C - Solubility

CO - Carbon Monoxide

CO_2 - Carbon Dioxide

D - Depth of indentation

E - Young's Modulus

E*, E_r - Reduced Young's modulus

eV - electron Volt

F - Force

F_{adh} - Force of Adhesion

F_{tip} - Force on tip

g - Gram

GPa / MPa – Gegapascal / Megapascal

h - Hour

H - Hydrogen

H - Zero load elastic deformation

$H^{/}$ - Zero load plastic deformation

K - Spring Constant

Kc - Spring Constant

K_D - Distribution Coefficient for steric exclusion

L - Length of Cantilever

Mg - Milligram

nm - Nanometre

^{o}C - Centigrade

OH - Hydroxyl

Pa - Pascal

R - Tip Radius

V_i - Total volume of solvent within the gel pores

V_o - Total volume of the mobile phase

V_R - Retention Volume

Vol. - Volume

w – Width

wt. % – Weight fraction

X - Deflection of cantilever

Zc - Deflection

α - Open angle

δ - Solubility Parameter

δD - The dispersion cohesion parameter

ΔE/V - Energy of Vaporization per unit Volume

δH - The hydrogen bonding cohesion parameter

δ_{isolv} - ith Hansen Parameter in a given solvent

δP - The polarity cohesion parameter

δ_T - Hildebrand Solubility Parameter

μm - Micrometre

Table of Contents

List of Figures

List of Tables

Chapter 1

Introduction

1.1. Introduction

The concepts that seeded the big word of ‘Nanotechnology’ which is tiny in scale but infinitely immense in possibility were first discussed in December 29, 1959 by the renowned physicist Richard Feynman in his talk at the California Institute of Technology entitled ‘’There is plenty of room at the bottom’’ where he discussed the ability to manipulate matter (Earl & Nancy Boysen, 2011). The term ‘’Nanotechnology’’ represents a revolution in materials science that started over thirty years ago and has expanded the scientific horizons of several fields in engineering, chemistry, and medicine with the development of new technological applications, new materials, and new knowledge on the properties of materials.

A new sub-discipline that emerged from these advances in nanotechnology is polymer based matrix nanocomposites PMCs or polymer nanocomposites PNCs which refers to heterogeneous solid materials that are composed from a polymer matrix with nanoscale reinforcements to reinforce that matrix. These nanocomposites can be classified according to the material of the host matrix and includes metal matrix nanocomposites MMNs, ceramic matrix nanocomposites CMNs, and the aforementioned PMCs that are the subject of research in this thesis.

In 2004, two researchers, Andre Geim and Konstantin Novoselov at the University of Manchester conducted some ground-breaking work in which they produced and characterised one atom thick, two dimensional nano material of carbon called graphene, for which they received the Nobel Prize in 2010. Graphene can be identified as a carbon crystal in which the carbon atoms are packed in a hexagonal lattice similar to a honeycomb. This material has unique properties such as high strength, high transparency, a large surface area, good thermal and electrical conductivity as well as excellent electronic properties.

Since its first discovery in 2004, graphene and graphene based nanocomposites has been the focus of world-wide research in many laboratories in industry and academia, with the aim of harnessing its potential for the myriad applications in which these material could be used.

These applications include flammability resistance, barrier properties, different kinds of sensors (electrochemical sensors, biosensors, etc..), and supercapacitors (Silvestre *et al*. 2016; Xu *et al*. 2017).

However, before the unique benefits of these materials can be realised in practical applications, and compete with existing technologies, several challenges need to be met. The most important of these is in developing bulk production techniques for graphene. Several approaches to meet this challenge, amongst them is graphene reflux adopted by (Rountree *et al*. 2016) at Texas A&M University, USA.

A second challenge is in finding the best polymer material that can be used in practical applications, and the research described in this thesis focusses on this challenge in PNCs. The research on PNCs has been aimed at finding ways of incorporating graphene into various polymer matrices such as nylon-6, polypropylene PP , and different epoxies and polyesters (Silvestre *et al*. 2016). However, as pristine graphene has a poor dispersion in polymers, alternative forms of modified graphene have been explored such as graphene oxide GO as these are easier to disperse. In this thesis, investigations into the production and incorporation of GO and its reduced form in the polystyrene PS with the required characterisation for the resulting nanocomposites have been carried out.

The extensive oxidation of graphite results in graphite oxide which has different oxygenated functionalities in the basal plane and peripheries and this offers an indirect route to creating GO. This is achieved by using sonication as part of the processing. (Shah *et al*. 2015; Loh *et al*. 2010). Figure 1.1. provides a simple overview about the concept of graphene, GO and polymer based graphene/GO nanocomposites (Shah *et al*. 2015).

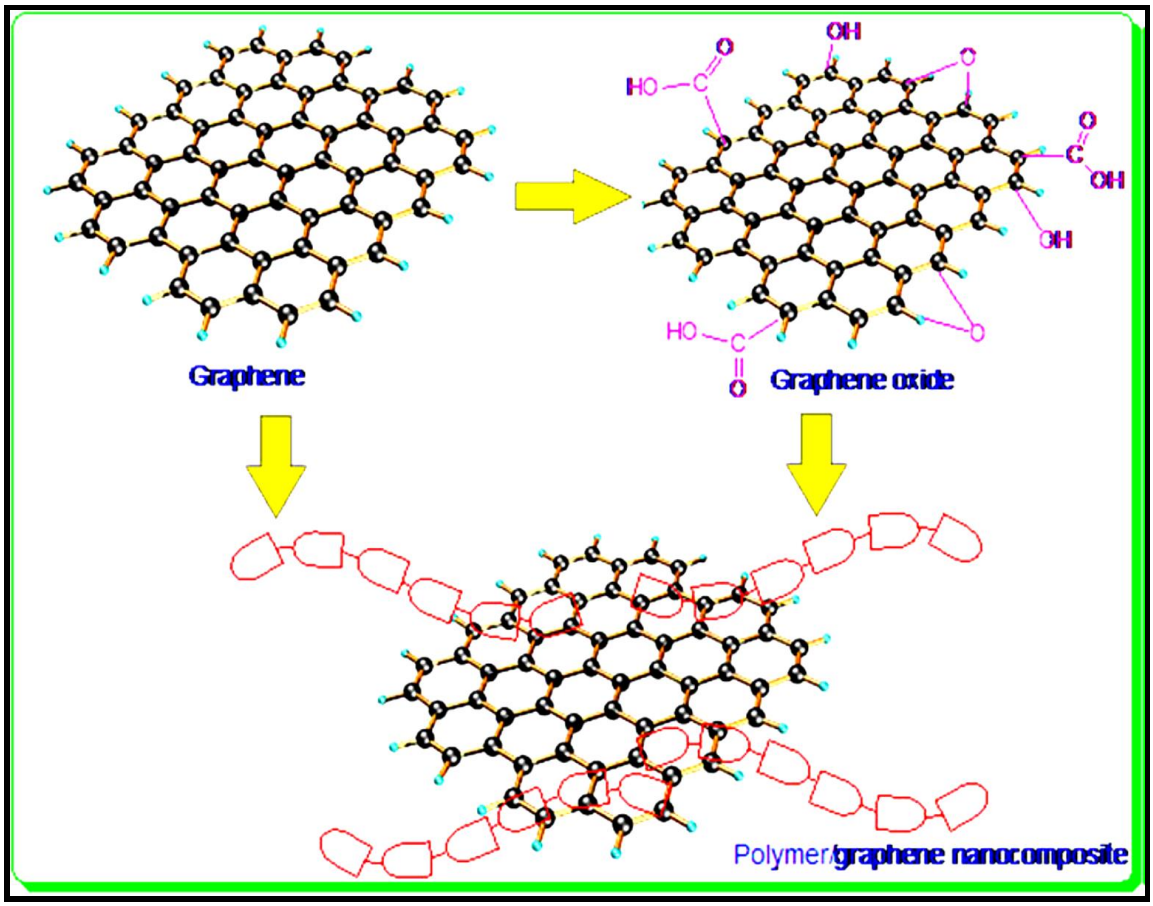

Figure 1.1. : Graphical abstract of graphene, GO and polymer graphene/GO nanocomposites. Adapted from (Shah et al. 2015) with permission from the publisher (Taylor and Francis group, LLC).

The graph illustrates the incorporation of graphene and GO into the polymer matrices which are presented by the long chains attached to the hexagonal lattice of graphene.

Considerable research has been focussed on efforts to improve the randomness of the dispersion of nanoparticles NPs in the polymer matrix, through specific preparation techniques. In-situ polymerization is a popular option in this respect, though rather less attention has been given to the effects on the processing conditions in the solution blending approach that involve shear mixing and sonication, and their benefits as dispersion techniques. The combination of the latter techniques have been mostly confined to the dispersion of low loadings of nanoparticles in thermoset polymers such as epoxy as shown in (Yasmin *et al*. 2006).

Little attention, however, has been given to the effects of combining these techniques in order to study the distribution of nanoscale reinforcements in thermoplastic matrices such as PS, poly (styrene –co- acrylonitrile) SAN. Prior to this work the technique used to obtain a homogenous dispersion was ultrasonication only as described in the work of (Chen *et al*. 2015).

In addition, few attempts have been made to study the nanomechanical behaviour of polymers and different nano reinforcements through a study of their cryogenically fractured surfaces. In addition to measurements of dispersion, the Young's modulus at the nanoscale in these nanocomposites was studied in this research and determined by local elastic deformation for the cryogenically fractured surface of nanocomposites using atomic force microscopy AFM and quantitative nanomechanical measurements QNM. Specific formula of contact deformation theories discussed in the next chapter, is applied in order to calculate the aforementioned parameter. Mainly, authors are carrying out these kinds of measurements to the bulk surface of the nanocomposites.

(Tian *et al*. 2015) employed quasi-static nanoindentation for finding the hardness and reduced modulus values for thin films of 40 μm thickness, of polycarbonate / graphite nanoplatelets PC/GNPs nanocomposites. Other workers used low loadings of fillers (0.1 and 1.0) wt. % of GNPs for testing different indentation depths. Furthermore, (Qiu *et al*. 2016) incorporated 0.1 wt. % of graphene nanosheets GNS in a thermoplastic polyester elastomer TPEE and the nanomechanical behaviour for the resulting nanocomposites was studied using quantitative nanomechanical mapping mode.

Different approaches for reducing GO have been studied extensively in recent years as a potentially efficient route for producing processable graphene in bulk quantities and at relatively low cost. (Park *et al*. 2014) used a chemical approach to reduce GO by employing hydrazine hydrate as a chemical reductant, and preparing nanocomposites of PS/ chemically reduced graphene oxide CRGO. The nanocomposites showed an improved electrical performance and high thermal conductivity.

(Xu *et al*. 2013) used an in- situ thermal approach by compressing PC/GO nanocomposites within 280 ^{o}C and the resulting PC/thermally reduced graphene oxide TRGO showed a good thermal, electrical and mechanical performance. Most studies have been content with these approaches, but a few investigations have focused more on in-situ reduction using significantly reduced temperatures.

Owing to the precautions in dealing with chemical reductants, and the apparently high temperatures utilized for reducing GO, there is a growing need to find a more efficient and eco-friendly approach for preparing graphene using low exfoliating temperatures. (Zhang *et al*. 2011) employed the vacuum as a means of assisted thermal exfoliation, and in-situ reduction of GO. They utilized different temperatures of 135, 145 and 1050 ^{o}C for 24 h under the influence of vacuum oven to obtain reduced graphene oxide rGO.

The obtained rGOs were then mixed with PMMA, and the produced nanocomposites behaved like highly conductive materials. In the current study (this thesis) reduced exfoliating temperatures of 130, 165, and 200 ^{o}C, with the assistance of vacuum, were used to produce rGO and then the resulted rGOs were mixed with PS to investigate the performance of the nanocomposites. Successful results were obtained at the lowest temperature of 130 ^{o}C which is amongst the lowest temperatures achieved for this process. In recent years research work has intensified on the study of PS reinforced with different kinds of nanoscale reinforcements including GO (PS/GO nanocomposites) owing range of potential applications offered by these materials. The proposed applications include gas permeability, food packaging, optoelectronics and many others.

However, little data has been obtained so far with SAN/GO nanocomposites. Several different nano reinforcements have been investigated in order to enhance the physical and mechanical performance of SAN such as clay (Wang *et al*. 2005), and carbon nanotubes CNTs by (Wang *et al*. 2008). Few authors used GO to be incorporated with SAN but rather they used the reduced form of GO with SAN such as the co-work of (Vu *et al*. 2016).

1.2. The project aims and objectives

The main aims of this research project were to prepare GO using Hummers' method, and obtain GO powder by freeze-drying. The GO powder was then incorporated into amorphous polymers using very low loadings and the performance for the resulted nanocomposites was investigated.

The objectives of the current study are listed below:

1- A study of the required processing conditions for ensuring a successful preparation of polymer graphene nanocomposites PGNs, and applying the processing techniques to produce pilot samples of neat polymer of PS reinforced with a specific weight fraction of GO (0.5 wt. %). An exploration of suitable solvents and dispersion techniques, to ensure a uniform distribution of GO nanosheets in polymer matrices. The study investigated the required time of dispersing GO nanosheets in the polymer matrices to optimise the conditions of preparation of nanocomposites by employing different dispersion techniques.

2- A study of the effect of different low weight fractions of GO in the range (0.01- 1.0) wt. % on the structural, morphological, physical and mechanical properties of the PS/GO nanocomposites.

3- Investigations on the nanomechanical behaviour of cryogenically fractured surfaces on the sample with the highest weight fraction of GO. This part of the research was undertaken in order to finding the reduced Young's modulus at the nanoscale for GO and PS. Many techniques were employed for drawing the required conclusions for this objective.

4- A study of the effects of the rGO obtained from low exfoliating temperatures on the different properties of PS/rGO nanocomposites with performing the required tests to verify the reduction. The obtained results of PS/GO and PS/rGO were then compared.

5- Investigations on another amorphous styrenic polymer which was SAN at different low loadings of GO, and studies of the resulting structure, morphology and properties.

Chapter 2

Literature review

2.1. Introduction

Composite materials can be defined as a heterogeneous combination of two or more materials having different properties. One of the materials in the composite acts as the matrix which occupies the main part of the volume, and the other material is the reinforcement to the matrix which is finely dispersed within the matrix. The appropriate combination of matrix and reinforcement materials leads to physical properties (e.g. electrical, mechanical and thermal) that are not only superior to those of the individual components, but may offer new characteristics that are not present in the components original form.

Composite materials can be fabricated from a wide range of materials for both matrix and reinforcement, and the reinforcement can vary in size from metres (e.g. reinforced concrete) to nanometres (Giannelis, 1996). Composites with reinforcements at this latter scale are known as nanocomposites, and the research described in this thesis is based on studies of nanocomposites 'preparation, characterization, and properties. The remainder of this chapter will provide the background research on the fabrication and characterization of these materials, along with the current status of the research in this field, and the potential practical applications of these material. Nanocomposites, refer to ultrafine phase dimension fillers reinforcing many types of matrices (Giannelis, 1996). Amongst these is the polymer matrix and polymer nanocomposites PNCs can be defined as including filling agents that have at least one dimension at the nano-scale in the polymer matrix.

The reinforcements may be one dimensional such as nano-fibres or carbon nano tubes CNTs, two dimensional 2D additives such as graphene sheets, or 3 dimensional 3D additives such as spherical particles (Salavagione *et al*. 2011).

The nano-scale covers the range of 1-100 nanometres nm (1 nm = 10^{-9} m) for the size of the incorporated fillers in the matrix (Paul & Robeson, 2008).

(Salavagione *et al*. 2011) reported that the earliest study on nanocomposites was in 1950 when the effect of exfoliated layered silicate was studied on latex based elastomers.

However, significant industrial and academic interest in nanocomposites began with the work of (Okada & Usuki, 1995) who were based at the Toyota central research and development laboratories in Japan. They highlighted and explained the considerable mechanical improvement obtained by reinforcing Nylon-6 with a type of clay known as montmorillonite MMT with which they successfully prepared a polymer clay nanocomposite. The property enhancement of PNCs can be achieved by incorporating low loadings of nanofillers in the matrix (typically at a 1-10 % volume fraction) which contribute to weight reduction facilitation of the processing (Vaia & Maguire, 2007).

(Rafiee *et al*. 2009) described the improvement in (Young's modulus and tensile strength) for epoxy reinforced with 0.1 wt. % of graphene. Two other reinforcements along with graphene platelets were investigated, namely single walled carbon nanotube SWCNT and multi walled carbon nanotube MWCNT and the results showed that epoxy reinforced with graphene nanoplatelets GNPs performed considerably better than epoxy reinforced with SWCNT and MWCNT in terms of enhancing a variety of mechanical properties including Young's modulus, tensile strength, fracture energy, fracture toughness and resistance to fatigue crack growth. For example, Young's modulus and tensile strength for the epoxy reinforced with 0.1 wt. % of GNPs were improved by (31and 40) % respectively compared to same weight fraction of SWCNT that reinforced the same polymer as the improvement showed (3 and 14) % only. Figure 2.1 is reproduced from the work of (Tjong, 2006) and shows the effect of low loadings of different nanofillers on the mechanical properties of nylon-6.

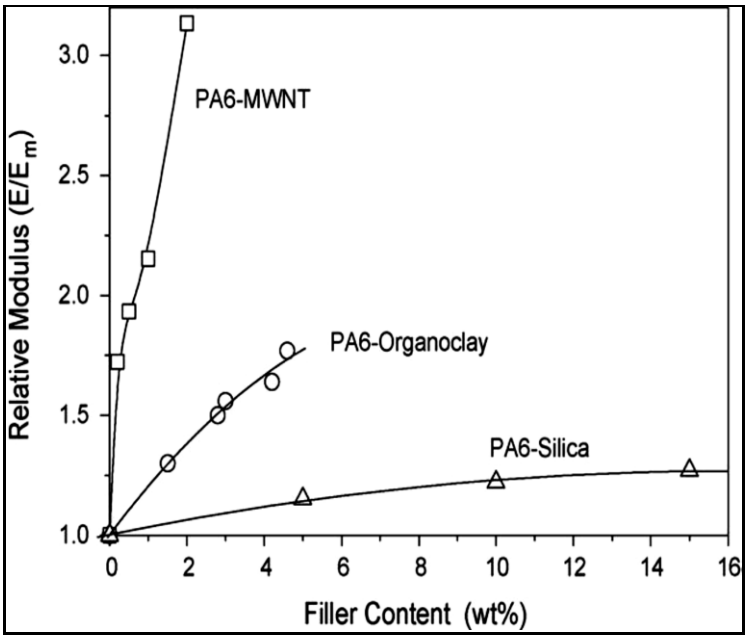

Figure 2.1. : The effect of weight fraction on the mechanical properties of Nylon-6. The figure was cited by (Tjong, 2006). Adapted with permission from the publisher (Elsevier).

Figure 2.1 shows the improvement in mechanical properties for nylon-6 reinforced with low loadings of MWCNT compared to higher loadings of different reinforcements to the same polymer.

PNCs are important because they offer a range of promising applications in the automotive, aerospace, marine, military and building industries (Pandey *et al*. 2005; Zeng *et al*. 2008). (Yu *et al*. 2014) demonstrated an efficient anti-corrosion application for PS reinforced with 2.0 wt. % modified GO.

Another potential application as a membrane (gas barrier) was reported by (Ionita *et al*. 2014) based on a polysulfone PSF matrix with very low loadings of GO (0.25, 0.5 and 1.0) wt. % . Table 2.1. below summarises some other commercial applications of various PNCs.

Table 2.1. : Commercial applications for some of PNCs. (Paul & Robeson, 2008).

Polymer matrix	**NP**	**Property improvement**	**Application**	**Company**
PA 6	Exfoliated clay	Stiffness	Timing belt cover, automotive	Toyota / Ube
TPO (Thermoplastic Polyolefin)	Exfoliated clay	Stiffness / Strength	Exterior step assist	General motors
Epoxy	CNT	Strength / stiffness	Tennis rackets	Babolat
Polyisobutylene PBI	Exfoliated clay	Permeability barrier	Tennis balls, tyres, soccer balls	InMalt LLC
SBR rubber	Not disclosed	Improved tyre performance in winter	Winter tires	Pirelli

In spite of the impressive potential for PNCs, there are many challenges that need to be solved before these applications can represent viable alternatives to existing technologies. The main challenges are given below:

1- The preparation of homogenous polymer nanocomposites represents a major challenge in the field. For example fabricating a homogenous dispersion of NPs or nanofillers in the matrix is a significant challenge in its own right (Tjong, 2006).

Figure 2.2. illustrates the meaning of homogenous dispersion for different kinds of NPs in the polymer matrix (Vaia & Maguire, 2007).

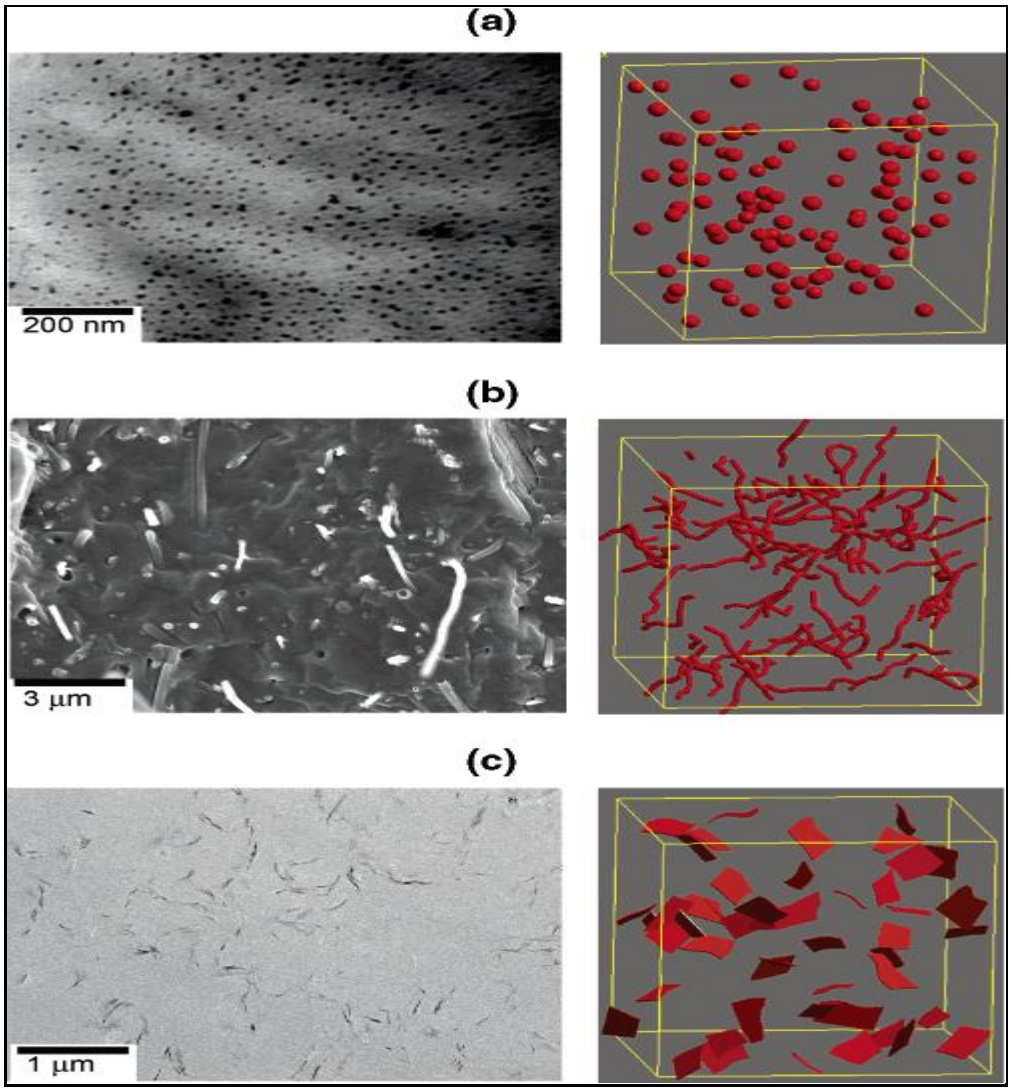

Figure 2.2.: Representative PNC's morphologies showing random dispersion of: a- Spherical 0D, b- Rod like 1D and c- Plate like 2D nanofillers (Vaia & Maguire, 2007). Adapted with permission from the publisher (American Chemical Society).

Part (a) of the Figure 2.2. represents the dispersion of 0D spherical CdSe/ZnS quantum dots dispersed in silk-elastin protein, Part (b) represents 5.0 wt. % rod like carbon nanofibers CNFs dispersed in thermoplastic polyurethane TPU, and part (c) represents 3.0 wt. % plates of MMT dispersed in cured epoxy. The homogenous dispersion for all of the aforementioned reinforcements in different kinds of polymer matrices can be seen.

Many techniques are employed to enhance the dispersion of the nanofillers in the polymer matrices. For example, longer mixing time and/or higher mixing speed using a twin screw micro- compounder contributed efficiently to creating the dispersion of 1.0 wt. % graphene nanoplatelets GnPs in the immiscible polymer blend of SAN (40.0 wt.%) and PC (59.0 wt.%).

A study published by (Liebscher *et al*. 2013). Some authors adopted different strategies related to functionalization to improve the dispersion of the nanofillers in the polymer matrices. For example, (Pour & Ghaemy, 2016) used polymer grafted GO to enhance the dispersion of GO in epoxy resin that led to better dispersion and consequently improvement in mechanical properties.

2- The addition of nanofillers to the matrix, for example clay, lead to improve the Young's modulus as well as the strength. The study published by (Fornes *et al*. 2001) supported the aforementioned approach. In some cases, the opposite might happen and this is another challenge needs to be investigated. (Stretz *et al*. 2005) showed that the addition of 3.2% of MMT to SAN led to decrease in the values of strength and strain at break compared to the neat polymer.

3- One of the most important factors regarding the performance of PNCs concerns the degree of adhesion between the matrix and the nanofillers. This is a significant gap in the field of PNCs because there are no specific techniques measuring the degree of adhesion of the nanofillers to the polymer matrices (Paul & Robeson, 2008).

4- The property- morphology correlation in PNCs refer to any possible change in mechanical, thermal and electrical properties generated from the change in morphology of polymer associated with the addition of the nanofillers. The understanding of this correlation is still in its early stages though some progress that has been recently achieved. This requires a comprehensive understanding of the interface properties, the nanofillers distribution, and identification of correlations between the nanofillers and nanofillers-matrix interactions and the way these impact on the various properties of the fabricated material (Vaia & Maguire, 2007).

(Zilg *et al*. 1999) have elucidated this where they showed the correlation between the morphology of the epoxy reinforced with different low loadings of organophilic layered silicate (2.5, 5.0, 7.5 and 10.0) wt. % and thermal and mechanical properties such as the glass transition temperature, toughness, and stiffness. The authors reported an improvement in the toughness (397 $J.m^{-2}$ for 2.5 wt. % of one type of layered silicate reinforcements compared to 158 $J.m^{-2}$ for pure epoxy) associated with the formation of dispersed anisotropic laminated nanoparticles consisting of intercalated layered silicates. A better understanding of the structure-property relationships in PNCs will pave the way towards customising materials with specific properties through the appropriate fabrication technique and optimum material trade-offs. Earlier approaches to exploring mechanical behaviour-morphology, such as Halpin- Tsai and Mori – Tanaka, have not been sufficiently consistent for explaining the structure-property trend across the spectrum of PNCs. Quantitative investigations on their degree of success has been hampered by many factors such as the interface, the dispersion of NPs and the morphology. (Vaia & Maguire, 2007) have stated that this gap in knowledge will require significant research efforts to address. These challenges listed above are the subject of research in various university institutes and industrial laboratories and the efforts are in progress to address them.

2.2. Polymer matrices

Thermoplastics, thermosets, elastomers, block copolymers and hydro / aerogels are the widely used matrices offering a diversity in chemical and physical properties that can be tailored to a variety of applications. All of these matrices are of significant interest to the graphene research community. For example, the hydro / aerogels polymers have important applications such as shock absorbance and thermal or electromagnetic shielding (Hu *et al*. 2014). The specialization of the current study is in thermoplastic and copolymer matrices due to their low cost, easiness in processing and the ability to employ them in wide range of applications in many fields such as medicine, military aspects, and aerospace. The selection of a polymer matrix for a particular application must take into account the following considerations:

1- The mechanical properties: In general, polymer matrices have modest mechanical properties compared with matrices composed of ceramics or metal. Exceptions can be found in the literature however, for some linear amorphous polymers with high elastic modulus.
2- The mechanical strength in polymer matrices is significantly decreased when heated to temperatures above the glass transition temperature T_g.

For the aforementioned reasons, a variety of additional reinforcing agents and nanofillers are incorporated in polymer matrices in order to enhance the mechanical performance as well as other physical properties such as conductivity (Hu *et al*. 2014). (Young & Lovell, 1990) classified these polymers as shown in Figure 2.3.

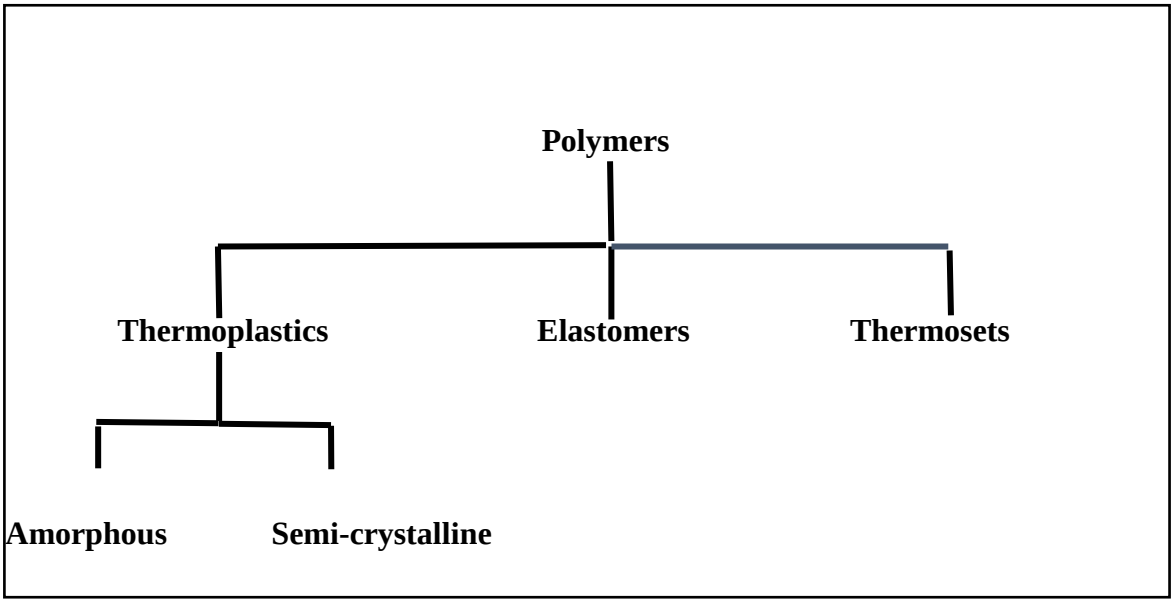

Figure 2.3. : The common way of polymers classification. (Young & Lovell, 1990).

Another form of classification described by (Stille, 1966) and adopted by Carothers consisted of two broad categories which are condensation polymers, and addition polymers and this is based on the method of polymerization. However, this approach was found unsatisfactory when it was recognized that some condensation polymerizations have the characteristic features of typical addition polymerization and vice versa (Young & Lovell, 1990). The polymers classified in Figure 2.3. are described separately below.

2.2.1. Thermoplastic polymers

Polymers flow when heated are known as ‘’ Thermoplastics’’. Many linear or branched polymers that are not extensively cross-linked can be softened upon heating and moulded into various shapes. These polymers can be moulded or remoulded by using specific processing techniques such as injection moulding and extrusion. Some thermoplastic polymers are totally amorphous and cannot be crystallized even upon annealing. Amorphous polymers are characterized by their glass transition temperatures, which mean the temperature at which the polymers transform from glassy to rubbery state. Polypropylene PP, polyphenylene sulfone PPS, polyether ether ketone PEEK and polystyrene PS are examples of thermoplastics (Stille, 1966; Moore, 1967; Sperling, 1992; Gay, 2015).

2.2.2. Thermosetting polymers

This kind of polymer is a rigid material and can be considered as network polymers (polymers that contain long and flexible branches connected at only a few sites along the chains). They have a high degree of crosslinking (many crosslinks for the polymer units) which restricts the motion of the chains. These polymers are intractable once formed, and undergo degradation at high temperatures in contrast with thermoplastics. The relative hardness and rigidity for these polymers compared to elastomers are acquired during the final stages of manufacturing by a process of solidification. The establishment of the three dimensional networking observed at the stage is referred to as ‘’Curing’’. Examples of these kinds of polymers are epoxies, polyesters and phenolics (Moore, 1967; Young & Lovell, 1990; Gay, 2015).

2.2.3. Elastomers

Elastomers are low crosslinking density polymers which gives them a rubbery quality. They can stretch to high extensions under applied stress and to recover their original dimensions when the stress has been removed. The rubbery polymer chains extend under deformation but are prevented from permanent flow by the crosslinks. The common rubber band is a typical example about this kind of polymer (Young & Lovell, 1990; Sperling, 1992).

2.2.4. Homopolymers and Copolymers

Polymers derived from one specific monomer (A molecule that can be bounded to other identical molecules to form a polymer) are defined as ‘’Homopolymers’’. The chemical structure of a homopolymer is represented by repeated unit between two brackets as follows:

A__ A__ A __ A __ A is symbolised as __[_A _]$_n$___. Where n is the number of monomers. A more complex monomer of ‘’Ethylene’’ $CH_2 = CH_2$ which is used to synthesize polyethylene is written as __[__CH_2 ___ CH_2_]$_n$__. Copolymers on the other hand are derived from more than one species of monomer. The molecules of such polymers include two or more different types of repeating units. A truly random copolymer can be represented as:

B__ B __ B __ A __ B __B __ A __ A ~ ~ ~

Whilst alternating copolymers can be represented as:

A __ B __ A __ B __ A __ B __ A __ ~ ~ ~.

Block copolymers are polymers where the repeating units are organised in long periodic sequence. For example:

A __ A __ A __ A __ B __ B __ B __ B ~ ~ ~.

Finally, graft copolymers are branched, and the branches have different chemical structure as compared with the main chain as illustrated below:

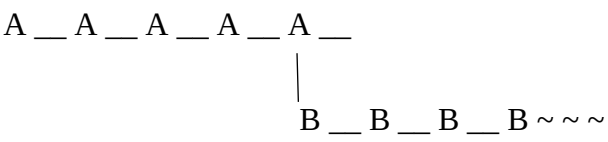

Table 2.2. shows the nomenclature for copolymers according to (Young & Lovell,1990).

Table 2.2.: The nomenclature of copolymers. (Young & Lovell, 1990).

Type of copolymer	**Nomenclature**
Unspecified	Poly (A-co-B)
Statistical	Poly (A-stat-B)
Random	Poly (A-ran-B)
Alternating	Poly (A-alt-B)
Block	Poly A-block-Poly B
Graft ‘’Poly B branches on a poly A main chain’’.	Poly A-graft-Poly B

Examples for these types of polymer are poly (styrene-b-isoprene-b-styrene) sis as a block copolymer and polystyrene – polyacrylamide copolymer (Verdejo *et al*. 2011; Guo & Dong, 2011). The next sub-section will describe two specific thermoplastic polymers used in the current study.

2.2.5. PS and SAN

PS $(C_8H_8)_n$, is a name that designates a family of plastics derived from a ‘’styrene’’ monomer. The monomer which is the building block for PS and other styrenic polymers was first synthesized in the laboratory in 1839 and for commercial purposes by Dow Chemicals Company in the U.S.A in 1938. It is a glassy amorphous homopolymer with remarkable clarity, gloss and processability. At the same time, it is inherently brittle and has a high resistance to water (Teach and Kiessling, 1960; Schiers and Priddy, 2003). The repeating unit for PS is a liquid with a boiling point of 145.2 ^oC, a freezing point of -30.63 ^oC and a refractive index of 1.5439. It is prepared commercially through the catalytic removal, at high temperatures, of hydrogen from ethylbenzene in the gas phase. Free radical polymerization is widely used for the commercial production for PS. The chemical reaction for commercial production of PS monomer (styrene) is shown symbolically in Figure 2.4. which clarifies that such a commercial production is carried out by the catalytic removal, at high temperatures, of hydrogen from ethylbenzene in the gas phase. PS as used commercially contains up to 2000 styrene units in the polymer chains, which are coiled and tangled in a random manner.

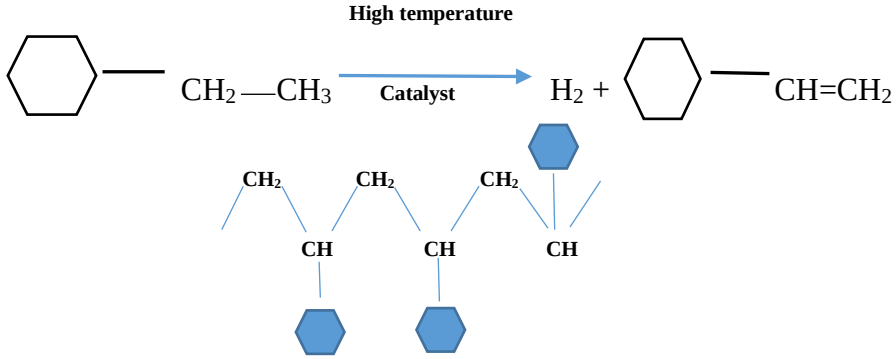

Figure 2.4. : The commercial production for styrene monomer (Teach and Kiessling, 1960).

The useful properties of PS include: Light weight, the ability of moulding using high speed injection moulders (300 mm/sec), good dimensional stability, odorless, and non-toxicity. It is a slowly burning material that leaves a sooty residue and the T_g for PS is 100 ^oC.

The amorphous structure of PS is called atactic PS. It has a wide range of applications such as disposal cups, food containers and toys (Teach and Kiessling, 1960).

SAN, that has a chemical formula of $(C_8H_8)_n$-$(C_3H_3N)_m$, is a copolymer which is hard, transparent and rigid. It has a good dimensional stability with a higher thermal stability than PS. T_g of SAN is higher than that of PS (~107 ^oC). SAN has superior mechanical properties (Tensile modulus is 3.27 GPa and tensile strength is 49 MPa) and high chemical resistance to fats, grease and mineral oils, which is attributed to the presence of acrylonitrile AN in its chemical structure. SAN which is currently available in the markets contains about 30 % of AN. SAN can be easily fabricated using traditional techniques such as injection moulding, extrusion and thermoforming. The method of fabrication includes mixing of 49 parts of styrene with 21 parts of AN. The resultant mixture should be mixed with 30 parts of solvent such as ethylbenzene. The whole mixture should be polymerized at 145-180 ^oC in a continuous unit. When the mixture contains 50% polymer then the unreacted monomers and the used solvent are removed using devolatilization. Finally, the polymer product can be extruded into granules with or without the addition of colorants.

Due to its polarity, SAN is a hygroscopic material, and can absorp up to 0.6% water in room temperature RT. With regard to applications, it is used in food and pharmaceutical Packaging, lenses, refrigerator shelves and automotive accessories. Dow chemicals,U.S.A is one of the commercial suppliers of SAN and which is also known as TYRIL. Figure 2.5. shows the structure of SAN (Teach and Kiessling, 1960; Olabisi, 1997; Kim & Ryu, 2015).

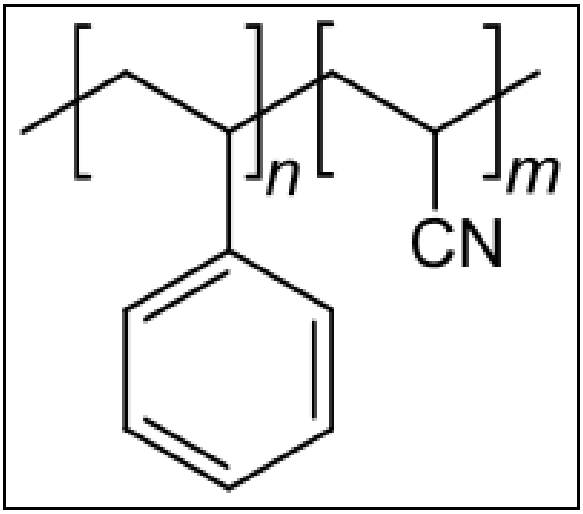

Figure 2.5.: The chemical structure of poly (styrene -co- acrylonitrile) polymer (Teach and Kiessling, 1960).

2.3. Types of Fillers

Fillers are used, in general, to enhance the mechanical and thermal properties of polymers. They have become an integral part in many applications particularly those in which the mechanical properties are important. There are many kinds of traditional fillers such as carbon black, talc and glass fibres. Incorporating fillers into a matrix however is not without its challenges and these are listed below (Bhattacharya, 2016):

1- For a modest enhancement in polymer properties a high loading (high weight or volume fraction) is required for traditional fillers, which are mostly have a micron size.
2- The high density of traditional fillers represents a trade-off for achieving light-weight composites.
3- The poor interfacial interaction between traditional fillers and the matrix leads to poor interfacial adhesion between the different components of the composite material and this can lead to failure.

(Namitha *et al*. 2013) reported that silicone rubber reinforced with nano- alumina showed better mechanical properties (high mechanical strength) compared with the same polymer reinforced with micron-scale alumina. Nanofillers can be classified according to their physical size. If one of the dimensions is at the nano-scale they are described as nanowires or nanotubes. For two nano-scale dimensions they are called nano plates and examples are graphene and nanoclay. Finally, with three nano-scale dimensions such as graphite, we have nanoparticles which can also be labelled spherical and cubical nanoparticles. The desirable characteristics of nanofillers for enhancing the performance of the nanocomposites are listed below (Bhattacharya 2016):

1- Nanofillers should have excellent mechanical properties such as high strength and Young's modulus.
2- For successful interactions with the polymers a high aspect ratio and high surface area.
3- Nanofillers must be homogenously dispersed in the polymer matrix and agglomeration must be avoided.

Figure 2.6. shows types of nanofillers derived from 2D graphene (Geim and Novoselov, 2007).

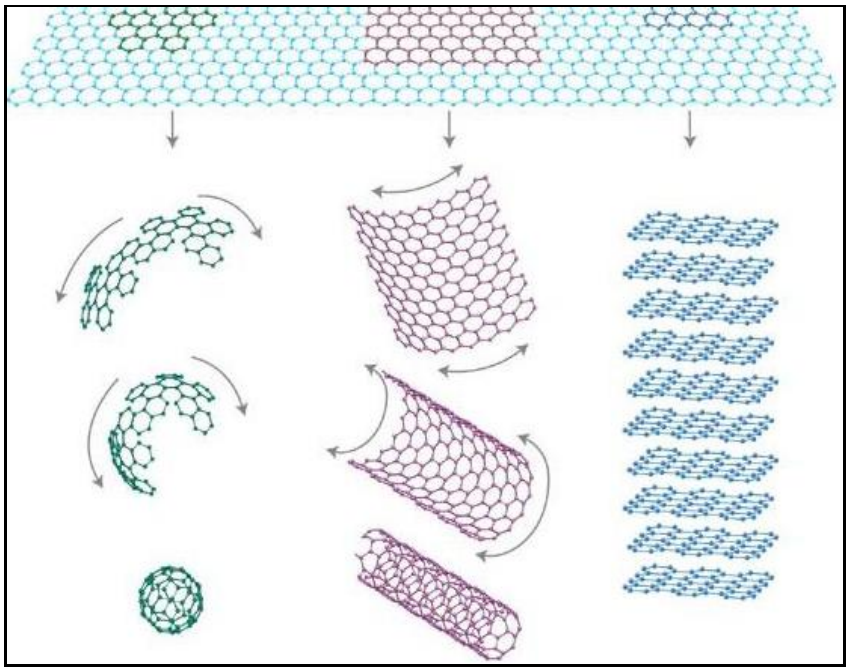

Figure 2.6. : Types of nanofillers derived from 2D graphene which can be wrapped up to 0D Bucky balls (left hand side column of spherical shapes) , 1D nanotubes (column in the middle), or 3D graphite (the last column in the right hand side). Adapted from (Geim and Novoselov, 2007) with permission from the publisher (Nature publishing group).

However, there are many challenges to be solved in the fabricating nanofillers with improved properties before they can be deployed nanofillers practical applications. Most of the research work has been carried out using one type of nanofillers and an important goal is to successfully incorporate more than one kind of nanofillers in the polymer matrix. (Bhattacharya, 2016). Recently however, (Asif *et al*. 2016) incorporated 3D graphene and CNT in a polyaniline PANI matrix for use in an electrode for a supercapacitor application.

2.3.1. Graphite oxide

The precursor of GO is graphite oxide which is a synthesized form of the natural flake graphite powder. One technique for obtaining GO from graphite oxide is exfoliation by ultrasonication. With constant mechanical stirring and ultrasonication the weak (around -0.047 to -0.054 eV/atom according to Birowska *et al*. 2011) but numerous Van der Waals attractive forces between graphitic layers can be overcome. Given the hydrophilic nature of graphite oxide this permits water molecules to intercalate between the stacking layers of the graphite oxide (Saravanan *et al*. 2014; Economopoulos & Tagmatarchis, 2013).

Graphite oxide was first produced in 1840 by Scafhaeutl and later by Brodie in 1859. The latter dealt with natural graphite with a mixture of potassium chlorate and fumes of nitric acid at a temperature 60 ^{o}C. In 1898, Staudenmaier prepared graphite oxide by oxidizing graphite with sulphuric, nitric acid and potassium chlorate. Many years later in 1958, Hummers and Offeman presented their method of oxidizing 100 g of graphite to produce graphite oxide with a water free mixture of concentrated sulphuric acid, sodium nitrate and potassium permanganate. The water free mixture is important to pursuit a high quality graphene (Hummers & Offeman, 1958; Gengler *et al*. 2010).

A modified Hummers method was published by (Hirata *et al*. 2004) in which 10 g of graphite was used. The same chemical species were later used to prepare graphite oxide in 2004 but with different quantities.

In 2010, Marcano and collaborators (Marcano *et al*. 2010) used 3 g graphite flakes with specific quantities of $NaNO_3$, $KMnO_4$ and H_2SO_4 to obtain a high yield of graphite oxide.

The same authors clarified the new approach of graphite oxide preparation which they called the Improved Hummers' method IHM. In order to improve the oxidation process, they excluded $NaNO_3$ from the reaction and increased the amount of $KMnO_4$ with a mixture of H_2SO_4/H_3PO_4. The oxidation process of the graphite flakes leads to the break-up of the SP^2 hybridized structure of the stacked graphene sheets which results in an increase in the distance between adjacent sheets from 3.35 A^{o} to about 6.8 A^{o} for graphite oxide. This will facilitates the delamination of graphite oxide to GO sheets through the assistance of low power sonication (Compton & Nguyen, 2010).

It should be mentioned that the Hummers' method was extensively used by researchers for preparing graphite oxide and GO afterwards. Compared with other methods such as Staudenmaier it presented a more efficient oxidation method with less hazardous reactive species (Eda & Chhowalla, 2010).

Nevertheless, it has been emphasized that the integrity of the resulting graphite oxide chemical structure is questionable due to the complexity of the material processing and the lack of detailed information available by the existing characterization techniques. The earliest structural models of graphite oxide assumed it is composed of regular lattices with discrete repeatable units. In the period 1946-69 different structures of graphite oxide were proposed by Hoffman, Ruess, Scholz-Boehm and Nakajima Matsuo (Dreyer *et al*. 2010).

The most accepted model of graphite oxide to emerge was the (Lerf-Klinowski) model which was supported by solid state nuclear magnetic resonance SSNMR measurements. This model suggested that carboxylic acid functional groups and carbonyls are located on the periphery of the basal plane whilst hydroxyls and epoxides can be found in the basal plane of the nanosheet (Lerf *et al*. 1998; Zhu *et al*. 2010).

Figures 2.7. and 2.8. illustrate the (Lerf-Klinowski) model of graphite oxide, and the solvent exfoliation approach for obtaining GO from graphite oxide respectively (Dreyer *et al*. 2010; Potts *et al*. 2011).

One of the challenges for the production of graphite oxide is the ethical requirement to develop a preparation technique that is Eco-friendly or green approach. The chemical components used to prepare graphite oxide are highly reactive and hazardous materials and some of them are explosive materials or highly toxic. (De Silva *et al*. 2017).

Figure 2.7. (b) shows the most accepted structure of GO which is the most widely adopted and cited model by the researchers in their work.

Figure 2.7. (a) shows the structure of graphite oxide according to Lerf–Klinowski model.

Figure 2.8. shows the difference in structure between the layered graphite oxide and the exfoliated GO obtained through liquid phase exfoliation.

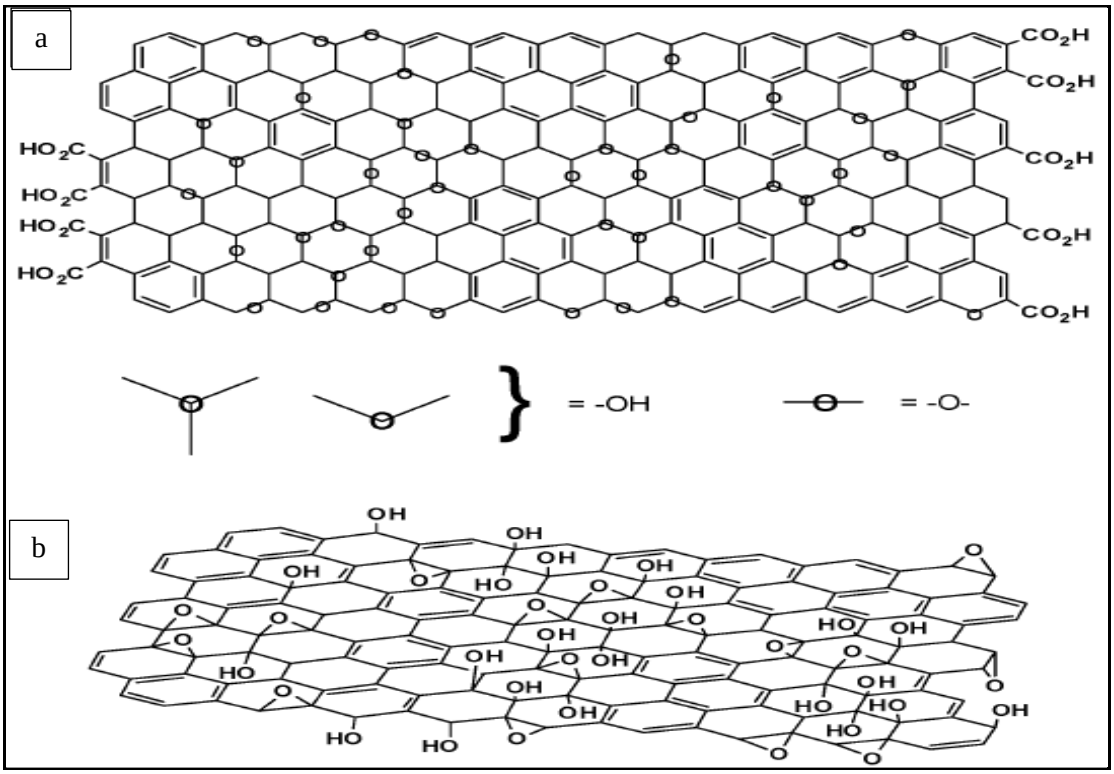

Figure 2.7.: (a) Lerf-Klinowski model of graphite oxide (b) The structure of GO. Adapted from (Dreyer et al. 2010) with permission from the publisher (The Royal Society of Chemistry).

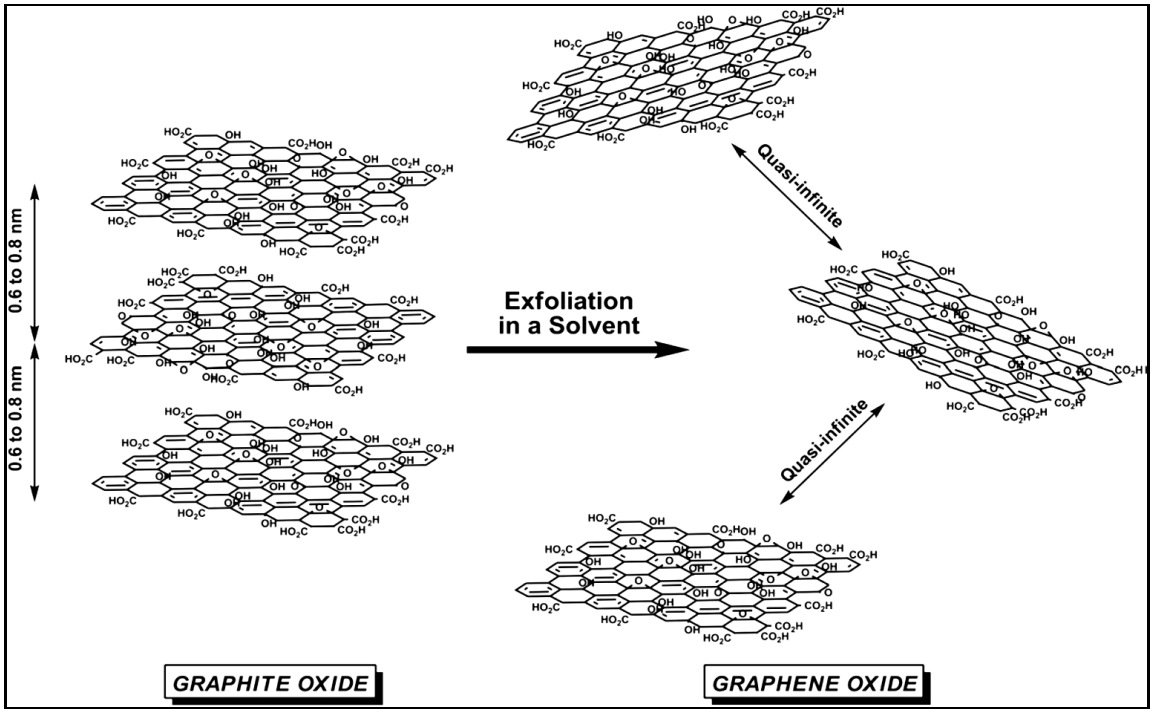

Figure 2.8.: The chemical structure of graphite oxide with exfoliation in the solvent of GO from graphite oxide. Adapted from (Potts et al. 2011) with permission from the publisher (Elsevier).

2.3.2. Graphene and GO

The production of graphene is regarded as a potentially revolutionary development in the discipline of materials science. It is a two dimensional material that shows promise of exceptional properties that could be exploited in a wide range of applications and with its discovery in 2004 it is at a relative early stage of development (Geim & Novoselov, 2007).

To quote from (Chen *et al*. 2013) 'It (graphene) generates an increasing interest both in fundamental science and potential applications due to its unique structure and remarkable properties such as excellent conductivity, high electron mobility, superior chemical stability and large surface to volume ratio'. Graphene is a monolayer material of SP^2 hybridized carbon atoms arranged in a honeycomb lattice in two dimensions 2D (Salavagione *et al*. 2011).

GO can be defined as a water soluble nanomaterial synthesised through a chemical reaction of graphite crystals with strong oxidizers in order to introduce oxygen containing defects in the graphite stack.

Some assumed models of this material suggest that GO is a group of sheets composed from many functional groups which including hydroxyls, epoxies, ethers, diols and ketones that work as a network to connect graphene-like sheets of GO together (Shen *et al*. 2009).

Graphite is an abundant material and can be used to prepare GO via a procedure of oxidation. GO has attracted the attention of researchers because it is regarded as a resource for preparing graphene (Alhassan *et al*. 2013). Powdered flake graphite is the material used to prepare GO by a chemical route using Hummers' method (Liu *et al*. 2014). GO is considered an effective reinforcement for improving the mechanical performance of materials such as polymers. This is achieved through the functional groups of GO that provide an interfacial strength with the polymer chains in nanocomposite material thereby enhancing the Young's modulus and tensile strength (Cano *et al*. 2013).

According to (Hu *et al*. 2014), GO is an amphiphilic material that facilitates an interaction with different functionalities having both hydrophilic and hydrophobic properties. The amphiphilicity of GO reflects two important facts described below:

1- The ability of GO to interact successfully with the polar and non-polar polymer matrix in order to enhance the mechanical performance. For example, (Gao *et al*. 2014) used a polar polymer, acrylonitrile butadiene styrene ABS with GO and (Yu *et al*. 2014) used PS which is non-polar polymer with GO. They both interacted successfully with GO which confirming the amphiphilic nature of the nanomaterial.
2- The interface can acquire greater strength by matching the heterogeneous nature of the matrix with GO. This means the hydrophobic and hydrophilic nature for GO and the polymer matrix can be assembled and this will consequently improve the interfacial reaction between GO and heterogeneous polymers. (Cai *et al*. 2012) prepared a polyurethane PU/GO nanocomposite. PU includes both polar and non-polar segments and though the matching between different domains is still under investigation.

2.3.3. Preparation of graphene and GO

Graphene can be prepared according to two general approaches as follows:

1- The TOP-DOWN approach, which involves a decomposition of bulk materials, such as CNT and graphite, to a graphene nano-structure.
2- The BOTTOM-UP approach, which refers to synthesizing graphene using hydrocarbon gases.

Both approaches entail a number of physical and chemical methods (Pumera, 2010).

The five most important of these are listed below(Compton & Nguyen, 2010; Guo & Dong, 2011):

1- Mechanical exfoliation of a single sheet of graphene from bulk graphite by applying Scotch tape over a silicon substrate and then removing it. This approach is regarded as an inefficient with a low yield of a single layer sheets of graphene having acceptable quality. Nevertheless, it was the first successful method for producing a single layer or few layers of graphene.

2- Epitaxial growth of graphene films on a silicon carbide substrate SiC which is a promising method for obtaining a uniform wafer size of graphene layers. The single crystal of SiC is heated up to 1400 ^{o}C in vacuum and graphene is growing epitaxially on the substrate. (Dharmaraj *et al*. 2014) used this method and achieved a large area of homogenously stacked bilayer epitaxial graphene SiC (0001) substrate.

3- Chemical vapour deposition CVD of the graphene monolayer. Transition metal surfaces are employed in this technique with the assistance of hydrocarbon gases. The deposition temperature is 1000 ^{o}C and (Tu *et al*. 2014) used a copper substrate with a flow of H_2 and CH_4 and controllably synthesized 1 and 7 layers of graphene.

4- Longitudinal unzipping of CNT describes several methods in which a large scale production of graphene nanoribbons GNRs is produced with a controllable width. Two unzipping methods include oxidative treatment of CNTs and plasma etching with nanoparticles of transition metals (Co or Ni) and high burning current. These techniques have been effectively developed in order to efficiently unzip CNTs to produce GNRs that have applications in electron devices. (C. Chen *et al*. 2013) demonstrated the unzipping of CNTs to ultra-narrow GNRs with smoother edges upon oxidation.

5- The reduction of GO where the oxidative exfoliation of graphite took place followed by thermal or chemical reduction. Low cost graphene with relatively large scale production can be achieved using this method with potential for applications in photovoltaic cells and electrochemical devices.

The hydrophilic nature of GO due to the presence of abundant oxygen functional groups is transformed to a hydrophobic form for graphene obtained by chemical reduction. The possibility of agglomeration for the resultant graphene via chemical reduction is high, though the solubility in organic solvents is limited which results in problem with further processing and applications. Nevertheless, this method still represents a vital strategy for obtaining graphene-like sheets in bulk even though there are other drawbacks associated with graphene production by that method. These drawbacks described earlier include hydrophobicity and agglomeration. (Zhang *et al*. 2014) chemically reduced GO using an eco-friendly reductant (sodium acetate trihydral) and this resulted in a few layers of graphene but with poor dispersion in water which confirmed earlier speculations.

Table 2.3. summarizes the methods for the production of graphene along with some of salient features of these approaches. (Guo & Dong, 2011).

Table 2.3. shows graphene's production methods with characteristics features. Modified from the reference of (Guo & Dong, 2011).

Method	**Precursor**	**Cost**	**Electronic quality**	**Number of layers**	**Size of layers**	**Throughput**
Mechanical exfoliation	Graphite	Low	High	Single and multiple	10 μm	Low
Epitaxial growth	Sic Wafer	High	High	Single and multiple	> 50 μm	Low
CVD	Hydrocarbons	High	High	Single and multiple	> 100 μm	Low
Unzipping CNT	CNTs	Low	Inferior	Single and multiple	Several μm	Low
Reduction of GO	Graphite	Low	Low	Single	Tens of nm-100 μm	High

Graphite oxide, the precursor of GO, is delaminated into a single layer of GO through low-power sonication in water. The presence of oxygen functional groups on the surface of GO plays a major role in the creation of a stable suspension of GO in aqueous media.

These functional groups support GO exfoliation in a number of solvents such as DMF and THF (Compton & Nguyen, 2010; Zhu *et al*. 2010).

Recently, GO was prepared as a foam (powder) that has a 3D macroscopic structure. The powder was prepared by processing graphene dispersions in aqueous media followed by a freeze-drying technique and is a promising route for preparing a highly fluffy and wrinkled GO suitable to disperse in different organic solvents and to prepare polymer nanocomposites afterwards. The GO suspension needs to be frozen in a refrigerator at -18 ^{o}C followed by freeze-drying under the influence of a condenser temperature of -20 ^{o}C at a very low pressure <20 Pa. The GO powder obtained by this method is unique in terms of its large active surface and high porosity. This new 3D structure is paving the way towards new applications especially in the field of energy storage (Ming *et al*. 2013; Li *et al*. 2015).

Figure 2.9. shows a scanning electron microscopy SEM image confirming the wrinkled morphology of GO prepared by freeze-drying (Li *et al*. 2015).

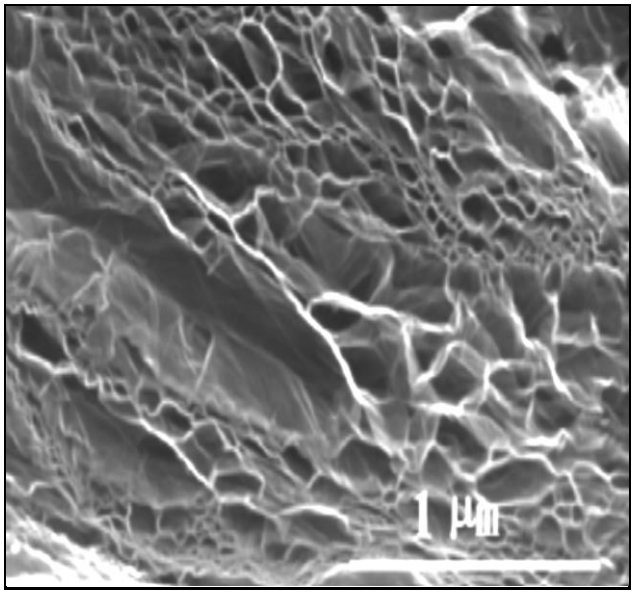

Figure 2.9. : SEM image confirming the wrinkled morphology of GO nanosheets prepared by the freeze-drying technique. Adapted from (Li et al. 2015) with permission from the publisher (Elsevier).

2.3.4. Structure of graphene and GO

Graphene is a flat 2D sheet of carbon atoms with a Van der Waals thickness of 0.34 nm. A CNT on the other hand is a rolled up monolayer of carbon atoms. Graphene has a high thermal and electrical conductivity of $5.1 * 10^{3}$ W m^{-1} K^{-1} and $6 * 10^{5}$ S m^{-1} respectively and measuring 1.0 nm is the thinnest known material. The width of graphene sheets is dependent on the method of production and can be from a few nanometres to many centimetres (Hu *et al*. 2014; Sun *et al*. 2013).

The graphene lattice is honeycomb shaped composed from two carbon atoms sub- lattices. The carbon atoms in the lattice and sub-lattices are bonded to each other with a σ bond (strongest type of covalent chemical bond). Each carbon atom in the lattice has a Π- orbital that participates in a delocalized network of electrons. The sheet of suspended graphene includes intrinsic corrugations. In a real 3D space however graphene might have other kinds of defects such as vacancies, topographical defects (pentagons, heptagons and/or their combination), adsorbed impurities which influences the shape of the structure in different ways (Zhu *et al*. 2010).

The structure of graphene is still a subject of discussion because, in one respect it appears as a 2D material with high crystal quality which enables the electrons to travel for some distance (submicron) without scattering. Some theories and experiments however show that perfect 2D crystals cannot be found in the Free State (does not react). On the other hand, the graphene structure studies so far are an integral part of a 3D structure, either embedded in a 3D matrix or supported by a bulk substrate (Meyer *et al*. 2007).

Graphene can form the following nanostructures according to constraints in the z-axis or the x-y axis as follows (Pumera, 2010):

i-) **z-axis constrained graphene** includes single, double and a few layers of graphene. This category also includes graphene platelets which are 10-100 layers of graphene with a thickness of about 3-30 nm.

ii-) **x-y-z axes constrained graphene,** which includes single layer graphene nanoribbons (zigzag or armchair graphene nanoribbons) prepared from SWCNTs. It also contains few layers of graphene nanoribbons prepared from MWCNTs. This structure also includes stacked graphene platelet nanofibres.

iii-) **Dimensionally unconstrained graphene** includes graphite as a bulk material consisting of hundreds of graphene nanosheets.

Graphite oxide is another sub-classification of this kind of graphene which was discussed earlier in section 2.3.1.

Figure 2.10. clarifies the structure of edges of graphene. Some of the graphene edges have zigzag geometry, while others have an armchair shaped geometry. The edges' shapes or geometries affecting the electrical properties of graphene (Pumera, 2010).

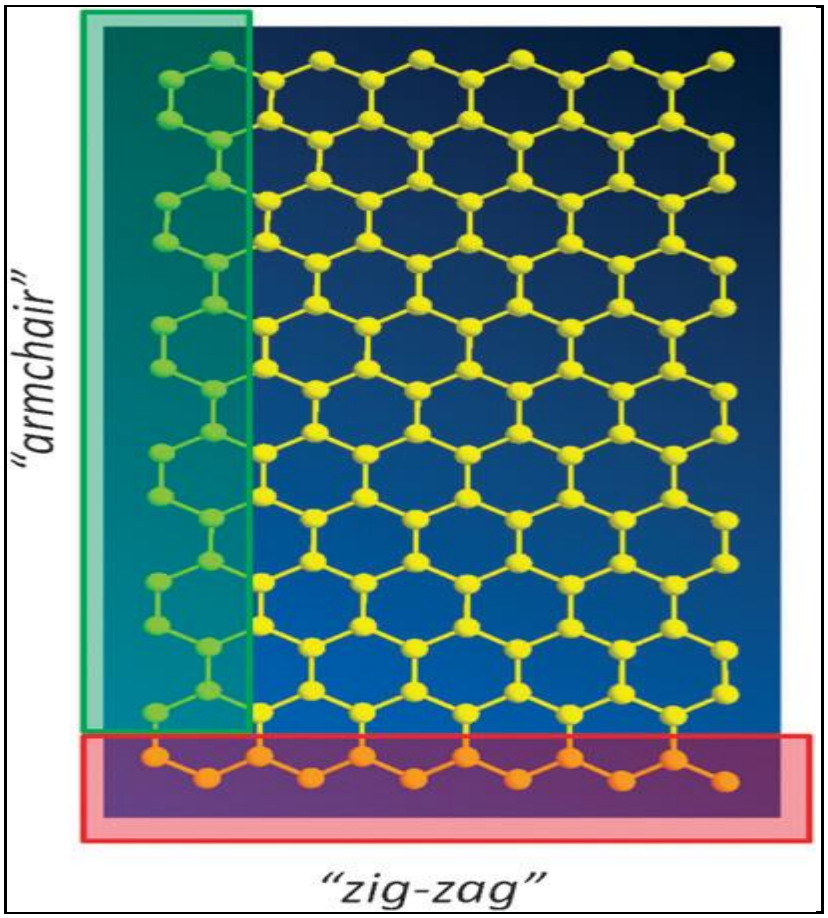

Figure 2.10. : The geometry of graphene edges. Adapted from (Pumera, 2010) with permission from the publisher (The royal society of chemistry).

GO is a relatively new nanoscale material that can provided an alternative path to the production of graphene. The structure of GO can be simplistically described as different oxygenated functionalities surrounded the graphene sheet. These oxygenated functionalities are carboxylic (—COOH) and carbonyls in the periphery of the graphene sheet.

The hydroxyls (-OH) and epoxies are located in the basal plane (Mkhoyan *et al*. 2009; Yongchao & Samulski, 2008) and the thickness of a monolayer sheet of GO is about (1-1.4) nm. This is thicker than a monolayer of graphene due to the oxygenated functionalities in the periphery and basal plane of the GO nanosheet and, adsorbed molecules and water - trapped molecules due to the hydrophilic nature of GO (Eda & Chhowalla, 2010). The structural analysis of GO can be derived from that of graphite oxide (Da Chen *et al.* 2012). Figure 2.11. refers simplistically to the difference in structure between graphene and GO (Hu *et al*. 2014).

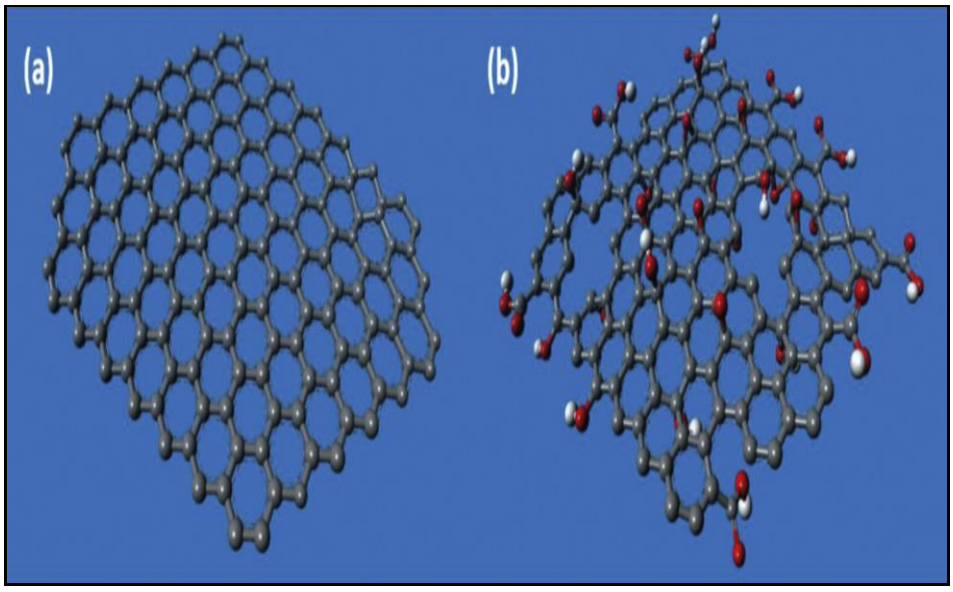

Figure 2.11.: Structural differences between graphene and GO. (a) The honeycomb lattice with hexagonal geometry that represents graphene. (b) The structure of GO. Grey, red and white balls represent different oxygen functional groups distributed in the basal planes and the edges. Adapted from (Hu et al. 2014) with permission from the publisher (Elsevier).

2.3.4.1. Reduction of GO

As discussed earlier the structure of GO can be viewed as a sheet of graphene with an abundance of oxygen functionalities (carboxyl, carbonyls, hydroxyls and epoxies) spread at the edges and basal planes. These functional groups have detrimental effects on the electrical properties of this material with regard to practical applications. For example, the planar SP^2 carbons of graphite are converted to SP^3 carbons and the Π-Π electronic conjugation of graphite is destroyed with the result that GO become an insulator (Kuila *et al*. 2013).

From an economic perspective, the direct approaches to producing graphene are not viable, exceeded $220 per Kg according to (E.L.Wolf, 2014), and efforts have been focussed on indirect approaches of starting with GO are more favoured by the research community. In order to produce graphene by this approach, techniques have been developed to deoxygenate the functional groups thereby leading to a partial recovery of the conjugated structure of graphene (Thakur & Karak, 2015). In short, the reduction of GO leads to an increase in the atomic ratio of C: O. and the higher the C: O ratio, the smaller the band gap which tends towards zero in pristine graphene (Glover *et al*. 2011).

The reduction of GO has the two main aims, of elimination of oxygen functionalities, and healing of structural defects (Pei & Cheng, 2012). Several different reduction methodologies have been employed to achieve the two important aims of, improving the efficiency of the reduction process, and enhancing the final properties of the reduced graphene oxide rGO sheets.

Figure 2.12. shows the meaning of reduction and the structural differences between graphite, GO, rGO and graphene (Mohan *et al*. 2015).

According to (Pei & Cheng 2012), the different strategies for reducing GO are summarised below:

1- Thermal approach: This includes several methodologies such as thermal annealing and microwave and photo reduction. For example, (Tu *et al*. 2015) used a thermal annealing methodology to reduce GO for nanoelectronics applications. Transitions between n-type and p-type was observed as the annealing temperature was increased. Graphene semiconducting properties were explored by the collaborators in their co-work.

2- Chemical approach: This includes a number of methodologies such as chemical reagents reduction, electrochemical reduction and photo-catalyst reduction. Hydrazine is a widely used chemical agent for GO reduction with this approach. (Park *et al*. 2011) used hydrazine for producing electrically conducting platelets by adding the hydrazine to the suspension of GO followed by stirring for 12 h in an oil bath under the influence of 80 ^{o}C. A black powder represents the rGO was obtained and this powder was dried under vacuum. A novel approach for reducing GO has been recently adopted by (De Silva *et al*. 2017) by using eco-friendly reductants to replace the highly toxic hydrazine. These reductants include sugars, proteins, plant extracts and other benign substances. The resultant rGO was highly dispersible and biocompatible.

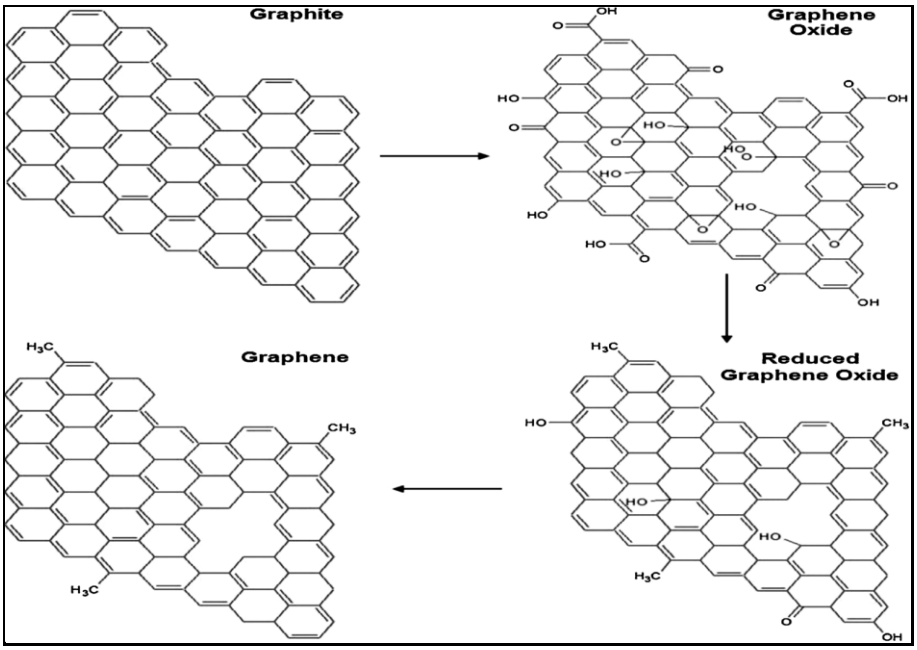

Figure 2.12.: The reduction process of GO followed by the proposed structure of rGO and graphene. Adapted from (Mohan et al. 2015) with permission from the publisher (Elsevier).

Figure 2.12. shows the stages of reduction starting from graphite followed by extensive oxidation that leads to form GO and the final stage shows the reduction of GO that refers to the removal of different oxygenated functionalities from the peripheries and the basal plane of GO that resulted in forming the sheets of graphene.

3- Multi-step reduction: In contrast with the aforementioned approaches which are single step process, multi-step reduction involves more complex processing involving two or more steps. (Wu *et al*. 2014) used a synergistic reduction for GO by using sodium hydroxide NaOH and microwave irritation (employing a microwave oven of 950 W for facilitating an efficient reduction). A higher degree of reduction was achieved with this approach resulting in 0.8 nm monolayer of graphene. Another multi-step reduction approach was adopted by (Jia & Zou, 2012) in which Iron powder was first used to obtain a partial reduction of GO. Then, aryl diazonium was used to make sulphonation that means producing sulphonic functional groups on the surface of the partially reduced GO to prevent the aggregation and enhance the specific surface area for the resulting graphene after finalising the reduction process by performing the third and final stage reduction that involved the addition of hydrazine.

The resulting graphene showed a high specific surface area of 464 $m^2.g^{-1}$ with a mean pore size of 3.3 nm and specific capacitance of 149.8 $F.g^{-1}$. This novel approach was designed for applications of graphene as a membrane which can be used in water desalination.

Figure 2.13. shows the range agents used with the chemical reduction approach including the more eco-friendly ones (De Silva *et al*. 2017).

However, there is still a lot of gabs in knowledge associated with this topic and some of these are listed below: (Pei & Cheng, 2012):

A- The extent of the elimination of functional groups is still uncertain and it is not certain that the entire elimination of GO functional groups is achievable.

B- The restoration of lattice defects that were formed during oxidation is another area of uncertainty. In other words, reduction of GO is a process that aims to produce a graphene-like material similar to pristine graphene. Though significant efforts have been done to achieve this target, but it is still a dream. Defects in the lattice which are intimately associated with oxidation process are altering the structure and the extent of restoration or healing of these defects through reduction process is still uncertain.

C- There is no clear measure of the defect density of graphene sheet and whether it is increased or decreased with the reduction process.

These gaps of knowledge are required to be filled through more detailed experimental investigations and characterization complement by better computer models of these materials. In most cases, computer simulations are used to elucidate the obvious chemical mechanisms as no direct observations of the reduction process have been developed. For instance, (Chen *et al*. 2014) modelled their understanding for the reduction mechanism of GO in NaOH a density functional theory DFT simulation.

Furthermore, a better understanding on how to control the oxidation of graphite is another area of investigation that will help to overcome the challenges associated with reduction process for GO.

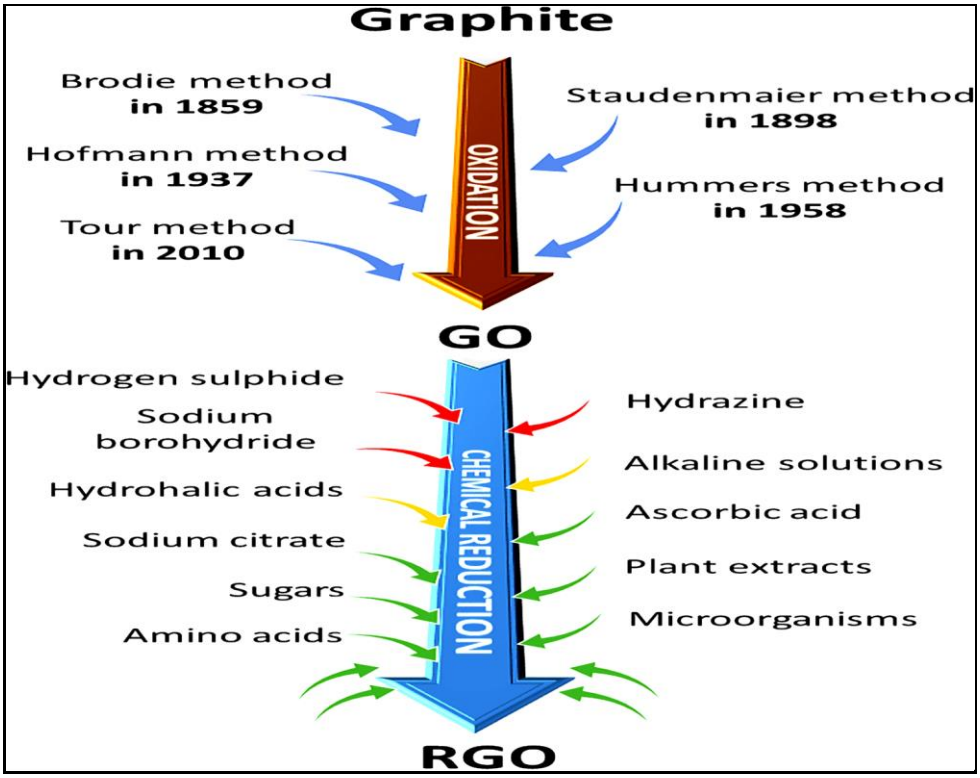

Figure 2.13. : The chemical reduction of GO. The reductants that have green arrows refer to 'green' reductants. Reductants with yellow and red arrows refer to chemical approach of reduction. Adapted from (De Silva et al. 2017) with permission from the publisher (Elsevier).

2.3.5. Dispersion of graphene, GO, and rGO

It has been deduced by (Bhattacharya, 2016) that pristine graphene is aggregated according to the intrinsic Van der Waals force. This represents a real challenge to exfoliation and for the incorporation of pristine graphene in polymer matrices with a homogenous dispersion. The research so far has shown that GO is a possible solution to this due to the abundance of oxygenated functionalities at the edges and basal planes (Xu *et al*. 2013).

In order to make a stable suspension in these materials, it is important to have a good understanding of the solubility parameters of the various solvents available (Park *et al*. 2009).

To this end Hansen solubility parameters are used to investigate the dispersion mechanism in the organic solvents for GO and rGO.

The dispersion cohesion parameter δD, the polarity cohesion parameter δP and the hydrogen bonding cohesion parameter δH are combined into the following formula:

$$\delta^2_T = \delta^2_D + \delta^2_P + \delta^2_H \text{ ---------- (1)}$$

The combination of these three parameters gives the Hildebrand solubility parameter which is δ_T. For a reasonable estimation of the three Hansen parameters, the following equation was applied:

$$(\delta_i) = \sum_{solv} C\delta_{isolv} / \sum_{solv} C \text{ ---------- (2)}$$

Where i= D, P, H or T, C is the GO and rGO solubility and δ_{isolv} is the i_{th} Hansen parameter in a given solvent (Konios *et al*. 2014).

As mentioned earlier, the solubility parameters are important in terms of the solvent selection for a given solute. It has been estimated that δ_T for GO is about 25.4 MPa ^{½} and for rGO about 22 MPa ^{½} . Solvents that have δ_T close to these values are expected to be good solvents for GO and rGO which means that a stable suspension with long term stability can be obtained. The values of δ_T for THF and DMF is (19.5 and 24.9) $MPa^{1/2}$ respectively. These values are close to δ_T for GO and rGO and were employed successfully to obtain long term stable suspensions (Konios *et al*. 2014).

(Hernandez *et al*. 2010) determined the main prerequisites for successful solvents. Among these prerequisites is that the Hildebrand solubility parameters for the solvent and the solute should be well matched.

(Paredes *et al*. 2008) showed that GO has a long term stability with THF, DMF and other organic solvents.

Furthermore, graphite oxide in these organic solvents can be exfoliated to a single layer GO nanosheet that has a lateral dimension that varies from few nanometres to few micrometres.

(Park *et al*. 2009) confirmed that homogenous colloidal suspensions for highly reduced graphene oxide HRGO can be achieved with THF, DMF and many other organic solvents and it was unattainable for other kinds of solvents such as 1, 2 dichlorobenzene DCB, diethylether and toluene.

Figure 2.14. (a) and (b) summarises the dispersion of GO and rGO in different organic solvents (Paredes *et al*. 2008; Park *et al*. 2009).

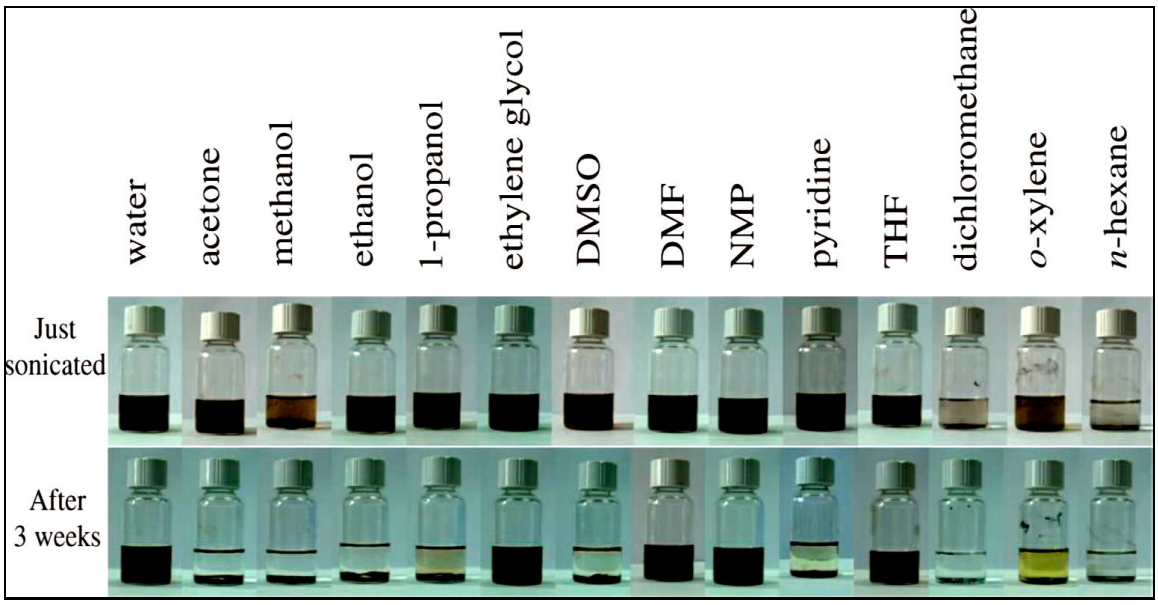

Figure 2.14.(a): Dispersion of GO in different organic solvents. Long-term stability was achieved in THF, DMF and many others. Adapted from (Paredes et al. 2008) with permission from the publisher (American Chemical Society).

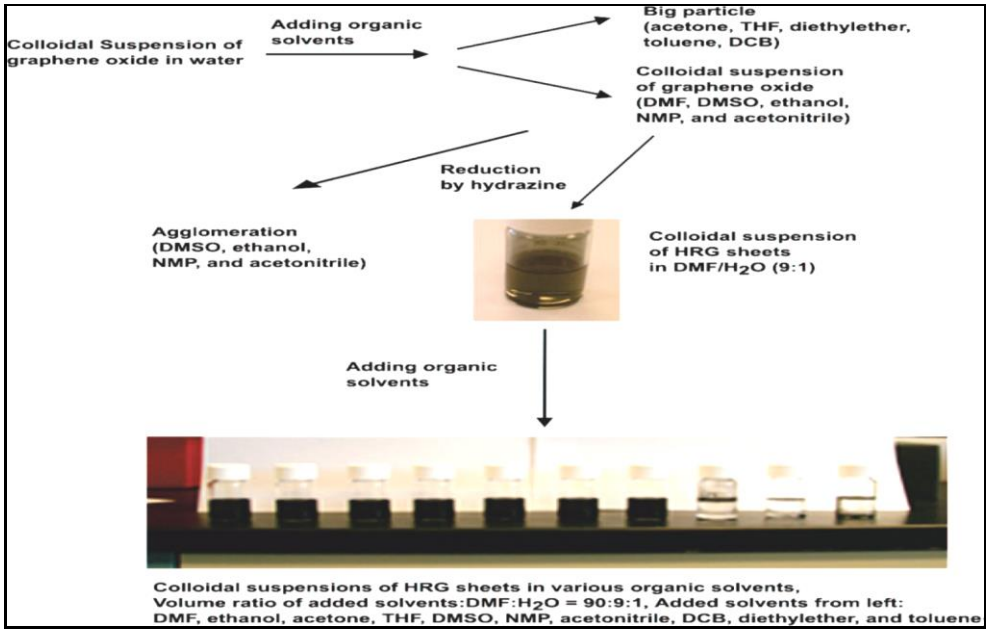

Figure 2.14. (b): Homogenous colloidal suspension for HRG with THF, DMF and other organic solvents. Adapted from (Park et al. 2009) with permission from the publisher (American Chemical Society).

Figure 2.14. (a) shows the dispersion of GO in 13 different organic solvents and water after making a sonication for 1 h and leaving all the samples in cupboard under observation for 3 weeks. GO was almost dispersed in water and all the solvents except dichloromethane and n-hexane, and, to a lesser extent, o-xylene and methanol. However, short-term stability was displayed by some of these dispersions and precipitated in a matter of hours to a few days such as acetone, 1-propanol, ethanol and many others. On the other hand, some dispersions were shown long-term stability for 3 weeks after the sonication and these dispersions were (ethylene glycol, DMF, THF, NMP, and water). The electrical dipole moment for the latter solvents and water was significant (2.31 D, 3.24 D, 1.75 D, 4.09 D, and 1.82 D) respectively, which gives the reason behind the stable dispersion of GO in these solvents and water for long time.

Figure 2.14 (b). shows that a 3 mg of GO was dispersed in 4 ml of water through 1 h of sonication. Then, DMF was added afterwards and a stable suspension was obtained. The chemical reduction then was obtained by adding hydrazine to the suspension. The same procedure described for DMF was followed with various organic solvents to obtain HRGO. The latter was achieved with many organic solvents including THF as shown in the above figure.

2.3.6. Properties of graphene, GO, and rGO

Graphene is a multifunctional material that can be utilized for enhancing the mechanical, thermal, electrical, optical, and gas barrier properties for polymer matrices. The high aspect ratio of graphene plays a crucial role in enhancing the performance of nanocomposites with low loadings compared with other carbonaceous derivatives. The potential applications for graphene based on their mechanical and electronic properties are in packaging, aerospace, automotive and electronics.

However, the optimum improvement in the final properties cannot be achieved without a homogenous dispersion of the graphene nanosheets in the matrix.

Equally importantly the applied load must be efficiently transferred through the strong polymer/filler interfacial interaction (Salavagione *et al*. 2011). Table 2.4. shows the most important properties for graphene, GO and rGO (Mittal *et al*. 2015).

Table 2.4. : Some properties of graphene, GO and rGO. (Mittal et al. 2015).

Property	**Single layer graphene**	**GO**	**rGO**
Young's modulus	1000 GPa	220 GPa	Not available
Fracture strength	130 GPa	120 MPa	Not available
Optical transmittance	97.7%	Not available (expected has a lower value due to defects in the functional groups	60-90% depending on the agent of reduction and fabrication method
Room temperature mobility	~ 200.000 $cm^2 V^{-1} S^{-1}$	Not available (expected to be a lower value due to disruption in mobility)	Not available (due to less defects it is expected to be intermediate)
Thermal conductivity	~ 5000 $W m^{-1} K^{-1}$	2000 $W m^{-1} K^{-1}$ for pure	0.14-0.87 $W m^{-1} K^{-1}$
Electrical conductivity	10^4 S cm^{-1}	10^{-1} S cm^{-1}	200-35.000 S cm^{-1}
Charge carrier concentration	1.4* 10^{13} cm^{-2}	Not available (expected to be lower due to defects in functional groups)	Not available

2.4. Polymer graphene/GO nanocomposites

The impressive properties of graphene paved the way for researchers to prepare, characterize, and investigate its properties and possible applications for PGNs. One specific area of interest with regard to graphene is its incorporation into different polymers in order to gain mechanical, thermal, thermos-mechanical, and electrical enhancements and this has been achieved at very low loadings of graphene, GO and its reduced form (Kuilla *et al*. 2010; Young *et al*. 2012).

For example, (Ammar *et al*. 2015) cited the work of (Ionita *et al*. 2014) where low loadings of GO (0, 0.25, 0.5,1.0 and 2.0) wt. % were used to reinforce a PSF matrix in order to improve the mechanical performance and thermal stability for the polymer which was used as a membrane.

(Yuan *et al*. 2014) confirmed that adding only 1.0 wt. % of GO to polyethylene oxide PEO led to a 260% improvement in thermo-mechanical stability for the polymer that was used in lithium-ion battery applications. This result was achieved according to the superior properties of GO and the strong interfacial interaction between GO and the surrounding PEO. (Cai *et al*. 2012) concluded that the toughness increased by 50% for polyurethane, which is commonly used in diverse industrial applications such as automotive, by adding 1.0 wt. % of GO without losing elasticity.

(Terrones *et al*. 2011) described different types of interaction between the polymer matrix and graphene. These interactions can be covalent functionalization, non-covalent functionalization such as _ Π-Π interactions_, electrostatic interactions, or polymer blending.

Figure 2.15. illustrates these types of interaction (Terrones *et al*. 2011).

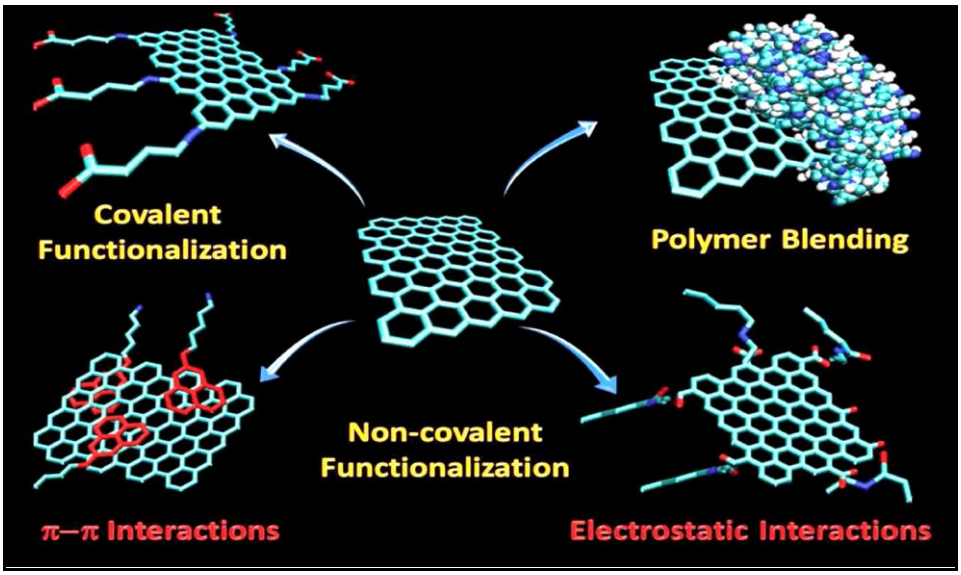

Figure 2.15. : Types of interaction between the matrix and graphene. Adapted from (Terrones et al. 2011) with permission from the publisher (WILEY-VCH Verlag GmbH & Co. KGaA, Weinheim).

Non-covalent interactions consolidate the attachment of organic molecules on the surface of graphene. Π-Π stacking, electrostatic or hydrophobic interactions are techniques for non-covalent interactions of polymers and surfactants with graphene surfaces. Beneficial modifications to graphene's surfaces can be achieved by adopting the non-covalent interactions and this will consequently help facilitate the preparation of PGNs (Chang & Wu, 2013).

For example, (Jiang *et al*. 2014) employed an electrostatic self-assembly approach to improve the dispersion of GNS in a poly (tetrafluoroethylene) PTFE matrix as the insolubility of PTFE made the interaction with GNs difficult. It was an eco-friendly approach where the well dispersed GO that was negatively charged mixed with modified positively charged PTFE latex. This approach is a type of Non-covalent interaction resulted in the formation of filler networks in the PTFE matrix, which led to an improvement in the mechanical and electrical properties. This was achieved with low loadings of GNS (0.5, 1.0 and 2.0) wt. %. Tensile modulus improved to 578 MPa for PTFE reinforced with 2.0 wt. % of graphene compared to the neat polymer that had tensile modulus of 356 MPa. In addition, electrical conductivity for PTFE/graphene of 2.0 wt. % recorded 1.5 S/m. Covalent interaction between the polymer matrices with graphene and GO can be achieved via several approaches such as amide bonding (also known as peptide bond, which is a covalent chemical bond linking two consecutive amino acid monomers along the protein chain), click chemistry (a method of attaching probe or substrate of interest to a specific biomolecule in a process called bioconjugation), and atom transfer radical polymerization ATRP (a polymerization process that lead to form a carbon – carbon bond through a transition metal catalyst). (Chang & Wu, 2013).

For instance, (Rajender & Suresh, 2016) prepared nanocomposites with low loadings of functionalized graphene sheets FGS (0.3, 0.8, 1.66, and 2.33) wt. % . The nanosheets incorporated covalently to PMMA using surface initiated SI-ATRP. The nanocomposites showed high thermal stability, improved rheological and mechanical properties.

For clarity, it is necessary to note that the word ‘’ graphene’’ is often used to describe the work done on GO. The vast majority of work in the field of PGNs is often referred to the work on GO and its reduced form (Young *et al*. 2012).

However, the functionalization of graphene in polymer matrices is in its infancy , and significant efforts are required to improve the present strategies and to find novel ones for promoting the utility of PGNs from the laboratory curiosities to practical components that have various technological applications (Layek & Nandi, 2013). Most importantly, the toughest challenge with these new materials is in achieving a comprehensive understanding the surrounding interphase (The intermediate region between two or more materials in equilibrium which will joint to form the nanocomposite). The characteristics of the interphase region, the reliance of this vital region on graphene's surface chemistry, and the apparent arrangement of the constituents and their relationship to different properties of PGNs are also challenges submerged within the over-arching challenge of engineering the interphase. There is a vigorous competitive scientific endeavour in various disciplines of materials science, chemistry, and materials engineering to meet these challenges, and to successfully prepare advanced graphene based nanocomposites (Das & Prusty, 2013).

2.4.1. Preparation of PGNs

There are a number of factors playing a crucial role in the preparation of graphene / GO based polymer nanocomposites. These include: the molecular weight, the polarity, reactive groups, and hydrophobicity. The most widely applied methods for preparing polymer graphene/GO nanocomposites are: in-situ polymerization, melt compounding and solution mixing or solution blending (Das & Prusty, 2013). These methods are discussed separately in the following sub-sections.

2.4.1.1. In-situ polymerization

This is a common way for synthesizing polymer graphene /GO nanocomposites and the result is a uniformly dispersed graphene/GO in the polymer matrices. In this method, the graphene or its precursors and the monomer are dissolved using a co-solvent and then ultrasonicated to obtain a uniform dispersion. Next, an initiator such as metallocene catalyst solution is added to the mixture to form the polymer.

The addition of the initiator starts the polymerization process which is initiated either by heat or radiation. Surfactants such as sodium dodecyl sulphate SDS might be employed to improve the dispersion. Overall, this method has a number of benefits such as simplicity, scalability, ease of manipulation, low cost, and lower environmental concerns. A variety of PNCs have been synthesized using this method such as isotactic polypropylene iPP reinforced with exfoliated graphene nanoplatelets xGnP prepared by in-situ polymerization. High ductility (38.5 MPa) and fracture toughness (16.2 $KJ.m^{-2}$) were achieved for nanocomposites prepared by this method compared with ductility and toughness of the neat polymer which recorded 38.4 MPa and 14.6 $KJ.m^{-2}$ respectively (Das & Prusty, 2013; Chee *et al*. 2015; Cromer *et al*. 2015; Kuilla *et al*. 2010).

2.4.1.2. Melt compounding

This method is commercially attractive with other methods. It refers to the direct inclusion in the graphene or any of its precursors of the melted polymer matrices by using a twin-screw extruder. The key variables of the screw that need to be optimised are time to complete the operation, the temperature, and the speed.

The major drawbacks with this method is the poor dispersion of graphene sheets in polymer matrices and this has a negative impact on the mechanical properties. Another drawback is the low bulk density of the thermally exfoliated graphene. A range of polymers have been prepared with different nanofillers using this method (Verdejo *et al*. 2011). A specific example is the work of (Zhang *et al*. 2010) who prepared polyethylene terephthalate PET/graphene nanocomposites using a melt compounding method in which the compounding temperature was 285 ^{o}C and the initial screw speed was 50 $rpm.min^{-1}$. and then it was changed to be 100 $rpm.min^{-1}$. The presence of 3.0 Vol. % graphene obtained in their work significantly enhanced the electrical conductivity of PET, which was transformed from insulator to semiconductor with a low percolation threshold.

2.4.1.3. Solution blending

This method has the appeal of simplicity and its proven capability for achieving a homogenous dispersion of graphene or GO in casted-polymer films made it an attractive proposition for researchers. In this method, graphene is dispersed in a solvent via sonication which is the act of applying sound energy to agitate particles in a sample then added to the polymer solution obtained from dissolving polymer pellets in the same solvent. The solution is then evaporated at ambient or an elevated temperature. For a rapid solvent evaporation a highly volatile co-solvent is selected (Chee *et al*. 2015). However, there is a significant challenge with this method in terms of the removal of the organic solvent from the obtained nanocomposites. Any remaining traces of the organic solvents have detrimental effects on the mechanical, electrical and thermal properties of the nanocomposites (Sun *et al*. 2013). As an example of this technique, (Lago *et al*. 2016) used a solution blending method for preparing polycarbonate PC/graphene nanocomposites to disperse single and a few layered graphene SLG and FLG by liquid phase exfoliation LPE in the polymer matrix. 1, 3 dioxolane was the co-solvent and the results showed an improvement of 26% in the elastic modulus for 1.0 wt. % of graphene in the matrix. To conclude this section, (Zhang *et al*. 2015) elucidated the benefits and drawbacks for each of the aforementioned methods as shown in Table 2.5. below.

Table 2.5. : Scale, advantages and disadvantages of PNCs preparation methods. (Zhang et al. 2015).

Preparation method	**Scale**	**Advantages**	**Disadvantages**
In-situ polymerization	Bulk	Highly effective, high level dispersion	Loss of polymerization rate at later stage
Melt compounding	Mass production	Eco-friendly, cost effective	Poor dispersion of nanoparticles
Solution mixing	Bulk	Versatile, good dispersion	Extensive use of organic solvents

Finally, it should be mentioned that the majority of researchers have classified their preparation methods of PNCs according to the above three main categories. Nevertheless, (Papageorgiou *et al*. 2017) has added an additional category very recently which is layer by layer LBL assembly. In this method, the desired nanostructures of multilayer thin films with a specific thickness are synthesized by alternating cationic and anionic phases on a substrate.

Novel materials can be prepared according to this novel approach with a diverse range of applications including capacitors, field effect transistors FET and membranes. (Harsini *et al*. 2017) used this approach to prepare branched poly (ethyleneimine) PEI reinforced with different kinds of nano-reinforcements (nanoparticles, nanosheets, and nanofibers). The resultant nanocomposites showed a unique combination of ductility and strength.

2.4.2. Processing conditions

The unusual properties of PNCs are manifested when there is an even dispersion of nanoparticles in the polymer matrix and this consequently results in the development of a strong interphase. The complete dispersion of the NPs will enable the maximisation of the available matrix- particle interphase then the organic- inorganic interaction. The latter is the responsible for the promotion of the properties of the resulting nanocomposites.

One of the key aims in the research in this field is to develop optimised strategies for processing for nanocomposites and nanostructured polymers with a view to achieving the ideal matrix-particle interaction. The quality of dispersion is determined by macroscopic processing factors such as mixing velocity, residence time and equipment design and it is important to ascertain what the trade-offs are with regard to achieving optimal processing (Peponi *et al*. 2014).

For instance, (Yasmin *et al*. 2006) employed several processing techniques for preparing epoxy reinforced with low loadings of expanded graphite EG (1.0-2.0) wt. % . They used direct mixing, sonication, shear mixing and a combination of the last two techniques. The findings showed that better values of Young's modulus (improvement of 15 % for epoxy/EG 1.0 wt. %) were achieved in samples prepared by a combination of shear mixing and sonication, whereas direct mixing gave the weakest results (improvement of 4% only for the same sample). The findings also confirmed the effect of sonication time on the mechanical properties. Longer sonication time proved a better choice for obtaining graphite nanosheets from EG, but the prolonged sonication time led to a deterioration in the mechanical properties due to the increase of the temperature which would negatively affecting the structure of nanomaterial. This work provided a good example of the emerging trade-offs that are encountered in the aiming for optimisation in the selected processing route.

Many efforts have focussed so far on the development and promotion of the best processing strategies of nanocomposite materials that result in the promotion of particle-matrix interactions. It is important to note that the quality of dispersion can be critically affected by processing factors such as mixing velocity, equipment design, and the time (Peponi *et al*. 2014). For instance, (Prolongo *et al*. 2008) investigated the dispersion homogeneity of CNFs in an epoxy matrix by diluting the nano fibres in chloroform. They used different dispersion techniques such as direct mechanical mixing, high shear mixing and ultrasonication to obtain dispersion in a consistent way to ensure homogenous dispersion of the nano fibres in the polymer. The employment of all the aforementioned dispersion techniques besides making the required chemical modification on carbon nano fibres led to good dispersion of the carbon nano fibres in epoxy with an important enhancement in storage modulus (2.5 GPa for nanocomposites prepared by using different dispersion techniques compared to 2.3 GPa for nanocomposites prepared by mechanical stirring only) as a consequence of this good dispersion.

In addition, (Cosmoiu *et al*. 2016) investigated the role of rotation speed of a shear mixer in the uniform dispersion of the MWCNTs in epoxy. They showed that high speed shear mixing led to better dispersion. The speed of shear mixing they selected was 1500 rpm. They also confirmed that 20% of researchers used the shear mixer for up to one or two hours. They showed that strength and stiffness might be increased in case of adequate dispersion of nanofillers in the matrix. The selected speed of shear mixing in the work described in this thesis was 1600 rpm for an hour, and the total time of dispersive techniques' employment (shear mixing and bath sonication) was up to couple of hours.

However, there are a number of other contributing factors that present challenges in the manufacturing process of PNCs. This includes increasing the range of dispersing solvents to include other solvents that are less toxic or highly volatile solvents, such as, alcohol and water. Moreover, the use of more scalable routes to improve dispersion, such as, shear mixing is another important option (Johnson *et al*. 2015).

In addition to these issues, there are others that can be classified as second tier challenges, such as, post-processing, safe handling and accurate characterisation.

Nonetheless, the issue of costs needs to be factored into selecting the best route to the required dispersion (Johnson *et al*. 2015).

2.4.3. Properties of polymer graphene/ GO nanocomposite

As graphene/GO nanosheets are randomly dispersed in the polymer matrices, the physical properties of the nanocomposites will be modified. The mechanical, thermal and many other properties will be affected by the inclusion of graphene to the different polymer matrices (Kim *et al*. 2010). Each of these is discussed separately below.

2.4.3.1. Mechanical properties

Stress-strain curves can be regarded as the easiest way to assess the improvement in the mechanical performance of polymers when adding graphene or any of its precursors. Large changes are observed upon the addition of low loadings of graphene to the polymer matrices, whilst the addition of high weight or volume fractions of graphene and its precursors led to less remarkable changes in the mechanical properties. In some cases, an inefficient stress transfer is observed and this is due to a weak interphase between the matrix and graphene or nanoplatelets. For this reason, GO is used as a reinforcing agent rather than incorporating pristine graphene into the polymer matrices because the oxygen functional groups makes the interphase stronger though this has not been optimised yet. Further improvement in the mechanical performance of the nanocomposites is possible by optimisation of the interphase and by improving the dispersion of GO so that it is homogenous. Another challenge is in, obtaining full exfoliation of graphene to a single or few layers of graphene over large lateral dimensions. The Final hurdle for improved mechanical properties of PGNs is in finding techniques for minimising damage on the flakes during production of GO (Young *et al*. 2012). Table 2.6. below modified from (Kim *et al*. 2010) summarises the mechanical properties for some polymer graphene/GO or thermally reduced graphene TRG nanocomposites.

Table 2.6. : The improvement in mechanical performance for polymer nanocomposites reinforced with different types of graphene precursors (Kim et al. 2010).

Polymer	Reinforcement	Processing	E_{Matrix} / MPa	Conc. Vol.%	E_{NCs} increase / %	$T.S_{NCs}$ increase / %
PVA	GO	Solvent	2100	2.5	128	70
PCL	GO	Solvent	340	2.4	108	36
Epoxy	TRG	In-situ pol.	2850	0.05	31	40
SAN	TRG	Solvent + melt	2350	2.3	34	N/A
PS	CRGO	Solvent	1450	0.4	57	N/A
TPU	GO	Solvent	6	2.4	900	-19
Natural rubber	TRG	Solvent + melt	1.3	1.2	750	N/A

2.4.3.2. Thermal properties

The outstanding thermal properties of graphene offers improvements in thermal performance for PGNs including thermal conductivity, thermal stability and dimensional stability. High carbon loadings is a major condition for gaining high thermal conductivities in PGNs compared with neat polymers (Potts *et al*. 2011). (Chen *et al*. 2017) confirmed this fact in their co-work when they showed that the incorporation of 10.0 wt. % of GO in PA-6 improved the thermal conductivity six fold compared with the neat polymer. Also, the incorporation of graphene, chemically modified graphene CMG, and GO participated effectively in enhancing the thermal stability of nanocomposites.

Thermal stability was defined as the maximum mass loss rate measured by thermogravimetric methods. The majority of studies have focused on the non-oxidative stability which means heating under the influence of an inert gas such as nitrogen or argon. The incorporation of GO in different polymer matrices leads to a better thermal stability using the non-oxidative approach. The onset of the degradation temperature T_d is improved by 20-30 ^oC and higher when GO and its derived fillers are incorporated in different polymers (Potts *et al*. 2011).

For example, (Yu *et al*. 2014) showed a significant improvement of thermal stability for PS when they reinforced the polymer with 2.0 wt. % GO and the thermal degradation temperature T_d increased from 298 ^oC for the neat polymer to 372 ^oC for the nanocomposite. The test was carried out by the non-oxidative approach as N_2 was purged. It has been reported that using graphene and its precursors in nanocomposites resulted in a shift in the value of the T_g. This behaviour can be explained by the altered mobility of the polymer chains at the interphase. The presence of nanoparticles in polymer matrix interphases led to restrictions in the chains mobility which consequently led to higher T_g.

On the other hand, repulsive interphases and free surfaces lead to free chain mobility which results in lower T_g. In other words, the T_g shift higher or lower depending on the specific interaction between the matrix and the filler (Potts *et al*. 2011; Paul & Robeson, 2008).

(Wan & Chen, 2012) showed that the T_g for PS shifted higher from 73.5 ^oC to 86.4 ^oC for PS reinforced with 1.0 wt. % of GO. Finally, it should be mentioned that graphite has a negative coefficient of thermal expansion which is $-1.5*10^{-6}$ ^oC in the basal plane near RT. Also, the thermal expansion along the thickness direction is much smaller than that of polymer materials ($2.7*10^{-5}$ ^oC).

Given the aforementioned, graphene can inhibit dimensional changes of PGNs if it is incorporated in polymers at an appropriate orientation rendering them more stable. According to (Tseng *et al*. 2013) GO is playing a positive role in dimensional stability enhancement in polyimide.

Table 2.7. below shows the change in T_g value for different polymers with different types of reinforcements (Paul & Robeson, 2008).

Table 2.7. : The effect of some nanofillers on the T_g of PNCs. Modified from (Paul & Robeson, 2008).

Polymer	**Nano-filler**	**T_g Change (^oC)**
PS	SWCNT	3
Poly (vinyl chloride) PVC	Exfoliated clay MMT<10.0 wt. %	-1 to -3
Poly(dimethyl siloxane) PDMS	Silica (2-3) nm	10
Natural rubber	Nano-clay (5.0 wt. %)	3
Poly(butylene terephthalate) PBT	Mica (3.0 wt. %)	6

2.4.3.3. Electrical properties

PGNs can act as efficient conductors due to their ability to provide a percolated pathway for electron transfer. Similarly, other carbon nano-fillers can play the same role. For example, carbon black CB, carbon nano-fibres CNF and expanded graphite all enhance the electrical properties of PNCs. However, the insulator to conductor transition can be supported by graphene with low loadings.

Thermally reduced graphene TRG has a high electrical conductivity and it can be melt-processed according to its high thermal stability (Kim *et al*. 2010). (Vu *et al*. 2016) found that the incorporation of 2.5 Vol. % of sulfonated reduced graphene oxide SRGO into SAN led to enhancements in the electrical performance of the nanocomposite. The electrical conductivity was found to be 21.9 $S.m^{-1}$ for the aforementioned sample.

2.4.4. Applications of polymer graphene/GO nanocomposites

PGNs have been proposed for a wide range of applications encompassing house hold design, electronics, medicine, energy, engineering, industrial and many others (Dhand *et al*. 2013). (Das & Prusty, 2013) have illustrated graphically the potential applications of PGNs as reproduced in Figure 2.16. below.

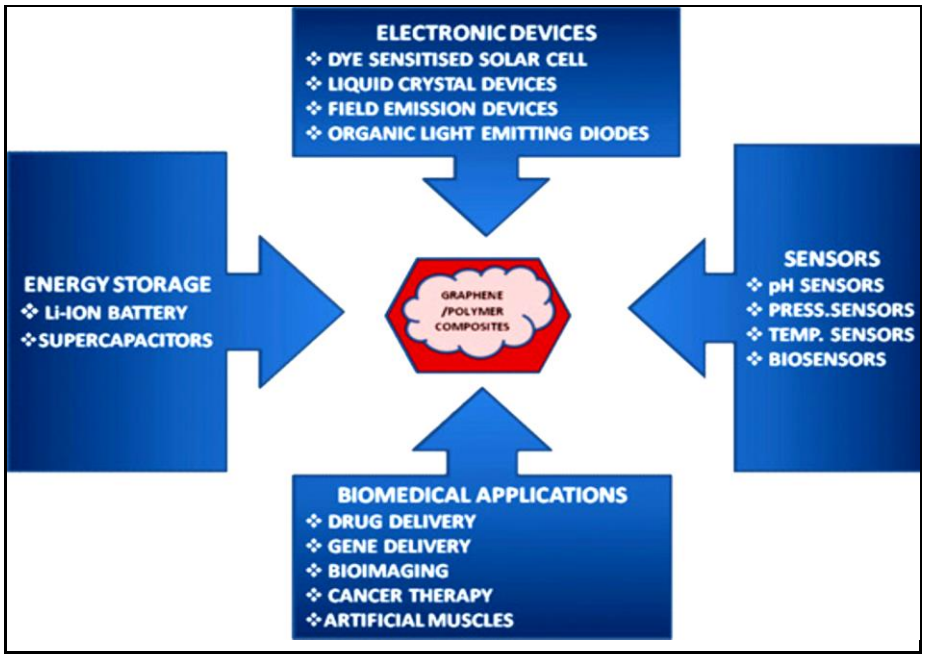

Figure 2.16. : Some applications of PGNs. Adapted from (Das & Prusty, 2013) with permission form the publisher (Taylor and Francis group, LLC).

The high carrier mobility, high electrical conductivity and high optical transmittance in the range of visible spectrum are features that suggest PGNs may have potential in electronic devices such as electrodes, liquid crystal devices LCD, organic solar cells, organic light emitting diodes OLED, field emission devices, touch screens, flat panel display and so on.

CVD graphene synthesized on a metal substrate and then transferred to various transparent films such as PDMS or PET. Moreover, conducting polymers such as poly (3-hexylthiophene) P3HT reinforced with graphene showed high power consumption efficiency compared with poly (3,4 ethyencdioxy thiophene) poly (styrenesulphonate) PEDOT:PSS (Das & Prusty, 2013). (Bkakri *et al*. 2015) showed that P3HT/graphene nanocomposites are efficient candidates for improved efficient electron transfer process that could be exploited for improving photovoltaic cell performance.

Regarding energy storage applications, lithium ion batteries LIB are currently considered the most promising storage systems. The benefits of LIB are high absolute potential (-3.04 V) and low atomic weight (6.94 $g.mol^{-1}$) which leads to a large energy density around 400 Wh kg^{-1}.

The LIB is a rechargeable battery, and it is a green solution for energy conversion and storage devices. It is also an efficient system with low cost compared with alternatives. Poly-(anthraqunionyl sulphide) and polyimide are the common polymers used to manufacture the cathode of rechargeable lithium batteries RLB (Huang *et al*. 2012; Das & Prusty, 2013). Electrochemical supercapacitors are another promising energy storage application that could be based on graphene based polymer nanocomposites. Polyaniline PANI and polypyrrole PPy are promising polymers to be used in nanocomposites for supercapacitor applications. The successful employment for these conducting polymers by using them to prepare PGNs contributed to develop the electrochemical capacitance applications (Sun *et al*. 2013).

(De Oliveira *et al*. 2013) incorporated 1.0 wt. % of graphene in PPy to produce high quality nanocomposites suitable for supercapacitors applications and obtained a capacitance of 277.8 F g^{-1}. Another range of applications for PGNs are in sensors. (Eswaraiah *et al*. 2011) showed that improved strain sensing was achieved by the inclusion of 2.0 wt. % functionalized graphene mixed with polyvinylidene fluoride PVDF through a solution blending method. They reported an improvement in strain sensing compared with graphene counterparts such as CNTs.

Drug delivery applications is another kind of application provided by graphene nanocomposites. This is due to the abundance of oxygenated functionalities in the basal plane and the edges of GO. This makes it a promising candidate for being able to chemically conjugate or physically adsorb a large amount of antibodies and anticancer drugs (Zhang *et al*. 2015). For example, (Justin & Chen, 2014) successfully reduced GO using a simple process of reduction and incorporated the resulting rGO in chitosan CS. This work provided a versatile platform for biomedical and biological applications including therapeutic delivery and tissue engineering.

For PS/graphene nanocomposites, there are many kinds of applications cited by the authors. For example, (Han *et al*. 2013) were successfully incorporated 5.0 wt.% of graphene and graphite oxide of different degrees of oxidation in PS using melt compounding approach. The prepared nanocomposites were employed as flame retardants and the sample of PS reinforced with graphene had the best thermal and thermomechanical performance. Furthermore, the other kinds of applications of PS/graphene nanocomposites include anti-corrosion productions, super conductive materials, FET, and many others (Yu *et al*. 2014; Pham *et al*. 2011; Eda & Chhowalla, 2009). In addition, there are many applications of SAN/graphene nanocomposites such as capacitors, decoupling capacitors and Electromagnetic Interference Shielding EMI (Panwar *et al*. 2017).

As well as the scientific applications mentioned in Figure 2.16., PGNs have other commercial applications such as in light weight gasoline tanks, fuel efficient aircraft, car parts, stronger wind turbines, plastic containers, sports equipment and medical implants (Das & Prusty, 2013). Finally, (Edwards & Coleman, 2013) were concluded a summary that connected the properties with application. In other words, which of graphene's properties are important for different applications. In Table 2.8. below, the green tick means (important), the red X means un-important and the black square was indicated that the property is sometimes important.

Table 2.8. : The relationship between graphene's properties with different applications (Edwards & Coleman, 2013).

Properties → / Applications ↓	**Electrical Conductivity**	**Strength**	**Elasticity**	**Surface area**	**Transparency**	**Thermal Conductivity**	**Chemical Inertness**	**Gas Impermeability**
Transistors	√	x	x	x	x	x	√	x
Energy storage devices	√	x	x	√	x	x	√	x
Electrodes	√	□	□	□	□	x	√	x
Electrically conductive inks	√	x	√	x	□	x	√	x
Polymer composites	√	√	√	√	□	√	√	□
Sensors	√	x	□	x	x	x	√	□

2.5. Nanomechanics

The investigation of material behaviour at the nano-scale is a newly emerging field which can be described as ''nanomechanics'' (Bhushan, 2005). Nanomechanics can be subsumed under the more general term of nanoscience along with other sub-classes such as nanomaterials and nanocomposites. The traditional physics and macro-mechanics has not become a sufficient solution for the problems that are intimately associated to nanoscience.

The mechanical properties for the materials that have nanoscale features is different to that of their bulk counterparts. This has been verified in a wide range of materials at the nano-scale including 1D and 2D nanostructures, nano-crystalline and nano-twinned materials, and biological materials with nano-scale components such as cells and proteins. However, much work needs to be done on the dynamics and mechanisms of solid-solid contacting during relative motion in order to improve the understanding of indentation and adhesion at the micro and nano-scale (Bhushan, 2005).

There is a real need for nanomechanics to respond to the inquiries associated to the engineering especially the required development for the nanomechanical properties of thin films and nano-devices related to the components of microelectromechanical systems and nanoelectromechanical systems MEMS and NEMS.

These functions are very important to develop many kinds of applications such as drug delivery systems, medical diagnostics and sensors.

The main tasks for ‘’Nanomechanics’’ are:

i- Filling the gaps in knowledge between the atomic scale and the continuum. In dimensional terms, this ranges from a nanometre to a few hundred nanometres.

ii- Providing an important limiting case for continuum mechanics that enables an understanding of the difference between molecular mechanics and continuum mechanics.

For the last three decades, the tools required for investigating the properties of different materials at the nano-scale have been acquired. For example, high resolution electron microscopy has enabled the imaging of atoms and investigating their features. Furthermore, scanning probe techniques can be used to manipulate atoms one at a time (Liu *et al*. 2004; Li and Wang, 2008).

Table 2.9. compares the operating parameters of different kinds of electronic microscopes used in nano-scale studies. The table shows the difference between surface force apparatus SFA, scanning tunnelling microscope STM and atomic force microscopy with friction force microscopy (AFM/FFM) which are extensively employed in nanomechanical and nanotribological studies (Bhushan, 2005).

Table 2.9. : Typical operating parameters for different microscopes used in nanomechanical studies. (Bhushan, 2005).

Operating parameter	**SFA**	**STM**	**AFM/FFM**
Radius of mating surface/tip	~ 10 mm	5 – 100 nm	5-100 nm
Radius of contact area	10 – 40 μm	N/A	0.05-0.5 nm
Normal load	10 – 100 mN	N/A	<0.1nN-500 nN
Sliding velocity	0.001 – 100 μm s^{-1}	0.02 – 200 μm s^{-1} (Scan size 1nm * 1nm to 125μm*125 μm, scan rate <1- 122 Hz)	0.02 – 200 μm s^{-1} (Scan size 1nm * 1nm to 125μm*125 μm, scan rate <1- 122 Hz)
Sample limitations	Typically atomically – smooth, optically transparent mica, opaque ceramic, smooth surfaces can also be used	Electrically-conducting samples	None

2.5.1. Force distance curves

There has been a rapid growth of interest in nanomechanics in recent years with the emergence of nano-scale materials, mechanics based applications of such materials, and novel mechanics phenomena at the nano-scale (Zhu *et al*. 2016). One important characteristic of these materials is the force versus distance curves, F-D curves, which provides information on elasticity, adhesion, hardness and other parameters and this can be measured using atomic force microscopy AFM. This measurement technique also enables imaging of the topology of solid surfaces at high resolution (Butt *et al*. 2005). AFM is a versatile tool for high resolution imaging of different solid surfaces, both conducting and insulating, and for providing data for plotting F-D curves. These curves provide important parameters such as the Hamaker constant, surface charge densities, hardness, elasticity (Young's modulus at the nanoscale) and the strength of the adhesion force (Butt *et al*. 2005).

In operation, the sample is spatially scanned with a specific tip that is mounted on a cantilever spring. While scanning, measurements are made of the force arising from the vertical deflection of the cantilever. A topographic image for a specific surface is acquired by plotting the deflection of cantilever versus the position of the sample. This is a non-contact mode where the image of the surface is formed from the deflection due to the interatomic force between the tip and the sample. The rectangular shape or ''Diving board'' and ''V'' shaped cantilever are the main two shapes of cantilevers used in AFM, both of which are mainly micro-fabricated from silicon or silicon nitride. The V shaped cantilevers are the most widely used cantilevers due to their high lateral stiffness which is important to investigate the nanomechanical properties (Clifford & Seah, 2005). The cantilevers for F-D curves are usually V-shaped to provide lateral stiffness (rectangular or diving board cantilevers are mostly used only for imaging purposes).

The typical length of cantilevers is about 100-200 μm with typical resonance frequencies of 20-200 KHz and they are made from silicon or silicon nitride. Figure 2.17. shows the V- shaped cantilever for obtaining F-D curves. L is the length of the cantilever, w represents the width, and α is the open angle (Butt *et al*. 2005). The spring constant is needed in determining the various parameters in the measurements and this can be determined in three ways: dimensional, static experimental and dynamic experimental.

It has been shown that the spring constants obtained via calculation are often different to the value obtained experimentally. One of the issues in this respect is related to the evaluation the thickness of the gold coating that is evaporated onto the cantilever to enhance its reflectivity. This layer adds mass to the cantilever and changes the resonance frequency thereby adding complications to the spring constant evaluation. In general, the most appropriate approach is to use the value obtained by experiment by applying a specific force F to the end of the cantilever and measuring the resulting deflection Zc. In this respect, the spring constant Kc can be calculated according to the following formula (Butt *et al*. 2005; Clifford & Seah, 2009):

$$Kc = F/Zc \quad \text{---------- (3)}$$

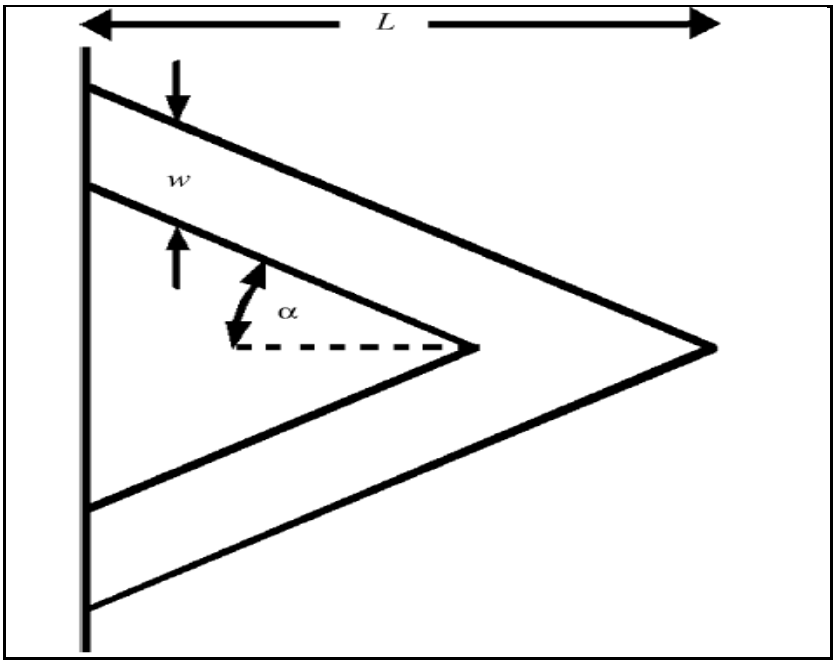

Figure 2.17. : V-shaped cantilever that used for measuring F-D curves. Adapted from (Butt et al. 2005) with permission from the publisher (Elsevier).

To ensure better quantitative measurements, the spring constant should be accurately evaluated. Spring constants are within the range of (0.01-130) N.m $^{-1}$ and a particular spring constant is selected according to the specific application required which could vary widely for example from finding the elastic modulus for polymers' surfaces to measuring the unfolding forces of protein molecules (Clifford & Seah, 2009).

The latter authors (Clifford & Seah, 2009) calibrated the spring constants for different cantilevers using static, dynamic and dimensional approaches.

(Domke & Radmacher, 1998) used F-D curves obtained by AFM for finding the elasticity (Young's modulus) of thin polymer films (down to 50 nm). The polymer was gelatine that was tuned by using propanol and water. Hertz theory (see section 2.5.2.) was employed as the mathematical model for finding Young's modulus.

Moreover, (Lee *et al*. 2008) used nanoindentation with the AFM for finding the elastic properties and intrinsic strength of a free-standing monolayer graphene membrane from the measured force-displacement behaviour.

Both approach and retract F-D curves are characterised by three main regions: the contact line, the non-contact region and the zero line. The latter is obtained when the tip is far away from the sample which means that the deflection of the tip is nearly zero. If the sample is pressed against the cantilever to the point of contact the distance between the sample and the tip is equal to zero. Lines obtained by the F-D curves in this condition are called ‘’ zero lines’’.

The more interesting regions in the F-D curves are the two non-contact regions which are ‘jump to contact’ and ‘pull-off contact’. These regions provide valuable information on the attractive and repulsive forces before contact.

The withdrawal or retract curve that includes the ‘jump-off contact’ gives information on the adhesion force F_{ad} which is related to the cantilever deflection and the spring constant.

The magnitude of the adhesion force is essential for evaluating the amount of deformation beside the contact area of the sample. The theories of contact region will be discussed later in section 2.5.2. (Cappella & Dietler, 1999).

Figure 2.18. and Table 2.10 give a conclusive explanation for F-D curves. The figure and the related clarifications are taken from (Modulation 2003)_Veeco support notes No.228, 2003.

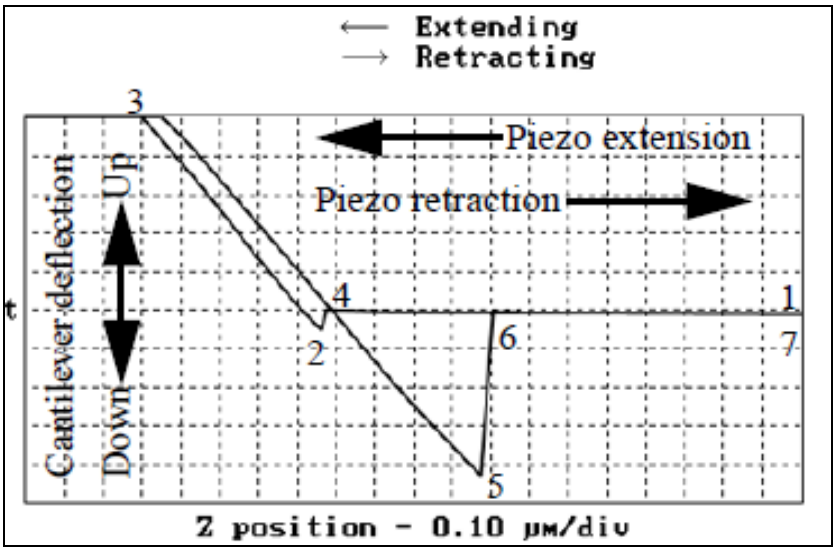

Figure 2.18. : F-D curve with all the steps of approach and retraction. (Modulation 2003)Veeco support notes No.228, 2003.

Table 2.10. : The corresponding meaning for each step mentioned in figure 2.17. (Modulation 2003)Veeco support notes. No.228, 2003.

	The sequence of motions as shown in the above figure 2.15.	The scientific meaning
Approach	1	The tip descends. No contact between the tip and the surface of the sample yet.
	2	The tip is pulled down by attraction force to the surface of the sample
	3	The cantilever bends upward as the tip is presses into the surface
Retract	4	The tip ascends until the upward force is cancel the surface attraction.
	5	Retraction process continues. The tip ascends further. The probe bends down as surface attraction holds onto the tip.
	6	Tip breaks free of surface attraction with the continuous ascendance. The probe rebounds sharply upward.
	7	The probe tip continues to ascent. No further interaction between the sample and the tip.

2.5.2. Contact deformation theories

There are several theories relating to contact deformation. The contact lines of the F-D curves play a vital role in determining the elasto-plastic behaviour of different materials. The overlap between loading and unloading curves means that the exerting force on the tip by the sample is equal to the force applied by the tip to penetrate the sample.

This in turn means that the material or the sample is elastic, and the shape of the sample recovers its original size. In the case of a plastic sample, no overlapping can be seen for the loading-unloading curves.

This means the sample is permanently deformed, the penetration depth will remain the same, and the sample will not regain its original dimensions. Most of the samples in these studies have a mixed behaviour which means that loading-unloading curves rarely overlap. In other words, at a specific penetration depth, the force of the loading curve is greater than the force of the unloading curve.

Figure 2.19. illustrates the meaning of different elasto-plastic behaviour for different samples (Cappella & Dietler, 1999).

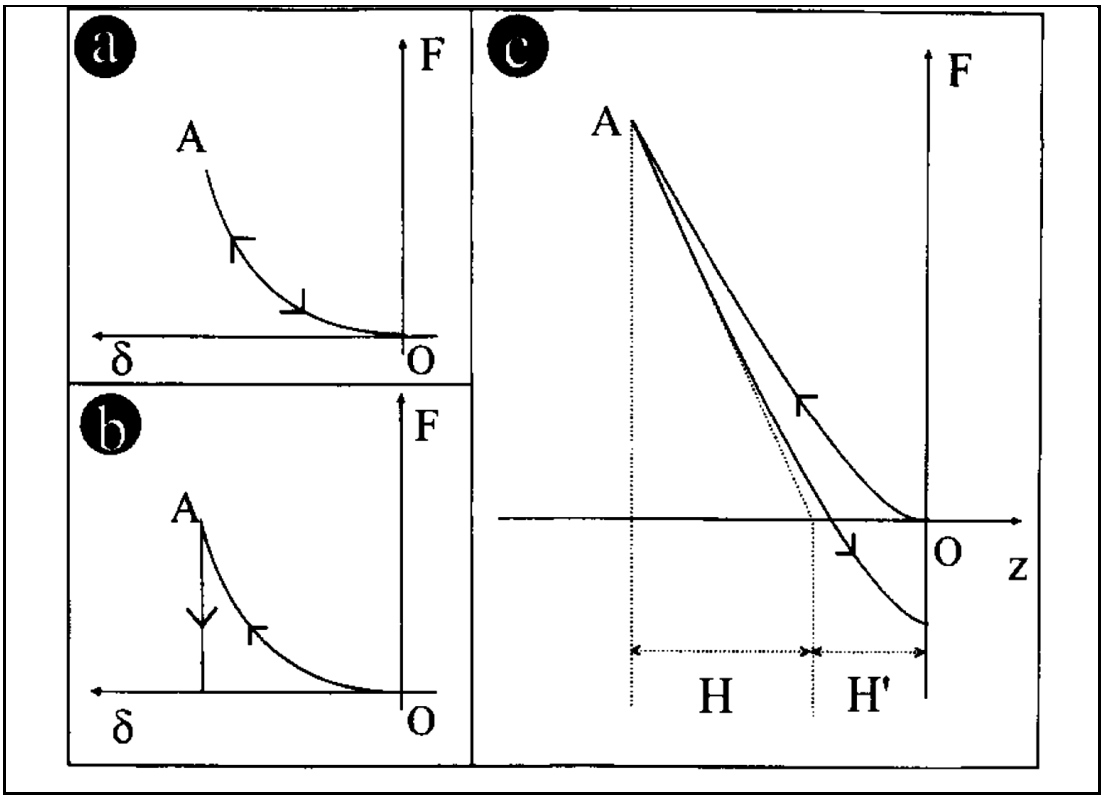

Figure 2.19. : Elasto-plastic behaviour for different materials. a- Ideally elastic material. b- Ideally plastic material. c- Elasto-plastic material. Adapted from (Cappella & Dietler, 1999) with permission from the publisher (Elsevier Science B.V.).

Figure 2.19. shows several curves of load against penetration depth. Panel (a) shows the typical elastic behaviour for a material, whereas panel (b) refers to an ideal plastic behaviour for a material.

Finally, panel (c) is a F-D curve that represents the elastic –plastic behaviour for a material. In panel (c), $H^{/}$ represents the zero load plastic indentation which can be defined as the depth at which the force of the unloading curve is zero. On the other hand, H represents the zero load elastic deformation which means the distance the sample regains.

The earliest theoretical model of contact was by Hertz and Sneddon in 1881. In this theory, neither surface nor adhesion is taken into account and the tip was considered a smooth sphere with elastic behaviour whilst the sample was described as a rigid flat surface. In the limits of high load and low surface forces, AFM can apply Hertz model.

Two other theories known as the Derjaguin Muller Toporov DMT model and the Johnson Kendall Roberts JKR model expanded the range of predictability in AFM measurements.

In DMT, the Hertz theory is applied for the deformation of an elastic sphere but with the addition of an external load. A further refinement in DMT is that the model takes account of the forces acting between two bodies outside the contact region because these forces cause a finite area of contact. DMT is applicable to systems that have a small tip radii, low adhesion, and a high elastic moduli. The DMT approach then can be considered a modified Hertzian model which takes into account the adhesive force between the surface and the tip. The reduced Young's modulus E_r can be given according to the following formula:

$$Er = \frac{3(F_{tip} - F_{adh})}{4\sqrt{Rd^3}} \text{ ---------- (4)}$$

Where: F_{tip} is the force applied onto the AFM tip, F_{adh} is the adhesion force between the tip and the sample, R is the AFM tip radius and d is the depth of deformation (Cappella & Dietler, 1999; Young *et al*. 2011; Bonnell, 2001).

The second model mentioned earlier JKR neglects the long range forces outside the contact area and consider the short range forces only that act inside the contact area.

Systems that have high adhesion, low stiffness and large tip radii are for modelling with JKR.

Between 1971 and 1984, there was an extensive controversy about the two theories (DMT and JKR) until it became clear that the two theories are applicable to the two different situations described earlier (Cappella & Dietler, 1999).

(Panaitescu *et al*. 2012) used the DMT model in conjunction with peak force quantitative Nano measurements QNM which is a novel AFM technique for finding the local interaction between a nanosilica and polymer matrix of styrene (ethylene-co-butylene) SEBS. This technique was also able to determine the elastic modulus for regions around the nanoparticles. DMT was the best model for characterising the nanomechanical properties in this study as there were other attractive forces outside the contact area between the tip and the sample such as electrostatic, capillary, Van Der Waals, etc.…

Other theories have been developed for predicting the effects of contact deformation and the following Table 2.11. due to (Bonnell, 2001) summarises them with their assumptions and limitations.

Table 2.11. : Comparison of different contact deformation theories. (Bonnell, 2001).

Theory	Assumptions	Limitations
Hertz	No surface force	Not appropriate for small loads
DMT	Long range forces act outside contact area, contact geometry remains Hertzian	May underestimate contact area
Burnham Colton Pollock BCP	Long range forces act outside contact area, surface allowed to bulge out	May overestimate contact area and underestimate the adhesion
JKR	Short range forces act inside contact area	Many underestimate loading owing to forces
Maugis Dugdale MD	Periphery of tip-sample interphase modelled as a crack	Parametric equation

Apart from these leading models there is also a numerically based one, The Muller – Yuscchenko- Derjaguin/ Hughes- White MYD/HW model. It is not widely cited in the literature but represents a promising approach (Bonnell 2001).

2.6. Fractography

A valuable deal of information about the materials can be achieved by fracturing them and investigating their fracture surfaces. In the research field, the fracture surface investigation is particularly important in those cases where quantitative data can be obtained. Fractography is the most important analytical approach used by materials scientists in attempting to explain structure-property relationships involving strength and failure of the materials. It also provides important information about the response of the materials to mechanical, thermal, and chemical environment (D.A. Ryder, 1971; Masters & Au, 1987). (Tseng *et al*. 2013) were studied the morphology of polyimide/GO nanocomposites via cryogenically fractured surface. The current study provides information about the morphology and nanomechanical behaviour for PS and its nanocomposites via the cryogenically fractured surfaces of these materials.

2.7. Summary of the Literature Review

The literature review has described the background research on composite and nanocomposite materials, and the effect of low loadings with different nanofillers on some of their properties, and in particular their mechanical properties.

It has been shown in the review that achieving the optimum conditions, particularly in the preparation of nanocomposites, is not a straightforward task. There are significant challenges in this field regarding the appropriate selection of preparation method, and the related processing conditions. Consequently, studying the properties of the resulting nanocomposites, and the more complex structure-property relationship demands a great deal more investigation. Transparency, low cost and ease of processing are the key factors related to the production of thermoplastic polymers, especially PS for potential applications.

Despite the long preparation time and high cost of materials, GO has attracted considerable attention as a successful precursor for dispersion in different polymer matrices. The oxygenated functionalities provided by GO pave the way towards successful preparation especially by the solution blending approach. This is because these functionalities provide an ease of solubility of GO in water and many organic solvents.

The appropriate selection of solvent for dissolving the polymer and GO is an important consideration in the preparation of nanocomposites. Following this, the development of the optimum dispersion technique and the time adjustment in that technique is equally critical because the duration of the processing can severely influence the properties of the resulting material.

The reduction of GO is another route for obtaining graphene though the extent to which the oxygen functional groups have been eliminated from the GO nanosheet is still unclear in all the adopted approaches that have been tried for reducing GO.

Nevertheless, adopting an eco-friendly approach is a desirable option for many researchers in order to avoid the detrimental effects of using chemical reductants. The thermal approach to reduction using a special vacuum oven is a more ecologically friendly option used by many other researchers to achieve the reduced form for GO and to incorporate the rGO into the polymers. However, it is another challenge to reduce the effect of vanishing oxygen functionalities and considering the amount of elimination of these functional groups. Studying the nanomechanical behaviour of the matrix and the nanomaterials incorporated onto the matrix, is essential for achieving a sufficient understanding about the materials that could be used in practical applications. The study of nanomechanical behaviour can be achieved with traditional techniques of AFM, nanoindentation and novel techniques such as QNM.

However, these techniques are susceptible to the classical theories of contact deformation which can affect the interpretation of the measured characteristics with regard that adopting the novel approach is giving a better perception for the nanomechanical behaviour according to high precision of these techniques. The nanomechanical behaviour of the interphase region is still not clear and the research community is focussed on developing more clarity on this key issue.

Chapter 3.

The effect of dispersion method and processing conditions on the structure and properties of PS/GO nanocomposites

3.1. Introduction

The convenience of processing and moulding and the benefits of other supporting characteristics such as good chemical resistance, low density and a high performance price ratio make PS one of the most widely used polymers for commercial applications (Han *et al*. 2013). See section 2.2.5. about PS. Graphene and its derivatives are the most promising filling agents for preparing PNCs. Graphene is an allotrope of elemental carbon comprising the SP^2 hybridized carbon atom. It is a 2D honeycomb lattice that has exceptional thermal and mechanical properties with a planar monolayer of carbon atoms arranged in it (Singh *et al*. 2011; Fan *et al*. 2013).

However, in spite of progress in graphene production the cost to produce it at high quality is still prohibitive for synthesising novel graphene based materials for practical applications. This is the reason why researchers have used wet chemistry to obtain exfoliated graphene through the oxidation of graphite leading to GO (Economopoulos & Tagmatarchis, 2013).

To ensure an efficient involvement for liquid phase exfoliation to produce graphene two distinct methods have been utilized and these are:- (i) the use of an exfoliation agent (solvent), and (ii) the use of surfactants (Economopoulos & Tagmatarchis, 2013).

PNCs represent a new frontier in materials engineering as the dimensions of additives have been reduced from the micro range to the nano range. The Processing stage of the nano composite materials is the formation of the structure of the material. By controlling the processing conditions the properties can be tailored at the nanoscale which ultimately leads to multifunctional composite materials with properties that are not attainable in traditional composite materials system (Thostenson & Chou, 2006).

The improvement in the physical and mechanical properties for the polymer nanocomposites is intimately associated with a good dispersion of the nano material in the matrix. The achievement of such an aim is linked with both the processing and synthesis techniques that lead to good dispersion in the matrix (Yasmin *et al*. 2006). Information about processing conditions were mentioned previously in section 2.4.2. (Zhao *et al*. 2010) confirmed that a significant improvement in the mechanical properties with an order of magnitude increase in Young's modulus and a tensile strength of 150% in PVA/graphene nanocomposites of 1.8 Vol.% under the condition of random dispersion of graphene nanosheets in the matrix.

The full exploitation of the physical and mechanical properties of the polymer nanocomposites also requires the right choice of the organic solvent or aqueous medium. Good dispersion of the nano material in the matrix requires adequate stability and concentration (Johnson *et al*. 2015). For instance, (Hasan & Lee, 2014) found that better dispersion and high stability for graphene sheets compared to CNTs in PVC obtained using THF. Section 2.3.5. discussed the dispersion of GO in organic solvents. By ensuring a well dispersed system, the surface area of the reinforcing filler will be maximized, which means that the neighbouring polymer chains will be affected and the properties of the entire system will be consequently enhanced (Verdejo *et al*. 2011). (Iqbal *et al*. 2016) found that a poor dispersion of graphene in polymer matrices led to poor performance of nanocomposites with limited applications. The colloidal dispersion option for GO is an advantageous route for many reasons. Different macroscopic materials can be processed using this route, such as, composites, coatings and thin films. Simple techniques of spray coating, spin coating and solution blending can also be employed (Ayán-Varela *et al*. 2014). Solution blending is a good strategy for preparing the PNCs according to its simplicity. It includes three major steps; dispersion of the nanoparticles in a suitable solvent using a specific technique such as sonication, the addition of the polymer, and finally the solvent removal by evaporation or distillation (See section 2.4.1.3.) that discusses solution blending.

Compounding methods could have detrimental effects on the mechanical properties of the nanocomposite materials especially at low weight fractions (Araby *et al*. 2014; Zhao *et al*. 2010; Verdejo *et al*. 2011). The work described in this thesis highlights the effect of processing factors, mainly the effect of organic solvents DMF and THF and the effect of mixing time adopted to operate bath sonication and shear mixer, on the structure and properties of PS and its nanocomposites. Bath sonication was used to disperse GO in the matrix with DMF as the organic dispersing medium. In THF, both bath sonication and shear mixing were used with two different periods of mixing time to disperse GO in a thermoplastic polymer. The investigations also included the effects on structural, mechanical, thermal, and thermomechanical properties. The weight fraction used for the polymer matrix was 0.5 wt. % which is considered to be a suitable fraction for structural applications (Gupta *et al*. 2013).

3.2. Experimental Section

3.2.1. Materials

The materials used in the investigations are described in Table 3.1.

Table 3.1. : Materials employed in the work with their characteristics and their manufacturer and supplier (if there is any).

Material	Characteristics	Manufacturer	Supplier
General purpose PS (Styron 634),	Odourless clear pellets, Melting point 240°C, Mw: 125000 g mol^{-1}.	Dow Chemicals, USA	Resinex, UK
Synthetic Graphite	Powder with grain size $\leq$ 20 μm	Sigma Aldrich, UK	Sigma Aldrich, UK
Potassium permanganate	Powder of 97% purity	Sigma Aldrich, UK	Sigma Aldrich, UK
Sodium nitrate	Powder of > 99% purity	Sigma Aldrich, UK	Sigma Aldrich, UK
Sulphuric acid	Solution of (95-98)% purity	Sigma Aldrich, UK	Sigma Aldrich, UK
Hydrochloric acid	Solution of 36.5% purity in water	Sigma Aldrich, UK	Sigma Aldrich, UK
Hydrogen Peroxide	Solution of (29-32) % purity in water	Sigma Aldrich, UK	Sigma Aldrich, UK
N,N- DMF	Organic solvent of >99.5 % purity	Sigma Aldrich, UK	Sigma Aldrich, UK
THF	Organic solvent of >99.5 % purity	Sigma Aldrich, UK	Sigma Aldrich, UK

3.2.2. Preparation of graphite oxide, GO, and PS/GO nanocomposites

The following diagram, Figure 3.1., is showing the plan of the chapter briefly before clarifying every single step in details in the context in the coming pages.

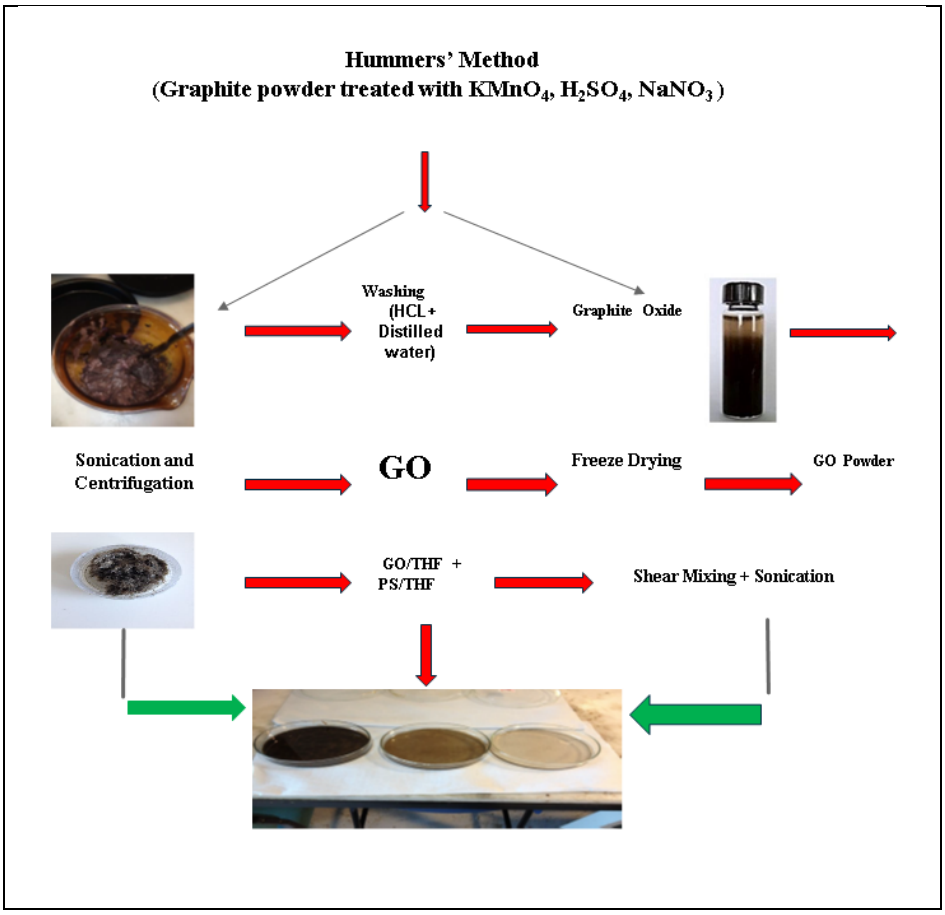

Figure 3.1.: The diagram of the experimental procedure of preparing graphite oxide, GO and PS/GO nanocomposites.

3.2.2.1 Preparation of graphite oxide

Hummers' method was used to prepare graphite oxide according to (Marcano *et al*. 2010). Six grams of graphite was mixed with three grams of $NaNO_3$ in a beaker. 138 ml of high concentrated H_2SO_4 (98%) was added to the beaker which was put in an ice bath to keep the reaction temperature below 35 °C. Then, 36 g of $KMnO_4$ was added gradually over 2 days. A magnetic stirrer was used to mix these chemicals at a speed of 200 rpm (image 1). This resulted in a yellow brown viscous mixture (image 2). To which 10-15 ml of H_2O_2 was added in order to reduce the viscosity. 400 ml of distilled water and 100 ml of HCL was then used for washing the graphite oxide. The resulting graphite oxide was stirred using electrical stirrer (image 3).

A centrifugation process utilizing centrifuges of (Manufactured by JOUAN, France and supplied by Richmond Scientific Limited, UK and Eppendorf, Germany) used for many times after adjustment to 8000 rpm for 1 h each time and the graphite oxide was washed with distilled water up to 18 h till the pH of the solution reached 5.5 (image 4). The following images in Figure 3.2. are showing the different stages of preparation of graphite oxide. It includes all of the aforementioned images (1, 2, 3, and 4).

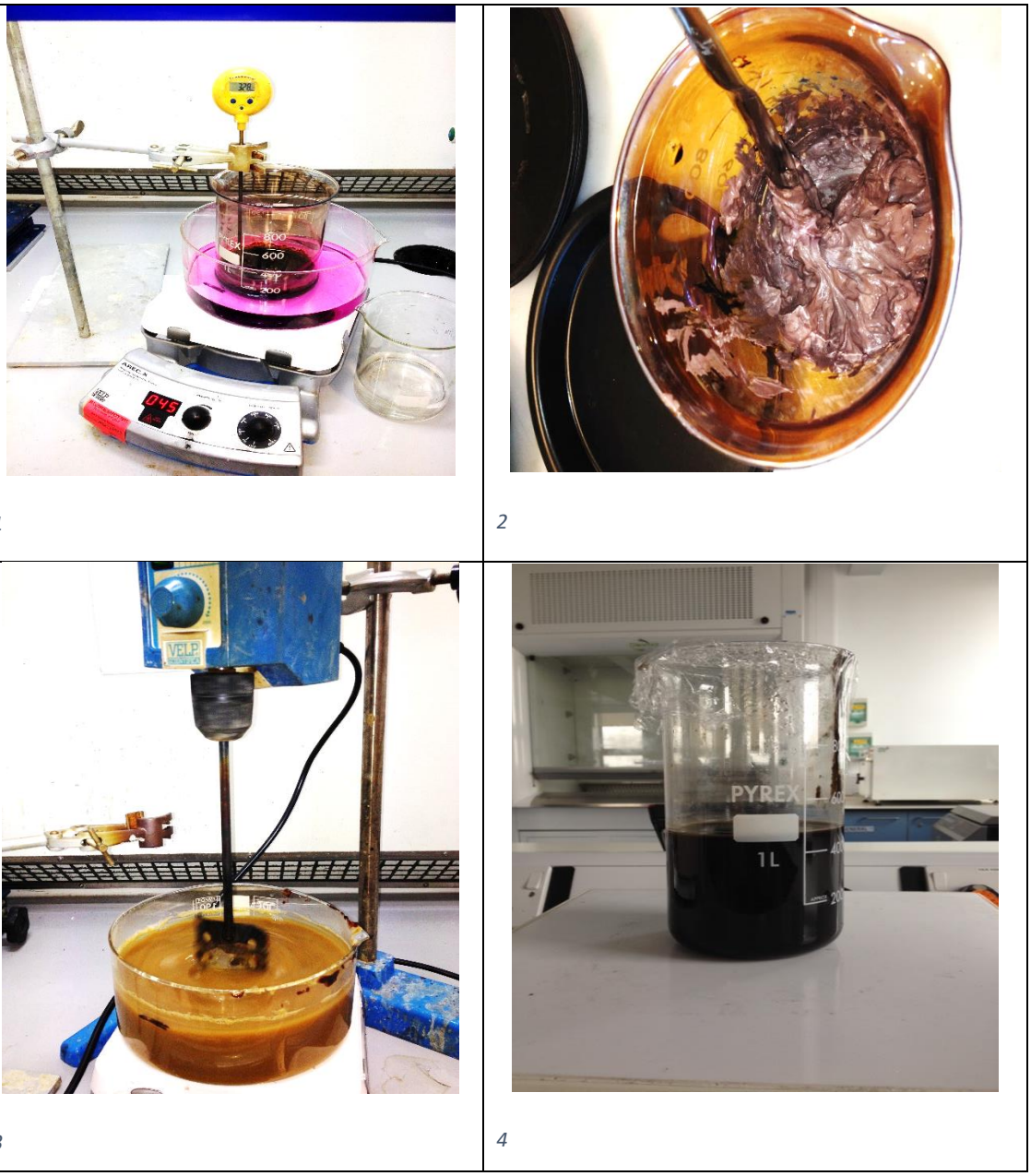

Figure 3.2. : Images show different stages of graphite oxide preparation. 1- Mixing of different chemicals. 2- The yellow brown viscous mixture. 3- The graphite oxide after adding H_2O_2 to reduce viscosity then 400ml water+100ml HCL. 4- Graphite oxide solution with a pH value of 5.5 obtained after many hours of washing using a couple of centrifuges.

3.2.2.2. Preparation of GO

The GO was then prepared by freeze drying according to (Ming *et al*. 2013) as shown below in this section. The graphite oxide was sonicated for 1 h (Fisher brand Elma, Germany, which has a power of 280 W and a frequency of 50/60 Hz), and centrifuged (Eppendorf, Germany) for 30 min. at 6000 rpm. The suspension was then casted in metallic dishes and left to be frozen in a freezer for 24 h at -40 ^{o}C.

The GO then was kept inside the chamber of a freeze drying machine (Bradley refrigeration. Edwards, UK) for 48 h under a pressure around 10^{-1} bar. The final product of GO by this processing was a fluffy powder (porous foam) material. Figure 3.3 is showing an image of the obtained GO that was a fluffy powder material.

Figure 3.3. : The fluffy powdered material of GO obtained by freeze drying.

3.2.2.3. Preparation of nanocomposites

Many trials were tried to achieve good samples of polymer and nanocomposites. The preparation of the latter was passed through different procedures until a relatively good samples with a homogenous dispersion of GO nanosheets was achieved.

3.2.2.3.1. The preparation of PS and nanocomposite using DMF and bath sonication only

The first sample of a nanocomposite was prepared by dispersing GO and dissolving PS in DMF. Twenty grams of PS pellets were first fully dissolved in 200 ml of DMF using magnetic stirring for 6 h at 600 rpm to obtain a clear solution as described in the co-work of (Jarusuwannapoom *et al*. 2005). 100 mg of GO were fully dispersed in 100 ml of DMF by magnetic stirring. The suspension was stirred for 4 h at 600 rpm and pre-sonicated for 1 h. The weight fraction used to prepare the nanocomposite was 0.5 wt. % beside the neat PS. The GO/DMF suspension and the PS/DMF solution were mixed with each other in one beaker and the final suspension was stirred for 6 h at 600 rpm and then sonicated for 1.5 h. The obtained suspension of PS/GO was poured in two open petri-dishes of size 130 mm to ensure a quick evaporation for the solvent. The two samples of PS and PS/GO of 0.5 wt. % were left in a fume cupboard for around 30 days and then in vacuum oven (Fisher Scientific, Korea) for 24 h at 40 ˚C to be fully dried. Poor samples with rugged surfaces were obtained. No clear conclusions were obtained about these samples as no measurements could be done on them.

3.2.2.3.2. Hot pressing for nanocomposites prepared by DMF and bath sonication

Hot pressing was a possible solution to deal with samples prepared according to what has been mentioned in the previous section. The samples were then ground using a coffee grinder and a pestle and mortar before being hot pressed at 180 ºC using a hydraulic press machine (George Moore and Sons, Birmingham, UK) for AFM imaging purposes. Figure 3.4. (a) and (b) shows a couple of images of a poor rugged and hot-pressed nanocomposite film prepared by DMF and bath sonication.

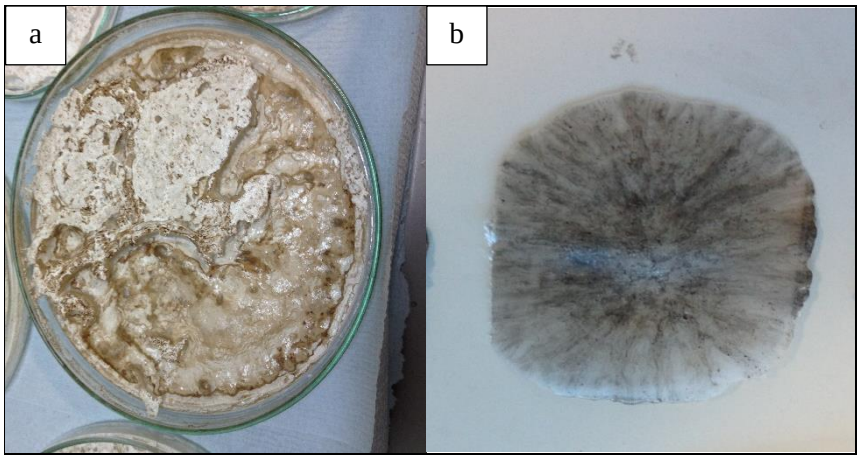

Figure 3.4. : (a).Corrugated film (b). A hot-pressed nanocomposite prepared by DMF. The samples are relatively poor.

3.2.2.3.3. Preparation of PS and nanocomposites using THF and combination of different dispersion techniques

The other samples of nanocomposites were prepared using THF with a different procedure as follows: - 20 g of PS pellets were fully dissolved in 200 ml of THF using a magnetic stirring for 2 h at 600 rpm. A sample of this solution was casted directly in a glass covered petri dish to obtain a polymer film of neat PS and another samples of the same solution was mixed with GO suspension to prepare the nanocomposites.

100 mg of GO were suspended in 100 ml of THF. The suspension was stirred for 2 h at 600 rpm and pre-sonicated for 0.5 h. The GO/THF suspension and the PS/THF solution were then mixed. The weight fractions for GO in PS/GO nanocomposites was 0.5 wt. %, and the mixed solution was stirred for 1.5 h. The sample was then sonicated for 0.5 h using a water bath sonicator followed by 1 h of shear mixing (Silverson, UK) at 1600 rpm /Amp 0.3 which is the current of the motor. This sample was labelled as PS/GO according to what has been considered as a neutral time of mixing.

The same materials and procedure were used to prepare the nanocomposite material, but with a longer time of 1 h and 2 h for sonication and shear mixing respectively. This doubling in the time duration was doubled in order to study the effect on these structure and properties differences for different periods of mixing time and the sample was labelled as PS/GO D considered as longer time of mixing.

The suspensions of PS/GO and PS/GO D obtained were poured in glass covered Petri-dishes of radius 135 mm to ensure a slower evaporation for the solvent. All samples were left in a fume cupboard for 1 week, and then in vacuum oven for 3 h and 40 °C to be fully dried.

3.2.3. Characterization

The characterisation techniques are described separately below:

1. Microscopy

a- Atomic force microscopy (AFM)

These measurements were carried out in order to obtain information about the GO flakes possibly present in nanocomposite prepared by DMF. A (Dimension3100, CLI digital instruments, Veeco) AFM device was used in the tapping mode to achieve this information. The tip that used for imaging was made from silicon by (Nanosensors ^{TM}, Switzerland) and it took a diving board shape with resonance frequency of (210-490) KHz.

b- Optical Microscopy (OM)

Imaging by OM (Swift, model M10 L Series, with an attached camera Swift DV, New York Microscope Co. USA) of the PS/GO samples prepared by THF was used to provide a basic indication for the distribution of GO in PS matrix. The resolution power used was 40X with a magnification scale of 0.5 mm.

c- Transmission Electron microscopy (TEM)

For investigation the quality of dispersion of the nanosheets in the matrix, TEM was used. Sample of PS/GO 0.5 wt. % was prepared in neutral time of mixing was snapped frozen in Liquid Nitrogen and placed in the FC6 cryo chamber to equilibrate for around 30 min. Ultrathin sections, approximately 90 -100 nm thick, were cut using a Leica UC 6 ultra-microtome and FC6 cryo-box both manufactured by (Leica Gmbh, Vienna, Austria and supplied by (Leica Microsystems, Cambridge, UK). The cryo-box was attached onto uncoated 200 mesh copper grids at temperatures of between -60 to -100 ^{o}C.

Sections were examined using a FEI Tecnai TEM at an accelerating voltage of 80 KV and 100 KV. Electron micrographs were recorded using a Gatan Orius 1000B digital camera and Gatan digital micrograph software. The camera and the related software were manufactured by (Gatan Inc. USA) and supplied by (Gatan, Abingdon, UK).

d- Scanning Electron Microscopy (SEM)

SEM (Inspect F, Poland) measurements were used to characterize the fracture surface for the samples and GO powder using different magnification powers. A gold sputter coater (Emscope SC500, England) was used for coating the polymer and the nanocomposites fracture surfaces. Samples were mounted to the sample holder of 25 mm diameter, 16 mm height with doubled angle 90^{o} made from aluminium manufactured by Agar Scientific, Germany. The other sample holder produced by the same manufacturer was slotted specimen stub made from aluminium with a slot and two grub screws for clamping the sample. Polymer and nanocomposite samples were coated manually with silver dag before coating them with gold using the sputter coater machine. This is important to improve the conductivity as the polymers are non-conductive materials and to minimize the charge build up that would affect the quality of the obtained image. Argon gas was purged and vacuum pump was utilised for vacuuming the chamber of coating. Argon gas was purged and vacuum pump was utilised for vacuuming the chamber of coating. Coating started when the vacuum inside the chamber was about 0.06 Tor. The current utilised for coating process was 15 mA and the time required for accomplishing coating process was 3 minutes apart of the time consumed to reach the required pressure inside the chamber which was about 10 min. Thickness of the gold coating was about 50 nm. GO powder was distributed over an aluminium pin stub of high purity and it was taken to SEM imaging after making gold coating only. There was no need for coating GO powder by silver dag.

2. Fourier Transform Infrared Spectroscopy (FTIR)

The device used for these measurements (FTIR Spectrum 100 Perkin Elmer, USA) with a range of 500-4000 cm^{-1} was used for characterizing GO, PS and PS/GO nanocomposites. Accumulations was 16 scans. The used source attached to the machine was MIR 8000-30 cm^{-1} and the detector was MIR TGS 15000-370 cm^{-1}. The scan speed was 0.2 $cm.sec^{-1}$ and the resolution was 4 cm^{-1}.

3. Thermal and thermomechanical properties

a- Thermal Gravimetric Analysis (TGA)

TGA Pyris 1, Perkin Elmer, USA was used to measure thermal degradation temperature. The atmosphere of the test was N_2 and the heating rate was 10 °C. min^{-1}. The range of temperature that used with GO, PS and PS/GO nanocomposites was from 28 to 600 °C. The weight of each sample inside the ceramic pan was 5 mg except the weight of GO powder that was few milligrams. Several samples were tested and only representative samples were shown.

b- Differential Scanning Calorimetry (DSC)

DSC 6 Perkin Elmer, USA was used to find out the value of Tg. The weight of the samples used in this experiment was about 10 mg placed in a sealed pan of aluminium with an empty sealed aluminium pan used as a reference. Both of the sample and the reference were put inside the machine under the influence of nitrogen gas purging at a rate of 50 $ml.min^{-1}$. The range of temperature was ramped from 25 °C to 240 °C at a rate of 10 °C. min^{-1}. T_g was measured from the 2nd run heating to remove any thermal and solvent history. Cooling rate was 10 $^oC.min^{-1}$. Several samples were tested and only representative samples were shown.

c- Dynamic Mechanical Analysis (DMA)

Perkin Elmer, DMA 8000, USA was used to find the storage modulus and tan δ for the neat polymer and nanocomposites where strain was 0.5% (0.05 mm), the range of temperature was 30 – 130 °C, the heating rate was 3 °C. min^{-1}. and the oscillatory frequency was 1 Hz. The deformation mode utilized in this test was single cantilever bending and the samples had

rectangular cross section. Dimensions for samples were (3-5) mm width, (4-10) mm length with thickness about 1 mm. Several samples were tested and only representative samples were shown.

4. Extensometer

The Young's modulus and Tensile strength were measured using an extensometer (Hounsfield, UK). The utilised load cell was 1000 N and the speed of the crosshead was 1 $mm.min^{-1}$. The specifications of the dumbbell used was according to standard (BS ISO 37 type 2), see appendix 3. The number of the tested samples was 4. Figure 3.5 shows a couple of images represent the dumbbell that was utilised to take the samples from the nanocomposites' films by applying a pressure using a hydraulic piston (Specac, USA) and a sample underwent a tensile strength test with a region of fracture.

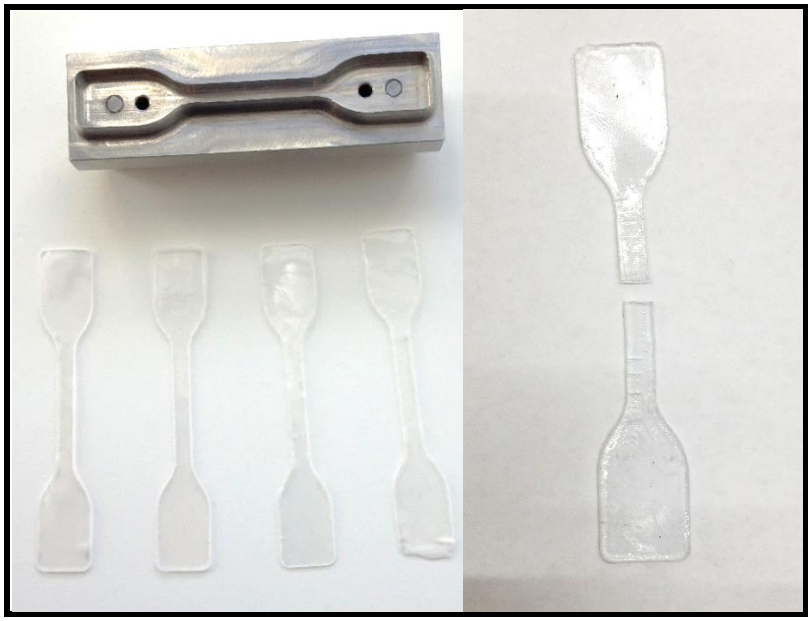

Figure 3.5.: The dumbbell, samples taken from the nanocomposites' films by the dumbbell, and the region of fracture for a tested sample

3.3. Results and discussion

3.3.1. Processing conditions

The GO material showed good dispersion in both DMF and THF. The dipole moment values are significant for these organic solvents, but solvent polarity is not the only required factor for obtaining a good dispersibility. Surface tension is another important factor to ensure a good dispersion for graphene and all of its derivatives. It has been shown that the presence of oxygen functional groups for graphene oxide lead to high surface energy.

The surface energy for GO was estimated to be 62 $mN.m^{-1}$. Because the surface tension for DMF and THF is quite high (37.1 and 26.4) $mN.m^{-1}$ respectively , they are good solvents for obtaining a stable suspension of GO (Konios *et al*. 2014). In addition, (Paredes et al. 2008) confirmed the dispersion of long term stability of the graphene oxide in DMF and THF compared with many other organic solvents. It has also been confirmed by these workers that the full exfoliation of graphite oxide to an individual and single sheet of GO can be achieved by sonication in these two solvents. Such stable dispersions of GO in these two solvents are comparable with the dispersion of GO in water. If the PS beads are stirred for a time exceeding about 6 h in DMF a non-stable suspension is produced, and a ball of gel can be formed.

On the other hand the beads of PS were dissolved smoothly in THF within 2 h and long-time stirring was not changed the nature of solution as happened with DMF. A long term stability was found for PS/GO dispersed in THF whereas corrupted samples were produced in the case of PS/GO dispersed in DMF because a non-stable suspension was formed especially when PS beads were dissolved in the DMF.

Figure 3.6. shows the images for PS and PS/GO 0.5 wt. % films in DMF and THF respectively and the nanocomposite samples after the solvent evaporation process was carried out in the fume cupboard and vacuum oven.

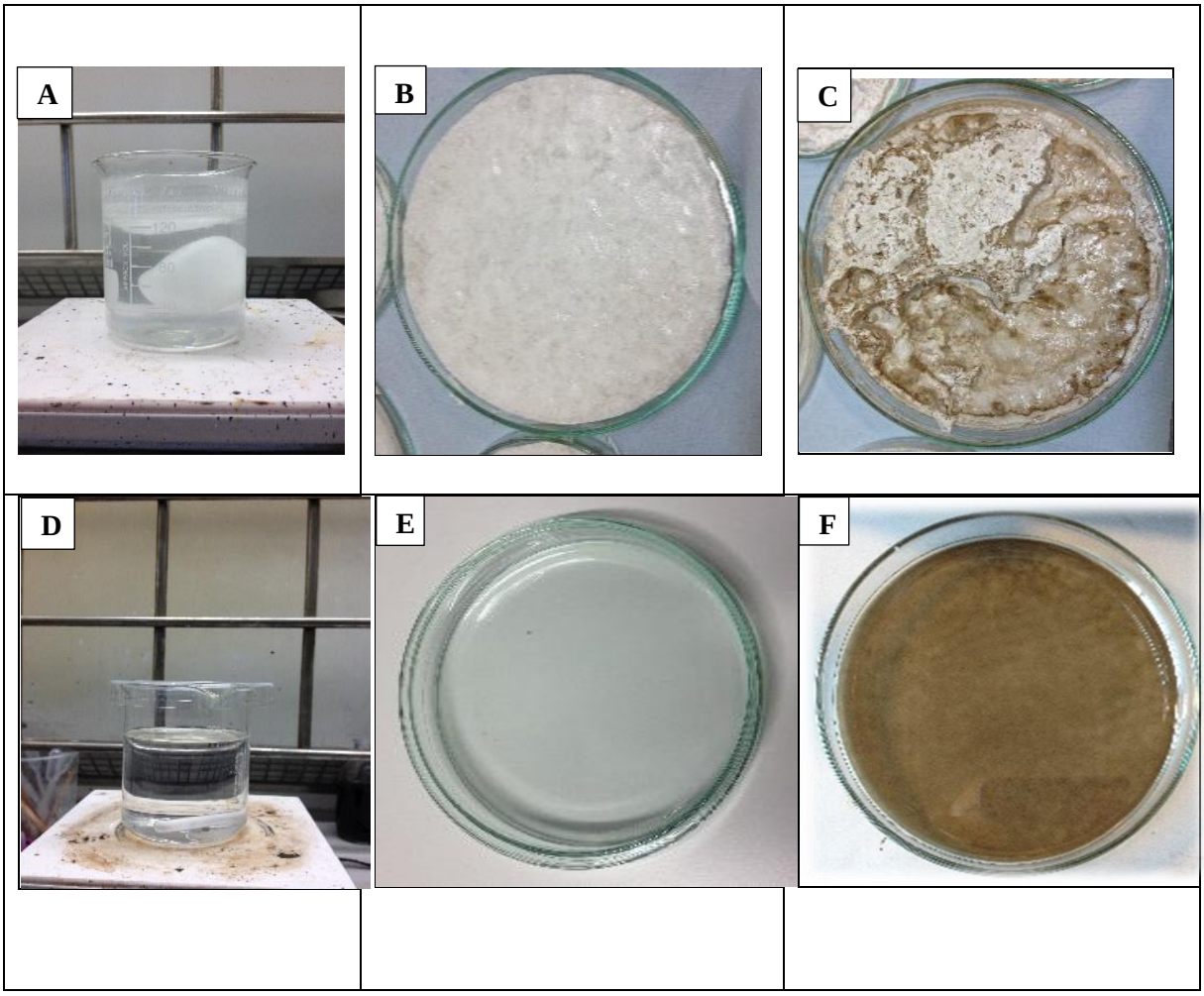

Figure 3.6.: Preparation of the polymer film and nanocomposite material film by a solution blending technique. A. A gel ball of PS in DMF. B&C neat PS film and PS/GO film both dissolved and dispersed in DMF with bath sonication used as the dispersion technique to disperse the GO nanosheets in the polymer matrix. The corrugated surface for both is clear. D. PS beads fully dissolved in THF. E&F dried PS and PS/GO 0.5 wt. % films both dissolved and dispersed in THF. Bath sonication and shear mixing were used as the dispersion techniques for different periods of time.

The dissolving process is very slow and includes two important stages: In the first stage the molecules of solvent are slowly diffusing into the polymer so a swollen gel can be produced, and this process was exactly what happened when dissolving PS in DMF. In the second stage a gradual disintegration of the gel into a true solution takes place and this stage did not appear in the case of DMF though it was verified when using THF. The solubility of the polymer in the solvent can be calculated by using the solubility parameter (delta) equation as follows:

$\delta = (\Delta E/V)^{0.5}$ ……………………………….. (1)

where $\Delta E/V$ is the energy of vaporization per unit volume or the cohesive energy density (Mori & Barth, 1999).

The solubility parameter for THF (19.5 $J^{0.5}/ cm^{1.5}$) is higher than the mean solubility parameter for PS (18.5 $J^{0.5} / cm^{1.5}$) which explains the reason why it was possible for THF to dissolve PS and this makes it a good solvent for PS, though this parameter is not sufficient to make predictions for solubility calculations, other parameters might play a key role in this process. These include Hydrogen bonding, dielectric constant and polar force parameters that should be taken into account. Moreover, the theta temperature (or Flory temperature which is the temperature where no interaction occurred between the polymer and the solvent which means that the polymer does not mix well with solvent which means that the solvent is poor) for THF is below room temperature, which is one of the requirements for a good solvent. On the other hand theta temperature for DMF is close to room temperature which makes it a poor solvent to many polymers (Mori & Barth, 1999). It has been shown by (Dawkins, 1976) that THF is a good solvent for PS and DMF is a poor solvent for PS as gel permeation chromatography GPC separation with DMF showed that there is a displacement to higher values of retention volume V_R when plotted against log hydrodynamic volume where V_R can be defined mathematically as:

$V_R = V_o + K_D K_P V_i$ ………………………….. (2)

where V_o is the total volume of the mobile phase which means the interstitial or void volume, V_i is the total volume of solvent within the gel pores, K_D is the distribution coefficient for steric exclusion and K_P is the distribution coefficient for solute – gel interaction. The reason behind the good performance for THF as a good solvent for the polymer is that the solvent tends towards an athermal mixture which means zero heat change. Then the molecules of PS will not display preferential affinity for the gel or the solvent so that the tendency for the solute retention by interacting with the gel is reduced significantly (Dawkins, 1976). Furthermore, in the case of THF the ‘monomer – solvent’ interactions are more favourable than ‘monomer – monomer’ interactions and for DMF the ‘monomer- monomer’ interactions are the prevailing interactions that lead to chain collapse (Beach, 2009).

It was mentioned that the petri dishes were covered with a glass lid and the reason for this in the case of using THF is to achieve a slower evaporation for the solvent as this factor has a significant bearing on the physical properties of the film. This in turn, will ultimately affect the mechanical properties as well. The slow evaporation allows the polymer network to set into the preferred orientation depending upon the chemical structure of the molecule. The slow processes such as casting evaporation process result in materials of high mechanical performance due to probable orientation of the nanoparticles during the processing of the film (Peponi *et al*. 2014).

In the case of DMF the petri-dishes were left open which considerably affected the apparent structure of the produced samples as shown in figure 3.6. Nevertheless, the solvent did not evaporate quickly and poor samples were obtained. The technique used to prepare the nanocomposite sample using DMF was bath sonication besides the direct mixing using the magnetic stirring. On the other hand the techniques of magnetic stirring, bath sonication and shear mixing are used to prepare the nanocomposite samples with the use of THF.

(Hasan & Lee, 2014) concluded that the mixing technique of bath sonication is not suitable for dispersing the nanofillers they had used in the thermoplastic polymer matrix, as this led to aggregation of the nanofillers in different regions of the prepared film.

It has been emphasised in many studies that the combination of dispersion techniques such as ultrasonication and shear mixing lead to the targeted aim of the even dispersion of the nanoparticles in the polymer matrix (Chandrasekaran *et al*. 2013; Yasmin *et al*. 2006).

Figure 3.7. shows the results of AFM images for the hot-pressed nanocomposite samples prepared by DMF and SEM images for the GO powder. The top couple of images of AFM did not show but traces of solvent and polymer agglomerates.

(Sun *et al*. 2013) confirmed the challenges concerned with the complete removal of organic solvents from the polymer matrix of nanocomposites, and that might affected the thermal,

mechanical and electrical properties of the nanocomposites in a negative way. The lower couple of images of SEM in Figure 3.7. for the pristine GO nanosheets surface show that the surface is clean and it has a wrinkled morphology due to deformation upon exfoliation and restacking processes (Fu *et al*. 2013). The wrinkled nature of graphene sheet confirmed by (El-Khodary *et al*. 2014).

Figure 3.8. shows in the top couple of images obtained by the OM the apparent homogenous distribution for the GO nanosheets in PS for different periods of mixing time. No aggregations of GO can be seen at a specific region of the samples. (Zhang *et al*. 2017) used OM to investigate the dispersion state of rGO nanosheets in the PS matrix. (Gudarzi & Sharif 2011) employed the transmission optical microscopy TOM to show the stable dispersion of GO in PMMA matrix. The TEM image in the bottom of the figure shows the fine dispersion for the flakes of GO in PS matrix. The image was taken for the sample of 0.5 wt. % prepared in neutral time of mixing. No aggregations can be found for the flakes in a specific region in the matrix. The flakes are curvy and look like black strips and they seem as single sheets of GO finely dispersed in the matrix that has a grey background and is easy to recognize.

The curvy and individual sheets of GO reflect the fact that the flakes have wrinkled morphology and they are exfoliated and well-incorporated in the PS which consequently means that they can act as a high effective and efficient nano-fillers for PS nanocomposites. (Ionita *et al*. 2014) reported their result of TEM for PSF/GO 0.5 wt. % which is the same concentration of GO used for the current study. The result showed the homogenous dispersion of single sheets GO on the PSF matrix with hardly any aggregations. This result is quite similar to what has been achieved in the current study with regard that phase inversion method was employed for preparing the nanocomposites of PSF/GO. This method included a continuous stirring for long time (24 h) followed by sonication for 60 min. and the co-solvent used was DMF.

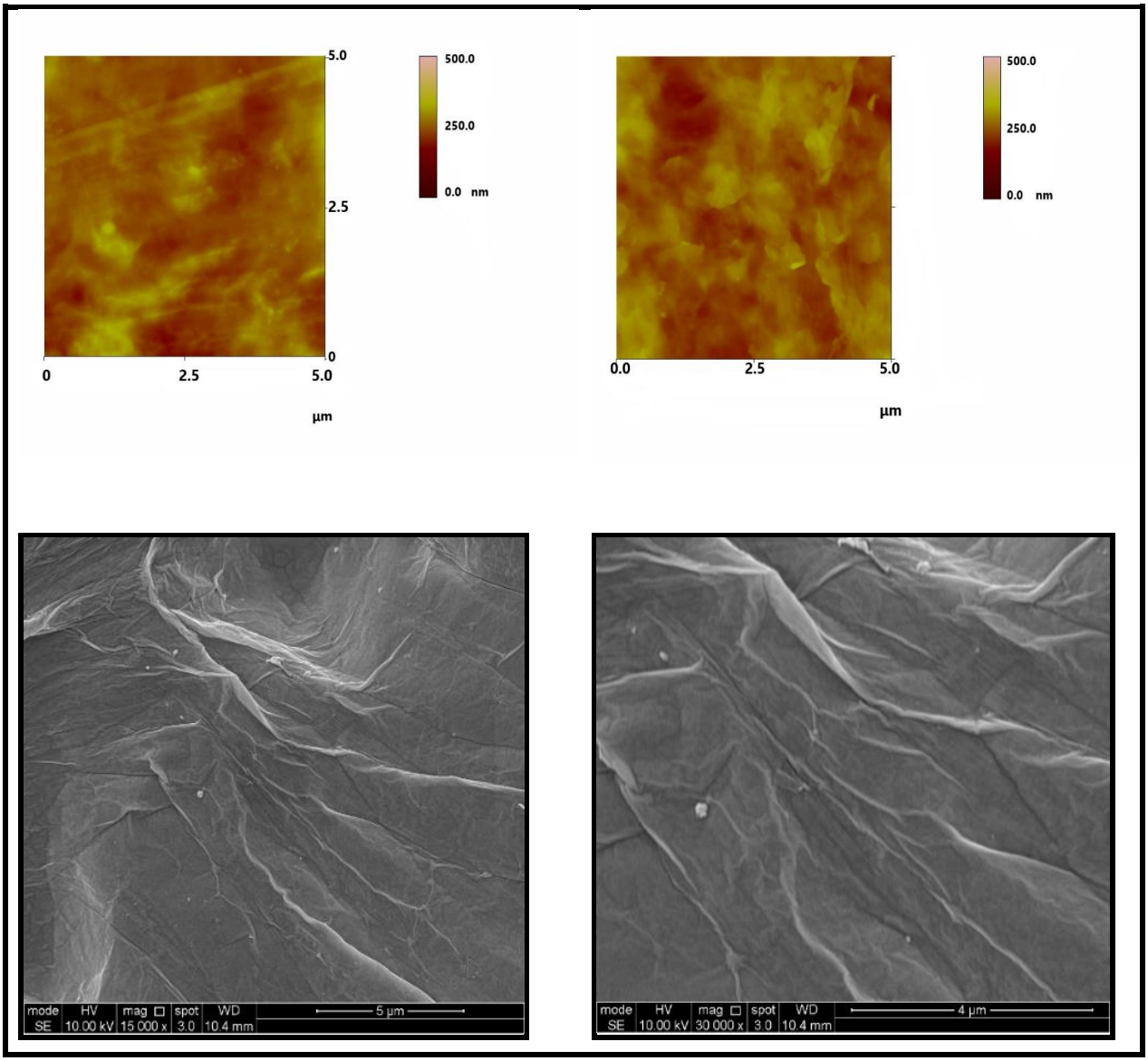

Figure 3.7.: The top two images are AFM images for the hot pressed samples of PS and PS/GO nanocomposites prepared by DMF. The lower images are SEM images that show the wrinkled morphology of the GO nanosheets.

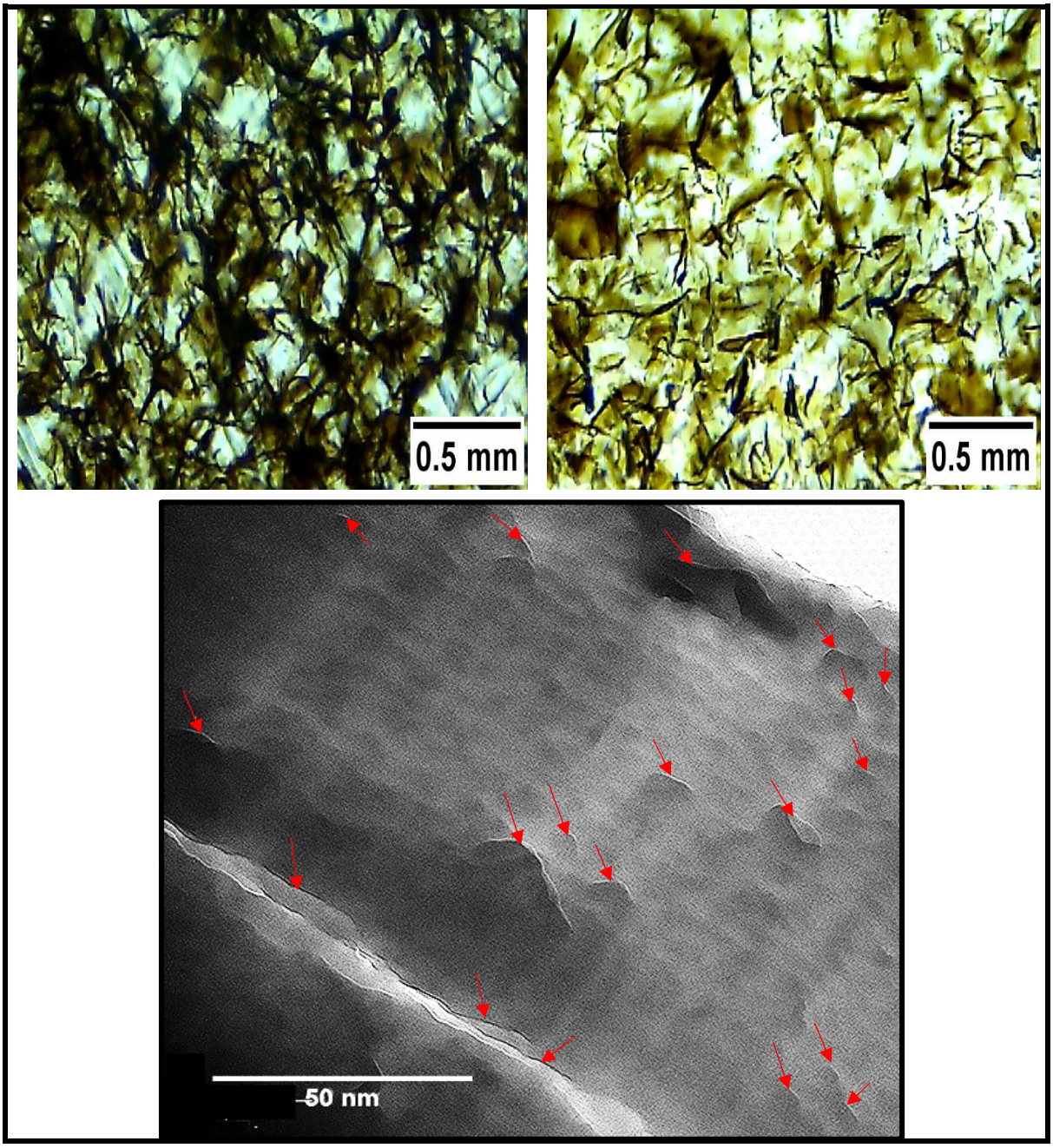

Figure 3.8.: The top couple of images are the OM images thst show samples of PS/GO and PS/GO D nanocomposites prepared by THF. The lower image of TEM shows the even distribution of GO in the PS for the sample prepared in nutral time of mixing PS/GO. Red arrows refer to the GO flakes.

3.3.2. Structure of PNCs and morphology of fracture surface

3.3.2.1. FTIR

The IR peaks obtained from the FTIR measurements for GO are shown in Figure 3.9. , along with the peaks of neat polymer and nanocomposites for different times of mixing. It is worthnoting that is possibile to utilize FTIR to analyse any possible chemical interaction between the polymer matrix and the nanofiller (Prolongo *et al*. 2008).

For the GO spectra, hydroxyl, epoxide and carboxylic acid can be shown as a rich collection of absorption bands and the O-H stretching vibration of hydroxyl groups can be seen at 3500 cm^{-1} . The range for the O-H stretching vibration is 3000-3600 cm^{-1}. C=O stretching vibrations can be seen at 1730 cm^{-1} from carbonyl and carboxylic acid groups as the range for this vibrations is 1730-1706 cm^{-1}. The sharp peak of 1625 cm^{-1} can be attributed to the unoxidized graphitic domain. This domain can be found within the range of 1680 - 1450 cm^{-1} which is attributed to the remaining C=C in GO. C-H bending vibration can be seen located at 1340 cm^{-1} with regard that this kind of vibrations has a range of 1465-1340 cm^{-1}. The sharp peak at 1045 cm^{-1} and the weak peak at 1238 cm^{-1} are related to C-O stretching vibratons with regard that the former represeted the epoxy groups. C-O stretching vibrations has a range of 1300-1000 cm^{-1}. The hydrophilicity of GO is arisen from the abundancy of these oxygenated functional groups (Ming *et al*. 2013; Yin *et al*. 2013). (Heo *et al*. 2012) reported the presence of OH , C=O and C-O groups in their sample of GO at quite similar wavenumbers compared with GO in the current study. The presence of the peaks at the following wavenumbers 3025, 2923, 1492, 1452 and 698 cm^{-1} means that the PS has been prepared successfully. The shoulders of 2923 and 3025 cm^{-1} are due to the presence of C – H stretching vibration of the aliphatic chain and aromatic ring, respectively. The peaks of 1452 and 1492 cm^{-1} represent the C – C stretching of benzene ring.

The peak at 1023 cm^{-1} confirm the interaction between PS and GO. Other possible interactions between GO and PS can be found in peaks located at 838 and 1068 cm^{-1}. These peaks are slightly shifted as compared with literature that referred to interaction between GO and PS at 803 and 1095 cm^{-1}. (Prolongo *et al*. 2008) showed that the enhancement of dispersion for the nanofibers in the polymer matrix led to improvement in the chemical interaction of the nanofibers functional groups with the functional groups of the polymer. However, the majority of peaks for PS have been confirmed for the samples of nanocomposite material of different times of mixing with no obvious peak related to GO.

The intensity of all nanocomposites' peaks have become sharper compared to neat PS. The reason behind this can be ascribed for the low content of the reinforcement agent in the polymer matrix (Yin *et al*. 2013; Vukoje *et al*. 2014). Appendix 4 shows all of the aformentioned FTIR bands with their references.

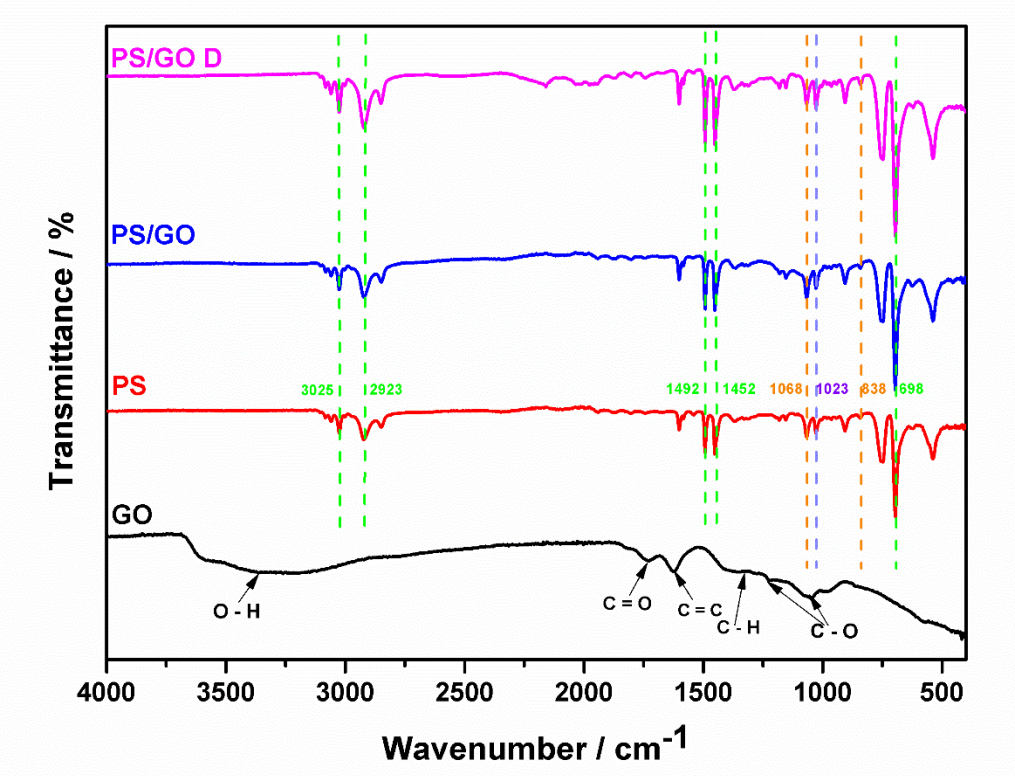

Figure 3.9. : IR peaks for GO, PS and PS/GO for different time of mixing. Orange dash lines refer to the peaks where interaction between PS and GO is possible. Purble dash line is a peak where interaction between GO and PS is confirmed. The green dash lines are the main peaks of PS.

3.3.2.2. SEM

The SEM images in Figure 3.10. show the fracture surface for neat PS and its nanocomposites that were prepared for two different mixing times. The irregular morphology for the majority of images can be seen apart from the smooth nature of PS. GO nanosheets embedded in the polymer matrix might play a major role in iducing the wrinkled surface on the nanocomposites. In addition, a smooth fracture surface for PS can be seen compared with the fracture surface for other nanocomposite materials which is more likely to be very rough.

The wrinkled and stretched style for the GO sheets gives an indication of the random dispersion of the nanosheets in the polymer matrix and this lead to the conclusion that there is good interfacial interaction between the matrix and the filler. Moreover, the images of the nanocomposites show no aggregations are located in the dense regions and this is due to the favourable Π-Π interaction between the nano sheets and polymer matrix (Yin *et al*. 2013; Ding *et al*. 2015). The images of PS/GO taken for the samples prepared in neutral time of mixing which are in the middle row show best GO flakes dispersion compared to the images of PS/GO D at the last row that are related to the samples prepared in longer time of mixing.

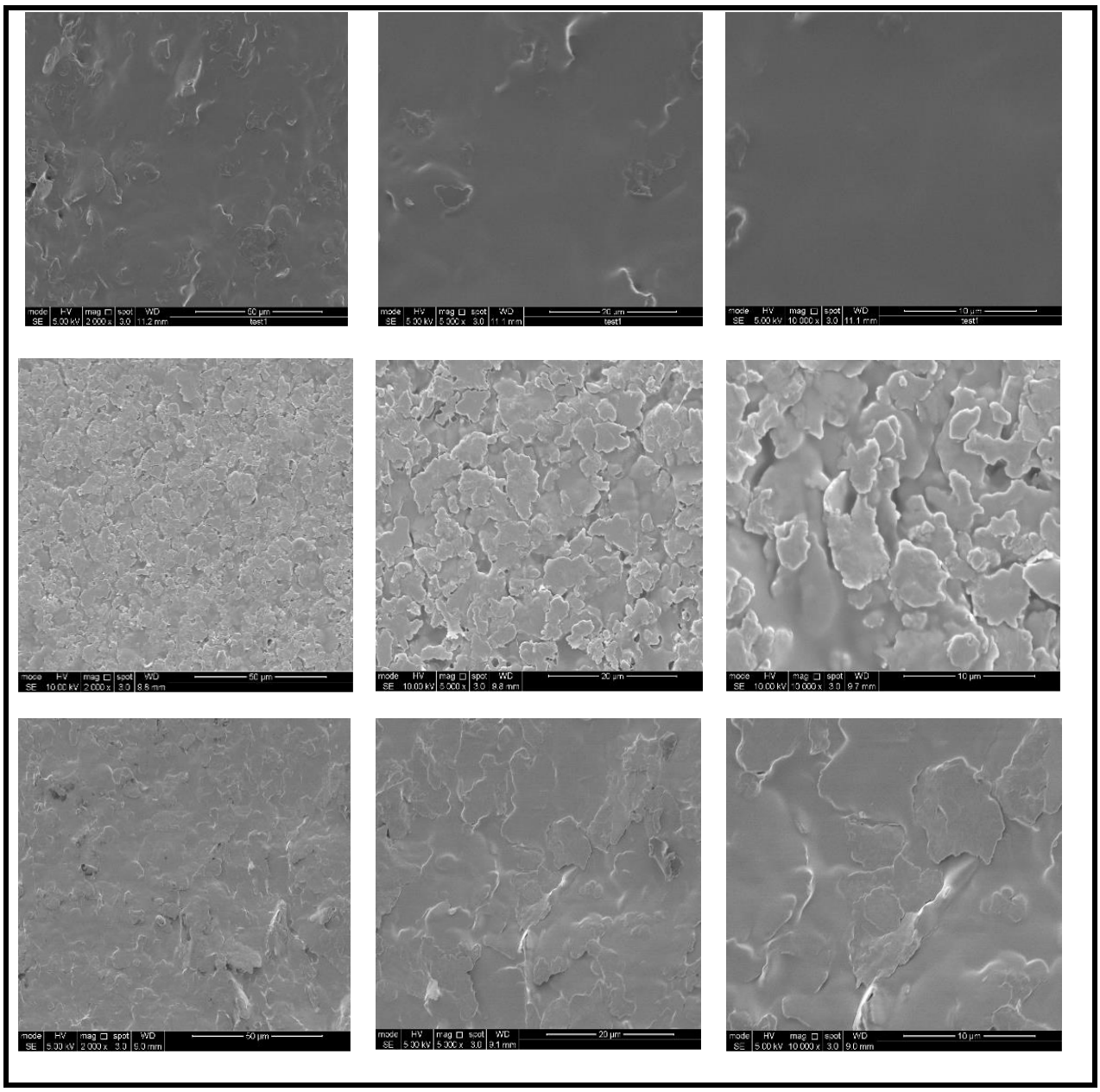

Figure 3.10. : SEM images for: PS ''1st row'', PS/GO '' 2nd or middle row'', and PS/GOD ''the last row''.

3.3.2. Thermal and thermomechanical properties

3.3.2.1. TGA

Figure 3.11. shows the TGA and DTG curves for GO, PS and nanocomposites. GO curve shows (4-5) % weigh loss at room temperature, attributable to buoyancy effects at the earliest stage of that curve as the method includes 5 minutes isotherm at 25 ^{o}C for gas purge before starting to increase the temperature. This step was important to flush the air out of the atmosphere before heating. The curve also indicates a major weight loss starting from 206 C. The pyrolysis of unstable oxygen functions attached to the graphene surface led to such a weight loss. Another reason is the evaporation of water molecules (below around 100 degrees °C). Gas generation is also associated with this drastic weight loss for GO including CO and CO_2 (El-Khodary *et al*. 2014; Tang *et al*. 2014). This result is in line with the result reported by (Zhang *et al*. 2014).

The onset decomposition for PS started at around 120 °C and significant decomposition started at around 316 °C as observed from TGA measurements. This degradation for neat PS is due to main chain pyrolysis. The maximum degradation temperature T_d peak of the nanocomposites has been increased compared with neat PS.

Nanofillers can cause a restriction to the mobilization of PS macromolecules which means a homogeneous heating rather than heat concentration. Furthermore, such range of high degradation temperatures compared with the neat PS suggests a consistent interaction between the matrix and the nanofillers, which means that good wetting can be confirmed. The higher value of wetting means the better thermal properties for the nanocomposite materials (Lee *et al*. 2013). Graphene based materials forming a jammed network of char layers that could efficiently retard the transport of the decomposed material. This explains the reason behind the enhanced thermal stability for the nanocomposites compared with the neat PS (Fan *et al*. 2013). The co-work of (Lim *et al*. 2003) studied the dispersion quality for a clay in the polymer matrix specifically by using an ultrasonication technique.

The dispersion quality is better for the sonicated samples compared with non-sonicated samples. This is because the thermal decomposition temperature was improved after using the ultrasonication technique as an efficient processing factor. The layer distance in clay particles was increased by using the ultrasonication technique which led to improvement in the thermal stability. Table 3.2. shows the T_d peak for the GO, PS and nanocomposites prepared in different times of mixing.

Table 3.2. : T_d peak for the GO, PS and nanocomposites prepared in different times of mixing.

Sample	**T_d peak / ^{o} C**
GO	224
PS	347
PS/GO	360.4
PS/GO D	361.5

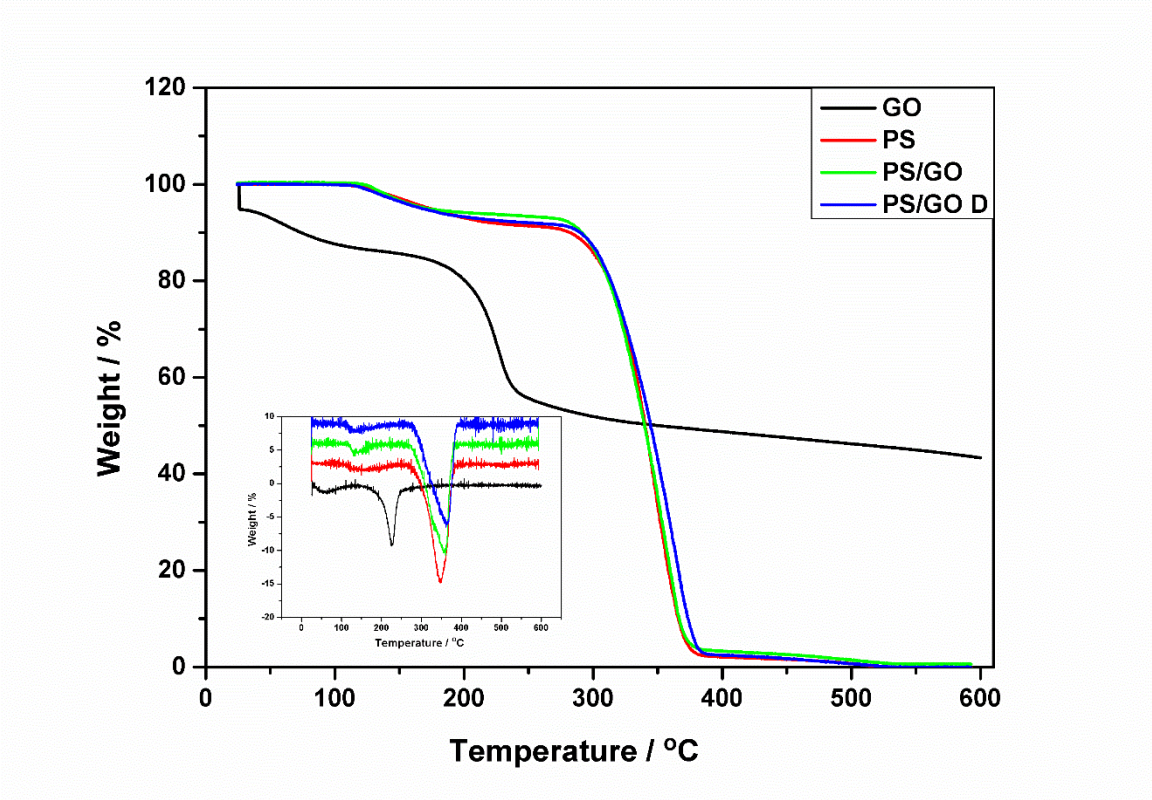

Figure 3.11. : TGA and DTG for the GO, PS and nanocomposites with different periods of mixing time.

3.3.2.2. DSC

Figure 3.12. shows the DSC curves for the neat PS and the PS/GO nanocomposites that have the same weight fraction and different times of mixing. It can be seen that the values of T_g was significantly shifted for the nanocomposites compared with the neat polymer. The incorporation of GO in PS improved the thermal performance for the nanocomposites compared to the pristine polymer for different periods of mixing time. T_g for PS was 99.4 °C whilst T_g for PS/GO was 103.03 °C and for PS/GO D was 104.4 °C. The major increment in the values of T_g with the matrix reinforcement with GO nanosheets refers to the fact that the interfacial interaction between the matrix and the nanosheets is sufficiently strong to hinder the polymer chains movement at the interface (Wan & Chen, 2012). (Chen *et al*. 2007) confirmed that sonication plays a crucial role in disintegration of the agglomerates. The same team found that the use of the speed mixer to mix the untreated CNT's with the polymer matrix led to improvement in thermal stability as T_g became higher. The reason behind this was the reduction of the mobility of the matrix molecules which resulted in strong interfacial strength between the matrix and the nanotubes.

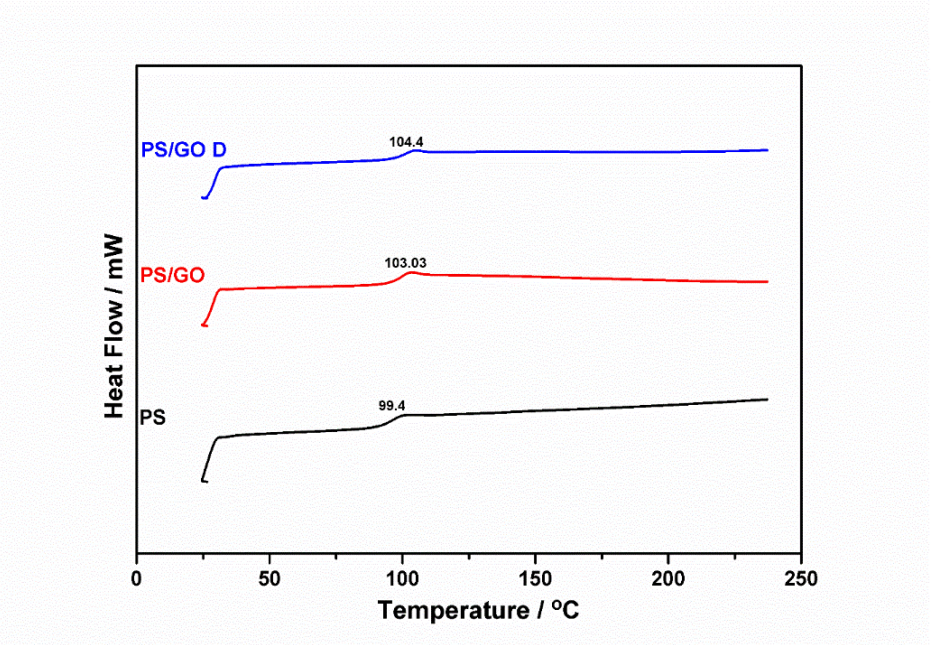

Figure 3.12. : T_g values obtained by DSC for the pristine polymer and nanocomposites prepared by different periods of time mixing.

3.3.2.3. DMA

DMA is used to measure the viscoelastic properties for the materials and it shows the amount of energy stored in the material as an elastic energy (Prolongo *et al*. 2008). Figure 3.13.A and B shows the variation of storage modulus and tan delta as a function of temperature for the polymer and nanocomposite materials using a single cantilever mode.

It can be observed that the values of storage modulus for neat PS and its nanocomposites decreases as the temperature increases. The explanation for this is based on the relation of polymer chains' movement with the increase in temperature that leads to energy dissipation. Drastic motion for the polymer chains is another main reason for a decrease in the storage modulus versus the increasing temperature. Adding GO to the polymer matrix leads to significant improvements in storage modulus values at the glassy stage (30 °C) at which the polymeric molecules are frozen. The shift in T_g values shown in figure 3.14. B shows a shift in values of T_g from around 91 °C for the neat PS to around 107.6 °C for PS/GO D.

The interfacial interaction between the matrix and the nanofillers is a result of high specific surface area and good dispersion of nanoparticles in the matrix. All of the aforementioned show the occurrence of restrictions in the segmental movement of the polymer chains and a shift in T_g values (Hu *et al*. 2010; Srivastava *et al*. 2011). Furthermore, the peaks of tan δ versus temperature become broader with increasing T_g values, reflecting restriction in segmental relaxation . The presence of filler led to higher thermal stability and higher glass transition temperature for the nanocomposites compared with the neat polymer (Hasan & Lee, 2014). However, the storage modulus for neat PS is 1.93 GPa, 2.33 GPa for PS/GO, and 2.02 GPa for PS/GO D. The long time mixing showed lower values of storage modulus compared with those of neutral time mixing.

This result was confirmed by (Hossain *et al*. 2015) when they found that 90 min. of sonication for 0.2 wt.% of nanoparticles in the polymer matrix gave a better value of storage modulus than 120 minutes of sonication . This indicates that this level of sonication facilitates suitable despersion without destroying the nanoparticles. In any case, the values of storage modulus for nanocomposites are much higher than the neat polymer. These results indicate that the usage of different dispersion techniques lead to enhancements in the reinforcement dispersion in the matrix (Prolongo *et al*. 2008). It is quite common to see humps and peaks on the storage modulus directly preceeding the drop of the curve with increasing tempreature. The same humps or peaks might be seen in DSC curves as well. These peaks or humps are associated with the rearrangement in the molecule to relieve stresses frozen in below the T_g by the processing method. These stresses are trapped in the material until enough mobility is obtained at the T_g to permit the chains to move to a lower energy state (Menard & Bilyeu, 2000).

Table 3.3. shows the storage modulus and T_g values obtained by DMA.

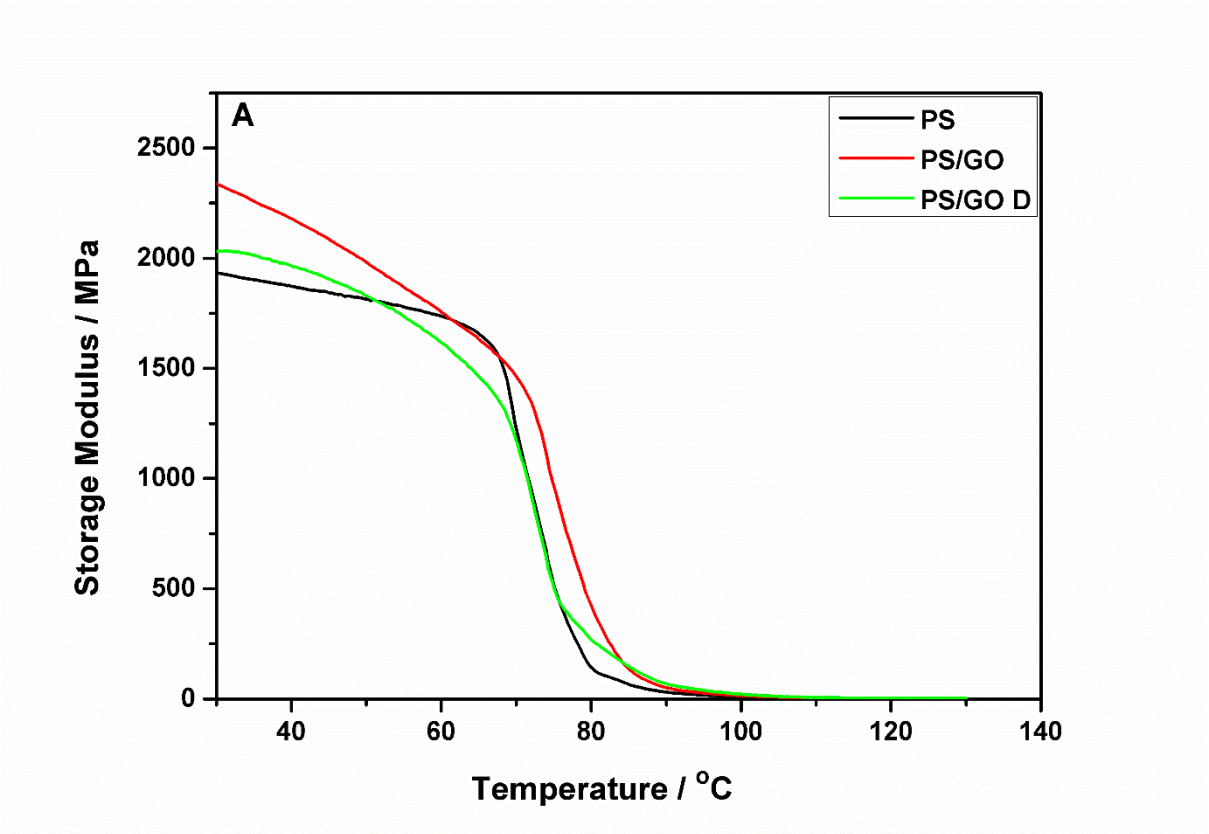

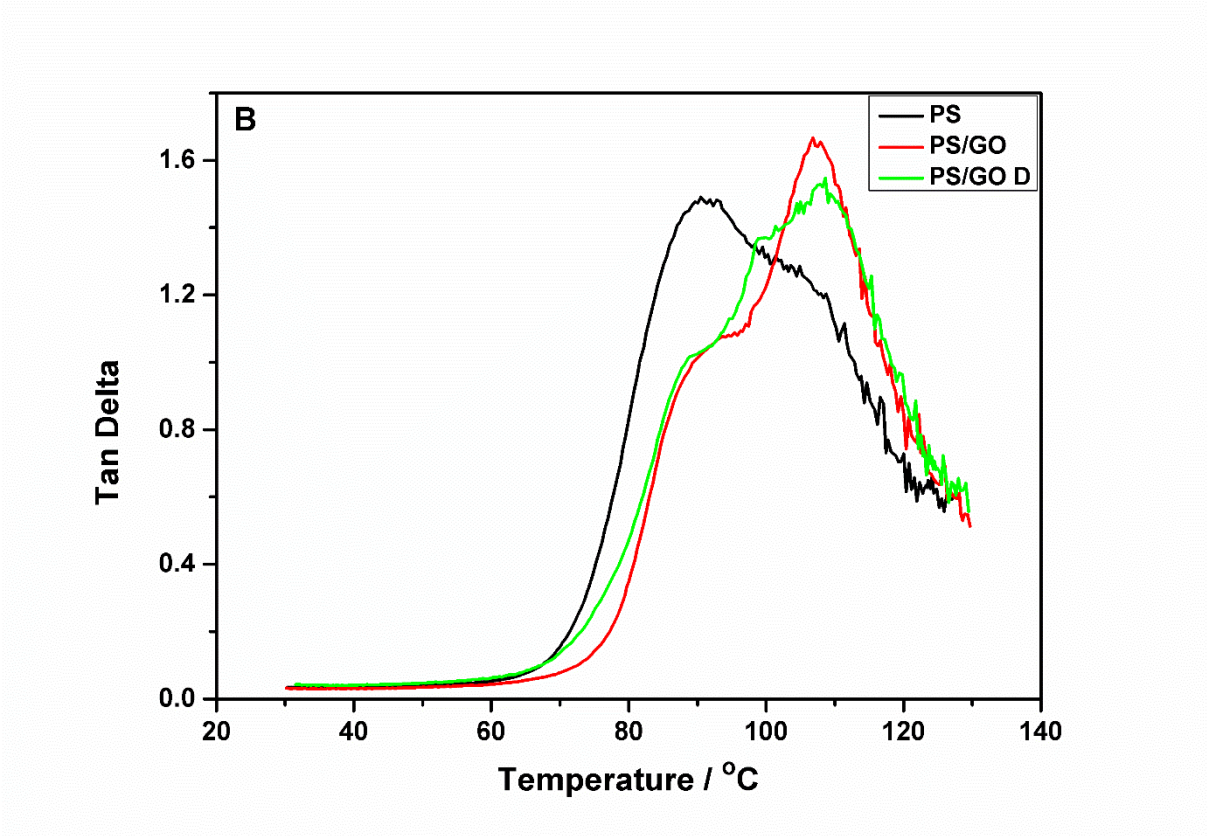

Figure 3.13. : A. Storage modulus and B. T_g values obtained by DMA for PS and nanocomposites prepared in different times of mixing.

Table 3.3. : The values of storage modulus and T_g for the polymer and the nanocomposites obtained by DMA.

Sample	**Storage modulus at 30 ºC / GPa**	**T_g / ºC**
PS	1.93	91
PS/GO	2.33	107.2
PS/GO D	2.02	107.6

However, according to (Leszczynska *et al*. 2007), the data obtained by both DSC and DMA showed that the glass transition temperature for polymer nanocomposites were higher compared to the neat polymer which indicated a better thermal stability for nanocomposites. This is because the oxygen diffusion was hampered by the labyrinth formed by the nanoparticles inside the nanocomposites.

In addition, heat conduction was thought to be reduced in nanocomposites compared to pure polymer which means additional thermal stabilization.

It is very important to mention that there are other factors that affect the T_g value such as chemical linkages, intermolecular forces, compactness (crystallinity), branching, crosslinking, molecular weight, free volume etc. The variation of the T_g value measured by different techniques has been described by (Karak, 2009). For instance, it has been shown that the values of T_g recorded by DMA for the nanocomposites are much higher than those recorded by DSC. The reason for this is sensitivity of DMA which is 100 times greater than DSC. However, there are multiple ways to measure Tg in DMA (storage modulus, tan delta, etc…). DMA can also resolve other kinds of localized transitions such as side chain movements that are unable to be detected by DSC. Furthermore, the technique permits a rapid scanning of the modulus and the viscosity of the material as a function of temperature, strain or frequency.

Plasticisation of the polymers by solvents is an important reason for monitoring the change of T_g for these polymers. The proposed value of T_g for PS is 100 °C and the value of T_g for PS in this work has been decreased to around 99.4°C. The use of THF as an organic solvent for preparing PS and nanocomposites beside other processing factors contributed to this reduction in T_g value. (Yoshioka & Tashiro, 2004) noticed that there was a significant shift in the values of T_g for syndiotactic PS sPS in a different organic solvent atmosphere. The original T_g for sPS was 100 °C. T_g was found to shift to (-90 $\pm$ 10) °C in chloroform atmosphere, to (-70 $\pm$ 10) °C in benzene and (-30 $\pm$ 10) °C in toluene. Figure 3.14(a) shows a conclusion about the thermal properties for the neat polymer and the nanocomposites obtained by TGA, DMA, and DSC. The figure is referring to two important facts:

1- The thermal properties of the nanocomposites are higher than the neat polymer. This means that the incorporation of GO nanosheets to the neat polymer improved the thermal performance.

2- As the time of mixing increased, the thermal properties were more improved. This means that the time of mixing played a main role in achieving better dispersion.

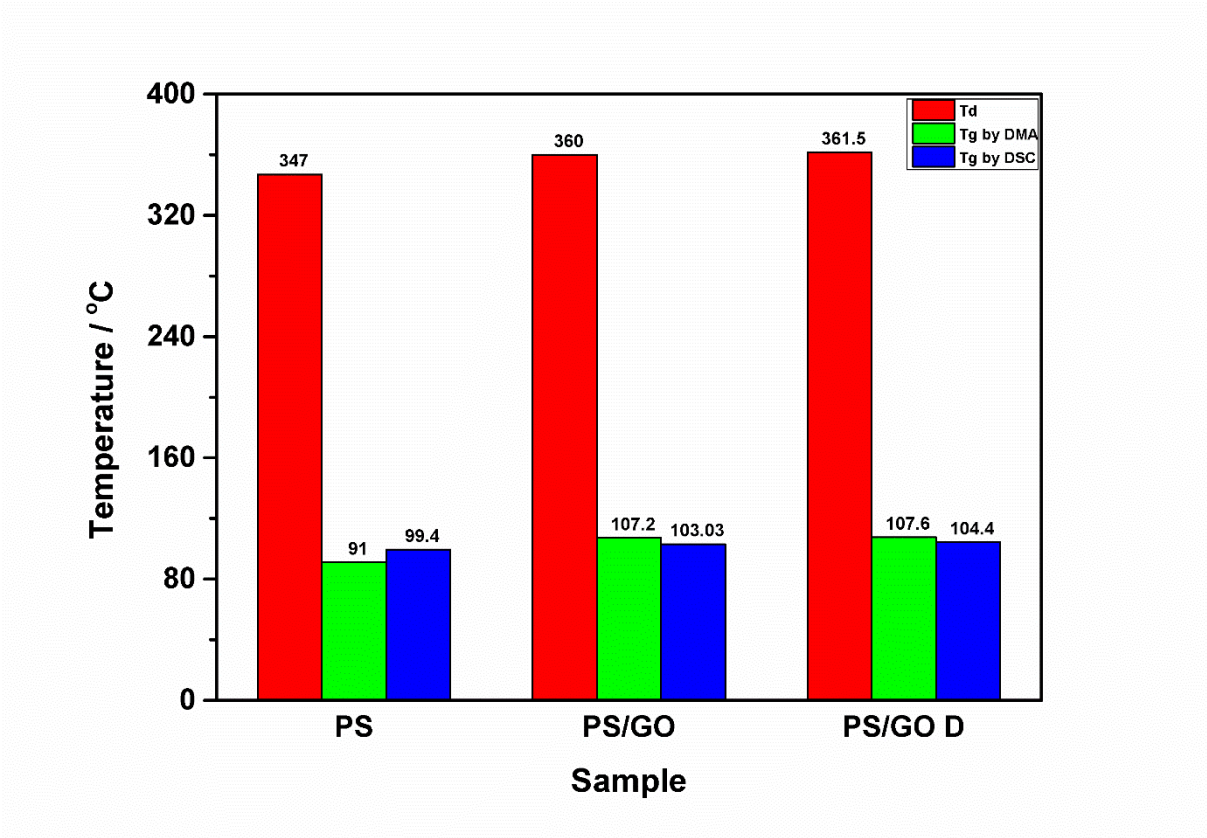

Figure 3.14(a). : Conclusion for the thermal properties for the neat polymer and the nanocomposites obtained via different mixing techniques.

Figure 3.14(b) shows the variation in values of storage modulus with the change in the time of mixing of nanocomposites' preparation compared to the storage modulus value of the neat polymer. The figure shows that nanocomposites prepared in neutral time of mixing have higher storage modulus compared to those prepared in longer time of mixing. All the nanocomposites have higher storage modulus compared to the neat polymer.

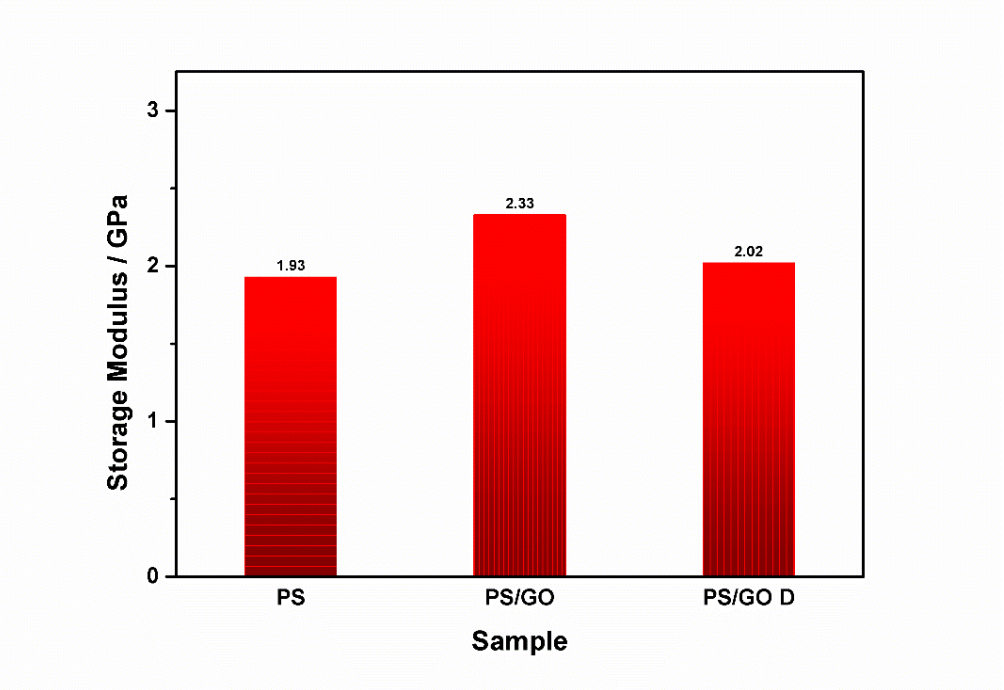

Figure 3.14(b). The variation of storage modulus values with time of mixing employed to prepare the nanocomposites.

3.3.4. Mechanical properties

Figure 3.15. shows the mechanical properties of the neat polymer and nanocomposites prepared in different times of mixing. It has been found that there is an increase in the values of Young's modulus and tensile strength for the nanocomposites compared with polymer especially for the nanocomposites that were prepared by using a longer mixing time. Young's modulus has been improved by around 122% for shorter time mixing and around 143% for longer time mixing.

Improvement in tensile strength values were 15% and 56% for the ordinary mixing time and long-time mixing respectively. It is clear that adding GO to the polymer matrix has had a considerable influence on the mechanical properties. The improvement in mechanical properties was achieved by combining the two methods of bath sonication and shear mixing for longer times.

This is a consequence of processing the nanocomposite in two steps: Firstly, breaking up the graphite into nanosheets due to employment of bath sonication. Secondly, exfoliation and homogenous dispersion for GO sheets in the polymer matrix by shear mixing technique.

The use of magnetic stirring (direct mixing) does not result in nanosheets although it can produce smaller sheets of graphite but not nanosheets. By contrast, the use of synergistic techniques of sonication and shear mixing leads to the formation of nanosheets with a good dispersion in the matrix (Yasmin *et al*. 2006).

Further sonication up to 30 min. with the effect of shear mixing as well also leads to significant decrease in strain failure compared with the neat polymer. Such behaviour is due to the large aspect ratio of GO sheets and the restriction of polymer chain movement due to the interaction between the polymer matrix and GO nanosheets (Li *et al*. 2013).

The brittleness is the prevailing approach that shown by the nanocomposites. Polar mismatches might be the reason behind this brittleness of the nanocomposites as GO is a polar material and the neat polymer is not (Gudarzi & Sharif, 2011). For the polymer itself, PS can be considered a fairly brittle polymer and so this means it will fail in tension, whereas tough materials generally fail in shear.

However, (Van Melick *et al*. 2003) discussed the brittle to ductile transitions in PS and they ascribed that behaviour to the circular voids in the structure that caused craze nucleation under the effect of tension. (Bird *et al*. 1971) discussed the details of crack formation and propagation and the type of fracture generated according to these details. The PS showed a ductile approach in the current study which contradicts the major body of literature such as (Wan & Chen, 2012) who confirmed the brittle nature for the fracture of PS.

The work of (Lan and Pinnavaia, 1994) cited by (Zunjarrao *et al*. 2006) confirmed that the values of tensile modulus was increased when mixing low volume fractions (0 - 2.0) % of nano-particles in the polymer matrix using both dispersion techniques of shear mixing and ultrasonication.

The same conclusion regarding mechanical properties (Young's modulus and tensile strength) was concluded by (Yasmin *et al*. 2006) when they showed that using both techniques of shear mixing and sonication led to better mechanical properties. It can be seen that the values of tensile strength for the PS and its nanocomposites are too low compared with those reported in literature such as what has been reported in the co-work of (Qiu *et al*. 2015). The incorporation of nanofillers that have large surface area in polymer matrix would alter the local stress state of the surrounding matrix. That means that the stress might be nonhomogeneous (i.e. varies from region to region) in the specimen as in necking and crazing. Moreover, other factors can come into play such as amorphous chain segment reorientation. For all of the aforementioned, tensile strength values might be negatively affected as reported in the current study (Tjong, 2006 ; Nielsen & Landel, 1994).

The increase in elongation at break for the nanocomposites refers to the strong interfacial interaction between the wrinkled GO and the PS chains, whilst the low values of energy at break for the PS and the nanocomposites refers to the brittleness of the material. (Wan & Chen, 2012) confirmed this interpretation for PS that was reinforced with different low weight fractions of GO. The effect of time dispersion can be seen. As the time of mixing went higher, the elongation at break was increased for the nanocomposites which confirmed better interfacial interaction between the polymer and the nanosheets. On the other hand, the increased values of toughness confirmed the nanocomposites brittleness compared to the neat polymer. The reasons of nanocomposites' brittleness were discussed somewhere previously in this section.

Table 3.4 shows the obtained values of Young's modulus, tensile strength, elongation at break and toughness through extensometer. Figure 3.16(a) and (b) shows the improvement in mechanical properties (Young's modulus and tensile strength) for nanocomposites prepared in different time of mixing compared to the neat polymer.

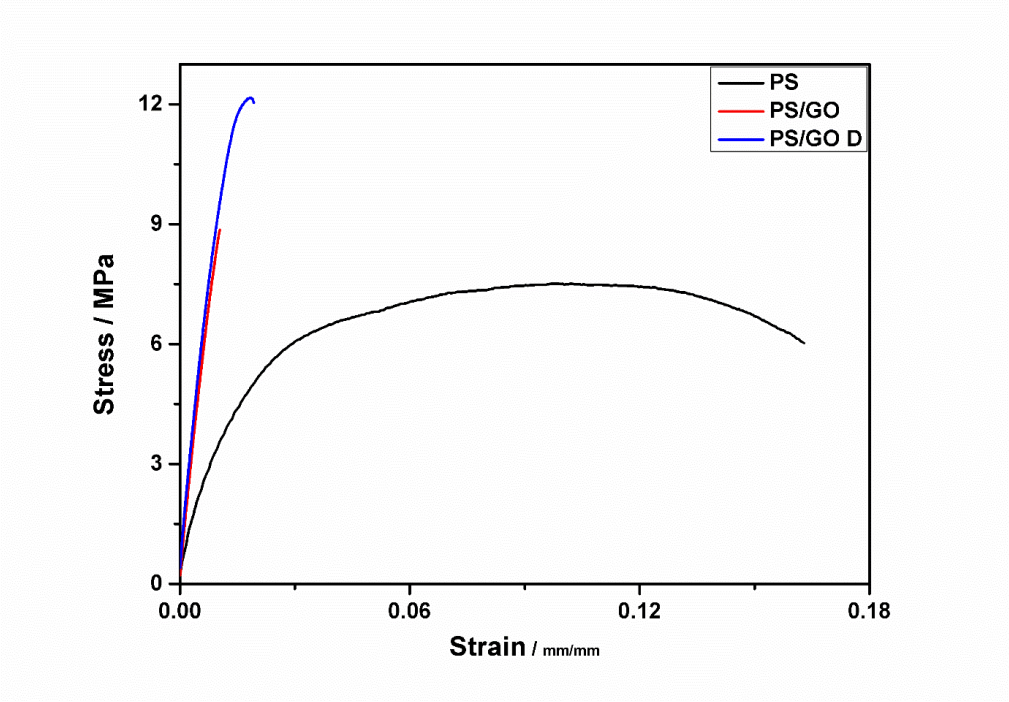

Figure 3.15. : Stress-strain curve for the PS and the nanocomposites.

Table 3.4. : Mechanical propertied for the PS and the nanocomposites.

Sample	**Young's modulus / GPa**	**Tensile strength / MPa**	**Elongation at break / mm**	**Toughness / M J.m^{-3}**
PS	0.49 ± 0.1	7.5 ± 3	0.12 ± 0.06	0.79 ± 0.57
PS/GO	1.09 ± 0.06	8.6 ± 1.6	0.013 ± 0.002	0.076 ± 0.025
PS/GO D	1.19 ± 0.12	11.7 ± 2.06	0.014 ± 0.004	0.098 ± 0.052

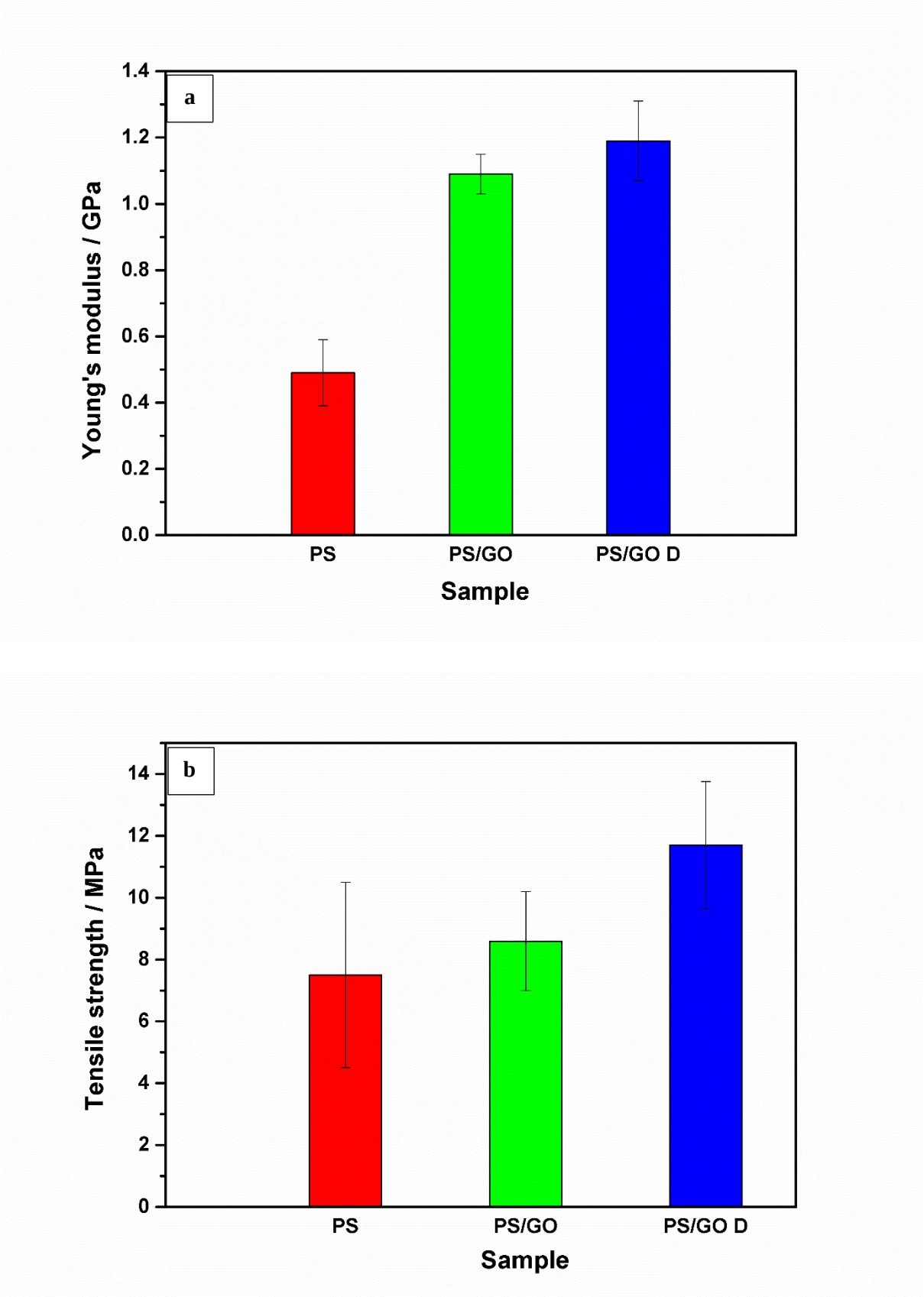

Figure 3.16. (a) and (b). : The improvement in mechanical properties (a) Young's modulus and (b) Tensile strength for nanocomposites prepared in different time of mixing compared to the neat polymer. Error bars based on ± standard deviation.

3.4. Conclusion

The effect of processing conditions has been investigated in the preparation, structure and properties of PS/GO nanocomposites. The processing conditions relate to identifying the co-solvent that suits both the polymer matrix and the nanofillers and to finding a suitable dispersion technique to ensure the best distribution of the nanofillers in the polymer matrix.

The first trial to prepare the nanocomposites by utilising DMF as a co-solvent for PS and GO and employing only one dispersive technique that was bath sonication resulted in poor samples which cannot be studied and cannot give a clear indication about their performance.

Hot pressing was the second trial to deal with these poor samples. There was a hope to obtain good samples from the resulting poor samples by hot press them but the problem was exacerbated and very corrupted samples with poor dispersion of nanosheets was obtained. The results of AFM for these hot-pressed samples confirmed that.

The successful recipe that was adopted in this chapter and other chapters afterwards was to find another organic solvent and efficient dispersion technique(s) to obtain good samples. The employment of THF as a co-solvent for PS and GO with a combination of bath sonication and shear mixing for different periods of time resulted in relatively good samples as different measurements showed. The role of direct mixing (magnetic stirring) cannot be denied as a complementary technique with the main ones.

It was found with measurements in the peaks of PS and its nanocomposites that an interaction between PS and GO occurred for both PS/GO and PS/GOD. Optical microscopy images confirmed the good distribution for the GO in the polymer matrix using bath sonication and shear mixing in combination with magnetic stirring for both a long and neutral mixing time.

Although an improvement in the mechanical properties (Young's modulus and tensile strength) was achieved, and T_g values obtained by DSC and DMA were observed slightly higher for nanocomposites prepared by long-time of mixing, the results of storage modulus and SEM confirmed that the neutral time of mixing is the efficient way to disperse the GO nanosheets homogenously without damaging them.

The peaks of the FTIR measurements showed that the interaction between GO and PS occurred for both a long and neutral time of mixing and this makes the PS/GO the more superior sample compared with PS/GO D.

The use of THF and bath sonication, shear mixing, beside the direct mixing (magnetic stirring) for dispersing nanosheets in the matrix resulted in the preparation of good samples compared with those prepared by DMF and by the use of bath sonication and direct mixing only. These techniques have been well established for thermoset polymers, not thermoplastics, in order to distribute the nano-particles homogenously in the matrix. These techniques played the major role in this work with a suitable organic solution (THF) to distribute GO nanosheets homogenously in a thermoplastic polymer (PS). Mostly, only one dispersion technique is enough to disperse the nanofillers in the matrix of thermoplastic polymers homogenously. One of the most important key findings of this work is that more than one dispersion technique was needed to ensure such random distribution for the nanofillers in the matrix.

Chapter 4

Studying the properties and the nanomechanical behaviour of PS/GO nanocomposites using very low loadings of GO

4.1. Introduction

A substantial improvement in polymer nanocomposites' performance can be achieved at very low loadings of nanofillers. The GO derived graphene materials are showing a remarkable improvement in different properties at very low loadings as these nanofillers possess high aspect ratio and large interfacial area that makes the low loadings of these nanofillers is sufficient to achieve the required improvement (Zhu *et al*. 2010). This will be important for manufacturing materials that have lighter weight but that are also stronger (Dhand *et al*. 2013).

For example, (Wan & Chen, 2012) reinforced many kinds of polymers with low loadings of GO nanoplatelets. Among the reinforced polymers was PS. It was reinforced with (0.3, 0.5, 1.0, and 2.0) wt. % of GO. The results showed a consistent improvement in mechanical and thermal performance for the PS/GO nanocomposites compared with the neat polymer. As described earlier the potential applications for GO in polymer matrices are in construction engineering, health products and biomedical applications. (Maheshkumar *et al*. 2014)

Since its invention in 1980, AFM has become an indispensable tool for investigating the nanomechanical behaviour of polymer matrices and nano-particles through its capability for imaging surfaces at very high resolution and measuring different short-range forces near the surface of a material. With regard to the force measurements, depending on the situation different forces including Van Der Waals, capillary forces, chemical bonding, electrostatic forces and magnetic forces can be characterized of distance to the AFM tip (Cappella & Dietler, 1999).

In operation a position on the surface is pre-selected and the probe is move towards the selected position and then retracted.

The cantilever deflection upon its movement to the surface is expressed by a signal which is provides the data for the generation of the force –distance F-D curve (See section 2.5.1. about the F-D curves).

Once the deflection of the cantilever (X) is known as distance, and given data on the spring constant (K) the force can be found using Hook's law:

$F = K X$ ……. (1)

One mode of operation of the AFM is called 'contact mode' and this is a very powerful technique for obtaining very high resolution images (Eaton & West, 2010).

There are four prominent models that deal with surfaces forces (See section 2.5.2. and table 2.10.). The Derjaguin- Muller- Toporov DMT model is useful for analysis using low loads in which the surface forces become important. There are limitations for this theory however and the most important is the assumption of Hertzian deformation only.

This assumption can lead to an underestimation of the contact area, but it is still within reasonable limits to justify its use. The theory of DMT is more applicable to systems that have low work of adhesion and high elastic moduli (Bonnell, 2001). Given the aforementioned assumption the DMT modulus can be calculated from the following equation:

$F_{tip} = 4/3\ E^* (Rd^3)^{1/2} + F_{adh}$ …….. (2)

Where F_{tip} is the applied force on the tip, R is the radius of the tip, d is the deformation of the sample, F_{adh} is the force of adhesion and E* is the reduced modulus (Smolyakov *et al*. 2016). It is important for compliant polymers that have high adhesive forces, large elastic deformation and viscoelastic behaviour, that the appropriate mathematical model is selected for determining the mechanical properties at the nano-scale(Chizhik *et al*. 1998). In recent years, a new version of AFM using the pulsed- force mode has been developed and this is known as QNM™.

Scientists and manufacturers in Bruker, USA have made an extension for pulse-force mode AFM for obtaining higher resolution, quicker data acquisition and better noise reduction.

F-D curves can be obtained by AFM but it is a time consuming approach for finding Young's modulus in nano-scale as compared with QNM ™ (Young *et al*. 2011).

(Panaitescu *et al*. 2012) investigated the Young's modulus at the nano-scale for PP nano-silica nanocomposites that contain SEBS using QNM. The authors used the DMT model with a silicon tip that has a nominal radius of 8 nm and the modulus for the PP nano-silica nanocomposites had the highest value compared with PP nanocomposites that contain SEBS.

(Young *et al*. 2011) used the same technique of peak force QNM and the DMT model, for measuring the Young's moduli for a number of polymers using a range of probes. They used three kinds of probes manufactured from different materials with different spring constants, and compared them with the results obtained by nano-indentation. Poly (methyl methacrylate) PMMA was found to have the highest value of Young's modulus.

The work described in this thesis investigated the effect of GO with different and very low weight fractions, on the structural, mechanical and thermal properties of PS/GO nanocomposites. It also investigated the nanomechanical behaviour of the PS and nanosheets via the cryogenically fractured surface. This task was accomplished by the employment of many techniques (different versions and models of AFM) with a comparison between the outcomes obtained through each technique. The preparation of graphite oxide, GO, PS and nanocomposites are studied in the last chapter and the optimum conditions of preparation have been confirmed. The appropriate procedure used to prepare the samples in the last chapter is followed here to prepare the samples as the dispersion techniques, time required to disperse the nanosheets in the matrix, and the processing conditions are known and followed to make further investigation for different properties.

4.2. Experimental section

4.2.1. Materials

Explained in details in section 3.2.1. DMF is the only solvent that was not used in this chapter.

4.2.2. Preparation of graphite oxide, GO and nanocomposites of PS/GO

The diagram 3.1. was showing the procedure of preparation of graphite oxide, GO and the nanocomposites. The same procedure showed in diagram 3.1. was followed in this chapter.

4.2.2.1. Preparation of graphite oxide

Graphite oxide was prepared according to (Marcano *et al*. 2010). It was explained in details in section 3.2.2.1. and Figure 3.2 showed the stages of graphite oxide preparation.

4.2.2.2. Preparation of GO

GO was prepared according to (Ming *et al*. 2013). It was explained in section 3.2.2.2. and Figure 3.3. showed the GO powder.

4.2.2.3. Preparation of PS/GO nanocomposites

The nanocomposites samples were prepared using THF. 20 g of PS pellets were dissolved in 200 ml of THF using magnetic stirring for 2 h at 600 rpm. Different weight fractions (concentrations) of GO were suspended in specific volumes of THF for each concentration. The weight fractions for GO in PS/GO nanocomposites were (0.01, 0.05, 0.1, 0.25 and 1.0) wt. % beside the neat polymer. The suspensions of GO/THF were stirred for 2 h at 600 rpm and pre-sonicated for 30 min. Each concentration of GO/THF suspension was mixed with 200 ml of PS/THF solution. The mixed solutions were stirred for 1.5 h.

Then, to ensure a good dispersion of GO nanosheets in PS matrix, a bath sonication (Fisherbrand, Germany) was used for 0.5 h and shear mixing (Silverson, UK) was used for 1 h at mixing speed of 1600 rpm /Amp 0.3. This is the neutral time of mixing using different dispersion techniques for nanocomposites' preparation that was selected in the previous chapter in section 3.2.2.3.3. as a successful method compared with many others.

The obtained suspension of PS/GO was poured in a glass covered Petri-dishes of radius 135 mm to ensure a slower evaporation for the solvent. All samples were left in a fume cupboard for 1 week and then in a vacuum oven for 3 h at 40 °C to be fully dried. Table 4.1 shows the chemical compositions of the suspensions used to prepare the neat polymer and its nanocomposites.

Table 4.1. : The prepared PS and PS/GO nanocomposites of different GO weight fractions.

Sample No.	GO Conc. / wt.%	PS / g	THF/ ml to dissolve PS	GO/ mg	THF/ ml to obtain GO suspension
1	0	20	200	0	0
2	0.01	20	200	2	2
3	0.05	20	200	10	10
4	0.1	20	200	20	20
5	0.25	20	200	50	50
6	1	20	200	200	200

4.2.3. Characterization

The characterization techniques are described separately below.

1. **Microscopy**

    a. **AFM**

2 ml of graphite oxide was mixed and stirred with 200 ml of distilled water. This mixture is sonicated and centrifuged for 30 min. each. An aqueous suspension of GO was formed via sonication in bath sonicator which led to direct exfoliation. This approach was adopted by (Potts *et al*. 2011). Small drops were taken from the solution and precipitated over small black sheet that had been taped over a slide of glass and this was followed by mechanical exfoliation using scotch tape. The slide was left overnight to be dried ready for AFM imaging.

The AFM measurements were carried out by (3100 dimension, CLI digital instrument, USA) for finding the lateral size and thickness of graphene sheet.

Real time scanning was carried out at ambient temperature and the image was recorded using Nanoscope software. Non-contact-tapping mode was used to characterize the graphene. The tip used for imaging was made from silicon by (Nanosensors ^{TM,} Switzerland) and it had a 'diving board' shape with resonant frequency of (210-490) KHz.

b. OM

An optical microscope (Swift, New York Microscope Co. USA) was used for imaging the nanocomposite samples to determine the distribution of GO in the PS matrix. The microscope had a resolution of 10X with a magnification scale of 0.5 mm.

c. TEM

For investigation the quality of dispersion of the nanosheets in the matrix, and to obtain an idea about the morphology of the pristine polymer, transmission electron microscopy TEM was used. Samples of PS and PS/GO 1.0 wt. % were snapped frozen in Liquid Nitrogen and placed in the FC6 cryo chamber to equilibrate for around 30 min. Other details regarding this test mentioned in section 3.2.3. subsection 1, item c.

d. SEM

. Cryogenic fracture surfaces were obtained via snapping samples in liquid nitrogen. The neat polymer and the PS/GO 1.0 wt. % were immersed in a container of liquid nitrogen for 5 min. and snapped inside the container to obtain clean fracture surfaces to be tested by SEM. Other details regarding this test mentioned in item d, subsection 1, of section 3.2.3.

2. Spectroscopic measurements

a. FTIR

FTIR Spectrum 100 Perkin Elmer, USA which had a wavenumber coverage of range of 400-4000 cm^{-1} was used for characterizing graphite, graphite oxide, GO, PS and PS/GO nanocomposites. The setting of the machine was similar to the setting adopted in the last chapter which was mentioned in section 3.2.3. subsection 2.

b. Raman Spectroscopy

Raman spectra were recorded with equipping a CCD detector for graphite, GO, PS and the nanocomposites using the Reinshaw inVia Raman microscope, England. The wavelength of the source was 514.5 nm argon-ion laser at a power of 20 mW and resolution of 1 cm^{-1}.

3. X-Ray diffraction XRD

To investigate the crystal structure of graphite, GO, PS and its nanocomposites D2 Phaser, X-ray diffraction analyser Bruker, USA was employed with Ni filter and Cu target. The size of the slot was 1 mm, operating current 10 mA, operating voltage 30 KV and scanning range (2 theta) was from 5° to 50 °. The time was 0.3 and the steps was 3700. The detector was Lynxeye (1D mode) and the wavelength was 0.154051 nm. The total scan time for each sample was 20 min.

4. Thermal and thermomechanical properties

a. TGA

Thermal Gravimetric Analysis (TGA Pyris 1, Perkin Elmer, USA) was used to measure thermal degradation temperature. The atmosphere used in the test was N_2 and the heating rate was 10 $°C.min^{-1}$. The range of temperature used with graphite, GO, PS and PS/GO nanocomposites was from 28 to 700 °C. The weight of each sample inside the ceramic pan was 5 mg except the weight of graphite and GO powder that was few milligrams. Several samples were tested and representative samples were shown.

b. DSC

Differential Scanning Calorimetry (DSC 6 Perkin Elmer, USA) was used to determine the value of the Tg which is the temperature at which the polymer transforming from glassy state to rubbery state. 10 mg of each sample was placed in a sealed pan of aluminium with an empty sealed aluminium pan used as a reference. Aluminium was selected as a sample holder and as a reference as it has a high heat capacity over a range of temperatures.

T_g was measured from the 2nd run heating to remove any thermal history and any possible remaining traces of solvent from the sample.

Both of the sample and the reference were placed inside the machine and subjected to a nitrogen gas purge at a rate of 50 ml.min^{-1}. The range of temperature was ramped from 25 °C to 240 °C at a rate of 10 °C. min^{-1}. The cooling rate was also 10 ^{o}C. min^{-1}. Several samples were tested and only representative samples were shown.

c. DMA

Dynamic Mechanical Analysis (DMA Perkin Elmer, DMA 8000, USA) was used to find the storage modulus for the neat polymer and nanocomposites where strain was 0.5% (0.05 mm), the range of temperature was 40 – 130 °C, the heating rate was 3 °C. min^{-1}. and the oscillatory frequency was 1 Hz. The deformation mode utilized in this test was single cantilever bending and the samples had rectangular cross section (length was twice as its width). The values of the aforementioned parameters are the most suitable ones to characterize the polymers and their nanocomposites thermo-mechanically and they have been widely adopted by authors in a growing body of the literature. Tg was found by extrapolating the onset temperature of storage modulus curves. Tangents were drawn from the initial and final stages of the curves (see appendix 6) and their intersection point represented Tg. This approach was clarified by (Turi,1997). Several samples were tested and only representative samples were shown.

5. Nanomechanics

a. AFM

Young's modulus in nanoscale for the cryogenic fracture surface of PS/GO 1.0 wt. % for the polymer and the incorporated graphene was obtained by applying the DMT approach. The sample was immersed in a container of liquid nitrogen for 5 min. and snapped inside the container to ensure a clean fracture surface. Then, it was fitted over a sample holder.

The thickness of the measured cryogenic fracture surface was ~ 1 mm. The instrument (3100 dimension, CLI digital instrument, USA) was used for finding force measurement curve by adopting DMT approach.

The used cantilever for this purpose was manufactured from silicon nitride (PNP-TR20 by Nano World, UK). The length of the cantilever was 200 μm, the spring constant was 0.08 Nm^{-1}, the resonance frequency was 17 KHz and the tip radius was 5 nm.

b. QNM

Local mechanical properties at the nano-scale for the same cryogenically fractured surface were obtained via peak force QNM mode of multimode 8 AFM by Bruker, USA.

Deflection sensitivity was found for the cantilever (TESPA-V2) after making 10 indentations over a surface of Sapphire and the average for them was considered as the average deflection sensitivity which was 69.8744 $nm.V^{-1}$. Thermal noise method (an analysis of the power spectral density of displacement fluctuations of the cantilever in contact with a thermal bath) was performed for finding the stiffness of the cantilever which was 45.6023 Nm^{-1}.

The tip radius was found to be 17 nm after performing indentations over a binary alloy made from PS/LDPE and measuring the dimension of the print. The maximum applied force on the tip was 10 nN which mostly led to deformation of 1-3 nm as shown in Figure 4.1. The other specifications for this tip which was used for finding the modulus are the following: The length of the cantilever was 127 μm, the resonance frequency was 320 KHz, single crystal silicon is the material of the cantilever which had the back side coated in reflective aluminium. Measurements were carried out at ambient temperature.

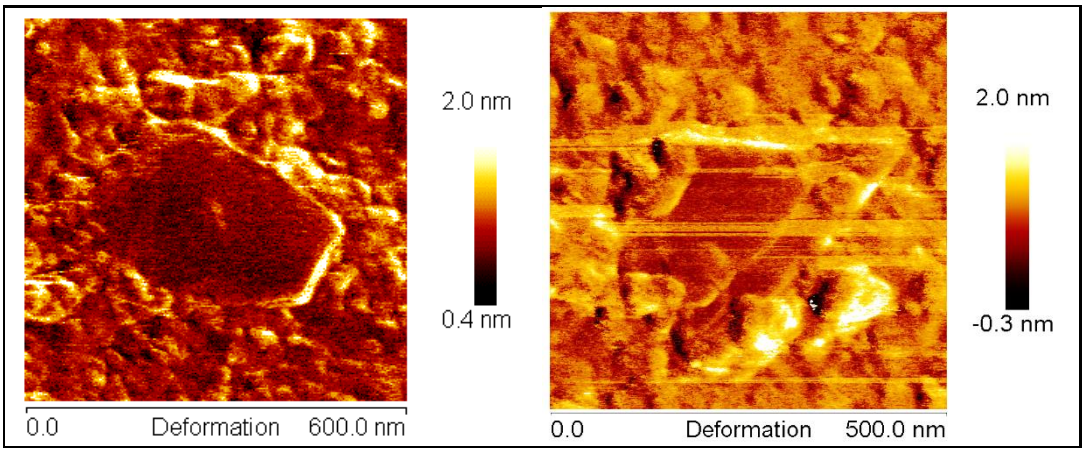

Figure 4.1. : The deformation of upper left and lower right GO flake.

A cantilever of tapping, non- contact mode, was used prior to the aforementioned one for imaging the surface before making contact and finding the modulus.

The cantilever (TESP-V2) was made from silicon with a lever length of 125 μm and resonance frequency of 320 KHz. Gwyddion software was used for drawing a mask over flakes in the DMT modulus channels. Nanoscope software was used for calculating the DMT modulus of GO flakes and PS matrix around them. The obtained images have a resolution of (256x256) pixels and scanning rate of 0.528 HZ for the upper left GO flake and (512x512) pixels with a scanning rate of 0.476 HZ for the lower right GO flake. Scanning size started from (30*30) μm^2 and it went significantly down up to (1.5*1.5) μm^2 with the detection of GO flakes. Indentations were made for every single pixel in the two flakes. Force curves generated with every single indentation and the machine gave the average value of reduced Young's modulus for PS and the GO flakes with the standard deviation. Figure 4.2. shows the cryogenically fractured surface studied by AFM and QNM for investigating the mechanical properties in nanoscale.

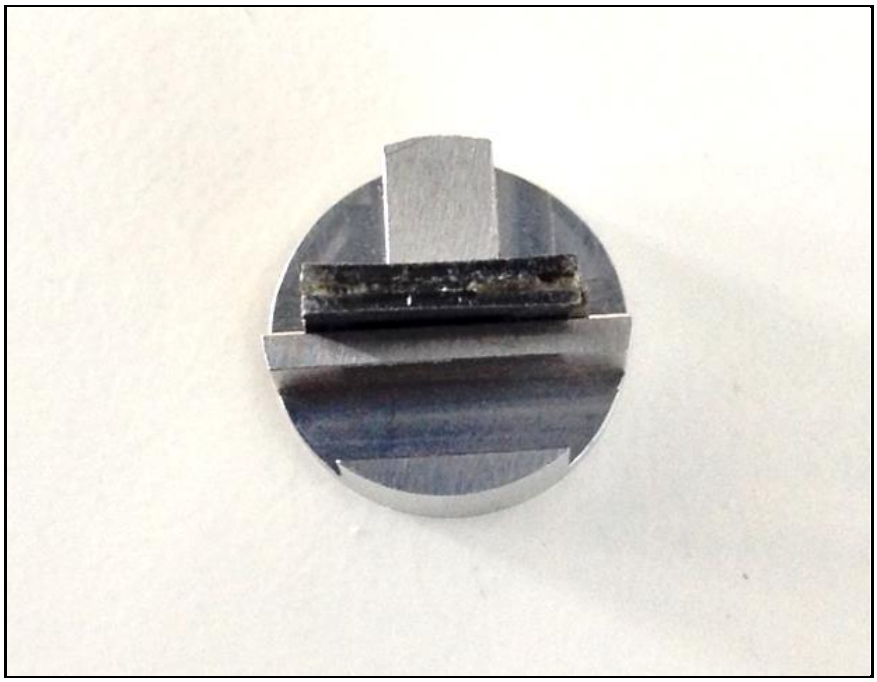

Figure 4.2. : The cryogenically fractured surface employed for investigating the nano-mechanical properties.

4.3. Results and discussion

4.3.1. AFM

A dilute and clear colloidal suspension of GO was obtained in distilled water as illustrated in experimental section. In order to overcome the attractive Vander Waal forces between the graphitic layers, liquid phase exfoliation was applied and assisted by mechanical exfoliation to obtain small graphene nanoparticles that have lateral sizes up to 1 μm.

The use of liquid phase exfoliation generally, and sonication specifically leads to detrimental effects on the nano sheets in terms of defect formation in the periphery of the sheets. However, the approach is still desirable and extensively applied because single layer GO sheets can be obtained and it is an environmentally friendly approach (Economopoulos & Tagmatarchis, 2013; Mkhoyan *et al*. 2009; Potts *et al*. 2011).

Figure 4.3. shows the dimensions of GO flakes with the section analysis. It confirms the thickness of the GO sheets varies between 0.7- 1.1 nm and the lateral size varies between 863 nm to 1.2 μm for the different sheets.

(Eda & Chhowalla, 2010) have shown that the thickness of a monolayer GO nanosheet is 1-1.4 nm, whilst the thickness of a single layer of graphene is about 0.34 nm. The reason behind this variation can be attributed to the presence of adsorbed molecules and functional groups. The same authors elucidated the reasons behind the wide range of lateral sizes for the GO nano sheets as follows: The multistep oxidation process for the large crystals of graphite increase the possibility of obtaining large GO sheets with lateral size up to 3 mm. (Singh *et al*. 2012) identified another reason why GO sheet is thicker than graphene sheet. They suggested that it is due to the presence of covalently bound oxygen atoms. Furthermore, the slight displacement of SP^3 hybridized carbon atoms above and below the original graphene plane also led to thickness differences.

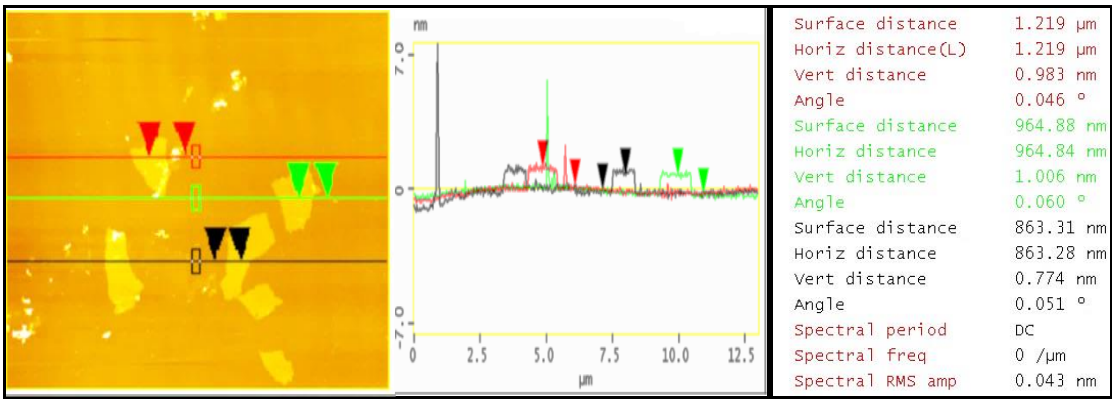

Figure 4.3. : AFM image and the section analysis for the GO nanosheets.

4.3.2. OM

Figure 4.4. refers to the relative even distribution of GO in the polymer matrix. The images that were taken by optical microscopy for the neat polymer film, and different concentrations of GO in the matrix, clarify the nature of distribution of the nanofillers in the polymer. The optimum properties of the nanocomposites are only achievable with a homogeneous distribution for the nanofillers in the polymer matrix.

The performance of the nanocomposites is severely affected as the nano-scale reinforcements tend to coalesce into macro size agglomerates (Paul & Robeson, 2008). (Prolongo *et al*. 2008) used OM to study the dispersion of carbon nanofibers in an epoxy matrix.

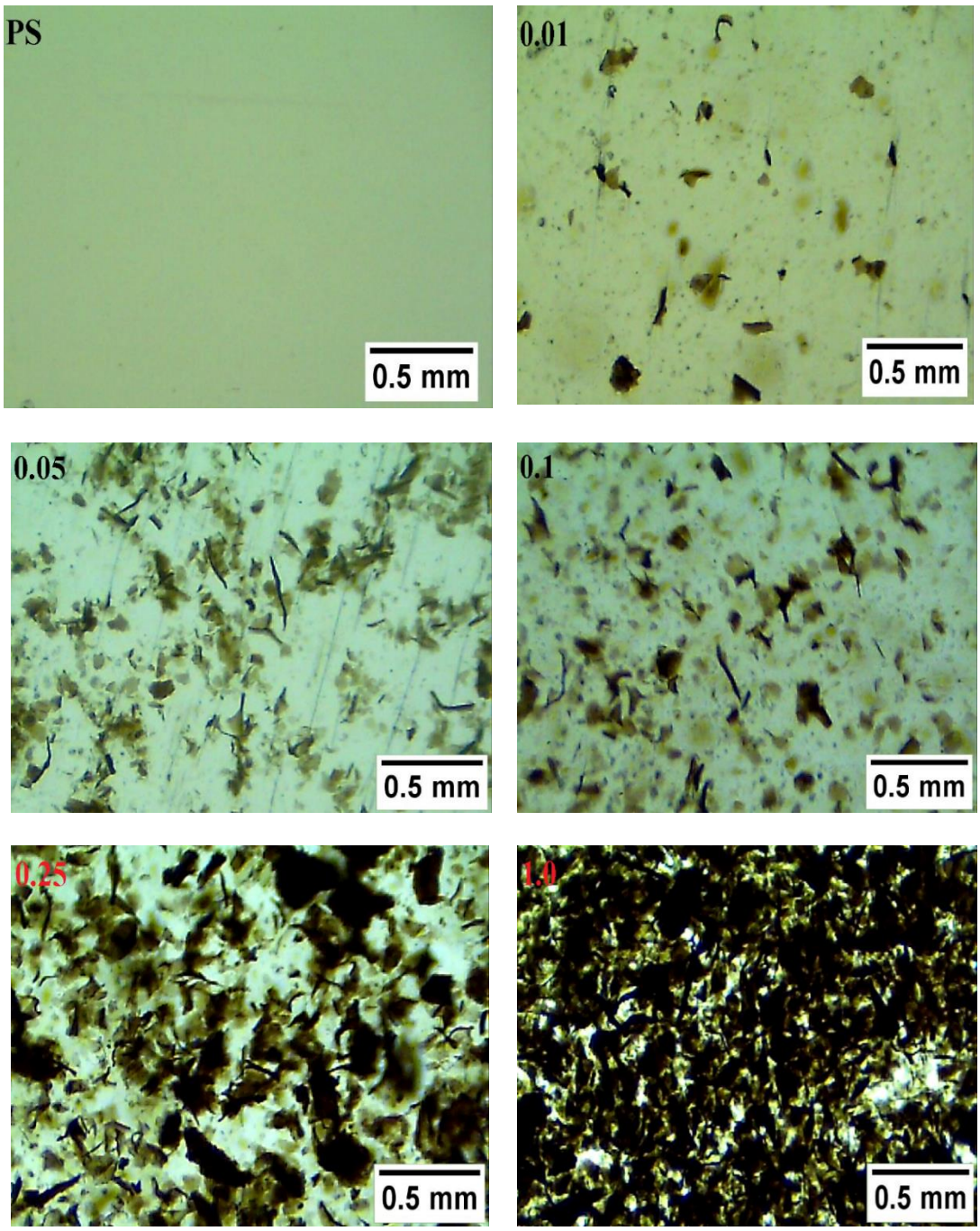

Figure 4.4. : The OM images for the PS and the nanocomposites with different weight fractions.

4.3.3. Spectral properties, FTIR and Raman spectroscopy

4.3.3.1. FTIR

Figure 4.5. (a) shows the IR of graphite, graphite oxide and GO. The IR instruments are recording the data within the range of 400-4000 cm^{-1} considering the optics of the instrument is based on potassium bromide KBr. For this reason, the spectral region should be recorded as high to low cm^{-1} (Coates, 2000).

The spectrum of graphite does not display any peaks that appear in its oxidized forms. This result reflects the fact of the absence of any functional group from the structure of graphite (Kattimuttathu *et al*. 2015). This result is confirmed by (Hontoria-Lucas *et al*. 1995).

For the graphite oxide and GO spectra, the effect of oxidation process is clearly recognized as the peaks are attributed to the presence of oxygen functional groups.

For the graphite oxide spectra, two main peaks can be found, the first one is the most prominent one that has a peak in 3286 cm^{-1} which is formed according to the C-OH stretching vibrations of the hydroxyl group. The other peak that can be seen for the graphite oxide is nearly at 1620 cm^{-1} which is formed due to C=C skeletal vibration for the graphite which is not oxidized (Drewniak *et al*. 2016). (Hontoria-Lucas *et al*. 1995) were confirmed similar results for graphite oxide as they were reported a presence of broad peak located between 3000 - 3700 cm^{-1}due to free and adsorbed hydroxyl functional groups. They also reported the presence of peak that was located at 1620 cm^{-1}, and this peak was ascribed to the deformation vibration of adsorbed water molecules.

The peaks of GO can be explained as: hydroxyl, epoxide and carboxylic acid groups and can be shown as a rich collection of absorption bands. The abundance of oxygenated functionalities can be seen from the obtained curve. The O-H stretching vibration can be seen in 3500 cm^{-1}. The other absorption peaks of C = O from the absorption of carbonyl and carboxylic acid groups, C = C from the unoxidized graphitic domain, C – H and C – O from the absorption of epoxy groups can be seen at the wavenumbers (1720, 1450, 1340 and 1100) cm^{-1} respectively. All of the vibrations are stretching vibrations apart from the C – H group which has a bending vibration (Ming *et al*. 2013; Yin *et al*. 2013). (Xu *et al*. 2015) were confirmed the presence of O-H, C=O, C=C, and epoxy C-O in their sample of GO.

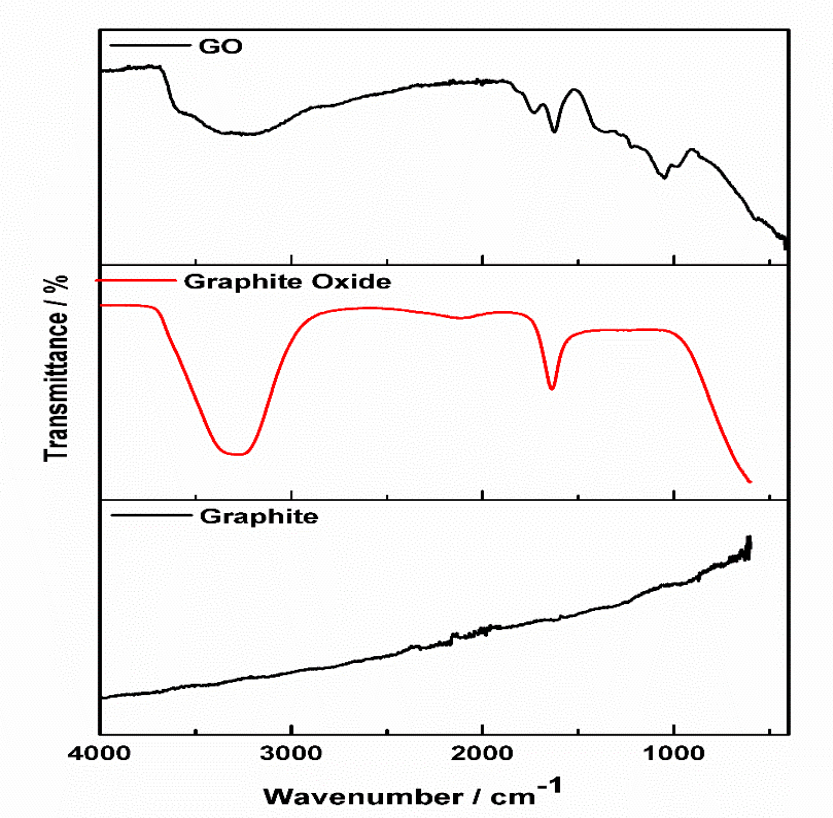

Figure 4.5(a). : IR spectra for graphite, graphite oxide, GO, PS and its nanocomposites.

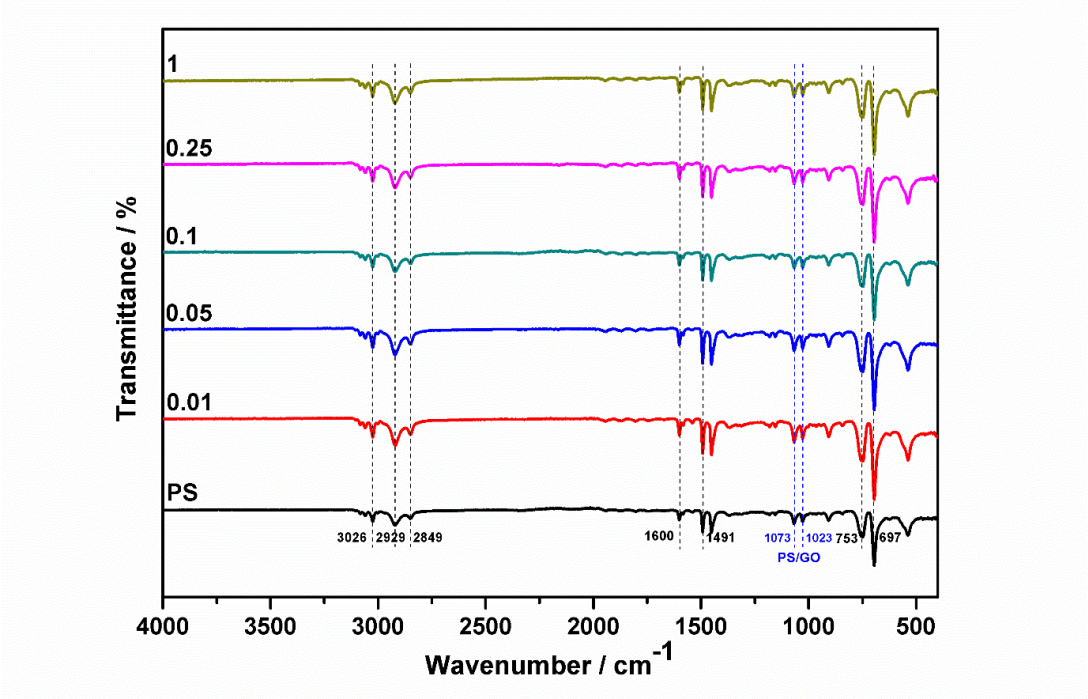

Figure 4.5(b). : IR spectra for PS and its nanocomposites. The black dash lines are refer to PS, whereas the blue dash lines are refer to interaction between PS and GO.

Figure 4.5 (b) shows the peaks related to PS which refer to =C-H aromatic stretching vibration in the range of 3100-3000 cm^{-1}. A symmetric and symmetric stretching associated with vibration stretching of CH2 can be noticed at peaks of 2929 cm^{-1} and 2849 cm^{-1} respectively. Peaks at (1600, 1580, 1491) cm^{-1} are attributed to the stretching vibration of benzene ring. The C-H out of plane bending vibration of the benzene ring can be seen at 753 and 697 cm^{-1}. The weak shoulder at 1073 cm^{-1} confirms the interaction between PS and GO but a typical peak for GO cannot be found due to an overlap with PS peaks, or it is a weak peak (Han *et al*. 2013). (Yin *et al*. 2013) confirmed that the peak of 1023 cm^{-1} is another peak of interaction between PS and GO and the type of interaction is most likely to be Π-Π stacking. See appendix 4.

4.3.3.2. Raman Spectroscopy

Raman spectroscopy is a non-destructive technique for investigating the structure, electronic properties, doping level, defect structures and defect density of graphitic materials. It is also an efficient tool for characterizing and analysing the order crystal structure of graphite's derivatives. The crystal structure for graphite and GO using Raman spectroscopy is shown in figure 4.6. A, and figure 4.6. B shows the crystal structure of PS and the nanocomposites. The G band is usually related to E_2g phonons by SP^2 carbon atoms at 1575 cm^{-1}. The D band is associated with the breathing mode of k point photons of A_{1g} symmetry and this band is at 1350 cm^{-1}. These peaks referred to by (Ma *et al*. 2013; Liu *et al*. 2016) of the G and D band were found in the current sample of graphite used in this research. The spectrum of graphite includes few Raman invisible active bands as it is a highly ordered material.

The weaker band (D band) in Figure 4.6. (a) is caused by graphite edge defects, bond length disorder, bond angle disorder and vacancies. On the other hand, the sharp band (G band) appears due to in-phase vibrations of the graphitic lattice (Mohan *et al*. 2015; Krishnamoorthy *et al*. 2013). At around 2680 cm^{-1}, the D band has an overtone peak which is called the 2D peak.

The shape and shift of this peak is intimately associated with the number of graphene layers and its position in the current graphite sample is appearing at around 2700 cm^{-1}.

The reason for the appearance of this peak is due to the double resonance transitions resulting in the production of two photons with opposite momentum. Another important feature of this peak is that it is a clear and prominent peak even with the absence of defects in graphene sheet which is unlike the D band peak that is only active when defects are present (Eda & Chhowalla, 2010).

(Liu *et al*. 2016) confirmed the D and G band for graphite at 1594 cm^{-1} and 1358 cm^{-1} respectively with a clear 2D peak at around 2700 cm^{-1}.

The oxidation process for the graphite caused a considerable change in the lattice structure of graphite due to the formation of oxygen functional groups at the edges and at the basal plane. It can be seen that the peak of the G band is shifted higher to 1589 cm^{-1} in accordance to the oxidation of graphite as a new SP^3 carbon atom is formed in the graphitic lattice. In addition, the D band is shifted slightly higher (1357 cm^{-1}) and the intensity of the D band is also higher compared with its intensity in the graphite spectrum. These outcomes observed in GO can be attributed to the formation of disorder and defects such as aliphatic chain, grain boundaries and the presence of in-plane hetero-atoms. The oxidation reaction is behind the weakening or disappearance of the 2D peak as the stacking order is broken (Krishnamoorthy *et al*. 2013).

The intensity ratio between the D band and G band (I_D/I_G) is used to evaluate the defective disorders or the graphitization quality for the crystalline graphite. The significant increase for this ratio as compared with graphite from 0.092 to about 0.97 refers to the increase of disorder structure in the graphene sheet as a result of the oxidation process (Tang *et al*. 2012). The literature of (Tripathi *et al*. 2013) confirmed the peaks of GO with a slight variation in the values of Raman shift and there was an increase in the ratio of (I_D/I_G) for GO as compared with pristine graphite.

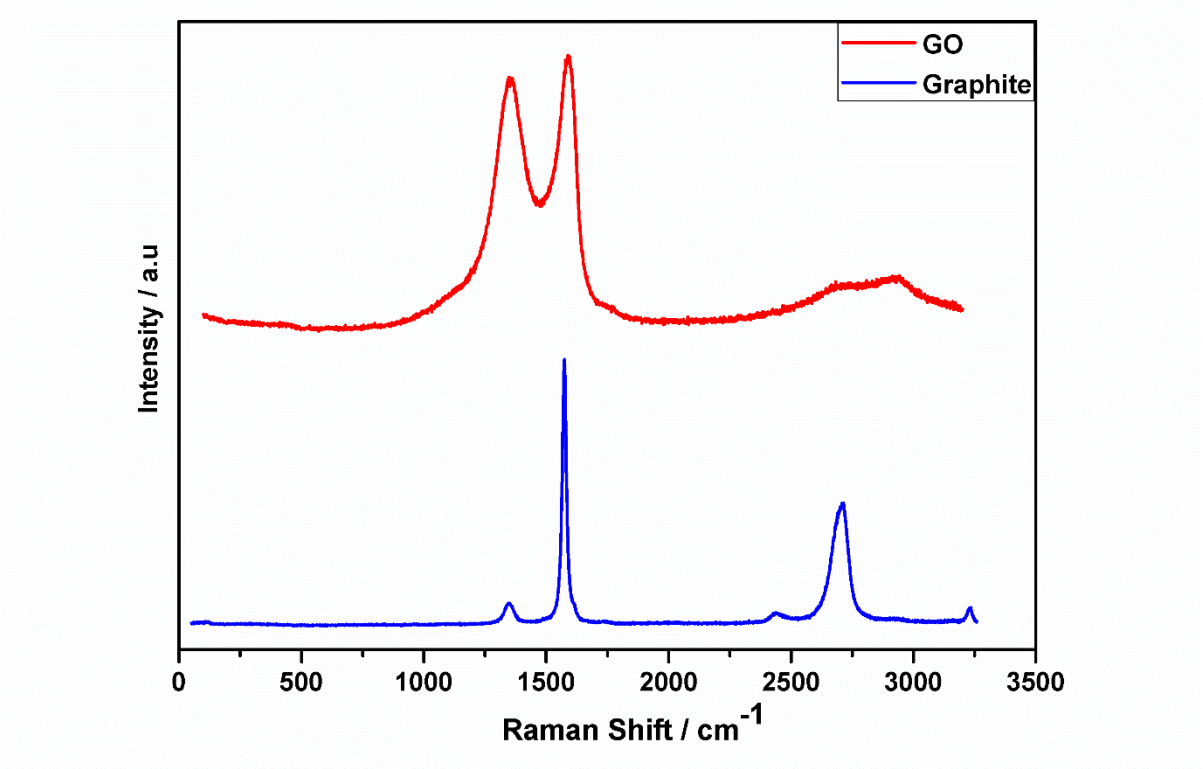

Figure 4.6(a). : The crystal structure for graphite and GO by Raman spectroscopy.

The Raman peaks of PS obtained by (Yan *et al*. 2012) are similar to what has been achieved for PS used in the current study. The C-H vibration is about 3000 cm^{-1}(2900 and 3052) cm^{-1}. Figure 4.6. (b) shows Raman peaks for PS and nanocomposites. The carbon in the former is related to the aliphatic chain, but in the latter to the aromatic chain. At about 800 cm^{-1} the low frequency C-C can be seen. At around 1600 cm^{-1} a strong C=C is noticed.

The sharp peak at 1000 cm^{-1} is due to the aromatic carbon ring. As the loading fractions are very low, no shift can be seen for the Raman peaks of nanocomposites. The peaks of PS are still the prevailing peaks. (Srivastava *et al*. 2011) confirmed that the G band peaks of PS reinforced with MWCNT are shifted to lower wavenumbers in (8.0 and 10.0) wt.% in spite of the identical shape of the peaks as compared with the sample that was reinforced with 6.0 wt.% and neat PS. The PS/MWCNT of 1.0 wt. % did not show any shift for any band. Appendix 5 shows the aforementioned Raman bands with their references.

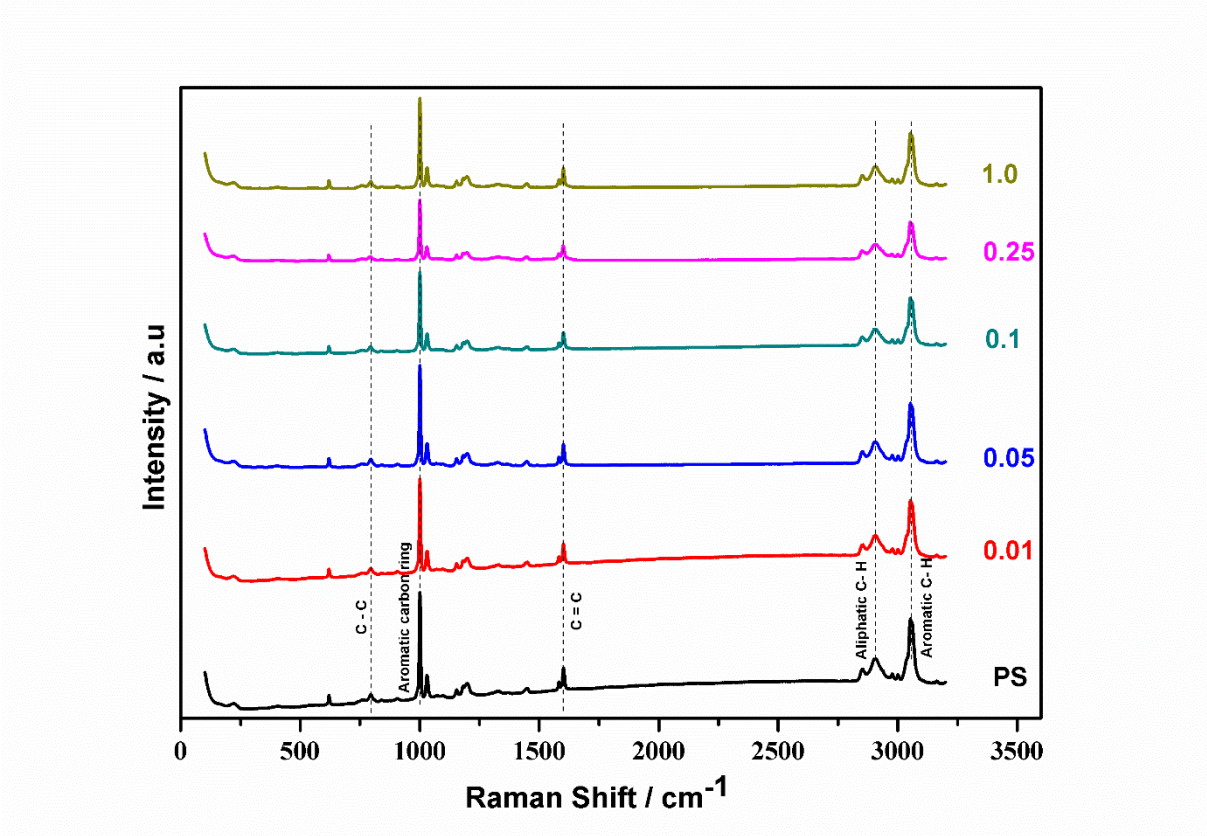

Figure 4.6(b). : Raman spectra for PS and its nanocomposites.

4.3.4. XRD

Figure 4.7. shows the XRD patterns of graphite, GO, PS and the nanocomposites. It is worth mentioning here that some researchers are using XRD which is a powerful and efficient tool in characterizing layered materials such as GO, and as a reliable provider for the completion of oxidation process. (Han *et al*. 2013; Szabo *et al*. 2006).

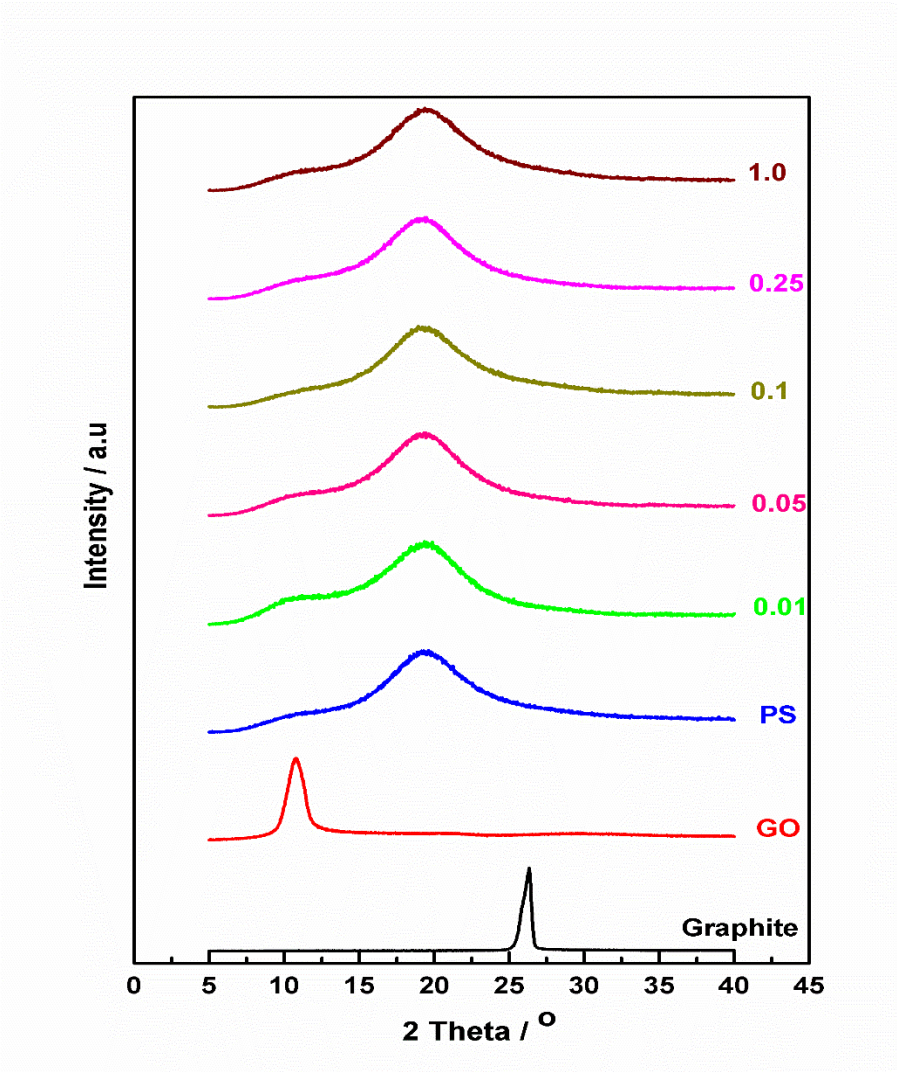

Figure 4.7. : XRD patterns of graphite, GO, PS and its nanocomposites.

The natural graphite peak shows a sharp characteristic peak at 26.3°. This peak verifies the abundance of unoxidized graphite substances. A new peak is formed at 10.7° which indicates the disappearance of a sharp peak of graphite, reduction in graphite's crystal structure and formation of GO sheets which consequently refer to a successful oxidation process. These peaks for graphite and GO were found by (Zhang *et al*. 2011).

(Yu *et al*. 2014) found that the interlayer spacing was shifted higher from 0.33 nm for graphite to 0.81 nm for GO. The same approach is found here as the interlayer spacing is going higher from 0.33 nm for graphite up to 0.82 nm for GO which confirms the accommodation of oxygen functional groups in the graphitic gallery that led to this result. The peaks of PS at 19.5° with the very broad and weak peak at 10° confirm the amorphous structure of PS.

The same peaks for PS were found by (Qian *et al*. 2013). For the nanocomposites, the only prominent peak is that related to PS and no obvious peak for GO can be found. This can be attributed to exfoliation of GO in the matrix with random dispersion, and the decline in the peak intensity of GO is due to dilution of the polymer matrix and the broad peak of PS. For all of the aforementioned reasons, the periodic structure of GO could not be found in the XRD patterns of the nanocomposites. (Yang *et al*. 2013; Szabo *et al*. 2006; Han *et al*. 2013). (Ionita *et al*. 2014) reported that the incorporation for (0.5 and 1.0) wt. % of GO to PSF did not result in clear appearance for a peak related to GO in the XRD patterns for these nanocomposites. Instead a single broad peak was observed that indicated a factual change in the structure of the polymer which indicated the dispersion of GO in the amorphous structure of PSF.

4.3.5. SEM

Figure 4.8. shows SEM micrographs that clarify the morphology of the neat polymer and the 1.0 wt. % of GO reinforcing the polymer matrix. It can be concluded that the cryogenically fractured surface for PS is smooth and uniform which is totally different to the micrographs of the nanocomposite where the roughness is noticed with the incorporation of GO flakes. Aggregates of GO in a few random places can be seen in the morphology of the lower couple of images for the nanocomposites. However, good dispersion of GO flakes in PS can be seen according to the employment of synergistic techniques of dispersion.

Interesting findings by (Basu *et al*. 2013) referred to the few stacks of 1.0 wt.% of graphene in the PS matrix. As the concentration of graphene was increased, higher amount of agglomerations can be seen. They also referred to the uniform morphology of the PS, and the somewhat decreased roughness for the nanocomposites as they included different weight fractions of graphene nano-powder. All the findings for the matrix and nanocomposites were obtained via the cryogenically fractured surfaces.

(Yadav & Cho, 2013) obtained findings using SEM that referred to aggregations of graphene nano-platelets in a PU matrix with loading up to 2.0 wt. %.

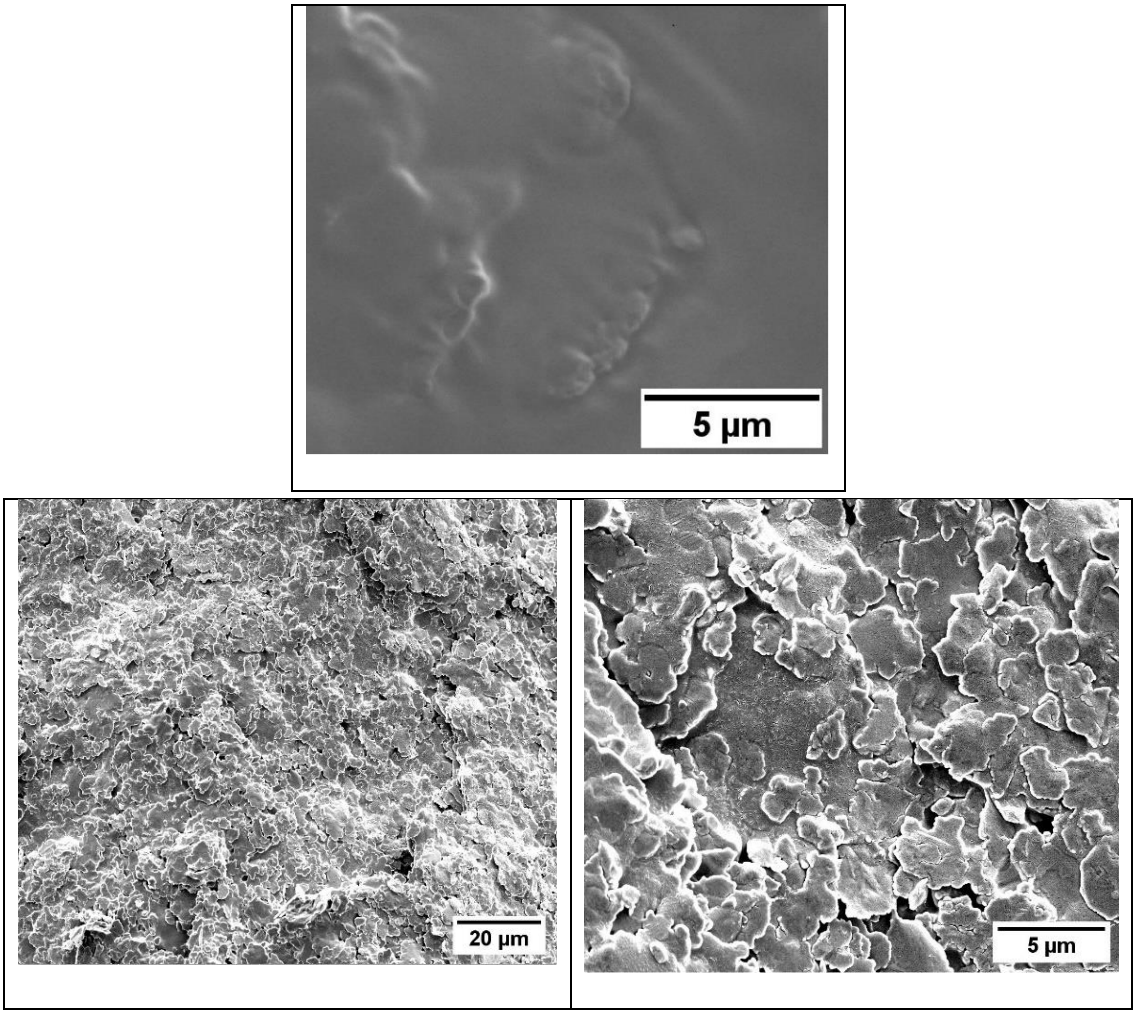

Figure 4.8. : SEM micro-graphs of pure PS'' top image'' and the cryogenic fracture surface for PS/GO 1.0 Wt. %

4.3.6. Thermal and thermomechanical properties

4.3.6.1. TGA

In Figure 4.9 (a) and (b), the thermal degradation behaviour is investigated for graphite, GO, PS and the nanocomposites.

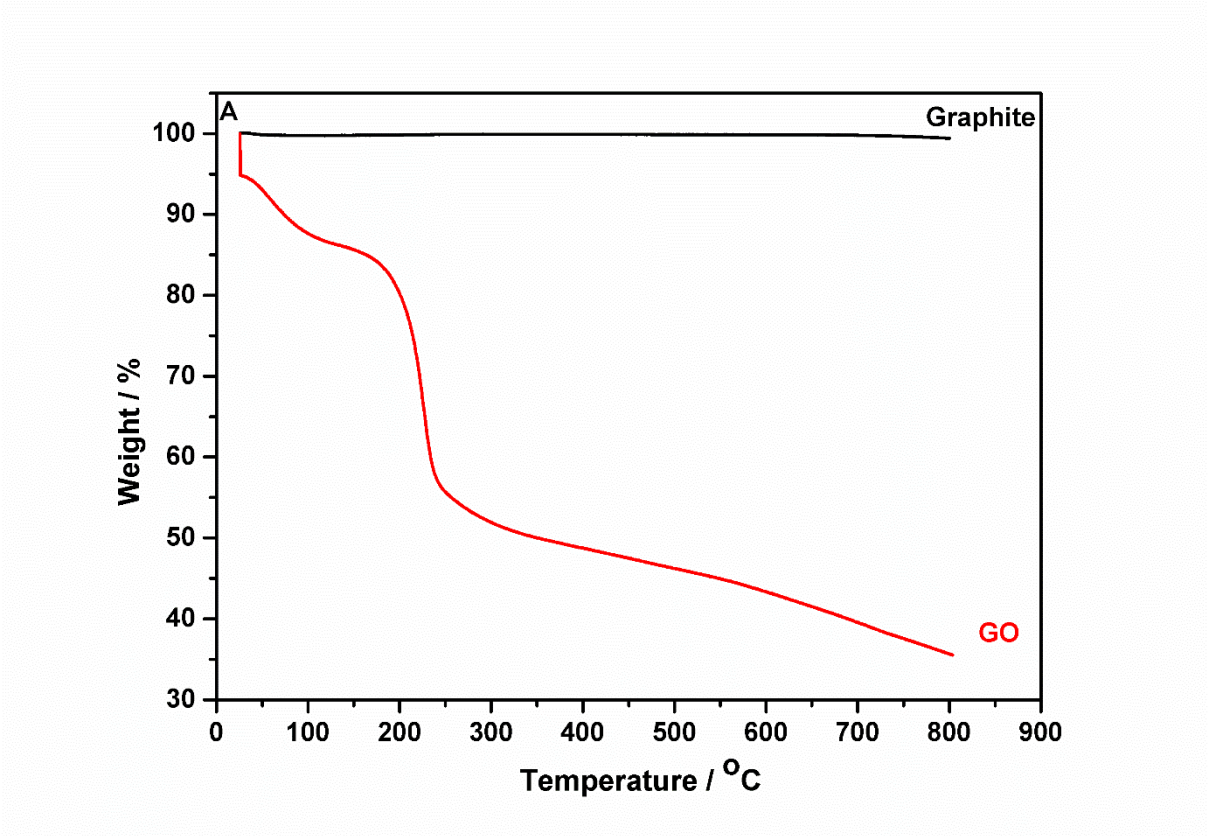

Figure 4.9(a). : Thermal degradation behaviour for Graphite and GO.

No weight loss for graphite powder was observed even at high temperature (around 800 °C) which confirmed the thermal stability at high temperatures for this material. This is because of the highly graphitized structure (Tang *et al*. 2014). Another study in the same year by (El-Khodary *et al*. 2014) indicated the good thermal stability of graphite up to 800 °C.

It can be noted for GO that it is thermally unstable due to significant mass reduction with increasing temperature (T.K. *et al*. 2014). There is a gradual weight loss with the increment of temperature up to (170-180) °C and this rising weight loss is ascribed to the evaporation of water molecules in the GO structure. The major weight loss occurs at around 204°C which is attributed to the decomposition of different kinds of oxygen functional groups in the structure of GO (Malas & Das, 2015). This drastic weight loss is accompanied by the emission of H_2O and CO_2 gases as the main decomposed functional groups are hydroxyl and carboxylic functional groups.

The third stage starts from around 350 °C up to 800 °C and here maximum weight loss appears which is around 60%. At this stage, the generation of CO gas is associated with the decomposition of carbonyl functional groups as a consequence of thermal treatment up to 500 °C (El-Khodary *et al*. 2014).

(Chen *et al*. 2010) observed that the thermal degradation behaviour for GO includes two main steps, the 1st one is the mass loss up to 100 °C due to the removal of absorbed water, and the 2nd step occurred around 200 °C due to the decomposition of the oxygenated functional group.

The thermal degradation temperature T_d for GO in the current study is 224 °C. This is different to that found by (Yu *et al*. 2014) when they measure T_d for GO when it was found to be 161°C. A possible explanation for the obtained result (high T_d for the GO in the current study) is the abundancy of functional groups that led to this high T_d temperature. On the other hand, the T_d temperature obtained by (Tripathi *et al*. 2013) is in accord with this current study.

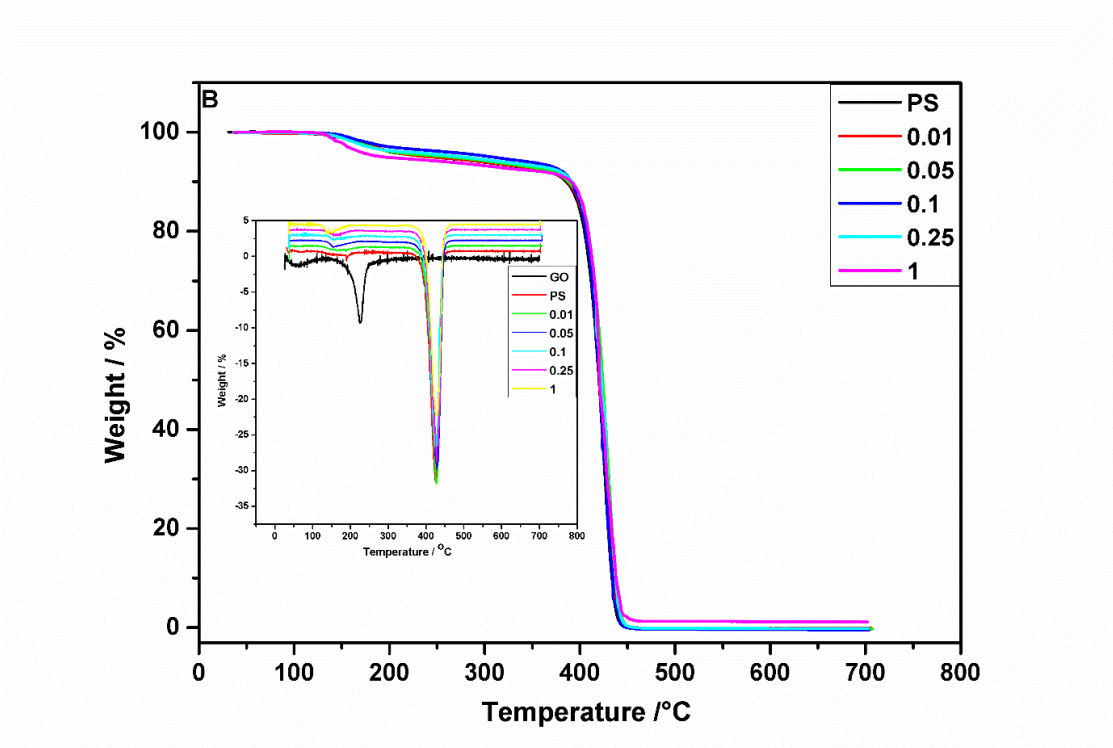

Figure 4.9(b). : TGA curves for PS and its nanocomposites. The background figure is the DTG curves for GO, PS and its nanocomposites.

For PS and nanocomposites, it is clear that the incorporation of GO nanosheets in the polymer matrix contributes positively in improving the thermal stability of the nanocomposites compared with pristine PS. It is clear there is a delay in onset decomposition for the PS/GO 1.0 wt. % compared with the neat PS.

The pristine PS starts to decompose at around 142 °C and it is fully decomposed at around 450 °C. The main reason for the PS decomposition is the main –chain pyrolysis (Wu *et al*. 2012). The T_d temperature gradually increases with increasing weight fraction addition to the polymer. This represents an improvement in thermal stability for the nanocomposites and can be attributed to the homogeneous distribution of the GO nanosheets in the matrix. This leads to a more efficient dissipation of heat throughout the polymer matrix, and better retardation in terms of thermal decomposition (Hassan *et al*. 2013).

This behaviour was emphasized by (Qiu *et al*. 2015) when they showed that the T_d temperature is increased for PS when it is reinforced with different weight fractions of functionalised GO (0.1,0.5 and 1.0) wt.%. Here the improvement in thermal stability was successfully obtained for the PS nanocomposites under the influence of air and nitrogen atmosphere respectively. Hence, it could be conceivably demonstrated that the incorporation of low loadings of graphene or any of its derivatives or reductants to different polymer matrices will lead to improve thermal performance as confirmed by (Xu *et al*. 2013; Sheng *et al*. 2015).

4.3.6.2. DMA

Figure 4.10. illustrates the thermomechanical behaviour for the PS and its nanocomposites. It should be emphasized that the polymer and nanocomposites are in a glassy state at room temperature as the chains are frozen and motionless but they transform to the rubbery state as the temperature is raised (Hasan & Lee, 2014). The inverse relationship between temperature and storage modulus can be clearly seen.

As the temperature increases, cooperative motion for the polymer chains occurs and this motion of the chains is accompanied by energy dissipation leading to a decrease in storage modulus. The former measures the stored energy, representing the elastic portion of the curve.

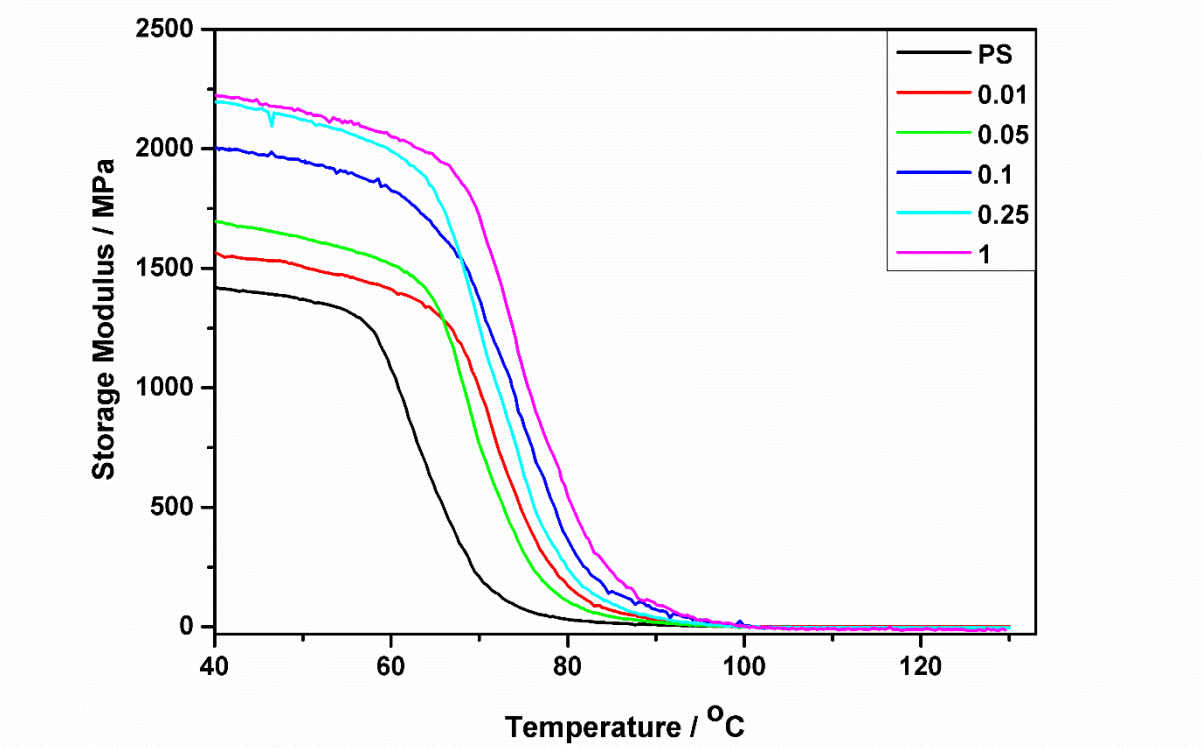

Figure 4.10. : DMA curves for PS and the nanocomposites.

The second set of analyses discusses the assessment of the GO addition to the polymer in terms of storage modulus improvement. The storage modulus increases consistently with the addition of increasing weight fractions of GO to the neat polymer, consistent with an increase in the rigidity of the nanocomposites compared with the pristine polymer.

The restricted movement of the polymer chains, the larger aspect ratio of GO nanosheets, the higher modulus for GO nanosheets, the stronger interfacial interaction between the polymer and the nanofillers, and the homogeneous distribution of GO nanoparticles in the polymer matrix are the most important reasons for the consistent improvement of the thermomechanical performance for the nanocomposites compared with the neat polymer (Yang *et al*. 2013; Tang *et al*. 2014; Yu *et al*. 2014). (Ren *et al*. 2011) confirmed the same behaviour for the PS when it

is reinforced with different very low weight fractions of graphene. Section 3.3.3.3. discusses the reasons behind the appearance of humps in the storage modulus curves.

Unexpected findings had been reported by (Srivastava *et al*. 2011) when they highlighted the negative thermomechanical performance for the PS when it was reinforced with higher weight fractions of multi-wall carbon nano tubes. They highlighted a decrease in storage modulus for PS with the incorporation of 8.0 and 10.0 wt. % of MWCNT compared with 6.0 wt. % and other lower concentrations. The authors attributed this to the agglomeration of nanotubes that led to poor interfacial interaction between the nanoparticles and polymer molecules.

4.3.6.3. DSC

Figure 4.11. shows the values of T_g that were recorded by the DSC measurements as part of this study. It can be seen that there is a slight increase in the values of the glass transition temperature T_g with increasing weight fraction of GO in the PS. This behaviour can be explained by the retardation of the molecular motion due to interaction with the GO nanosheets that have high surface area.

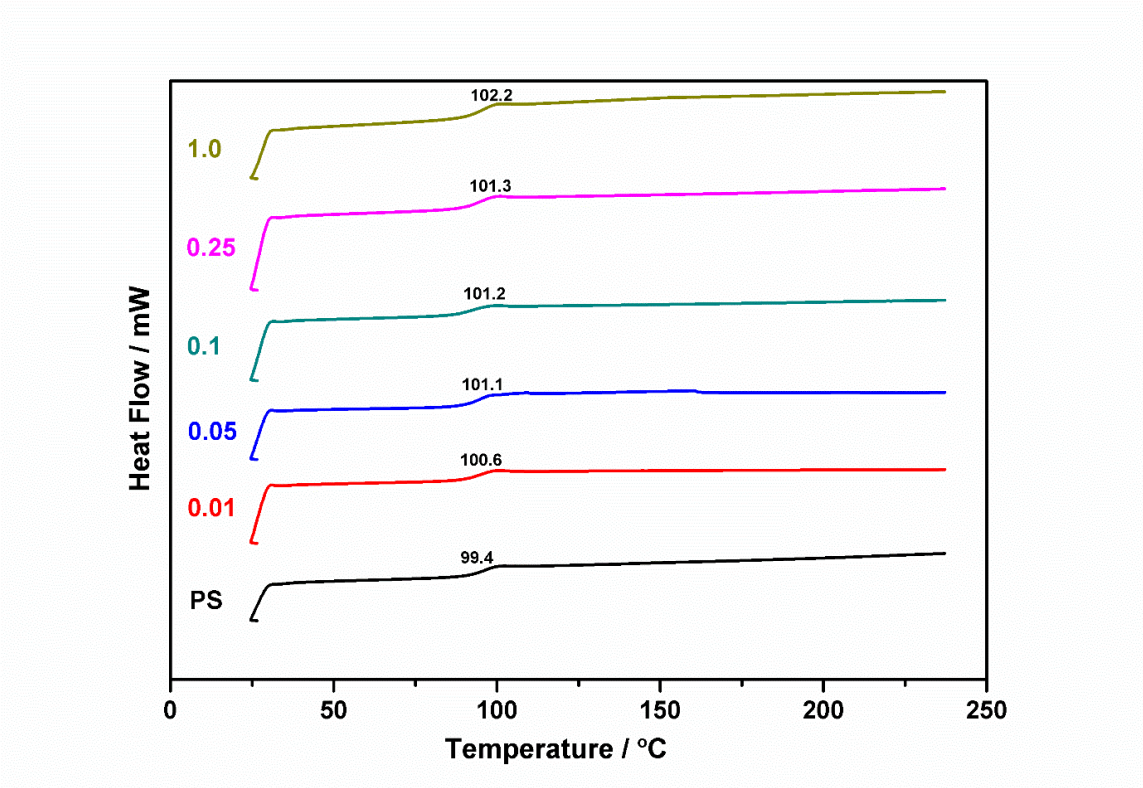

Figure 4.11. : DSC curves for PS and nanocomposites.

The observed increase in the values of T_g can be attributed to the fine dispersion of GO in the PS because several dispersive techniques have been employed. The large surface area of the nanosheets produced confinement in the polymer chains and this leads to a higher glass transition temperatures for the nanocomposites compared with the neat polymer (Basu *et al*. 2013). It is important to report that no surface treatment is carried out for the GO. Despite the fact that some SP_2 network of graphite sheets is damaged by the process of oxidation, the residual hexagonal honeycomb lattice might form conjugations with the PS adding more confinement for the GO with the plate structure of PS segments. This will result in an improvement in the values of T_g for the nanocomposites higher than PS (Yang *et al*. 2013). (Wan & Chen, 2012) reported the effect of low loadings of GO on the PS matrix, and they confirmed what has been observed in the current study. As the loading of GO increases from (0.3 to 2.0) wt. %, so the T_g increases which is a consequence of the strong interfacial interaction between the nanosheets and the polymer. This strong interfacial interaction inhibits free mobility of the adsorbed polymer chains in the interface. Table 4.2. below presents a summary of the results obtained in the thermal measurements in this study detailed earlier in Figures [4.9(a) and (b), 4.10, and 4.11.].

Table 4.2. : Thermal and thermomechanical properties for PS and the nanocomposites.

Sample	**T_d / °C**	**T_g DSC / °C**	**Tg DMA / ºC**	**Storage modulus at 30 ºC / GPa**
PS	425.58	99.4	57.5	1.41
PS/GO 0.01wt. %	426.90	100.6	60.4	1.56
PS/GO 0.05 wt.%	427.70	101.1	68.4	1.69
PS/GO 0.1 wt.%	427.90	101.2	67.4	2.0
PS/GO 0.25 wt.%	427.50	101.3	66.8	2.19
PS/GO 1.0 wt.%	428.70	102.2	68.7	2.23

It can be clearly seen that the incorporation of low loadings of GO results in an enhancement of the thermal and thermomechanical performance of PS.

An analysis and interpretation of the results compared with published data in the literature was provided in the body of the text in this section.

4.3.7. TEM

The spatial dispersion for GO nanosheets in the PS matrix as well as the morphology of the nanocomposite and the neat polymer are checked using the TEM technique. Figure 4.12. shows that.

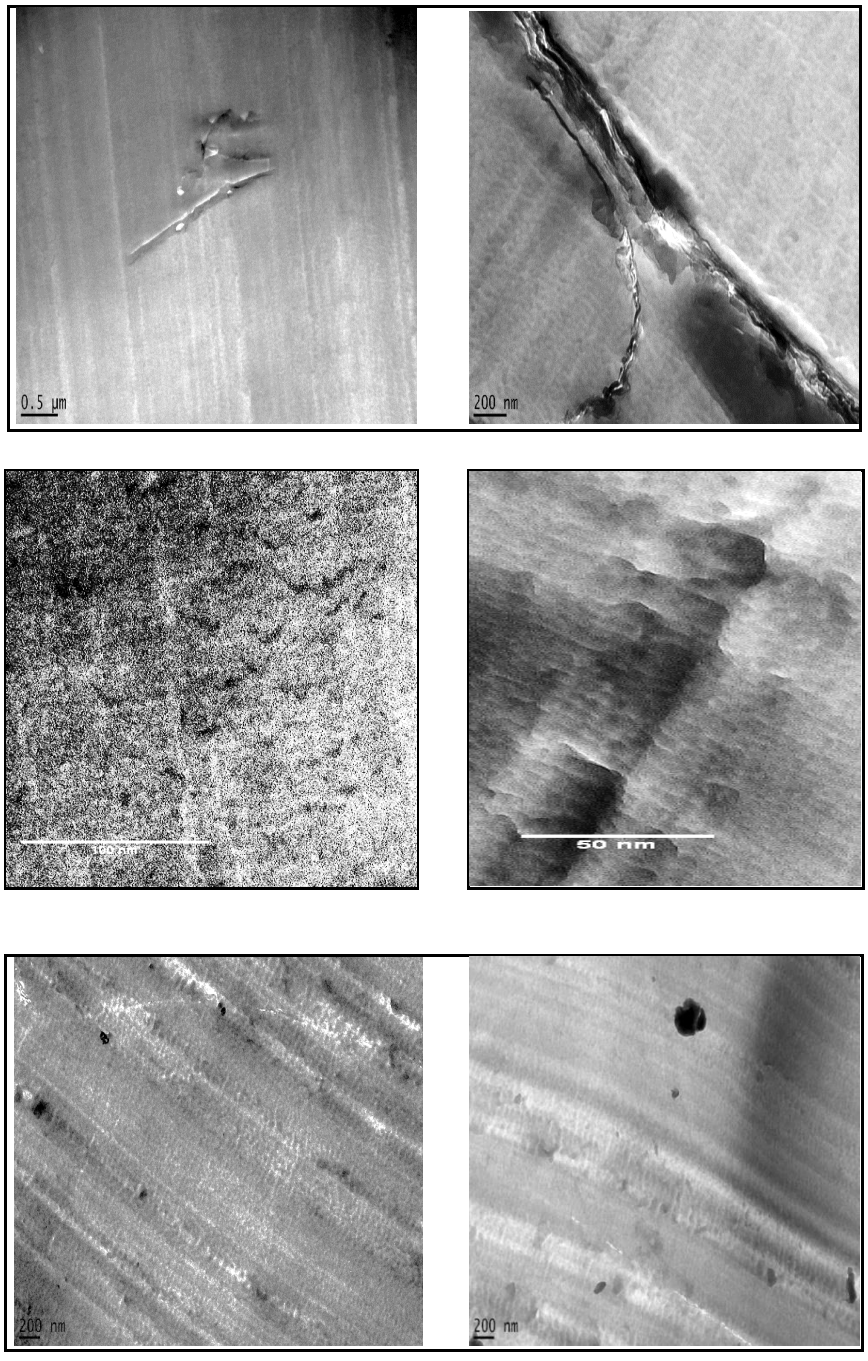

Figure 4.12. : TEM micrographs of PS/GO 1.0 wt. % and pure PS.

The black sheets represent the nanosheets and the grey background are the results obtained with the polymer. In the 1st couple of images and at higher magnifications, curved and partially peeled nanosheets can be seen which provide an impression of the morphology of the nanocomposite material. At the lower magnifications of 100 and 50 nm the individual and finely dispersed sheets can be seen in the matrix. No stacking or aggregations for the nanosheets of GO can be found in the PS matrix. These results are quite similar to the results obtained by (Wan & Chen, 2012). In order to show the difference in morphology between the neat polymer and the nanocomposite, images for pristine PS were also recorded.

Figure 4.12. shows a series of TEM images and it can be clearly seen from the bottom two that no interesting nanosheets or recognizable morphology for the nanofillers can be confirmed. The images look more like that of a pure polymer with no reinforcing GO nanosheets, and the prevailing style for the images is the traces of cryo-micro sectioning that are due to preparation of the samples for imaging using TEM.

4.3.8. Nanomechanics

4.3.8.1. AFM

In order to estimate the Young's modulus of PS and GO nanosheet at the nano-scale, force-distance curves are measured using AFM with a cantilever that has a very low spring constant as described earlier. The Young's modulus was calculated from the data using the DMT mathematical formula (Derjaguin *et al*. 1975; Muller *et al*. 1983).

Figure 4.13(a) and (b) shows the measured force – distance curves for PS and the GO in the nanocomposite respectively along with AFM images for each measured material. These curves and images were taken for the cryogenic fracture surface. Both force-curves for the polymer and the nanosheet show a sawtooth shape in the region of the pull-off force but it is much more prominent for the GO compared with PS. This means that no artefacts were observed during the pull-off force measurements (Beach *et al*. 2002).

(Thio & Meredith, 2007) reported in their co-work that the adhesion forces for different kinds of tips and different polymer surface including PS is within the range (- 1.5 nN to -8 nN). It is estimated that the adhesion force for the PS force-distance curve is about -10 nN. The mounting of fracture surface to the cantilever's tip was a challenge as the thickness of the surface is quite low and as a result detecting this surface topography was not easy to perform.

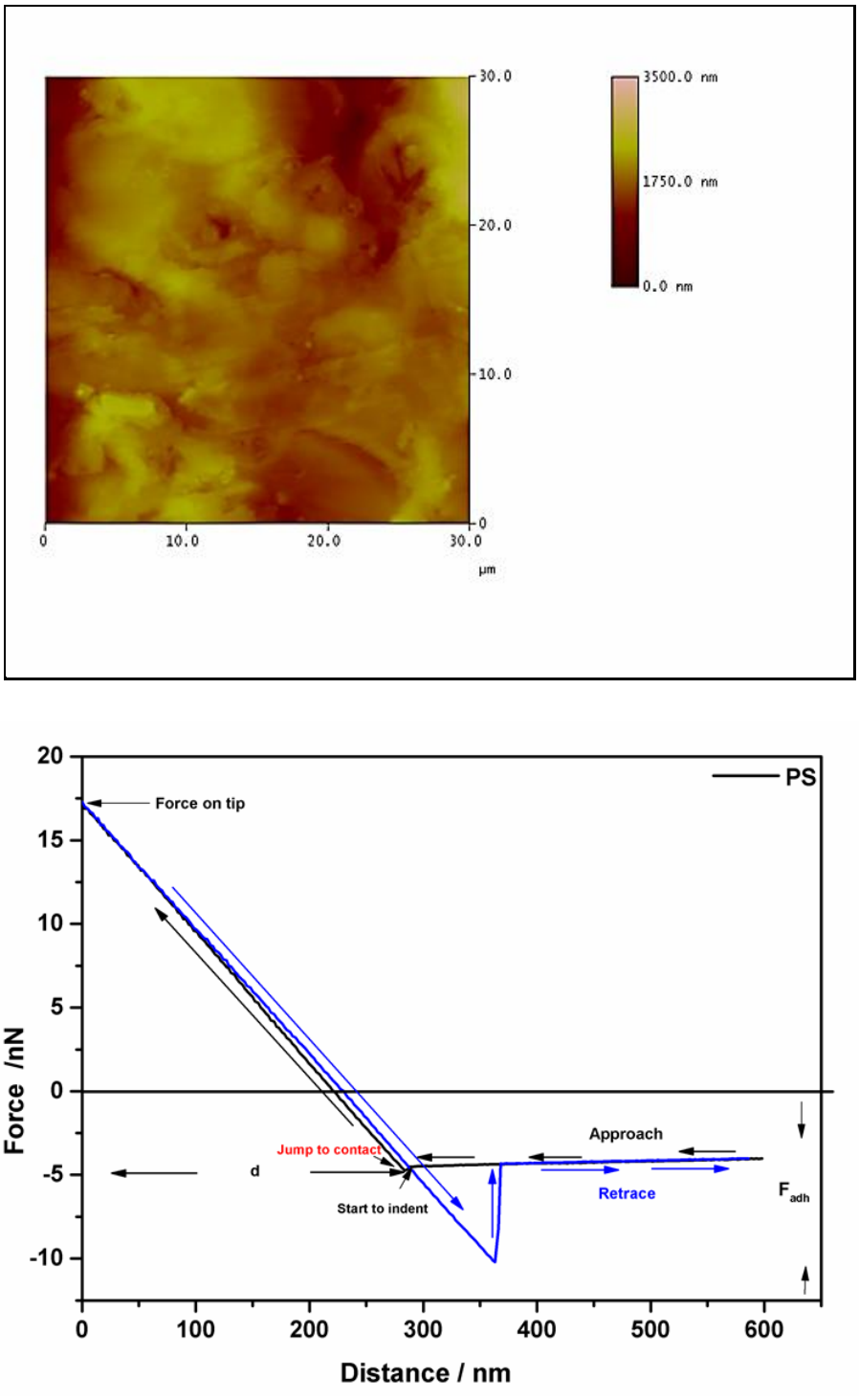

Figure 4.13 (a). : Force-Distance Curve for PS with AFM image for the area where the tip was indented.

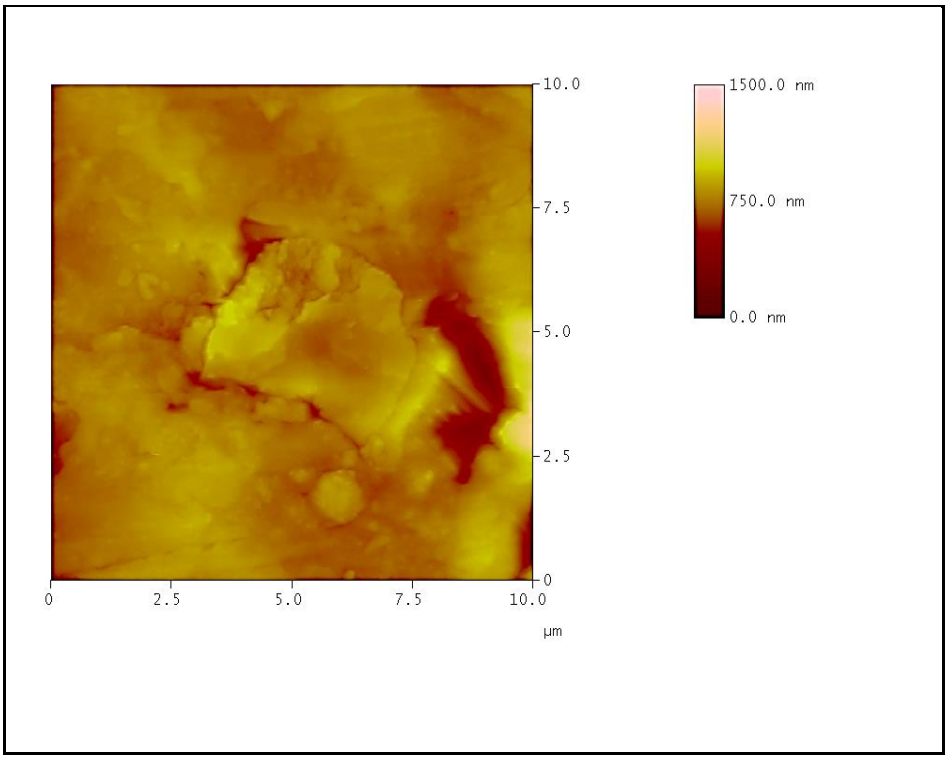

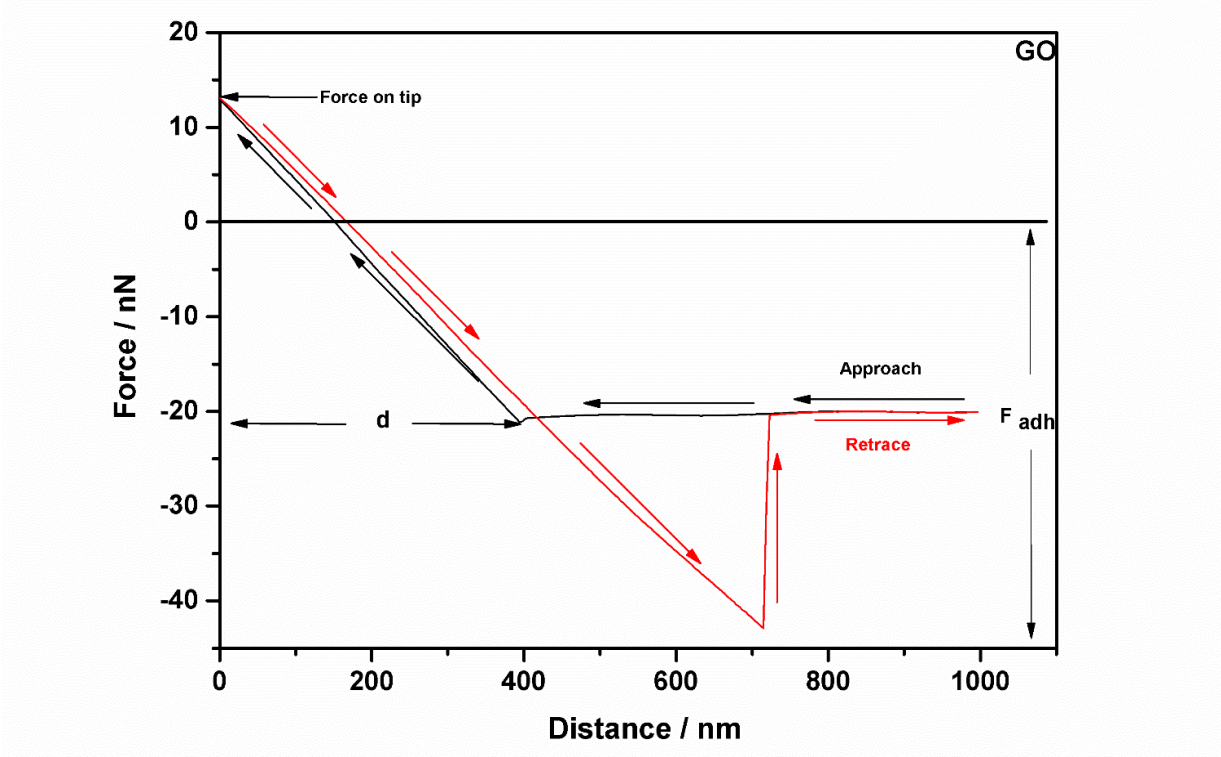

Figure 4.13(b). : Force-Distance curve for GO nanosheet with AFM image where the tip was indented.

The procedure for obtaining the force – distance curves begins by adjusting the tip so that it initially stands away from the studied fracture surface. Gradually, it is brought towards the cryogenic fracture surface.

The tiny deflection in the curve indicates that the forces of attraction near the surface pull the tip down when it is in very close proximity with the surface. The tip is then traversed across the surface and deflected by varying degrees by the surface features. When the tip retracted from the studied surface, it ascends until the forces are in equilibrium with other surface forces and the cantilever relaxes downwards. As the probe is lifted from the surface, the cantilever bends downward as the attraction forces hold onto the cantilever, and finally it breaks free with a sharp rebound upwards. The remainder of the force curve shows the operation of the tip leaving the surface back to its original position (Xing *et al*. 2010).

Section 2.5.1. in the literature is clarifying these concepts in details. Many of the data obtained from adhesion force test were scattered widely with poor reproducibility. Some of the more important sources of error in these measurements leading to a poor evaluation for the adhesion force are: 1- The wrong consideration for the surface roughness. 2- The varying deformation of the tip and the surface. 3- The adsorption of contaminants for both the tip and surface (Thio & Meredith, 2007). As regarded previously, the cantilever was made from Si_3N_4 with 200 μm length and spring constant of 0.08 Nm^{-1} provided by the manufacturer. (Xing *et al*. 2010) used a cantilever that had a spring constant of 0.58 Nm^{-1} provided by the manufacturer as well. The plan in this work was to gain an impression of the nano-mechanical behaviour for the PS and GO before carrying out the QNM measurements.

The thickness of the cryogenic fracture surface was about 1 mm. It should be emphasized that the main reasons for the selection of this surface rather that the wide flat surface of the sample is that the reduction of the contact area (which is originally obtained cryogenically) plays a dominant role in the reduction of surface roughness and in the reduction of any possible contamination. Moreover, the selected cantilever has a very low spring constant in order to obtain high sensitivity. Another consideration as well as the small thickness is also the length of the cantilever in order to obtain a large deflection at small force. V- Shaped cantilever was selected for this test and the QNM measurements to ensure high lateral stiffness.

The nominal spring constant of the cantilever is adopted for this measurement as it is a test for a possibility for obtaining force curves for the cryogenic fracture surface and as the evaluation methods of spring constant are not simple, not reliable and not precise as well. (Butt *et al*. 2005).

The data for the force distance curves are the results of two contributions, the elastic force of the cantilever, and the tip – sample interaction (Cappella & Dietler, 1999). According to the DMT model, Young's modulus is calculated via unloading part of the force-distance curve. The DMT is a modified Hertzian model that takes into account the force of adhesion between the tip and surface of the sample (Young *et al*. 2011). The force-curves show clear contact point, repulsive range in the approaching part, and a pull-off point in the retracing part.

The Young's modulus for PS was recorded at 2.66 MPa and 8.93 MPa for the GO flake shown in AFM image. Young's modulus at the nano-scale for PS and GO is much higher than these values. The maximum applied load in these experiments was not sufficient to obtain values that were similar to theoretical values or what has other authors achieved (Thio & Meredith, 2007).

(Lin & Kim, 2012) used the JKR and Hertz models for finding the elastic modulus of PS and other polymers with force curves obtained using a steel micro-spherical probe tip attached to a silicon cantilever with spring constant of 42 Nm^{-1}. They found that the elastic modulus for PS was 4 MPa at a specimen deformation of 120 nm. The specimen deformation for the current study for PS is higher than the latter value which makes the elastic modulus axiomatically lower than that measured by (Lin & Kim, 2012).

4.3.8.2. QNM

Peak force QNM has the capability for determining the local mechanical properties at nano-scale resolution unlike the conventional AFM used to characterize the structure and morphology (Panaitescu *et al*. 2012). Quantitative measurements for Young's modulus can be carried out with this machine by performing a force-distance curve at every pixel in the image and using the peak force as a feedback. Nanoscope software was utilized for finding the modulus using the DMT model (Panaitescu *et al*. 2013).

(Smolyakov *et al*. 2016) also provided an explanation of the theoretical background of peak force QNM. Figure 4.14 –a- is the result of a 30 microns morphological characterization of the height sensor channel showing the general topography of the cryogenic fracture surface. A randomly selected area shown with an arrow in the same image is specified for looking to nanofillers where two recognizable GO nanosheets were found using the tapping mode. This tapping mode characterization is paved the way towards finding the modulus for the polymer and the GO nanosheets using the DMT approach.

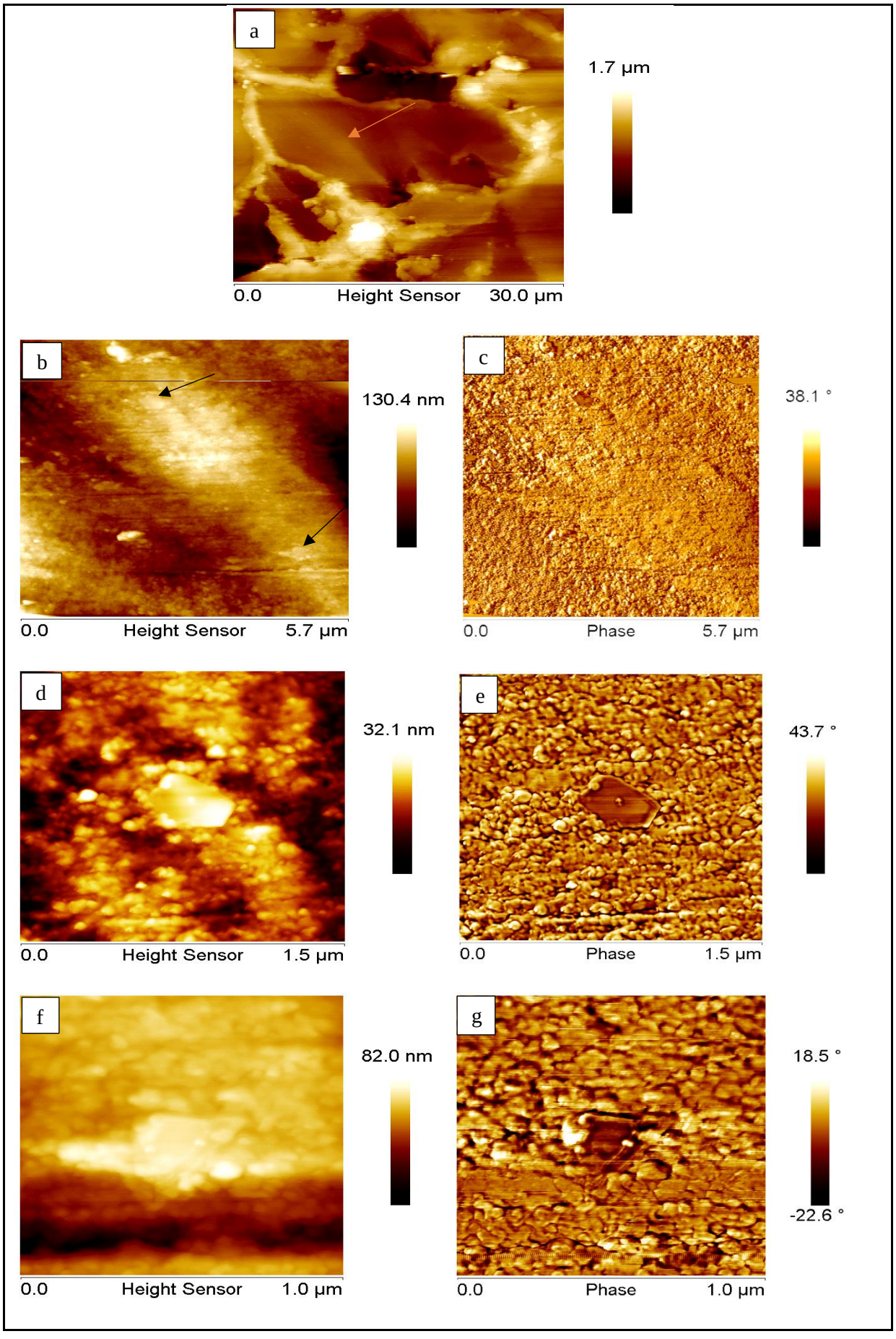

Figure 4.14. (a-g): Tapping mode QNM images for a specific area in a cryogenic fracture surface.

These measurements provide insightful and comprehensive details of the nanoscopic morphology for the nanocomposites and is deployed as a mapping technique for the nanocomposites before exploring the local nanomechanical properties (Panaitescu *et al*. 2012). Figure 4.14(b) shows the topography of the area indicated by the orange arrow in Figure 4.14 –a- and this topography is shown by the height sensor channel. The light diagonal feature across this image (-b-) shows two flakes. These are in the upper left and the lower right of the light diagonal area. It should be noted that finding two flakes in a randomly selected area in the cryogenic fracture surface gives an indication of the even distribution of GO flakes in the polymer matrix. The size of these flakes can be estimated as the height differences shown in (image –c-) does not have any effect on these topographic maps (Grigorescu *et al*. 2016). Image –c- represents the phase channel of the previous image. The contrast in this channel is related to the energy dissipation from the cantilever. In other words it is related to material properties of the tip sample contact.

Images –d- and –e- in Figure 4.14 show the height sensor channel and the phase channel respectively, for the upper left flake that appear in images b and c. This flake appears in the centre of the images –d- and –e-. Images –f- and –g- in Figure 4.14 show the height sensor channel and the phase channel of the lower right flake. It was hypothesized that images cantilever phase in tapping mode AFM are intimately associated to maps of dissipation. The phase images –c-, -e- and –g- in Figure 4.14 are all smaller than 90°. These are the phase angles for all the aforementioned phase images that are plotted in standard imaging.

As long as all the phase angles are smaller than 90° , so that means that these phases are repulsive. Attractive phases normally associated with phase angles higher than 90°. The phase contrast can be clearly seen in these images as the tip-sample interaction is used and energy dissipation is generated according to this interaction that consequently lead to this contrast. No competition between attractive and repulsive phases can be seen as there is no change in phase angle from higher than 90° to smaller than 90° (Cleveland *et al*. 1998).

The scale bars related to images –a-, -b-, -d- and –f- of Figure 4.14. represent the Z-axis which shows ‘’the distance ramped by the piezo scanner in the vertical direction’’ (Martínez-Tong *et al*. 2014). After producing the tapping mode imaging, the peak force QNM was used for nanomechanical characterization purposes. This was carried out for both the two detected GO flakes on the cryogenic fracture surface and the polymer matrix of PS surrounding them. The DMT modulus maps were used to achieve this goal.

Figure 4.15. includes images of DMT modulus maps for GO flakes and the PS matrix around them. Table 4.3. shows the modulus and standard deviation for the flakes and the matrix achieved by the nanomechanical characterization using peak force QNM.

Image –a- in Figure 4.15. shows the height sensor channel of the lower right flake. The mean height of the flake with respect to the matrix above it is 6.5 nm. Image – b – shows the DMT modulus channel for the same flake. Image – c- shows the DMT modulus channel with a mask drawn over the flake (the red area) and this mask is drawn by using a software tool described in the experimental section. The mean and standard deviation of the pixel values within and outside the mask allow the modulus of the flake and the matrix to be estimated.

Image –d- in Figure 4.15. shows the height channel sensor for the upper left flake of GO. The mean height of the flake with respect to the matrix is 9.5 nm. Images e and f show the modulus channel and the mask over the channel for the upper left flake respectively. The mask is drawn over the flake, and in the DMT modulus channel and the mean of the pixel values is calculated inside and outside the mask.

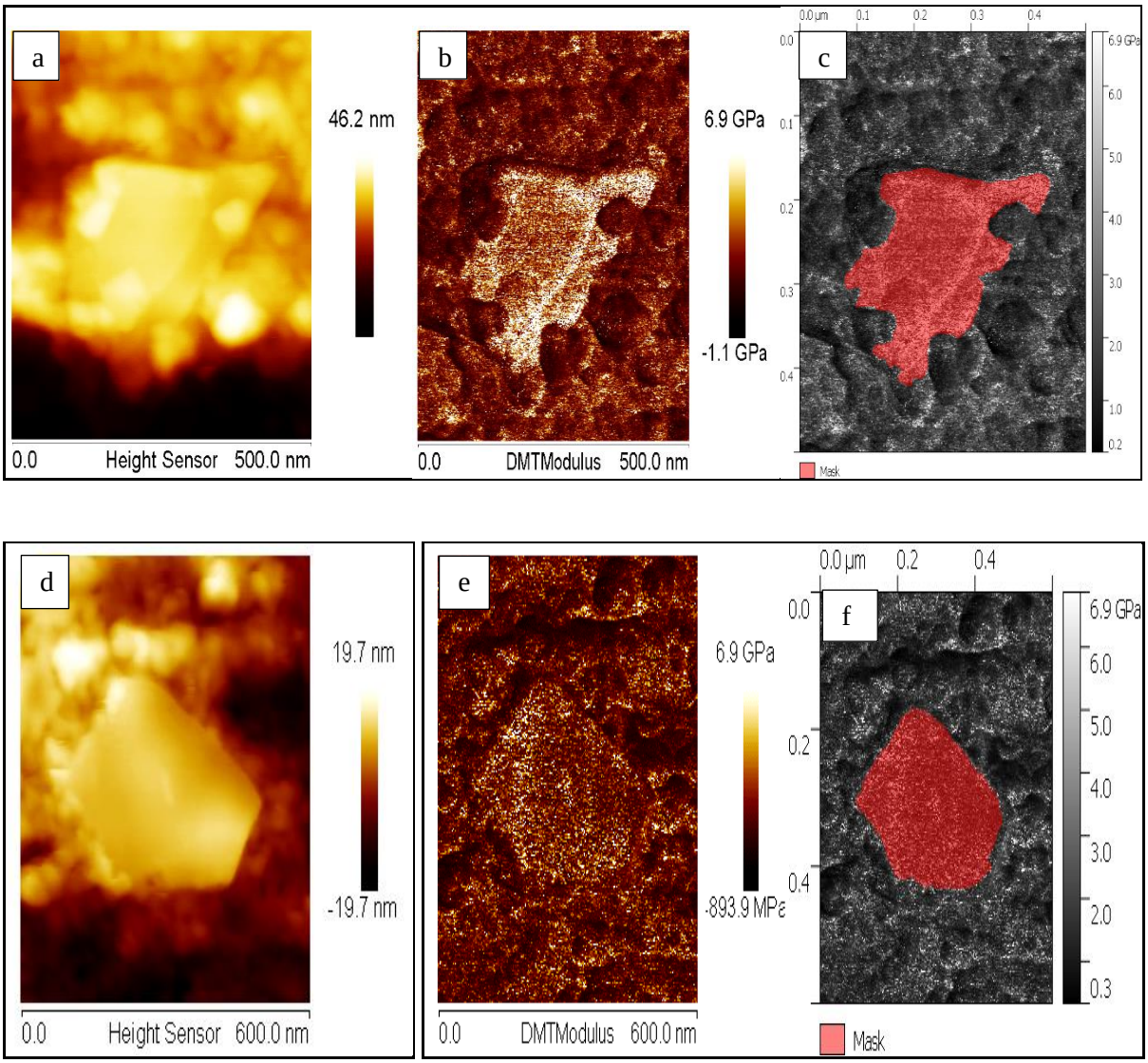

Figure 4.15. (a-f): Height sensor channels, DMT modulus channels and the red mask for DMT modulus channels for both the lower right GO flake (a-c images) and upper left GO flake (d-f images).

Table 4.3. : Quantitative nano-mechanical measurements for GO flakes and PS.

Sample	**DMT Modulus / GPa**
GO flake (Lower right)	3.7 ± 1.9
PS matrix around lower right flake	1.9 ± 1.1
GO flake (Upper left)	2.4 ± 1.3
PS matrix around upper left flake	1.7 ± 1.0

The polymer chain orientation and the crystallinity of the polymer at the nano-scale play an important role in measuring Young's modulus for polymers. The standard deviation is obtained for GO and PS as this technique can provide repeatable measurements of Young's modulus at the nano-scale using a range of probes with taking in consideration the inevitability of providing the required calibration.

The lower standard deviation for the above results shown in Table 4.3. indicates a high accuracy of measurements. The considerable difference between the results obtained by the conventional AFM and peak force QNM can be ascribed to the difference in indentation depth between the two techniques as well as the stiffness of the used cantilevers and the length of scale. The indentation that can be achieved by AFM is up to tens or hundreds of nanometres. In contrast, the peak force QNM is designed to obtain the modulus within 2 nm deformation (Young *et al*. 2011). Regarding the experimental section, the radius of the tip used is very fine (less than 25 nm) and this is a requirement for obtaining better imaging resolution with optimum indentations at the nano- scale (Veeco,Support notes 2005).

In many cases, the Young's modulus at the nano-scale for polymers is measured by depositing the polymer film with a specific thickness over the silicon substrate. For the current study, the modulus is taken by indenting the tip on the cryogenic fracture surface directly. (Lin & Kim, 2012) deposited many polymers, including PS, over a silicon substrate and they used a specific probe to find the modulus for these polymers at the nano-scale. The obtained modulus using this approach is expected to be overestimated as the deformation of the sample exceeded 10% of the thickness of the film (Smolyakov *et al*. 2016).

Other authors such as (Young *et al*. 2011) studied the nanomechanical properties for the polymer surface for several polymers including PS. This approach requires a careful selection of the tips and cantilevers in order to obtain the right modulus.

These authors used a range of tips starting from Berkovich indenter of nanoindentation and three other different cantilevers manufactured from different materials with high spring constants ranging from 56 Nm^{-1} to 227 Nm^{-1}. The results showed a slightly higher modulus for PS (3.24 GPa) compared with the modulus provided by the supplier of (3 GPa) and the standard deviation in the four cases was low suggesting a high accuracy.

The values of Young's modulus for the polymer in the current study are quite reasonable. Despite the fact that (Lin & Kim, 2012) used the JKR model for finding Young's modulus for PS, they used a tip that has a spring constant quite similar to the one used in the current study. The result refers to 2.6 GPa at a deformation of about 1.7 nm which is slightly higher to that obtained in the current study and the study of (Young *et al*. 2011).

The moduli for GO flakes appear to be underestimated. (Sun *et al*. 2013) reported the value of Young modulus for a single layer graphene sheet at 1100 GPa. The Molecular Dynamics MD simulation was used to calculate Young's modulus for GO and it was found that the value of the modulus varies from (290-430) GPa for amorphous GO and from (380-470) GPa for ordered GO depending on the coverage of the functional groups (Liu *et al*. 2012).

Furthermore, (Kang *et al*. 2013) investigated the mechanical properties of free standing GO by using nanoindentation combined with the dynamic contact module DCM. The deposited GO film of thickness ~50-60 nm had a Young's modulus of (695 $\pm$ 53 ~ 697 $\pm$ 15) GPa which is higher than the modulus of a single layer of graphene sheet (0.25 TPa). The high value of Young's modulus is related to the number of GO layers. In the study of (Kang *et al*. 2013), the crack propagation of 50-60 nm thickness of GO free standing film started to appear at loads of 65 and 72 μN. The tip used was a Berkovich indenter of nanoindentation. In the current study, the applied load was 10 nN only for the flakes that have a thickness of few nanometres.

The cantilever used in the current measurements is unlikely to be stiff enough to provide sufficient indentation on the GO flake. In the event of further force applied over the tip, then the tip geometry will be changed and this will result in blurry images.

Furthermore, there are other limitations for peak force QNM that can adversely affect the results (for both the polymer and the flakes). One important example is the complex force interaction between the tips and different surfaces that arises from tip - surface contact. This leads to inaccurate measurements. As described in the introduction, the most used mathematical relations for finding the Young's modulus at the nano-scale for polymers and nanoparticles are Hertzian, DMT and JKR. All of these are estimated on the basis that the contact is carried out between the spherical tip of specific radius and a flat surface of the sample. However in many cases, such as the current study, the surface of the sample is not flat at all. Moreover, ''the tip apex may differ from an ideal sphere'' which can lead to major errors in calculations of the modulus. The AFM tip is also prone to lateral and buckling movement (as rotation) and this is another important reason for the unexpected results for nanomechanical measurements. Tip-surface shear forces are generated as a result of this rotational movement during the cantilever deflection and they are not accounted for in the aforementioned mathematical models (Young *et al*. 2011).

4.3.9. Conclusions

In this study, different low loadings of GO were incorporated homogenously into a PS matrix and different structural, thermal properties were studied as well as the nanomechanical behaviour for the polymer, and the nanosheets imaged in the cryogenically fractured surface. The incorporation of low loadings of the GO led to improvement in thermal and thermomechanical performance as the results of TGA, DSC and DMA indicated. As the homogenous dispersion for the nanosheets in the polymer matrix is a prerequisite for a good performance, this kind of dispersion was verified via different microscopic techniques carried out in this study. These techniques included OM, SEM and TEM.

According to the very low weight fractions used in this study, no sharp peaks of GO appeared in Raman spectroscopy for the nanocomposites. Weak shoulders appeared in FTIR diagram and tiny humps can be seen in the curves of XRD.

These can be attributed to the low loadings of GO in the PS that led to dilution of GO in the polymer matrix. Force distance curves obtained by conventional AFM showed a higher Young modulus for GO obtained using the DMT model compared with the PS modulus obtained by the same relation.

These results were an indication that the nanomechanical behaviour of the polymer and the GO nanosheets can be investigated using the sophisticated technique of peak force QNM. This technique confirmed what was achieved by conventional AFM but with higher magnitudes for PS and the flakes of GO. This is because the stiffness of the used probe was higher than that used in conventional AFM. However, the stiffness was not sufficiently high to provide real and accurate magnitudes for the modulus of the GO flakes. Moreover, the imaging of the flakes and the matrix was more efficient in peak force QNM compared to the conventional AFM as high spatial resolution was employed to image the cryogenically fractured surface.

The novelty in this chapter represented by the successful imaging for the cryogenically fractured surface for the nanocomposite and finding the nanomechanical properties for the matrix (PS) and the nanosheets (GO) using different tools. The fracture surfaces are usually imaged by microscopic techniques such as SEM. The successful employment for AFM and most importantly for QNM in characterizing the cryogenically fractured surface and determining the nanomechanical properties for the nanocomposite was a novel approach that quite few authors have adopted in their work.

Chapter 5

Studying the properties of PS /thermally reduced GO nanocomposites using vacuum oven at low temperatures

5.1. Introduction

The partial removal of the oxygen functional groups from GO, which is known as reduction, has emerged as a powerful platform for obtaining graphene - like materials quite similar to pristine graphene, which can be directly produced using scotch tape i.e.'' mechanical exfoliation''. GO can be named as rGO (if it is thermally or chemically reduced) beside many other possible names such as functionalised graphene and chemically converted graphene (Pei & Cheng, 2012). Section 2.3.4.1. clarified the concept of GO reduction.

There are several thermal and chemical methods for practical applications (Mohan et al. 2015). The main aim is to increase the ratio of carbon to oxygen (C : O) with an increase in hydrophobicity which makes GO behave as a non-polar material. However, the subsequent incorporation of rGO in polymers leads to problems as the interaction of the solvent with sheets will be negatively affected (Glover *et al*. 2011). Nevertheless, some of the important properties of graphene can be partially restored by reduction. The chemical reduction of GO can be carried out using specific chemical agents such as sodium borohydride and hydrazine (Toselli *et al*. 2015), and (Muda *et al*. 2017; Chua & Pumera, 2016) have conducted experiments to reduce GO using these chemical agents. (Chen *et al*. 2010) has suggested other kinds of chemical reductants might be better than hydrazine such as Sulfur containing compounds.

There is however a trend towards the thermal approach for reducing GO because it is more eco-friendly and safer than chemical approach which is dealing with toxic agents to achieve GO reduction. Time and the processing temperature are the most important factors associated with obtaining rGO this way as well as the chemical structure of the polymer (Glover *et al*. 2011). For instance, (Sheng *et al*. 2015) reported the effective reinforcement of thermally rGO in PMMA nanocomposites.

A hot pressing approach at 200 ^{o}C was used to obtain in situ thermal reduction for GO nanosheets and the results showed a clear improvement in mechanical, viscoelastic and thermal properties. In addition, microwaves were used to induce thermal reduction of GO in an aqueous media.

(Chen *et al*. 2010) used mixed solution of N, N- dimethylacetamide DMAc and water as a medium for producing graphene and controlling the temperature of the reactive system up to 165 ^{o}C. The suspension that was produced was stable for many months at room temperature, and the conductivity of the graphene paper was considerably higher than that of GO paper. Melt mixing was an approach used by (Han *et al*. 2016) to prepare the nanocomposites of polystyrene PS with TRGO. The temperatures used were 200, 500 and 800 ^{o}C respectively. The storage modulus was significantly improved for the nanocomposites of rGO reduced by 500 and 800 ^{o}C. The same nanocomposites showed enhancement in flame retardant performance. Microwave assisted exfoliation is another thermal approach used by (T.K. *et al*. 2014).

The rGO obtained through this approach was given the name as 'Microwave Exfoliated Reduced Graphene Oxide' MERGO according to the residual functionalities obtained in the sheet surface. These functionalities provide an even dispersion of graphene in the matrix as well as a good chemical bonding between the polymer matrix and graphene. When MERGO was incorporated with low loading in an epoxy matrix, elastic, flexural moduli and fracture toughness improvements were reported (T.K. *et al*. 2014).

In order to avoid the harmful effect of reduction by chemical solvents, in situ thermal reduction was used. This way done by applying very low temperatures on the dried GO in a vacuum oven in order to increase the surface area of the obtained graphene. (Zhang *et al*. 2011) used very low temperatures (135 and 165) ^{o}C to obtained rGO with the assistance of a vacuum oven that helped to accelerate the expansion of graphene layers. The reduction was confirmed with the increase in the ratio of C: O. rGO was mixed with PMMA using solution blending and then the resultant nanocomposites were hot-pressed at 200 ^{o}C under a pressure of 10 MPa.

No DC electrical conductivity was obtained for PMMA/GO, but the conductivity was increased with the incorporation of rGO in the matrix and recorded at 0.3 $S.cm^{-1}$ for the nanocomposite blended with rGO obtained by applying at 1050 ^{o}C. The current study was based on the use of the PS as a host for the rGO. This polymer is the most inexpensive thermoplastic and it has a wide range of applications in the military, industry, construction, decoration and packaging because of its good mechanical properties, processability and water resistance (Qiu *et al*. 2015). The incorporation of rGO in PS provides a diverse array of applications such as photovoltaic devices, energy storage devices, liquid crystal devices, flexible displays and thin film transistors (Wu *et al*. 2012).

In the work described here, a relatively low temperatures were employed to obtain rGO using a vacuum oven. Three different temperatures (130, 165 and 200) ^{o}C were investigated with GO for periods of 24 h and different degrees of reduction were obtained. These temperatures were selected on the basis that there is a need to investigate the lowest temperatures that can be employed with GO to obtain rGO under the influence of a vacuum oven. Moreover, this approach can be considered as an ecologically friendly approach compared with the chemical approach. The structural, thermal and mechanical behaviour were then tested for GO, rGO and the nanocomposites obtained when GO and rGOs were incorporated in PS.

In the last couple of experimental chapters, the effect of processing conditions, dispersion techniques, and low loadings of GO on the properties of PS and its nanocomposites was studied.

This chapter tends to give a conception about obtaining graphene like material by employing an eco-friendly approach represented by applying low temperatures on GO using a vacuum oven. Then, the effect of GO and rGOs obtained by applying different temperatures on the performance of PS nanocomposites is investigated.

5.2. Experimental section

5.2.1. Materials

Explained in details in section 3.2.1. All the materials were used as they are according to the degree of purification mentioned in the label of each one. So, no further purification process was carried out for any material. DMF is the only solvent that was not used in this chapter.

5.2.2. Preparation of graphite oxide, GO, rGOs and nanocomposites of PS/GO and PS/rGO

5.2.2.1. Preparation of graphite oxide

Hummers' method was used to prepare graphite oxide according to (Marcano *et al*. 2010). 6 g of graphite was mixed with 3 g of $NaNO_3$ in a beaker. 138 ml of high concentrated H_2SO_4 (98%) was added to the beaker which was put in an ice bath to keep the reaction temperature below 35 °C. Then, 36 g of $KMNO_4$ was added gradually over 2 days. A magnetic stirrer was used to mix these chemicals at a speed of 200 rpm. A yellow brown viscous mixture was obtained. 10-15 ml of H_2O_2 was added to decrease the viscosity of the mixture. 400 ml of distilled water and 100 ml of HCL used for washing the graphite oxide.

The beaker was then left for 2 h of stirring of 800 rpm. The centrifugation process (Richmond scientific limited, UK and Eppendorf, Germany) were then used after adjustment to 8000 rpm for intervals of 1 h and the graphite oxide was washed with distilled water over a total time of 9 h till the pH of the solution reached 4~5 . In order to increase the value of pH, dialysis bags were used. These were Bio design dialysis tubing^{TM} (D014) manufactured by Fisher scientific. The length of each strip of these bags was 30.5 cm, the wet diameter was 21.3 mm, and the volume was 3.57 $ml.cm^{-1}$ as shown in Figure 5.1.

Graphite oxide was placed inside the dialysis bags which are totally immersed in a container of distilled water. A water pump was fitted inside the container to ensure a successful purification for graphite oxide. The distilled water in the container was changed every 72 h. After 144 h of washing using dialysis bags a pH of 6~7 for the graphite oxide was obtained.

Figure 5.1. shows the immersed dialysis bags in distilled water where the graphite oxide was placed. The pH of the solution was measured and the figure shows that pH of 6~7 was achieved.

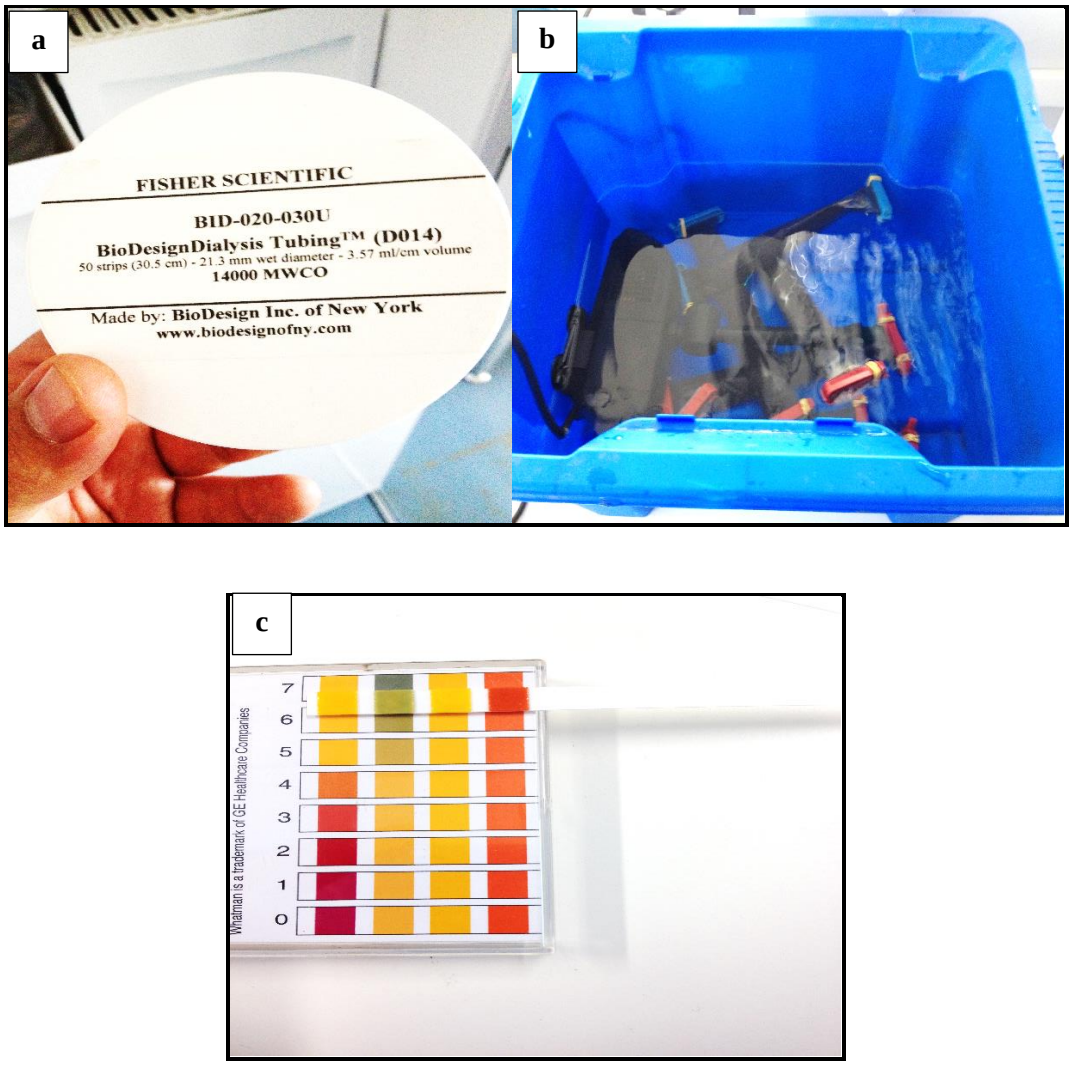

Figure 5.1. (a). : The specifications of the used dialysis bags, (b) The immersion of the dialysis bags in distilled water to purify the graphite oxide and increase its pH. (c). The obtained pH for the graphite oxide after 144 h of washing.

5.2.2.2. The preparation of GO

It was prepared according to (Ming *et al*. 2013). It was explained in details in section 3.2.2.2. and Figure 3.3 showed the GO powder.

5.2.2.3. The preparation of rGO

To obtain rGO, 0.2 g of this dry fluffy and powdered material was placed inside a vacuum oven at a temperature of 130 ^{o}C, and a pressure of -0.1 MPa for 24 h in order to produce TRGO. This procedure was repeated two more times with the same quantity of GO but at temperatures of (165 and 200) ^{o}C in order to produce different degrees of reduction.

The GO was put in a flask with a narrow neck and the spout was closed with a loosely tighten glass rod to permit the emitted gases associated with reduction process to be expelled and to prevent the fluffy particles of rGO from being volatilized in the atmosphere of the vacuum oven. After 24 h of exposing GO to the aforementioned temperatures, three samples which were named rGO130, rGO165 and rGO200 were obtained in the form of a dark black fluffy powder with an apparent volume expansion.

5.2.2.4. The preparation of PS, PS/GO, and PS/rGOs nanocomposites

The nanocomposite samples were prepared using THF as a co-solvent as the solution blending approach was used to prepare the polymer and the nanocomposites. 20 g of PS pellets were fully dissolved in 200 ml of THF using magnetic stirring for 2 h at 600 rpm. The clear solution of PS was then directly casted in a covered glass petri-dish with a radius of 135 mm to obtain a PS film. Another 20 g of PS pellets were fully dissolved in 200 ml of THF under the same aforementioned conditions and 0.2 g of GO and 0.2 g of each rGO were then suspended in 200 ml of THF. For providing a clear idea, the following Table 5.1. shows the quantities of PS, GO, rGOs and THF which were employed for preparing PS and its nanocomposites.

Table 5.1. : The quantities of PS, GO, rGOs, and THF that employed to prepare the polymer and the nanocomposites.

Sample	**Conc./wt.%**	**PS/g**	**THF / ml** ''For dissolving PS''	**GO and rGOs/ mg**	**THF/ ml** ''For obtaining GO suspension''
Neat PS	0	20	200	0	0
PS/GO	1.0	20	200	200	200
PS/rGO130	1.0	20	200	200	200
PS/rGO165	1.0	20	200	200	200
PS/rGO200	1.0	20	200	200	200

The suspensions of GO – rGOs /THF were stirred for 2 h at 600 rpm, and pre-sonicated for 30 min. GO/THF and rGOs/THF suspensions were mixed with PS/THF solution.

The weight fractions for GO and rGOs in PS was 1.0 wt. %, and all of the mixed solutions were stirred for 1.5 h.

The next step was 0.5 h of bath sonication using a water bath sonicator (Fisher Elma brand, Germany) followed by 1 h of shear mixing (Silverson, UK) at 1600 rpm /Amp 0.3. The obtained suspensions of PS/GO and PS/rGOs were then poured into covered glass Petri-dishes that have radius of 135 mm to ensure a homogeneous formation for polymer nanocomposite films with a uniform dispersion of nanoparticles in the matrix. All samples were then left in a fume cupboard for 1 week and then in a vacuum oven for 36 h and 50 °C to be fully dried.

5.2.3. Characterization

The characterization techniques are described separately below.

1. **Spectroscopic measurements**

a. FTIR

FTIR Spectrum 100 Perkin Elmer, USA was used for characterizing GO, rGOs, and PS with its nanocomposites. The setting of the machine was similar to what was mentioned in section 3.2.3. subsection 2.

b. Raman spectroscopy

GO and rGOs were characterized using Raman spectroscopy technique. The setting of the machine was similar to what was mentioned in section 4.2.3. subsection 2, item b.

2. **XRD**

To investigate the crystal structure of GO, rGOs, and PS with its nanocomposites D2 Phaser, X-ray diffraction analyser Bruker, was employed with Ni filter and Cu target. The setting of the machine was similar to that one mentioned in section 4.2.3. subsection 3.

3. XPS

X-ray photoelectron spectroscopy XPS was carried out using focused monochromatized

Al-Kά radiation (1486.6 eV) to confirm the presence of functional groups and to highlight the change in the atomic ratios of carbon to oxygen for graphite, GO and rGOs. The samples were all prepared for analysis by pushing a small amount of powder into soft indium foil. The indium foil had been previously adhered to a sample holder using double sided carbon tape.

The analyses were carried out using a Kratos Ultra instrument with the monochromated aluminium source, with one analysis point per sample. Survey scans were collected between 1200 to 0 eV binding energy, at 160 eV pass energy and 1.0 eV intervals. In addition, high-resolution C 1s, O 1s, and N 1s spectra were collected, as specified, over an appropriate energy range at 20 eV pass energy and 0.1 eV intervals. The analysis area was 700 µm by 300 µm. The data collected was calibrated in intensity using a transmission function characteristic of the instrument (determined using software from NPL) to make the values instrument independent. The data can then be quantified using theoretical Scofield relative sensitivity factors. The data was calibrated for binding energy by making the main carbon peak C 1s at 285.0, and correcting all data for each sample analysis accordingly.

4. SEM

GO, rGO, and the fracture surface for the neat polymer and PS/rGOs were characterised using SEM. Cryogenic fracture surfaces were obtained via snapping samples in liquid nitrogen. The neat polymer and the PS/rGOs 1.0 wt. % were immersed in a container of liquid nitrogen for 5 min. and snapped inside the container to obtain a clean fracture surface. GO and rGO (obtained by applying 130 ^{o}C for 24 h in a vacuum oven) powders were distributed over an aluminium in stub of high purity and it was taken to SEM imaging after making gold coating only. There was no need for coating GO and rGO powders by silver dag, gold coating was the only coating employed for these powdered samples. All the details regarding the model of the microscope,

the employed stubs, and the setting of the sputter coater were mentioned in section 3.2.3. subsection 1, item d.

5. Thermal and thermomechanical properties

a. TGA

TGA Pyris 1, Perkin Elmer, USA was used to study the thermal behaviour for GO, rGOs, and PS with its nanocomposites. The atmosphere of the test was N_2 and the heating rate was 10 °C.min^{-1}. The range of temperature that used for all the samples was from 28 to 600 °C. The weight of each sample inside the pan was 5 mg except the weight of graphite, GO and rGOs powders that was few milligrams. Several samples were tested and only representative samples were shown.

b. DSC

The neat polymer and the nanocomposites (PS/GO and PS/rGOs) were tested by DSC for finding Tg. The model of the machine, the adopted setting, and the circumstances of the test were similar to what was mentioned in section 4.2.3. subsection 4, item b. Several samples were tested and only representative samples were shown.

c. DMA

DMA was used to find the storage modulus for the neat polymer and nanocomposites. The model of the machine, the setting, the way of determining Tg from storage modulus curves, and the dimensions of samples were similar to what was mentioned in section 4.2.3. subsection 4, item c. Several samples were tested and only representative samples were shown.

6. Extensometer

Mechanical properties were calculated with the employment of the extensometer. The model of the machine, the setting, the specifications of the standard which was used to obtain the samples of the test, the model of the piston that was used to obtain the samples were similar to what was mentioned in section 3.2.3. subsection 4. The number of the tested samples was 2.

5.3. Results and discussion

5.3.1 Spectroscopic measurements

5.3.1.1. FTIR

The IR spectra for GO and rGOs are shown in figure 5.2. (a). For the GO peaks, the wide peak between (3000-3500) cm^{-1} is attributed to the presence of hydroxyl groups or the adsorbed bound water. The C=O carboxyl or carbonyl stretching vibration is observed at a wavenumber of 1723 cm^{-1}. The peak at 1387 cm^{-1} refers to the O-H deformations in the C-OH group. 1224 cm^{-1} represents C-OH stretching vibration. C-O stretching vibration in C-O-C in epoxide can be seen in the wavenumber of 1062 cm^{-1}. Arguments have been noticed so far regarding the peak at the wavenumber of 1621 $cm^{-1.}$ Some authors attributed this peak to the unoxidized graphitic domain. Whilst others consider that it is related to the oxygen containing groups such as ester absorbed H_2O (Wu *et al*. 2012).

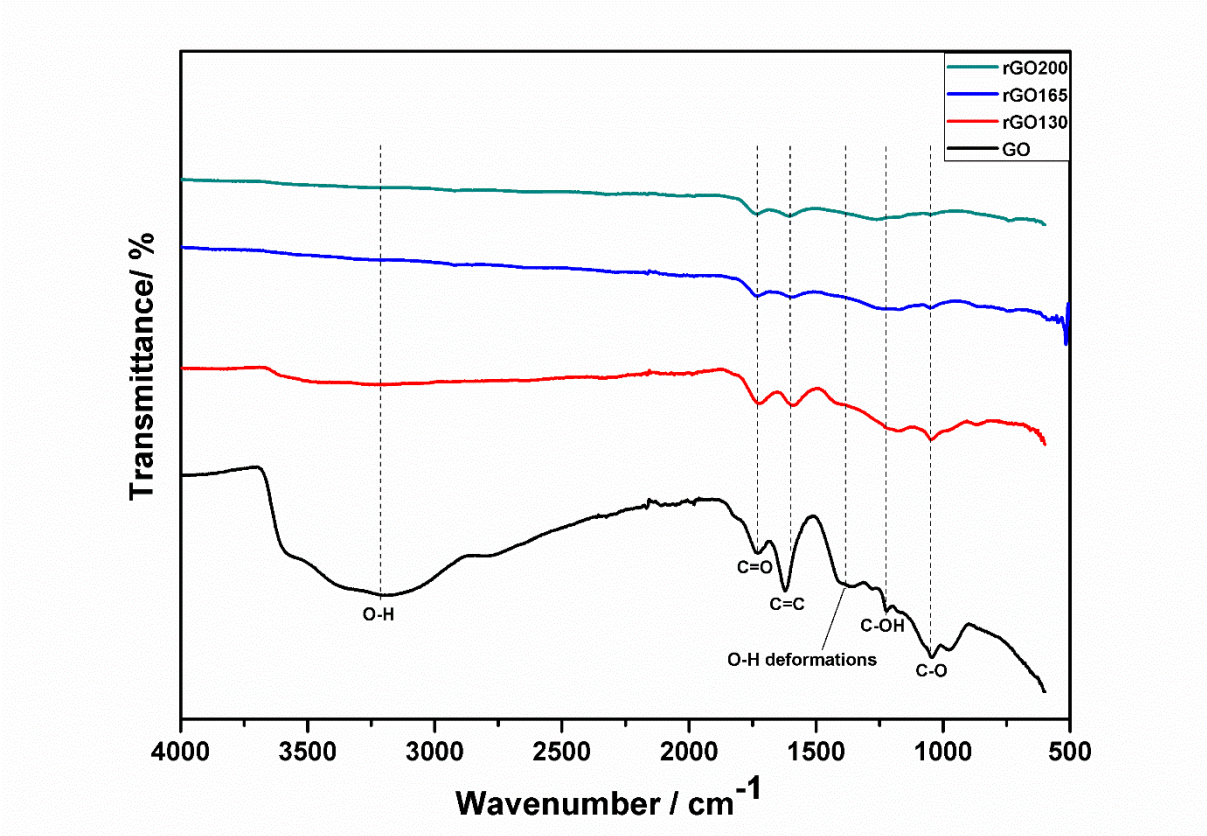

Figure 5.2.(a) : FTIR chart for GO and rGOs obtained in different temperatures in a vacuum oven. The dash lines refer to the reduction occurred to the majority of GO functional groups.

The aforementioned discussion confirms the presence and abundancy of oxygen functional groups in the periphery and basal plane of the GO nanosheets. (Xu *et al*. 2013) confirmed the presence of the oxygen functional groups of GO which concurs with the current study. The group found peaks of GO in the regions of O-H, C=O, C-O, and C-OH stretching vibrations.

A significant decrease in intensity of the GO peaks was observed after the thermal reduction due to the elimination of oxygen functional group. Hydroxyl groups are reduced at 130 ^{o}C and they totally disappeared for the rGOs at 165 and 200 ^{o}C respectively. Other peaks have also become weaker for GOs reduced in different temperatures compared with the peaks of GO thereby indicating a successful thermal reduction.

(Ju *et al*. 2010) supported their research regarding thermal reduction of GO with FTIR data that showed a clear removal of the majority of oxygen functional groups after exposing GO to 800 ^{o}C in N_2 atmosphere for 1 h and heating rate 5 ^{o}C.min^{-1}.

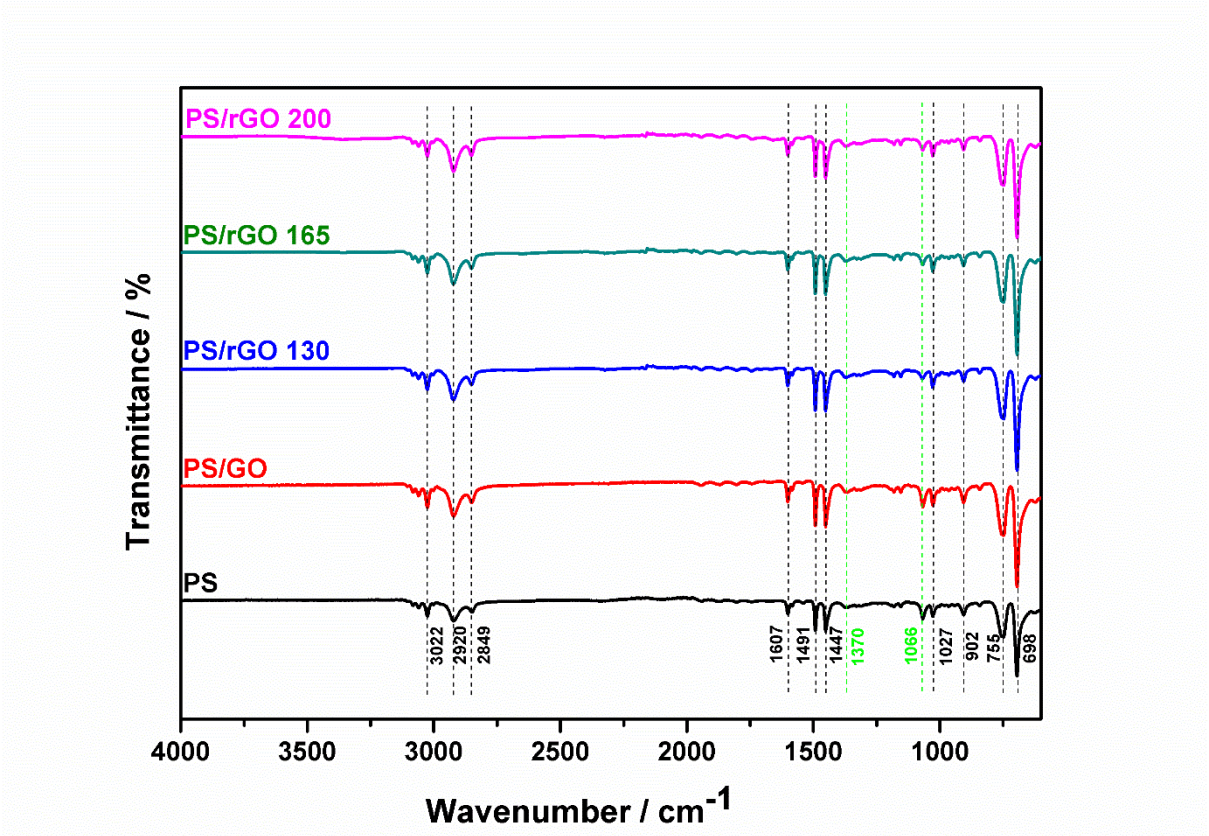

Figure 5.2. (b).: PS, PS/GO, and PS/rGOs. The black dash lines refer to the main peaks of PS. The green dash lines refer to the possible interaction between PS and GO/rGOs.

Figure 5.2. (b) shows the main IR peaks of PS, PS/GO and PS/rGOs. A series of peaks at 698 and 755 cm^{-1} that are related to C-H out of plane bending vibrations of the benzene ring, (902, 1027, 1447, 1491 and 1607) cm^{-1} are related to the stretching vibration of the benzene ring C=C, 2920 and 2849 cm^{-1} are associate with asymmetric and symmetric stretching vibrations of CH_2 respectively, 3022 cm^{-1} which is related to =C-H aromatic stretching vibration. All of the aforementioned IR peaks refer to the main peaks of benzene in PS and confirming the attachment of rGO planes to PS (Wu *et al*. 2012; Han *et al*. 2016). The majority of the PS peaks were confirmed by (Vukoje *et al*. 2014).

(Wan & Chen, 2012) considered the band of 1370 cm^{-1} which can be seen with a stronger intensity in nanocomposites as compared with neat PS is evidence of the presence of GO in the PS. This peak is related to –OH and it can be clearly seen in the current study for the spectra of PS/GO. (Hu *et al*. 2010) confirmed that the interaction between the PS and GO nanosheets occurred at 1392 cm^{-1} which is also related to the O-H deformations of the C-OH groups.

The same authors found that there is another strong band at 1060 cm^{-1} attributed to C-O stretching vibrations which could be evidence of interaction between PS and GO. Such a band can be found in the current study at about 1066 cm^{-1} for the PS/GO sample.

However, the intensity of this band is clearly attenuated for the samples of PS/rGOs. For PS/rGO, (Alsharaeh *et al*. 2014) found that there are many bands that refer to the Π-Π interaction between the matrix and rGOs. Amongst them is 1610 cm^{-1} which is corresponds to the C=C groups. In the current study, there is a slight shift within several wavenumbers about the latter band (1603~1607) cm^{-1}. This shifting is due to the interaction between the polymer and the nanosheets. The weakness or the overlap with the absorption peaks of PS are render the other peaks of rGO undetectable in the samples of PS/rGOs (Han *et al*. 2016). See appendix 4.

5.3.1.2. Raman spectroscopy

As an efficient tool to investigate the structure of graphene and its derivatives, Raman spectroscopy was used to characterize the structure of graphite, GO and rGOs as shown in Figure 5.3. D and G bands can be seen in all Raman spectra. D band is due to the breathing mode of k point phonons of A_{1g} symmetry.

On the other hand, G band represents first order scattering of the E_{2g} phonons. The defective disorders on the crystalline graphite and the quality of graphitization are important factors that can be evaluated by finding the ratio between I_D/I_G. The 2D peak can be seen at 2680 cm^{-1} (~ 2700 cm^{-1} in the current study).

It can be attributed to the double resonance transitions resulting in production of two phonons with opposite momentum. The number of graphene layer is the factor that determines the shift and shape of this peak (Eda & Chhowalla, 2010; Tang *et al*. 2012).

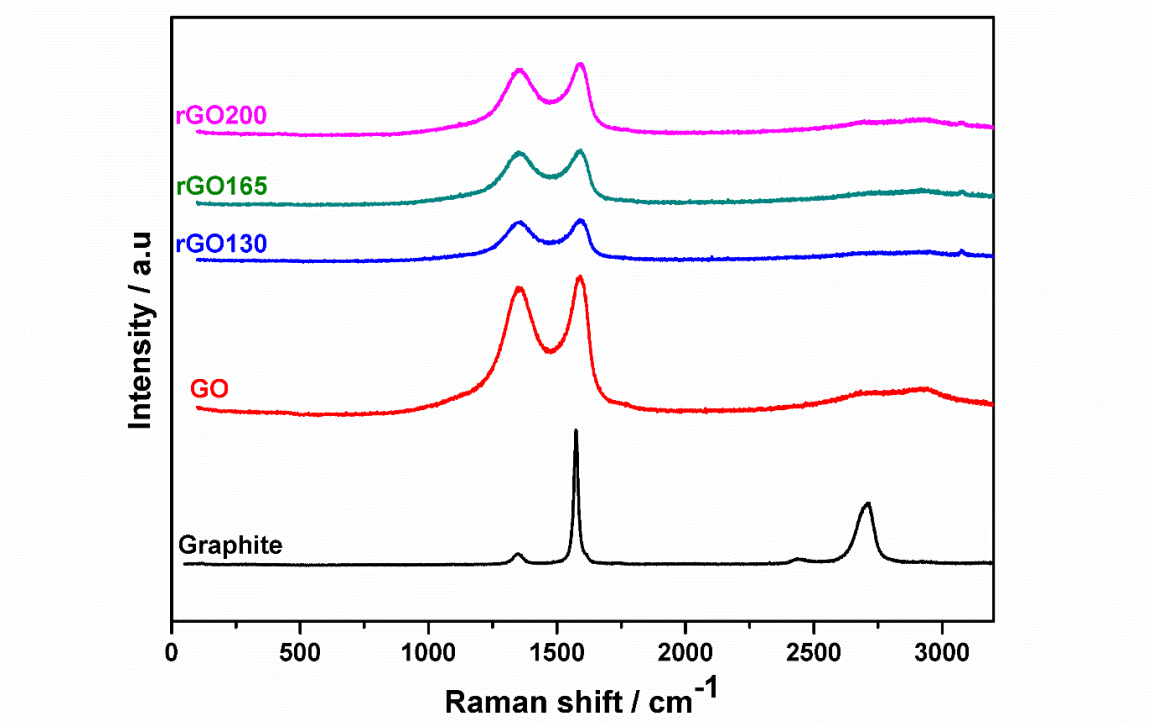

Figure 5.3. : The crystal structure shown by Raman spectroscopy for graphite, GO and rGOs.

The D band for graphite is 1350 cm^{-1} whilst the G band is acting at 1575 cm^{-1}. The positions of these peaks were confirmed by (Mohan *et al*. 2015) with a slightly higher shifting in the peak position of G band. The structure of graphene sheets have been drastically disordered according to the oxidization process.

The clear evidence about this is the increase of ratio of I_D/I_G for GO as compared with graphite (0.092-0.97). It has been emphasised that GO has two main peaks. The D band at around 1360 cm^{-1} (1357 cm^{-1} in this study) which can be attributed to disorder originating from defects. On the other hand, there is G band which is around 1593 cm^{-1} (1589 cm^{-1} in the current study) is correlated to C SP^2 in plane vibration (Li *et al*. 2013). (Chen *et al*. 2010) gave the same reasons about the positions of D and G bands peaks with two facts that are the peaks' positions for both bands for their GO (1355 cm^{-1} and 1602 cm^{-1} for D and G band respectively) were different with what has been previously mentioned about GO in this study and their GO showed a 2D peak which is cannot be seen in the current study.

The peaks of rGO are showing the following:

1- All the peaks have prominent D and G bands in specific positions.

2- It can be noticed that there is a slight difference in rGOs peaks' positions for D band as compared with GO whilst G band for all rGOs are keeping the same peaks' positions as compared to GO. D band peak can be found at 1353 cm^{-1} for all rGOs (1357 cm^{-1} for GO). This slightly lower shifting for D band peaks' positions can be related to the size of in plane SP^2 domain and formation of defects in the samples (Chen *et al*. 2010).

3- The calculations of the ratio between intensities of D and G bands showed that there is a slight increase for I_D/I_G for all of rGOs (0.99) as compared with that of GO (0.97). (Park et al. 2014) ascribed this tiny shifting to a higher value to generation of small graphitic domains after the reduction. (Chen *et al*. 2010) showed that I_D/I_G was increased from 0.95 for GO to 0.96 for rGO which confirms what was obtained in the current study.

(Stankovich *et al*. 2007) elucidated that these new graphitic domains are smaller in size as compared with those present in GO before reduction but the number of these domains is more numerous. This elucidation was associated with the confirmation of the lower shifting in D band peak position as compared to GO (1363-1352) cm^{-1} with regard that those authors were used the chemical approach for reducing GO.

A conclusion can be established from the aforementioned section of Raman spectroscopy is that thermal reduction of GO with the assistance of vacuum in a pressure lower than atmospheric pressure (-0.1 MPa) led to clear change in the structure which was noticed from the curves of rGOs.

Drastic changes in the obtained curves can be seen from the amorphization of graphite to the disordered GO to the rGO under the influence of different temperatures with the assistance of vacuum. Theoretical calculations showed that the maximum pressure that needed to overcome Van Der Waals forces that bind graphene nanosheets together is about 7.2 MPa.

To obtain the required exfoliation of GO nanosheets under the influence of very low pressure, the expansion force accompanied to the thermal decomposition of GO must be higher than Van Der Waals forces binding between nanosheets and higher than the atmospheric pressure. The vacuum is playing a major role as it made the exfoliation of GO easier.

The presence of vacuum means that it needed to overcome the Van Der Waals forces only. In addition, the presence of vacuum led to decrease the temperature required to obtain the GO exfoliation from 550 ^{o}C to 130 ^{o}C only in the current study and 135 ^{o}C in previous study. For all of the above, GO would be more unstable under vacuum (Zhang *et al*. 2011). See appendix 5.

5.3.2. XRD

As shown in the Figure 5.4. (a). , there is a sharp peak for pristine graphite at 2Ɵ = 26.3^{o}. This can be attributed to the highly regular crystalline pattern of graphite which is damaged by the oxidation process producing a wide peak of GO at 2Ɵ= 10.7^{o} (Chen *et al*. 2010). Simple mathematical calculations using Bragg's law showed that the interlayer spacing (d-spacing) was increased from 0.33 nm for pristine graphite to 0.82 nm for GO. This can be attributed to the oxygen functional groups that was produced in abundance following the oxidation process. The presence of these groups beside the water molecules intercalated between the layers led to the enlargement of the d-spacing between the GO nanosheets (Wu *et al*. 2012; Suresh *et al*. 2015). (Loryuenyong *et al*. 2013) confirmed in their co-work that the peak of pristine graphite was at 2Ɵ= 26.3 ^{o} and for GO was at 2Ɵ = 10.8 ^{o}. They also observed the shift of interlayer distance from 0.34nm for graphite to 0.82 nm for GO and this was also confirmed in this study. It is interesting to note that many peaks for rGOs appeared after reduction. The positions of these peaks appeared directly after the peak of GO were (12.3, 18.3 and 19.5) ^{o} referring to lower shifting of interlayer spacing of (0.73, 0.49 and 0.46) nm for rGOs (130, 165 and 200) ^{o}C respectively.

Table 5.2. Shows the new positions for the peaks of reduced form of GO obtained in different temperatures and the interlayer spacing.

Table 5.2.: The peaks' positions of reduced form of GO obtained by applying different temperatures with the interlayer spacing.

Temperature of reduction / ºC	**Peak position / º**	**Interlayer spacing / nm**
130	12.3	0.73
165	18.3	0.49
200	19.5	0.46

Some other broad peaks in various positions (e.g. at 29.5 º for rGO130 and at 42º for rGO200) can be seen for all the rGOs and all of them confirm the reduction. There are two main reasons for the variation of the d-spacing:

1- The oxidation of graphite leads to considerable increase in d-spacing for GO due to the functionalisation of the individual graphite's sheets surfaces that prevents the sheets from stacking or remain close to each other.
2- Applying reduction by adopting any approach (thermal, chemical, etc.) means the removal of many of the functional groups which are successfully generated by the oxidation process. As a result, the sheets will stack again or move closer to each other due to partially obstructed Π stacking.

As a result, rGO will have a quite similar structure to graphene with corresponding physical characteristics. It is important to note however that the mechanism of full reduction is not yet understood (Mohan *et al*. 2015; Kuila *et al*. 2013). Further support in the literature for the idea of reducing GO at very low temperatures is due to (Zhang *et al*. 2011) who obtained graphene at (135 and 145) ºC using a vacuum oven. Other reduction techniques than the thermal approach described here include:

a- Green reduction for GO using a specific kind of spice that called Cloves (buds of Syzygium Aromanticum) extracted by a reflux method at 100 ^{o}C for 30 minutes. Few layered of rGO were confirmed by TEM, UV- visible and XRD. This technique was adopted by (Suresh *et al*. 2015).

b- Chemical reduction for GO by hydrazine adopted by (Tripathi *et al*. 2013). The FTIR and XRD confirmed the reduction and then the reduced form of the GO was successfully incorporated in PMMA to investigate different properties.

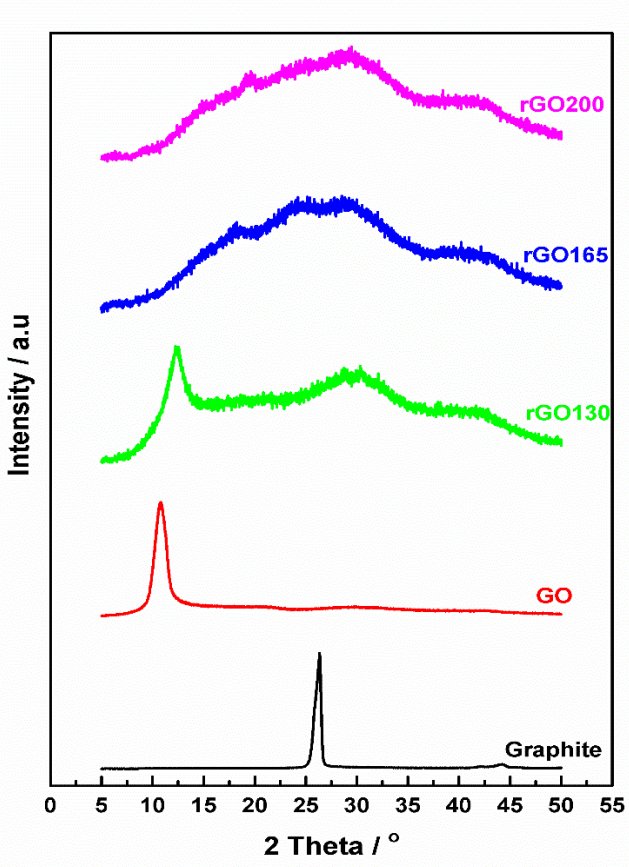

Figure 5.4. (a).: XRD for GO and rGOs reduced in different temperatures.

Figure 5.4.(b) discusses the effect of GO and rGOs obtained by different temperatures on the structure of PS.

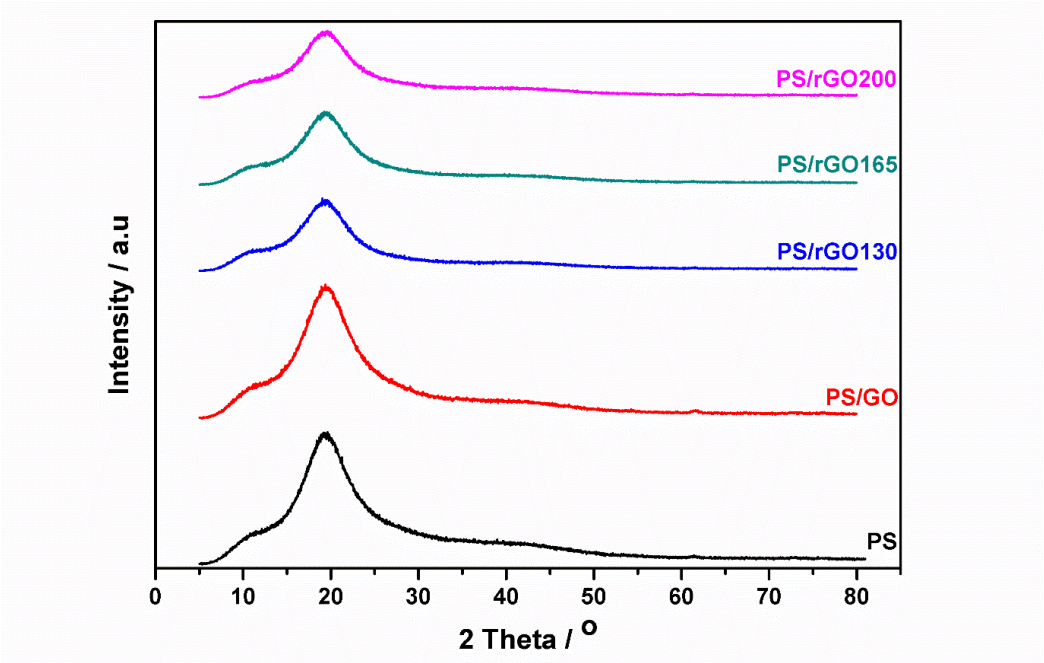

Figure 5.4. (b). : XRD patterns for PS and PS reinforced with rGOs obtained by different temperatures.

Two main peaks can be seen in the diffraction pattern of PS. The first one at around 10.5 ^{o} which is also known as '' the polymerization peak'' can be attributed to the size of the size group and the intermolecular backbone-backbone correlation. Another prominent peak of PS can be seen at 19.3^{o} which is related to the amorphous halo which is due to the Van Der Waals distance. A similar curve for (Han *et al*. 2013) was obtained with a slight difference in 2 theta position.

The peak of PS/GO structurally promoted with GO incorporation as the shown in the figure 5.4.B. The slight shift of the polymerization peak from 10.5^{o} to around 11^{o} confirmed this. (Qian *et al*. 2013) referred to the same effect of GO on the structure of neat PS where they observed the slight shift in the polymerization peak. Peaks of PS/rGOs are apparently broader than that of neat polymer and the PS/GO peak, and their intensities are weaker. The latter result is associated with the effect of rGO on the polymer that also affected the intensity and peaks width compared with the neat polymer. The results of PS/rGOs shown in Figure 5.4.(b) also confirm that the reinforcement was sufficient to overcome the dilution of the polymer and this affected the intensity of peaks providing clear evidence on the change in structure when rGO is incorporated into the polymer (Wu *et al*. 2012).

However, (Alsharaeh *et al*. 2014) confirmed the main peak of PS at 19.7^{o} , but they found another interesting peak at 43.5$^{o.}$ They attributed these peaks to the amorphous nature of PS and there is a consensus between other workers on this conclusion, but there are different opinions about the positions of these peaks.

5.3.3. XPS

Figure 5.5. (a). shows the survey scan obtained by XPS for the graphite, GO and rGOs and Table 5.3 shows the C/O ratio calculated from the element weight for the samples according to data taken from the XPS test. This technique was used as an efficient tool to characterize the surface chemical composition of the samples.

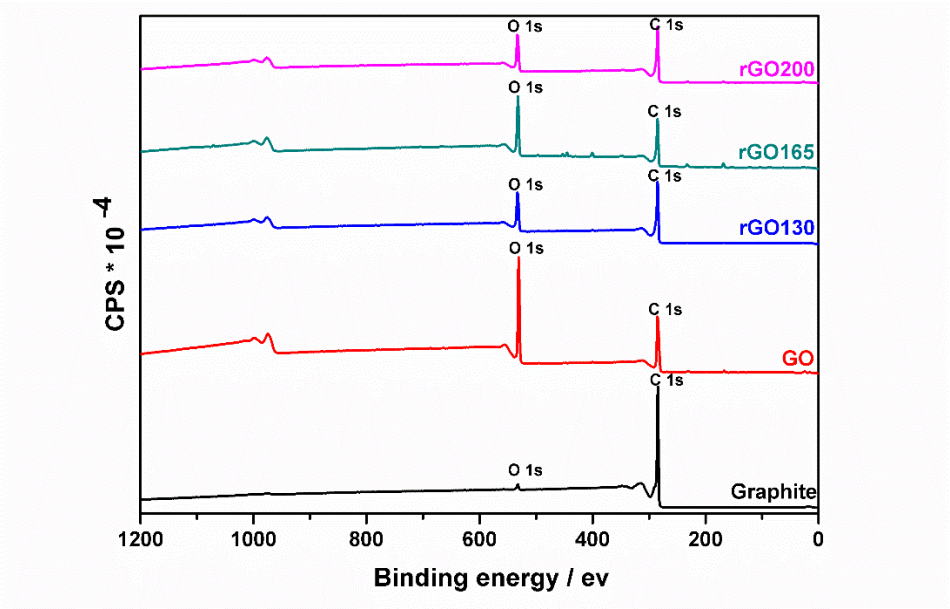

Figure 5.5(a) : Survey scan for pure graphite, GO and rGOs.

Table 5.3. : Element weight percentage of samples according to XPS test.

Sample	Graphite	GO	rGO 130	rGO 165	rGO 200
C %	98.39	65.88	81.39	67.10	80.90
O %	1.61	31.81	17.43	24.87	17.88
C / O	61.11	2.06	4.66	2.69	4.52

The survey scan spectra for pure graphite shows a tiny peak of O 1s which can be attributed to slight atmospheric oxidation.

The sharp peak of C 1s that can be seen for the bare graphite centred at 284.1 e.V. is due to the Π bond shake up satellite (shake up satellite are due to sudden change in Columbic potential as the photo ejected electron passes through the valence band) (Szabo *et al*. 2006). Confirmation on this result was provided by (Tang *et al*. 2014) where they referred to the small trace of O and rich C in quite similar positons. The C/O ratio was found to be 61.11 for the current sample which is close to C/O ratio for graphite used by (Wu *et al*. 2012) which was 64.79.

For the survey scan spectra of GO, it can be clearly seen that the O 1s peak is significantly sharpened and acquired a higher intensity with oxidation treatment. The oxidation process led to the formation of oxygenated functional groups on the surface such as hydroxyl, epoxide and carboxyl. As a result, the concentration of O was considerably increased (Yang *et al*. 2013). (T.K. *et al*. 2014) obtained the same results in the survey scan spectra for GO confirming the positions of C 1s and O 1s at 286 e.V and 531 e.V respectively (285.7 e.V and 531 e.V for the current study). The binding energies are obviously higher than for SP^2 bonded carbon shown in graphite which was 284.1 e.V in the current study.

From table 5.3. , it can be seen that C increased for increasing temperature to reduce the GO and O decreased for increasing temperature. This suggests a successful removal for the functional groups from the nanosheets surfaces (Han *et al*. 2016). The C/O ratio for all rGOs are higher than that ratio for GO which confirms a successful thermal reduction. The C/O ratio for GO in the current study was found to be 2.06. (Ma *et al*. 2012; Tang *et al*. 2014) found that the C/O ratio for GO was 2.6 and 2 respectively which is quite close to the results obtained in the current research.

For the GO reduced at 130 ^{o}C, the C/O ratio was 4.66 which agrees very well with the measurements by (Zhang *et al*. 2011) where they reported a C/O ratio of 5 using GO reduced by 135 ^{o}C in a vacuum oven for 24 h.

There are several reasons for the variation of the C/O ratio, and the intensities of O 1s under the conditions of reduction. (Zhang *et al*. 2011) justified the presence of a notable O 1s peak for GO reduced in 145 ^{o}C due to residual oxygen atoms on the graphene nanosheets.

The same reason was reported by (Tang *et al*. 2014) in CRGO and the O 1s peak was clearly observed. Another reason for the variation of the C/O atomic ratio is that arising from the different content of GO used in the protocol of reduction. The rGO might retain some oxygen functional groups on the surface and these groups will contribute to the chemical functionalisation when preparing the nanocomposites in the next stage.

(Xu *et al*. 2015) reported the aforementioned clarification noticed a clear difference of the C/O atomic ratio for GO reduced in different green reductants, and taking a similar approach here, the reduction was confirmed but with a variation in the C/O atomic ratio for all the reduced GOs. These findings were unexpected as compared to what has been mentioned in literature that was assured the increase in the atomic ratio of C/O as the temperature of reduction is going higher.

However, the common outcome achieved here represented by higher C/O ratio for all rGOs compared to GO can be seen in the co-work of (Zhang *et al*. 2011; Xu *et al*. 2013; Han *et al*. 2016).

In Figure 5.5. (b). , more details on the C 1_S spectra was obtained by referring to the functional groups in the raw materials, graphite and GO (A and B) and the reduced form of GO obtained by applying different temperatures (C,D and E). In addition, table 5.4.shows the binding energy and the relevant functional groups for graphite, GO and rGOs.

In chart A referring to graphite, the main peak of C=C or C-C related to SP^2 and SP^3 hybridized species are located at the binding energy of 284.6 e.V. Other small oxygenated functional groups with low intensity can be seen at the binding energies of 286.4 and 288.3 e.V.

These groups are assigned to C-O and O=C-OH respectively. (Krishnamoorthy *et al*. 2013) confirmed the peak of C-C stretching for pure graphite located at 284.5 e.V. The peak of carbonyl observed in the current work was confirmed by (Wu *et al*. 2012) at the binding energy of 286.4 e.V. The peak of the lowest intensity assigned to the O=C-OH functional group reported by (Wollbrink *et al*. 2017) with a binding energy of 288.1 e.V.

For GO, the peaks of oxygen functionalities become more intense and the low intensity of the carbon peak is worth noting. (Pei & Cheng, 2012) have suggested the main reason for the intense peaks of oxygen for GO is due to significant oxidation. GO was deconvoluted into three types of carbon atoms which were C-C or C=C located at 285 e.V, C-O or carbonyl located at binding energy of 287.08 e.V and C=O located at 288 e.V.

The same groups for GO were reported in the co-work of (Sheng *et al*. 2015) but with slight differences in the values of binding energies for each functional group. For the rGOs, it can be noticed that the main functional groups deconvoluted for GO were also present in rGOs but with different intensities and a slight different locations.

Table 5.4. shows the peak locations for rGOs with the assigned functional group for each one.

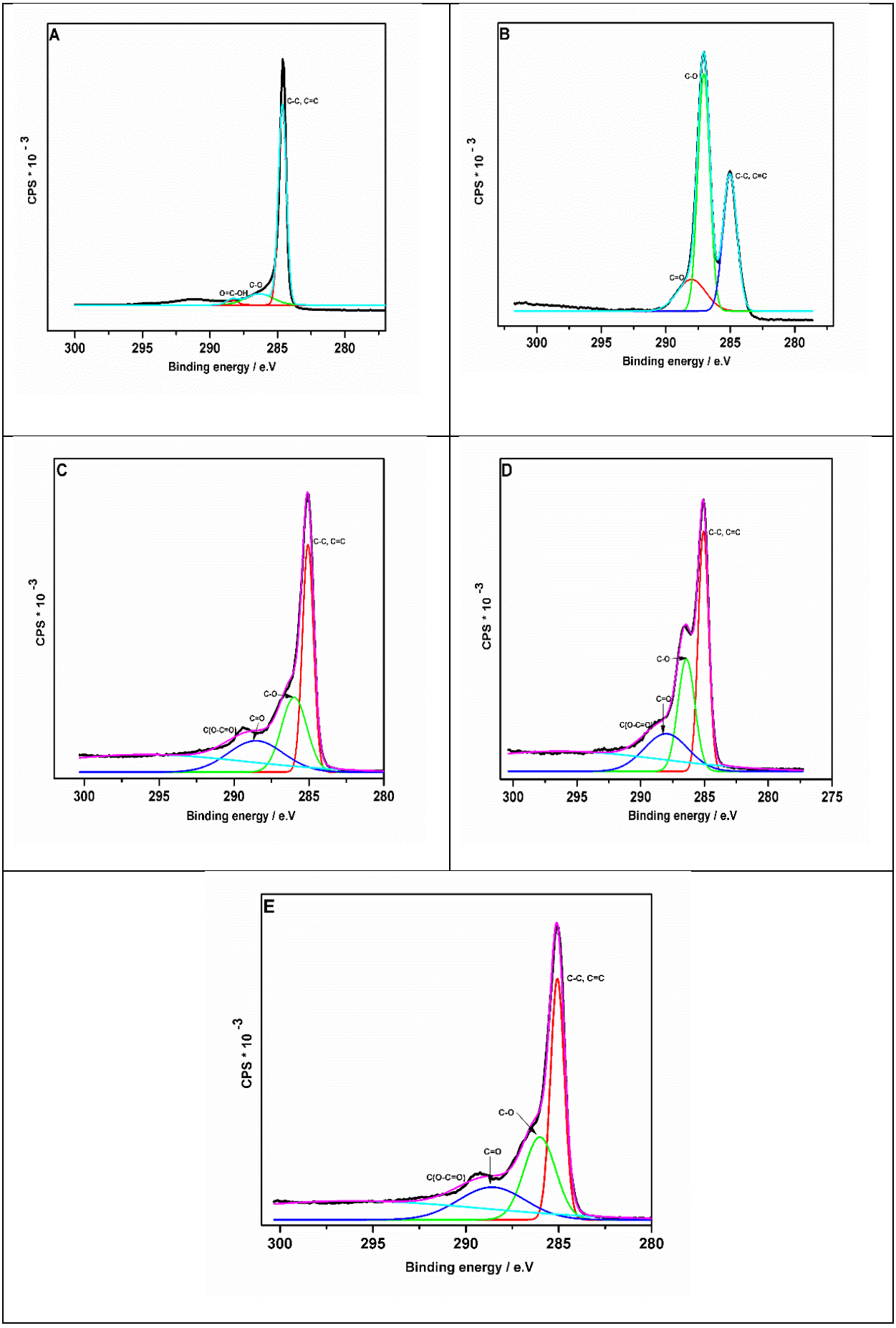

Figure 5.5. : XPS spectra for: A- Graphite. B- GO. C- rGO 130. D- rGO165 and E- rGO 200.

Table 5.4. : The oxygenated functional groups for rGOs with their binding energies obtained by XPS.

Sample	C-C, C=C(e.V)	C-O (e.V)	C=O (e.V)	COOH (e.V)
rGO 130	285	286.01	288.6	290
rGO 165	285.08	286.40	288.07	289.4
rGO 200	285.07	286.03	288.5	289.9

As shown in graphs C, D and E, all the rGOs had the same functional groups that appeared for GO, but the intensities of these groups are lower. This is attributed to the successful de-oxygenation using the vacuum assisted low temperature treatment.

An additional peak can be seen for the reduced GOs corresponding to the peak of the carboxylic group that appears at higher binding energies ~(289-290) e.V. (Tang *et al*. 2012) reported that the same main functional groups of GO appeared for the reduced form of their GO sample as reported here.

(Tang *et al*. 2012) work referred to a thermal reduction for GO, and they obtained a carboxylic functional group for the reduced form located at 289 e.V. which is the same binding energy for all the rGOs in this research, but with a slight difference in binding energies.

(Wu *et al*. 2012) also obtained the same functional groups for their GO reduced by hydrazine. (Xu *et al*. 2013) achieved the same result to that reported here when they used in- situ thermal reduction for GO in a PC matrix. The GO peaks indicated three main functional groups similar to that observed in the current study.

The rGO deconvoluted to four main functional groups of which three similar to GO but with lower intensities beside a carboxylic functional group located at 289.9 e.V, which is quite similar to all the rGOs obtained in this work.

5.3.4. SEM

Figure 5.6. shows SEM images for some of the samples in the current study. The top image refer to cryogenically fractured surface of PS (image a). The morphology of GO (image b) can be observed with an average size of 10 μm and is a highly exfoliated lamellae that has a folded layered structure with obvious wrinkles.

The appearance of wrinkles on the surface means that GO nanosheets are thin with a high flexibility (Sheng *et al*. 2015; Traina & Pegoretti, 2012; Yang *et al*. 2013).

(Liu *et al*. 2016) first confirmed the layered structured morphology, and the crumpled nature of GO nanosheets, but interestingly they estimated the thickness of the GO nanosheet at a few to tens of nanometres with a clear confirmation that the SEM is not accurately providing the information.

A 2D thin sheets is the structure of rGO130 (image c) and the sheets are crumpled and wrinkled due to Van Der Waals interactions between the graphene sheets. Following the reduction, the surface of rGO130 has become more corrugated compared with less wrinkled morphology of GO. The morphology of the rGO130 surface can be ascribed to the elimination of oxygen functional groups after the process of reduction (Saravanan *et al*. 2014; Tripathi *et al*. 2013; Mohan *et al*. 2015).

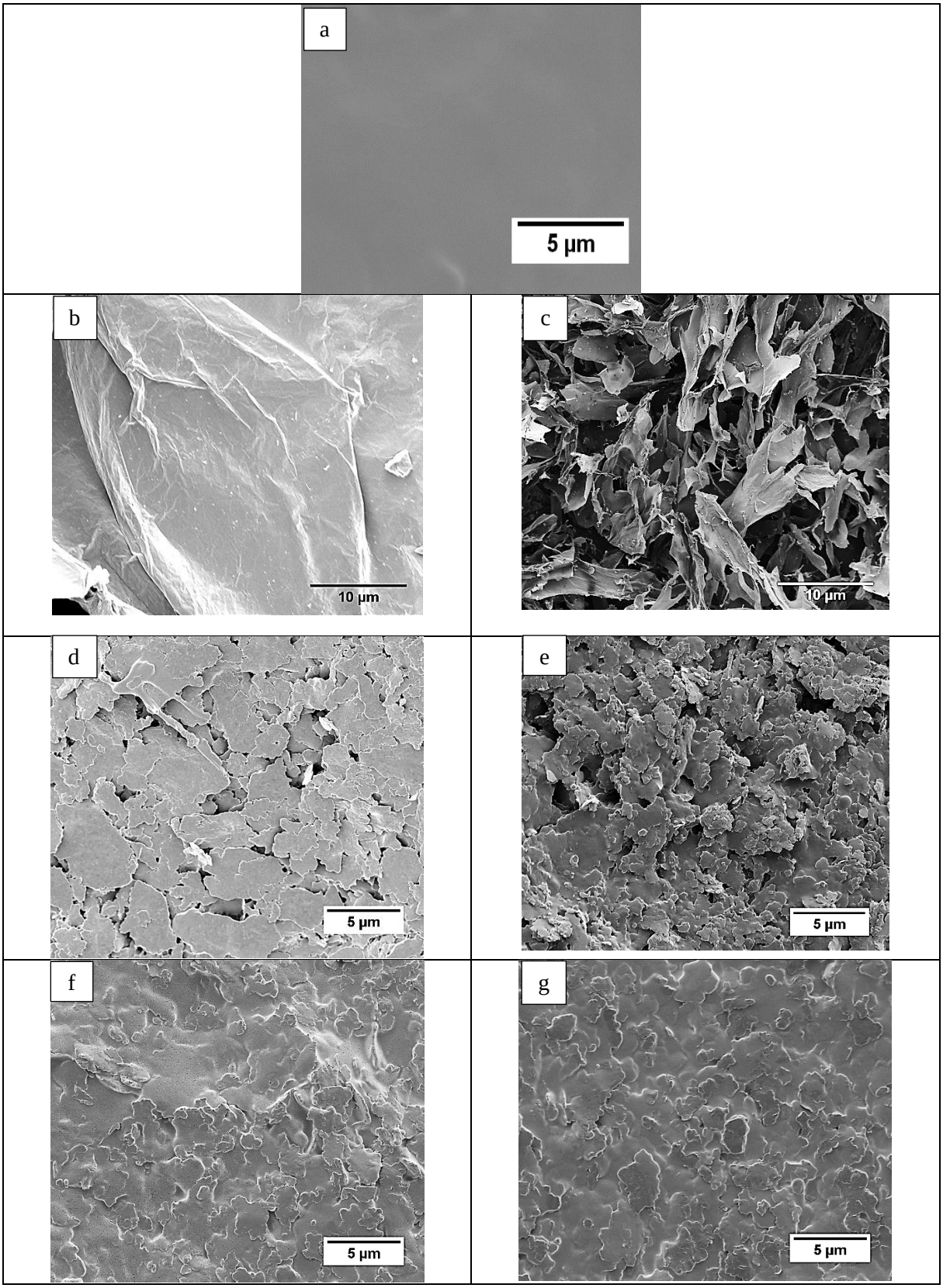

Figure 5.6. : SEM images of: a- Neat PS. b- GO nanosheet. c- rGO at 130 ºC. d-e-f-g are the cryogenically fractured surfaces of PS/GO 1.0 wt. %, PS/rGO130, PS/rGO165, and PS/rGO200 respectively.

(Xu *et al*. 2013) reported the crumpled and wrinkled morphology of rGO nanosheets in an investigation where GO was reduced thermally in a polycarbonate matrix by in situ thermal processing of the nanocomposite at 280 ^{o}C.

Neat PS (image a) appears to have no specific microstructure, and it shows a relatively smooth fracture surface. The smoothness of neat PS was confirmed by (Alsharaeh *et al*. 2014).

Generally, the comparison between the freeze fractured surface of the pristine polymer and the cryogenically fractured surfaces of PS reinforced with rGOs shows that the latter have rough surfaces compared with the smoother surface of the former. (Tang *et al*. 2012) using a thermal reduction process, reported the same surface roughness observation from SEM images of pure polyvinylidene fluoride PVDF compared with PVDF/rGO. It can be seen from figure 5.6.that the PS reinforced with GO (image d) shows GO nanosheets with micrometre size exfoliated into irregular flakes. The flakes are well dispersed in the matrix with some random restacks. Similar observations for the cryogenically fractured surface of PS/GO confirmed by (Han *et al*. 2013). The rGO130 nanosheets (image e) are tightly adhered to the PS, with some agglomerates in random positions.

The dispersion improved for the rGO165 (image f) as the agglomerates in the polymer had nearly disappeared. The best dispersion was obtained for the last sample of PS/rGO200 (image g) due to Π-Π interaction between the aromatic rings of the polymer and graphene sheets. The negative oxygen functionalities generated by thermal reduction, disturb the Π-Π interaction between the reduced nanosheets and PS. As a result, further increase in the reduction temperature leads to successful removal for the oxygen functionalities from GO which consequently led to a better dispersion of reduced nanosheets in the PS (Han *et al*. 2016). Similar results can be found in the co-work of (Han *et al*. 2013).

5.3.5. Thermal and thermomechanical properties

5.3.5.1. TGA

Figure 5.7.(a) shows the TGA curves for graphite, GO and rGOs that confirmed the thermal reduction.

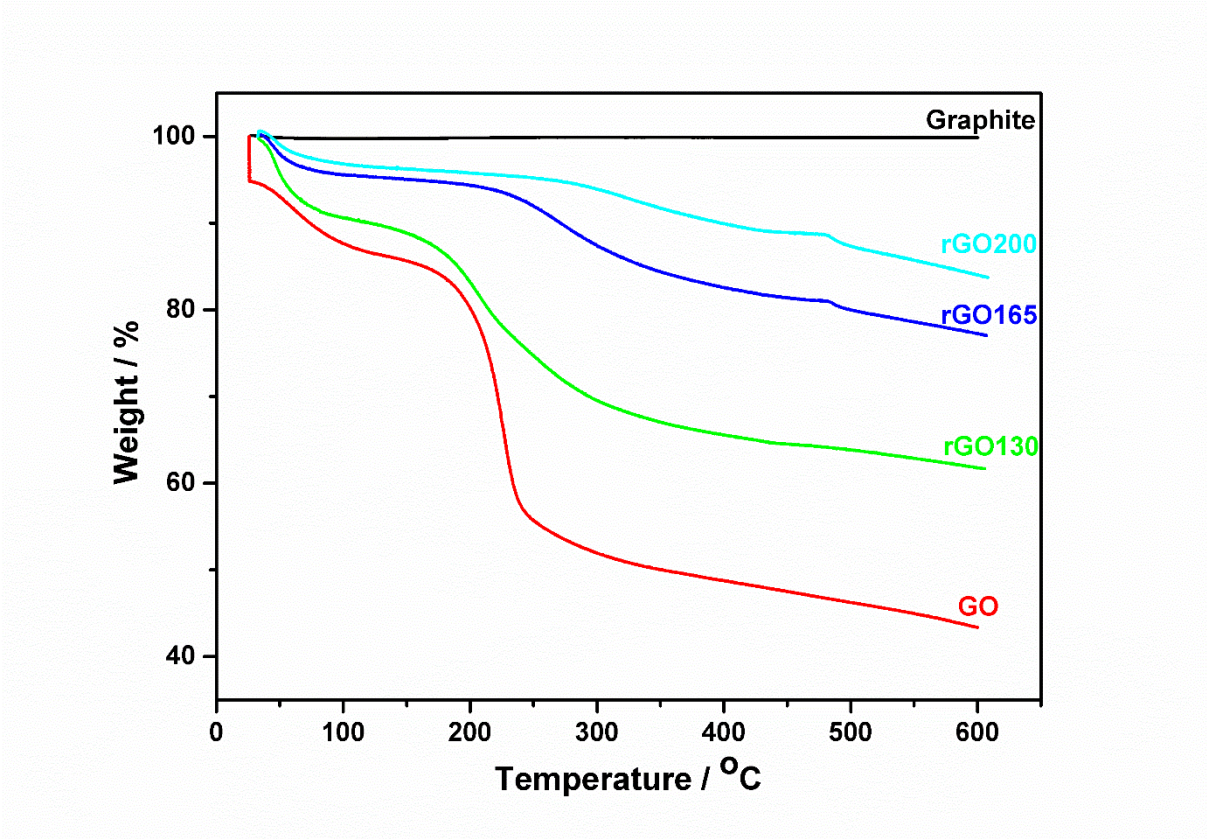

Figure 5.7.(a). : TGA curves for graphite, GO, and rGOs obtained by applying different temperatures.

Graphite has a high thermal stability up to 600 ºC (can show thermal stability up to 900 ºC) due to its highly graphitized structure so there will be no weight loss even at a high temperature (T.K. *et al*. 2014; Tang *et al*. 2014). This result was confirmed by (El-Khodary *et al*. 2014). By contrast, a significant weight loss is observed for GO between around 200-400 ºC. In fact, for the current sample, the weight loss commenced below 100ºC. The main reason for this is the pyrolysis of the unstable oxygen functional groups which are attached to the surface of the graphene nanosheets. This pyrolysis is accompanied by emission of gases such as CO, CO_2 and H_2O (Tang *et al*. 2014). This result was emphasized by (Lee *et al*. 2013).

GO continuously loses weight after 400°C up to 600°C. The remaining functional groups are stable, and require even higher temperatures to be totally removed (Xu *et al*. 2013).

Thermal stability is the main feature for other rGOs as shown in the curves of Figure 5.7(a). especially for the samples reduced at 165 and 200 ^{o}C, as the main functional groups are almost totally removed. In comparison, GO reduced at 130 ^{o}C still had weight loss as not all the oxygen functionalities were removed from the graphene surface. The residual contents for GO at around 600 ^{o}C is 43.5 %. On the other hand, the residual contents at around 600 ^{o}C were (59.3, 77 and 82.9) % for rGOs at (130, 165 and 200) ^{o}C respectively, which clearly means that the residual contents were going higher as the temperature employed for reduction went higher. This means that better thermal stability is obtained at higher temperatures. The other important observation is that reduction for GO was confirmed with the assistance of vacuum at these apparently low temperatures in agreement with earlier work by (Zhang *et al*. 2011). (Wu *et al*. 2014) obtained an obvious reduction when they used a microwave irritation of 950 W in parallel with a chemical agent to reduce pristine GO. Figures 5.7.(b). shows the TGA traces of PS, PS/GO, and PS/rGOs and T_d peaks obtained by DTG curves for these samples under the influence of N_2 and heating rate 10 ^{o}C.min^{-1}.

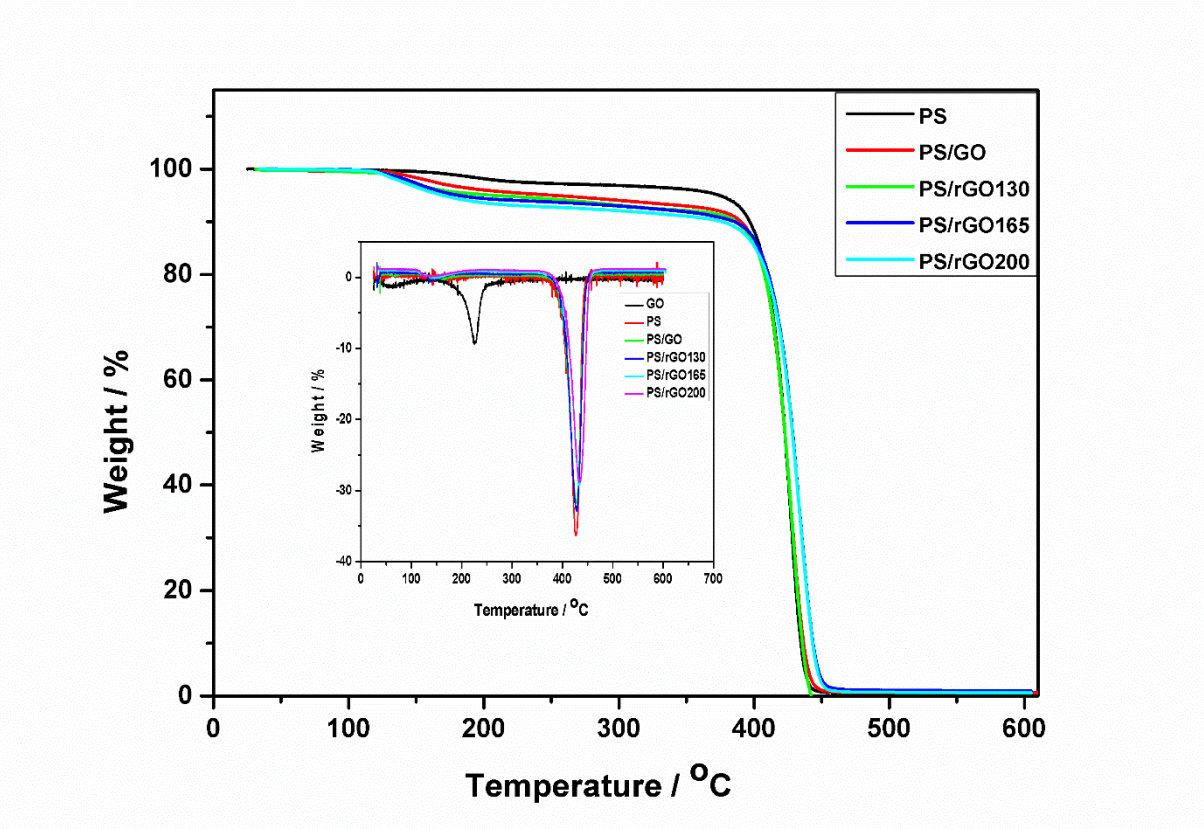

Figure 5.7. (b). : TGA traces for PS, PS/GO and PS/rGOs with DTG curves for GO and the other samples.

GO is thermally unstable and as mentioned earlier. It starts to lose weight below 100 ^{o}C. The T_d temperature for GO in the current study was measured at 224 ^{o}C. (Zhang *et al*. 2011) reported a T_d for GO at 260 ^{o}C, and they attributed this result to the pyrolysis of oxygen functional groups accompanied by the generation of gases.

(Wu *et al*. 2012), observed that the pristine PS is degraded thermally as a result of main chain pyrolysis. They observed that PS commenced to decompose at 350 ^{o}C, and it totally degraded at 430 ^{o}C. These results are quite similar to those obtained with the current sample of PS as the T_d temperature was 426.8 ^{o}C. However, the thermal stability was improved after the incorporation of GO in the neat PS, and it was more improved with the incorporation of rGOs in the matrix. The improved performance for the polymer with the incorporation of pristine and rGO can be ascribed to the homogenous dispersion of GO and rGO nanosheets in the matrix as well as the improvement of interfacial interaction between the nanosheets and the matrix. The barrier effect of the nanosheets, in both the pristine and reduced cases, played a crucial role in inhibiting the heat and diffusion of low molecular mass produced by thermal degradation (Qiu *et al*. 2015; Yang *et al*. 2013). (Alsharaeh *et al*. 2014) discussed the improvement in thermal performance for PS reinforced with RGO compared with the neat polymer. They attributed this to the aforementioned mechanisms as well as another reason which concerns the random alignment of the nanosheets in the matrix. Table 5.5. shows the T_d peak for all the aforementioned samples and gives an evidence on the improvement of the thermal performance with the incorporation of GO and rGOs in the neat polymer.

Table 5.5. : Thermal degradation temperature for GO, PS, PS/GO and PS/rGOs.

Sample	**T_d / ^{o}C**
GO	224
PS	426.8
PS/GO	427.4
PS/rGO 130	428.2
PS/rGO 165	433.3
PS/rGO 200	435.1

5.3.5.2. DSC

In Figure 5.8., glass transition temperature obtained by DSC can be shown for the polymer and the nanocomposites.

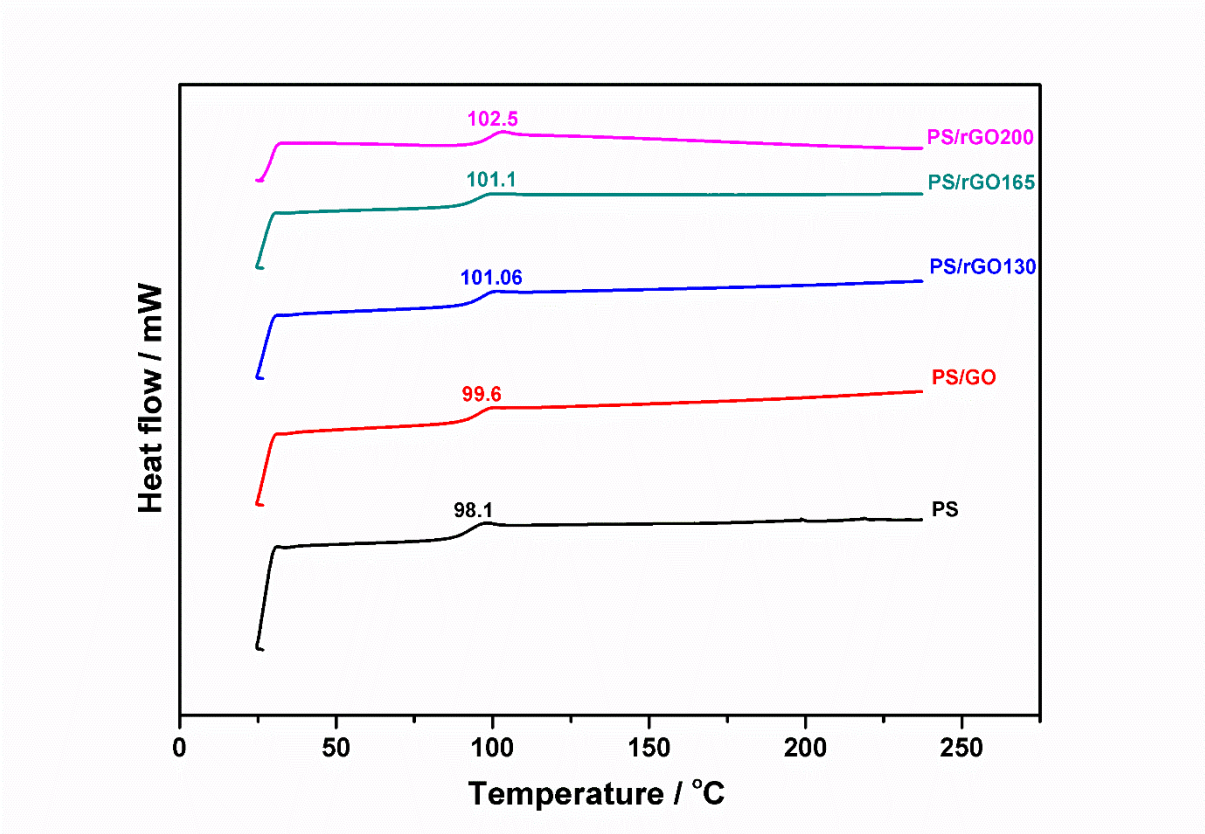

Figure 5.8. : DSC curves with T_g for the neat polymer and the nanocomposites.

The figure shows that T_g is higher for the nanocomposite of PS/GO compared with PS and more so for the PS reinforced with rGOs. There is a trend of higher T_g for a higher temperature of reduction. Similar observations were reported by (Han *et al*. 2016) and they attributed this increasing T_g trend to the significant effect of the rGO nanosheets on the motion of polymer chains. The presence of GO and rGO nanosheets played an important role in providing an obstruction to the segmental movement of the polymer chains which leads to an increase the value of T_g. This confirms the notion of a strong interfacial interaction between the polymer matrix and the nanosheets (Xu *et al*. 2013; Sheng *et al*. 2015; Alsharaeh *et al*. 2014). It is important to note in this study that the noticeable improvement in thermal and thermo-mechanical properties for PS reinforced with rGOs was due to the efficient reduction obtained by using the vacuum oven.

As the temperature of reduction increases, the GO nanosheets behave like a graphene material in which more and more functional groups have been removed from the basal plane and the periphery.

5.3.5.3. DMA

Figure 5.9.(a) shows the thermomechanical behavior for the neat polymer, PS with GO and PS reinforced with rGOs.

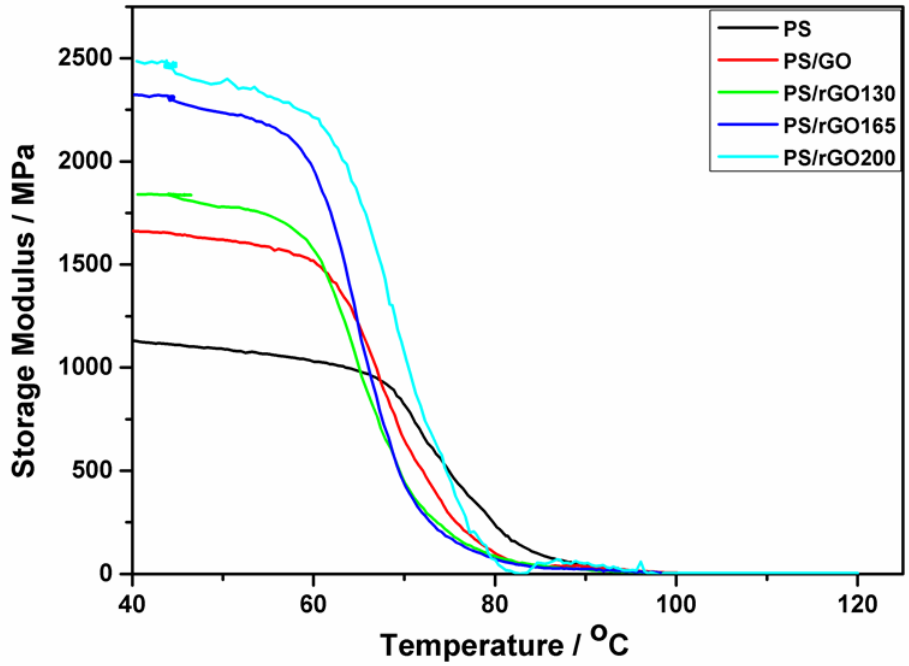

Figure 5.9.(a). : Dynamic mechanical behaviour for PS, PS/GO and PS/rGOs.

Storage modulus is the reaction of the elastic response upon the action of deformation. There is a significant increase in the values of this parameter for the nanocomposites that include GO and rGOs compared with the pristine polymer. The considerable increase in the values of storage modulus can be attributed to the homogenous dispersion of the GO in its pristine and reduced forms in the matrix which led to promote the interfacial interaction between the polymer and the nanosheets.

The outcome of this is a greater restriction to the segmental movement of the polymer chains that led to the enhancement of the thermomechanical performance of the nanocomposites (Han *et al*. 2016).

(Xu *et al*. 2013) provided this explanation for similar behaviour when they reinforced PC with different weight fractions of thermally reduced GO. In their work, the storage modulus exhibited a gradual increase with increasing weight fraction of rGO. This work described here concurs with these observations.

Table 5.6. lists the values of storage modulus for the neat polymer, and the samples of neat polymer with the embedded nanosheets of GO and rGOs.

Table 5.6. : Storage modulus for the polymer and other nanocomposites.

Sample	**Storage modulus at 30 ºC / GPa**
PS	1.12
PS/GO	1.66
PS/rGO 130	1.83
PS/rGO 165	2.32
PS/rGO 200	2.48

Figure 5.9. (b). shows the effect of reduction temperature on the thermomechanical properties (storage modulus). It can be concluded that as the reduction temperature increased, the storage modulus is also increased. The interpretation for this improvement was discussed previously in this section.

Figure 5.10. is giving a conclusion about the thermal behaviour of the neat polymer and the nanocomposites (PS reinforced with rGO) that reduced by applying different low temperatures with the assistance of vacuum. It can be clearly seen that as the temperature of reduction increased, the thermal behaviour (T_d and Tg) improved.

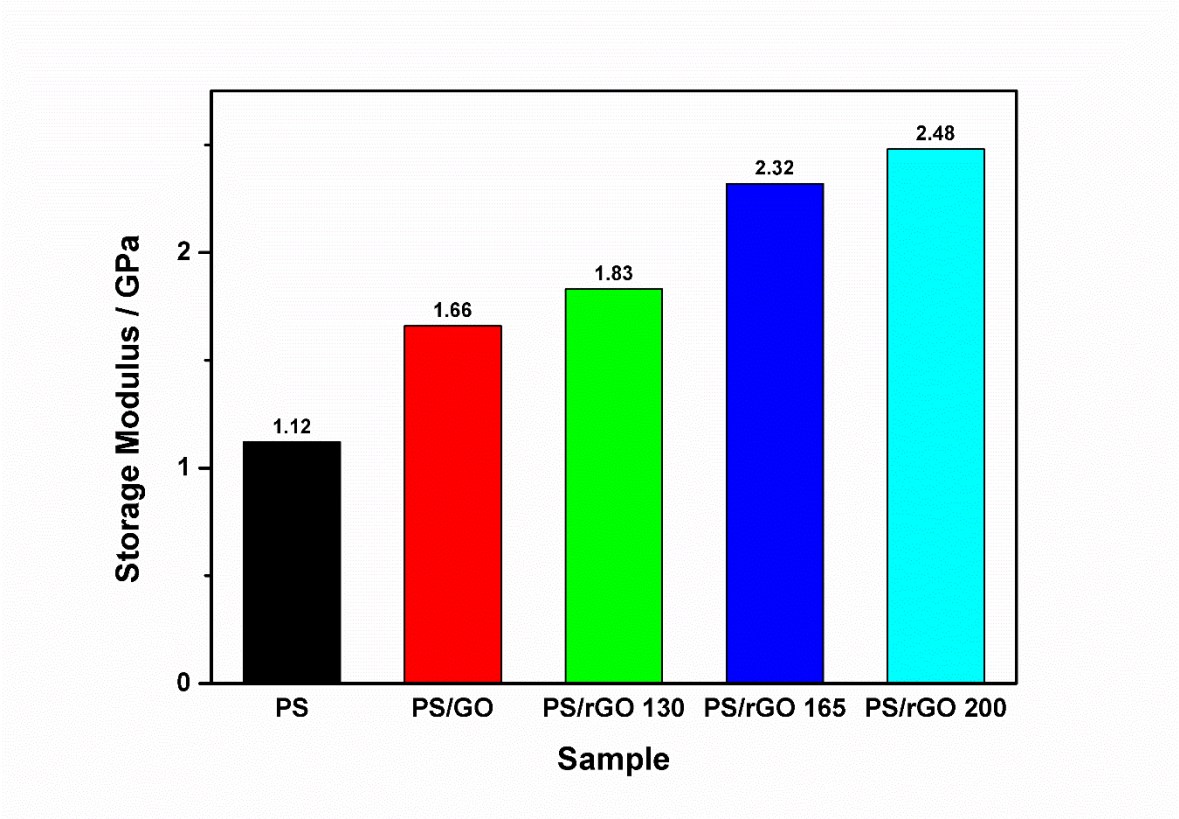

Figure 5.9(b): The improvement of storage modulus with the increase in temperature employed to reduce GO.

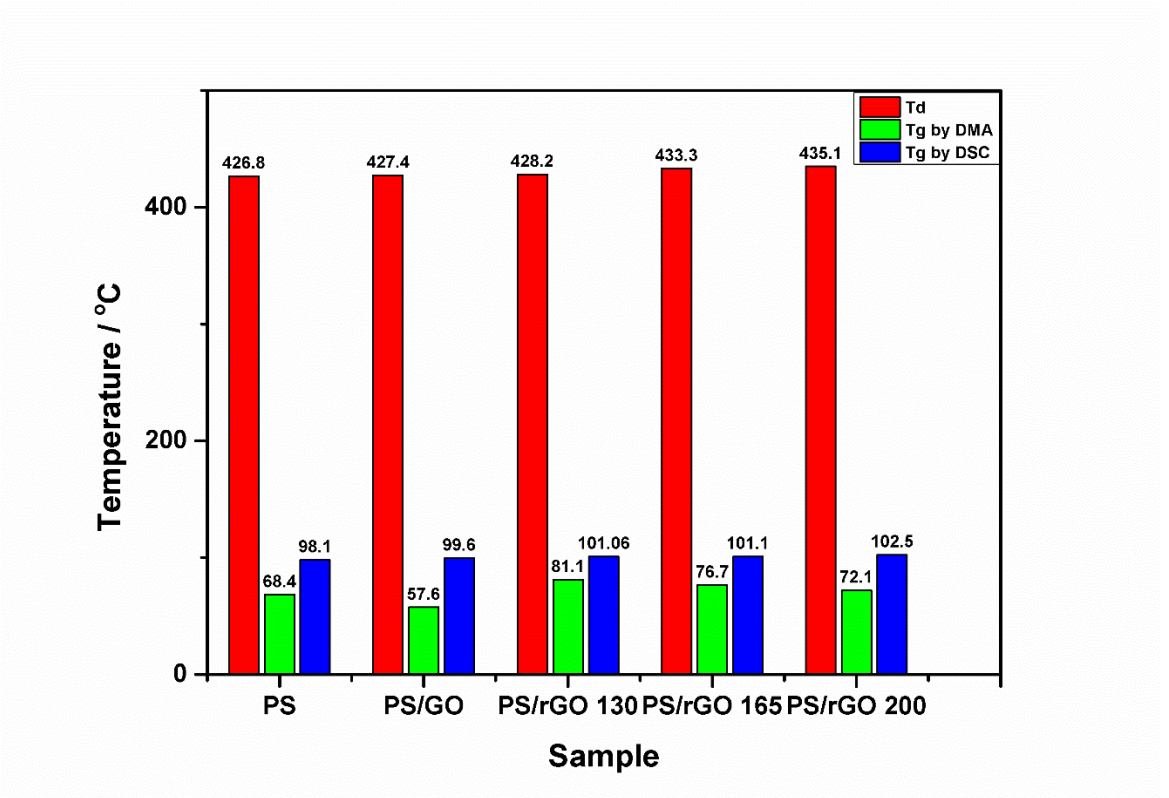

Figure 5.10. : Summary for the thermal behaviour of PS and its nanocomposites obtained by different temperatures which employed to obtain GO reduction.

5.3.6. Mechanical properties

In Figure 5.11., the curves show the static mechanical properties of neat polymer and other nanocomposites reinforced with GO and rGOs. Table 5.7. shows the details about these static properties.

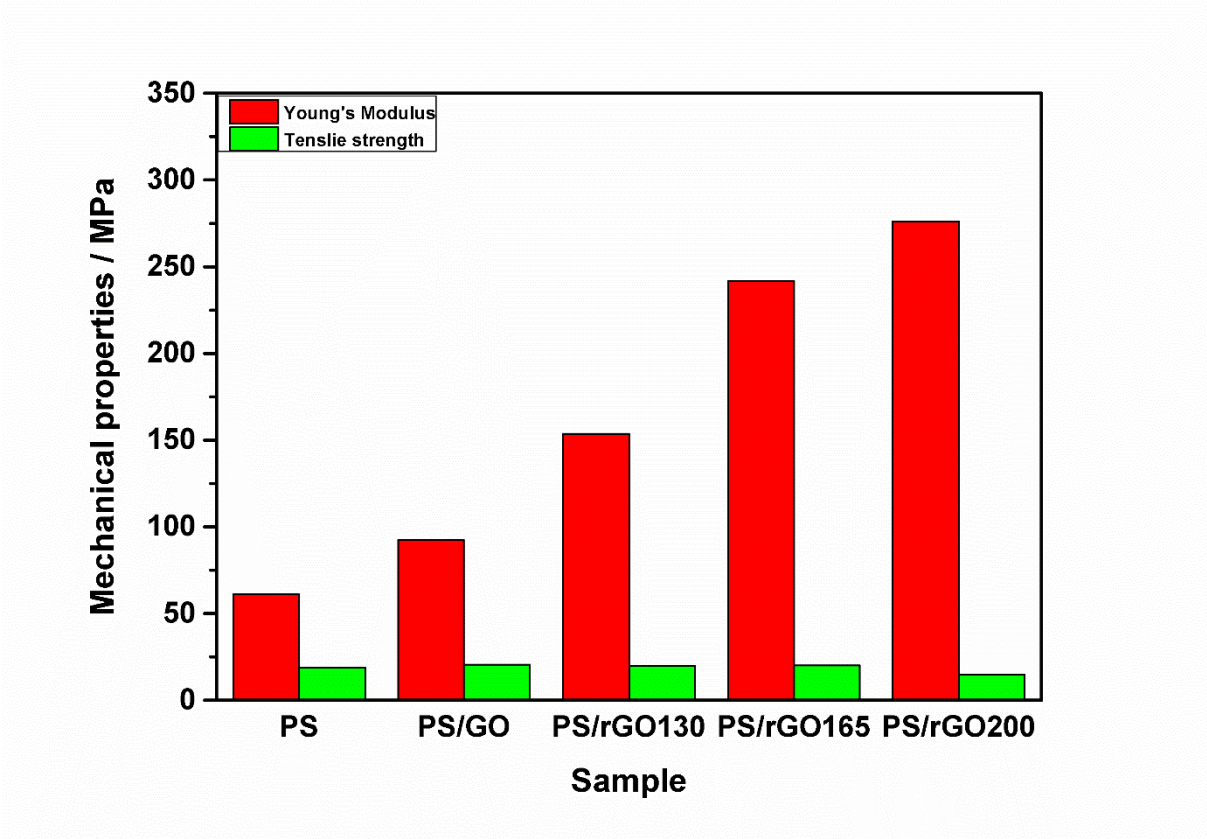

Figure 5.11. : Static mechanical properties of PS and nanocomposites. Data points per sample represent an average based on 2 repeats"

Table 5.7. : Static mechanical properties of PS, PS/GO and PS/rGOs.

Sample	E / MPa	T.S / MPa	Elongation at break / mm	Toughness / $MJ.m^{-3}$
PS	61.3 ± 41.5	18.9 ± 2.02	0.11 ± 0.028	0.69 ± 0.021
PS/GO	92.4 ± 7.0	20.5 ± 1.5	0.11 ± 0.001	0.77 ± 0.014
PS/rGO 130	153.7 ± 7.5	19.7 ± 0.8	0.13 ± 0.028	0.88 ± 0.140
PS/rGO 165	241.8 ± 54.7	20.2 ± 3.7	0.08 ± 0.012	0.69 ± 0.250
PS/rGO 200	276.2 ± 55.2	14.8 ± 1.79	0.09 ± 0.021	0.60 ± 0.160

The increase in tensile strength value for PS reinforced with GO is due to the efficient load transfer between the nanofillers and the matrix, as well as the homogenous dispersion of the nanofillers in the matrix. The improvement in mechanical properties can be attributed to the stronger interaction offered by the polymer chains in the surface of the GO nanosheets that consequently leads to better load transfer across the interphase.

On the other hand, the presence of defects and the size reduction of the GO nanosheets via the thermal approach led to a negative result regarding tensile strength. (Chen *et al*. 2011) reported that the lateral size for the rGO thin sheet obtained by mixing hydrobromic acid and GO suspension with refluxing the mixture of GO/HBr at 110 ºC for 24 h was between (150-250) nm. The value of tensile strength recorded for PS/rGO200 was the weakest compared with the remaining results which is in line with what has been reported by (Wang *et al*. 2016) when they showed that the lowest value of tensile strength was recorded for PS reinforced with rGO compared to those values of the same parameter recorded for the PS reinforced with functionalised graphene sheets and MWCNT.

(Goumri *et al*. 2017) have given the same reasons with regard to the mechanical improvement of PVA with the incorporation of low loading of GO, but the results were completely different regarding rGO incorporation into the same matrix. The mechanical performance was negatively affected with rGO incorporation, and the authors ascribed this behaviour to the better dispersion of GO in the polymer matrix compared with the poor dispersion of rGO nanosheets that were reduced chemically by hydrazine hydrate. These results are quite different to the observations in this study as the Young's modulus showed a significant increase for increasing of degree of reduction.

However, the improvement in the Young's modulus through reinforcing PS with rGOs means that the stiffness is increasingly improved for the nanocomposites, and this was confirmed by (Tripathi *et al*. 2013).

5.4. Conclusion

GO was reduced using vacuum assisted low temperatures under the influence of very low pressure. Solution blending was used to prepare the nanocomposites reinforced with GO and rGOs. The reduction was confirmed using several characterization techniques, and the effect of the rGO on the performance of nanocomposites was studied. From the perspective of potential applications with these materials, it was observed that the reduced form of GO improved the performance of the nanocomposites.

A graphene like material was obtained under the influence of vacuum, low temperatures and very low pressure which was a more ecologically friendly approach compared with techniques involving hazardous chemical reductants that generate highly reactive species with high toxicity.

The novelty of this chapter represented by obtaining graphene like material by employing very low reducing temperatures to reduce GO in vacuum oven. The temperature of 130 ^{o}C was amongst the lowest temperatures employed for obtaining rGO with the assistance of vacuum. Other temperatures (165 and 200) ^{o}C considered as very low temperatures as the thermal approach adopted by some authors focused on obtaining rGO by employing high temperatures (1000 ^{o}C and over). Successful reduction for GO was obtained for all the low temperatures employed in this study. Most importantly, the adopted approach (thermal reduction by using vacuum oven) classified as an ecologically – friendly approach that avoids the employment of any hazardous chemical reductants. This issue (the eco-friendly approach or the green approach) for reducing GO has recently become a priority for researchers and academic institutions.

Chapter 6

Properties of SAN /GO nanocomposites

6.1. Introduction

SAN is defined as one of the PS counterparts. It is an amorphous and transparent copolymer composed from acrylonitrile and a styrene monomer. The salient features of this polymer are dimensional stability, high strength, rigidity, high thermal stability and good chemical resistance. In addition, SAN has a resistance to chlorinated and aliphatic hydrocarbons, fats, various oils and household detergents. In its pristine state SAN is used in oil hoses and lining materials whilst capacitors, and electromagnetic interference EMI shielding are some of applications of SAN nanocomposites (Panwar *et al*. 2017; Singh *et al*. 2016; Vu *et al*. 2016). Section 2.2.5. provides information about SAN.

A range of low weight fractions of carbon nanotube CNT (0.1-3.0) wt. % were employed by (Wang *et al*. 2008) to reinforce SAN using an in situ polymerization approach to prepare the nanocomposites for testing its tribological properties. Results showed that highest wear resistance and lowest friction coefficient were achieved for SAN/CNT 1.0 wt. % and for a CNT content below than 1.0 wt. % micro-hardness was significantly improved.

Substantial improvement in heat resistance for possible fire proofing applications and an increase in Young's modulus by 20% was achieved by (Mainil *et al*. 2010) when they incorporated 3.0 wt. % of clay (montmorillonite) in a SAN matrix using a water assisted extrusion approach to fabricate the nanocomposite. (Vu *et al*. 2016) investigated the effect of reduced graphene oxide sulfonated by Sulfanilic acid, on the mechanical properties of SAN nanocomposites.

The team reported an increase in storage modulus of 46% when they incorporated 4.0 wt. % of SRGO in SAN. The literature shows that the researchers were trying to improve the thermal and mechanical performance of SAN by reinforcing it with different kinds of nanoscale reinforcements.

This is important to employ SAN in wide range of applications such as fire proofing, automotive, and so on. It is also important to find relevant materials to the PS with better properties. SAN is belonging to the PS family with better thermal and mechanical properties compared to PS. It will become much better with incorporation of the nanoscale reinforcement. The work described in this thesis is trying to investigate the performance of the SAN and SAN/GO nanocomposites and compare after then with the results obtained with PS and its nanocomposites. The effect of low weight fractions of GO on the structure and properties of SAN is investigated. The literature which can be found regarding this approach is quite limited.

6.2. Experimental section

6.2.1. Materials

The materials used in the investigations are described in Table 6.1.

Table 6.1. : Materials employed in the work with their characteristics, the manufacturer and the supplier.

Material	Characteristics	Manufacturer	Supplier
SAN (Tyril 790)	(70-80)% styrene. (20-30)% acrylonitrile AN. Odourless pellets, transparent with blue tint. Melting point ~ 250 ^{o}C, Mw: ~150000 g.mol^{-1}	Dow Chemicals, UK	Dow Chemicals, UK
Synthetic Graphite	Powder with grain size $\leq$ 20 μm	Sigma Aldrich, UK	Sigma Aldrich, UK
Potassium permanganate	Powder of 97% purity	Sigma Aldrich, UK	Sigma Aldrich, UK
Sodium nitrate	Powder of > 99% purity	Sigma Aldrich, UK	Sigma Aldrich, UK
Sulphuric acid	Solution of (95-98)% purity	Sigma Aldrich, UK	Sigma Aldrich, UK
Hydrochloric acid	Solution of 36.5% purity in water	Sigma Aldrich, UK	Sigma Aldrich, UK
Hydrogen Peroxide	Solution of (29-32) % purity in water	Sigma Aldrich, UK	Sigma Aldrich, UK
THF	Organic solvent of >99.5 % purity	Sigma Aldrich, UK	Sigma Aldrich, UK

All the materials listed in table 6.1. were used in the supplied purification without any additional processing.

6.2.2. Preparation of graphite oxide, GO and SAN/GO nanocomposites

6.2.2.1. Preparation of graphite oxide

Graphite oxide was prepared using Hummers' method according to (Marcano *et al*. 2010) . The full details about the preparation of graphite oxide was mentioned in section 5.2.2.1. and Figure 5.1. showed the dialysis bags and the obtained pH for the graphite oxide.

6.2.2.2. Preparation of GO

GO was prepared according to (Ming *et al*. 2013). It was explained in details in section 3.2.2.2. and Figure 3.3. showed the GO powder.

6.2.2.3. Preparation of nanocomposites

The nanocomposites samples were prepared using THF. 10 g of SAN pellets were dissolved in 100 ml of THF using magnetic stirring for 2 h at 300 rpm. 200 mg of GO were then suspended in 200 ml of THF. The suspension was stirred for 2 h at 250 rpm and pre-sonicated for 30 min. The GO/THF suspension was then mixed with SAN/THF solution for 3 h at 200 rpm. This was repeated for different weight fractions of GO (0.1, 0.25, 0.5 and 1.0) wt. % beside the neat polymer. The mixed solution was stirred for 1:5 h. Finally, the mixture was placed in a water bath sonicator for 0.5 h and 1 h of shear mixing (Silverson, UK) at 1600 rpm /Amp 0.3.

The suspension of SAN/GO obtained was poured in glass covered Petri-dishes that have a radius of 135 mm to ensure a slow evaporation for the solvent. All the samples were left in a fume cupboard for 2 weeks, and then placed in a vacuum oven for 24 h hours at 50 °C to be fully dried. Table 6.2. shows the quantities of SAN, GO and THF that employed to dissolve the polymer granules and to obtain a GO suspension. Arrows are used in the table to clarify this.

Table 6.2. : The quantities of SAN, GO and THF employed for preparing the neat SAN and its nanocomposites.

Sample	Conc./wt.%	SAN /g	THF/ ml	GO/ mg	THF/ ml
Neat SAN	0	10	100	0	0
SAN/GO	0.1	10	100	10	10
SAN/GO	0.25	10	100	25	25
SAN/GO	0.5	10	100	50	50
SAN/GO	1.0	10	100	100	100

6.2.3. Characterization

The characterization techniques are described separately below.

1. FTIR

FTIR was used for characterizing GO, SAN, and its nanocomposites. The model of the machine and its setting were similar to what was mentioned in section 3.2.3. subsection 2.

2. XRD

To investigate the crystal structure of GO, SAN, and its nanocomposites XRD was employed. The model of the machine and its setting were similar to what was mentioned in section 4.2.3. subsection 3 apart of the scanning range (2 theta) which was from 5^{o} to 80^{o}.

3. SEM

SEM was used to characterize the cryogenically fractured surfaces for the neat polymer and the nanocomposite of SAN/GO 1.0 wt. %. The model of the microscope, the specifications of the used stubs, and the setting of the sputter coater was similar to what was mentioned in section 3.2.3. subsection 1, item d.

4. Thermal and thermomechanical measurements

a- TGA

TGA was used to study the thermal behaviour for GO, SAN, and its nanocomposites. The model of the machine and its setting were similar to what was mentioned in section 4.2.3. subsection 4, item a. Several samples were selected and only representative samples were shown.

b- DSC

DSC was used to determine Tg for the neat polymer and its nanocomposites. The model of the machine, the setting, and the weight of samples were similar to what was mentioned in section 4.2.3. subsection 4, item b. Several samples were tested and only representative samples were shown.

c- DMA

DMA was used to find the storage modulus for the neat polymer and nanocomposites. The range of temperature was 30 – 130 °C. The model of the machine, its setting, the way of determining Tg from storage modulus curves, and the dimensions of the samples were similar to what was mentioned in section 4.2.3. subsection 4, item c. Several samples were tested and only representative samples were shown.

5. Extensometer

The mechanical properties were measured using the extensometer The model of the machine, the setting, the specifications of the standard that was used to cut the samples from films, and the model of the piston which was used to apply load for cutting the samples were similar to what was mentioned in section 3.2.3. subsection 4. The number of samples was 2.

6.3. Results and discussion

6.3.1. FTIR

Figure 6.1. shows the spectra of GO, SAN and nanocomposites. The GO spectrum shows a broadband peak of a hydroxyl group centred at about 3300 cm^{-1}. C=O represented by the stretching vibration is centred at 1730 cm^{-1}. Moreover, the in plane stretching vibration of C=C can be seen at around 1625 cm^{-1} which is attributed to the skeletal vibration of unoxidized graphitic domains. The C-O group can be seen centred at 1040 cm^{-1}. All of the above oxygenated functional groups that are present in the GO nanosheets confirm the successful oxidation of graphite (Heo *et al*. 2012; Liu *et al*. 2016; Pawar *et al*. 2016).

(Qiu *et al*. 2015) confirmed the presence of O-H, C=O and C-C in a GO nanosheet with the addition of a wide peak centred at 1345 cm^{-1} attributed to an O-H deformation vibration. This peak can also be seen in the current study.

For pure SAN, the monosubstituted benzene peaks can be seen at 700 and 750 cm^{-1}. The aromatic C=C group is presented in a range of peaks at 1450, 1500 and 1600 cm^{-1}.

The –C≡N stretching which is related to the nitrile group AN was observed at 2240 cm^{-1} and the aromatic C-H is located at 2924 cm^{-1}. The latter can be found within a range of vibrations from 2900-3200 cm^{-1}. These peaks were confirmed by (Wang *et al*. 2005). They also confirmed an interaction between the clay nanoparticles and pure SAN in many regions and one of these was centred around 1100 cm^{-1}. It is thought that a possible interaction between SAN and GO may have occurred at the same vibration in this study. This outcome is contrary to the findings of (Panwar & Mehra, 2008). These authors incorporated 2.0 wt. % of graphite sheets in SAN, and the spectra of the nanocomposite was similar to the neat polymer but with an attenuated intensity due to the incorporation of graphite sheets. The same outcome was seen in the nanocomposites' samples in this study but with addition that the intensity was remain without change according to very low weight fractions incorporated in this study. The majority of SAN peaks found in the current sample were confirmed by (Jang & Wilkie, 2005). See appendix 4.

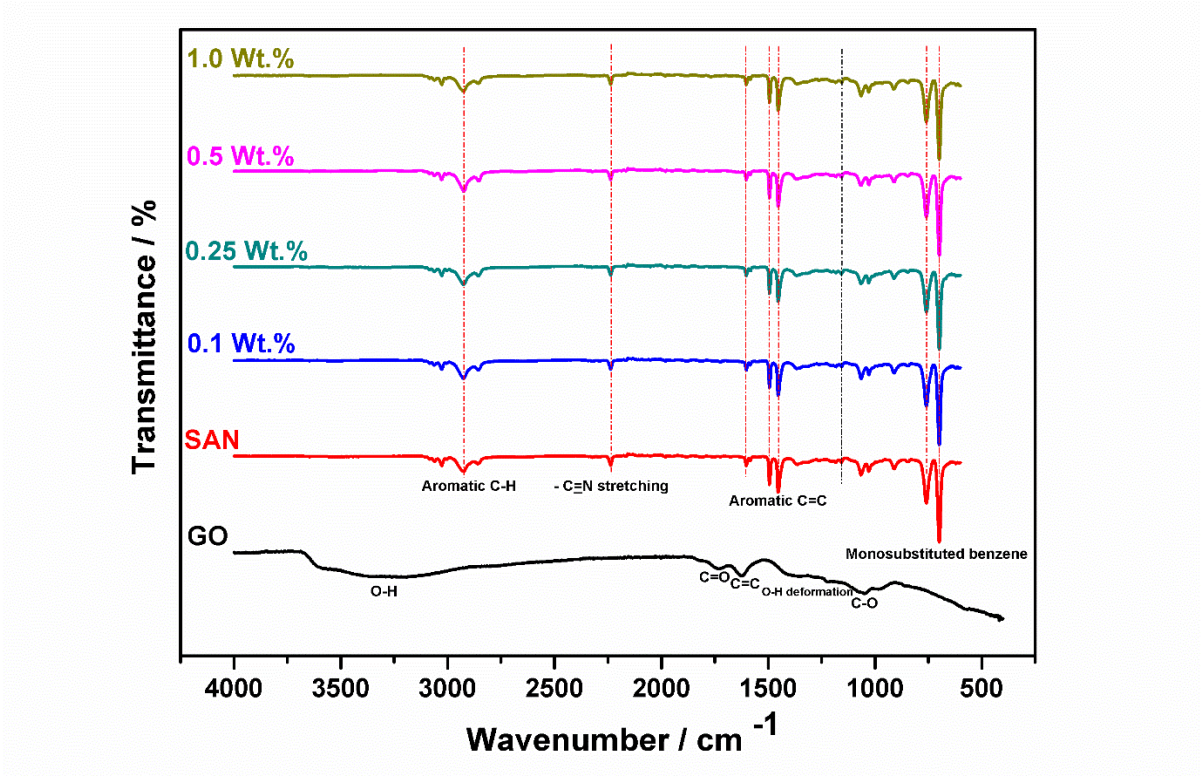

Figure 6.1. : FTIR spectra of GO, pure SAN and SAN/GO nanocomposites. The red dashed lines are related to the main groups of SAN. The black dashed line represents the region of possible interaction between SAN and GO.

6.3.2. XRD

In Figure 6.2, the XRD patterns for GO, SAN and its nanocomposites are presented. The main peak for GO can be seen at 10.7^{o} and the interlayer spacing is 0.82 nm. (Malas & Das, 2015) reported a quite similar result for their GO sample where they found located peak at 10.72^{o} with an interlayer spacing of 0.81 nm. For SAN and nanocomposites, the diffraction peak of SAN was located at 2Ɵ= 3.47^{o} which means that the interlayer spacing for the amorphous polymer is 2.56 nm.

A quite similar result was reported by (Zhang *et al*. 2006) where they measured 2Ɵ= 2.4^{o} for SAN. A small hump can be seen for all of the SAN nanocomposites at ~ 20^{o} which means that the d-spacing is 0.45 nm. (Wissert *et al*. 2010) observed the presence of a small peak of chemically reduced graphite oxide CRGO located at ~ 25 ^{o} (0.35 nm). The result indicated that the GO nanosheets were homogenously dispersed in the SAN matrix and the intercalated morphology had been formed successfully.

It can also be seen that the interlayer spacing was almost the same for the nanocomposites. A possible explanation for this is that the polymer chains did not penetrate the gallery space, but it may also be that the gallery has already been expanded sufficiently, and is ready to accept additional material without the need for further expansion (Cai *et al*. 2007).

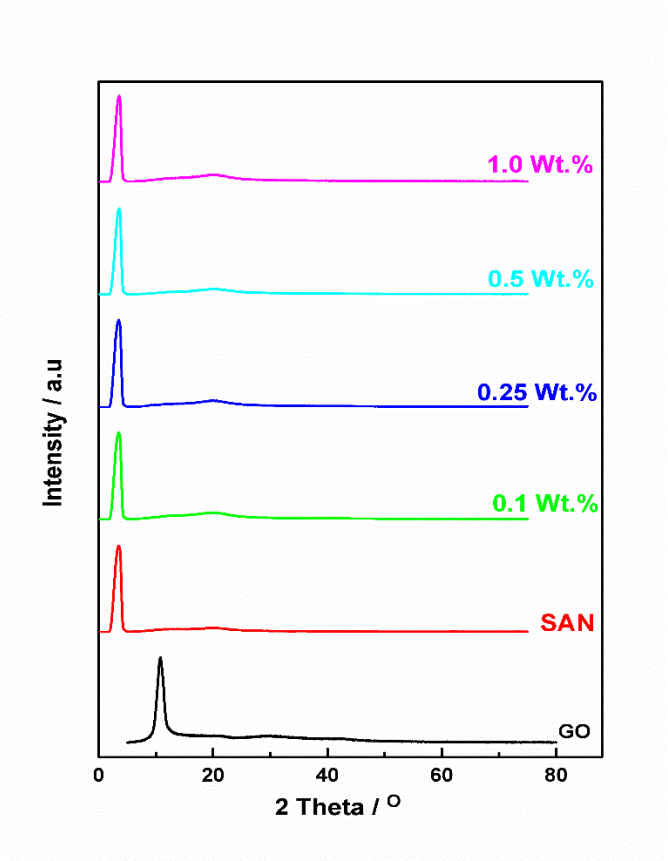

Figure 6.2. : XRD patterns of GO, SAN and nanocomposites.

6.3.3. SEM

Figure 6.3. shows the morphology of the neat polymer and the nanocomposite material on a cryogenically fractured surface.

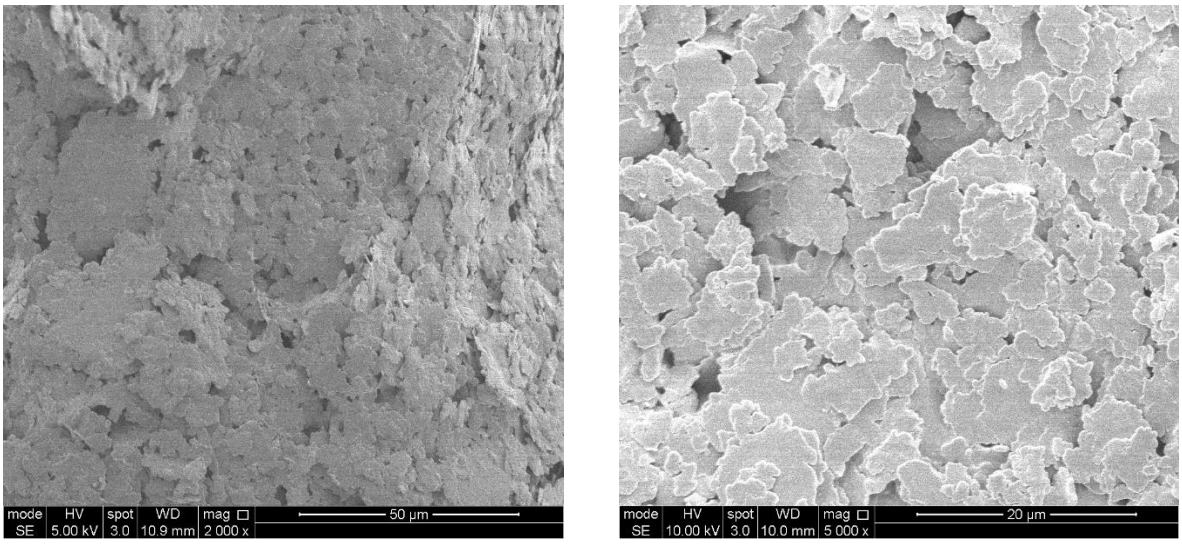

Figure 6.3. : Cryogenically fractured surface SEM images for SAN (left) and SAN/GO 1.0 wt. %.

It can be seen for the neat SAN that it is rough with no specific shape observed on the fracture surface. (Singh *et al*. 2016) observed the same morphology of pure SAN. However, this result is in contrast with that of (Panwar & Mehra, 2008) when they reported the morphology of pure SAN as a uniform layered structure. For the morphology of the nanocomposite SAN reinforced with 1.0 wt. % of GO, the cryogenically fractured surface showed a random distribution of the GO nanosheets in the matrix of SAN. This result indicates that the GO nanosheets are randomly dispersed between the interfacial regions of the neat polymer. It can also be seen that clusters of nanosheets were formed in some regions in the fracture surface of the nanocomposite. (Panwar & Mehra, 2008) reported the formation of graphite sheets clusters of 3.0 wt. % in the SAN matrix, and they reported the merits of the electrical properties of these clusters.

6.3.4. Thermal and thermomechanical properties

6.3.4.1. TGA

Figure 6.4. refers to the thermal properties of GO, SAN and the nanocomposites.

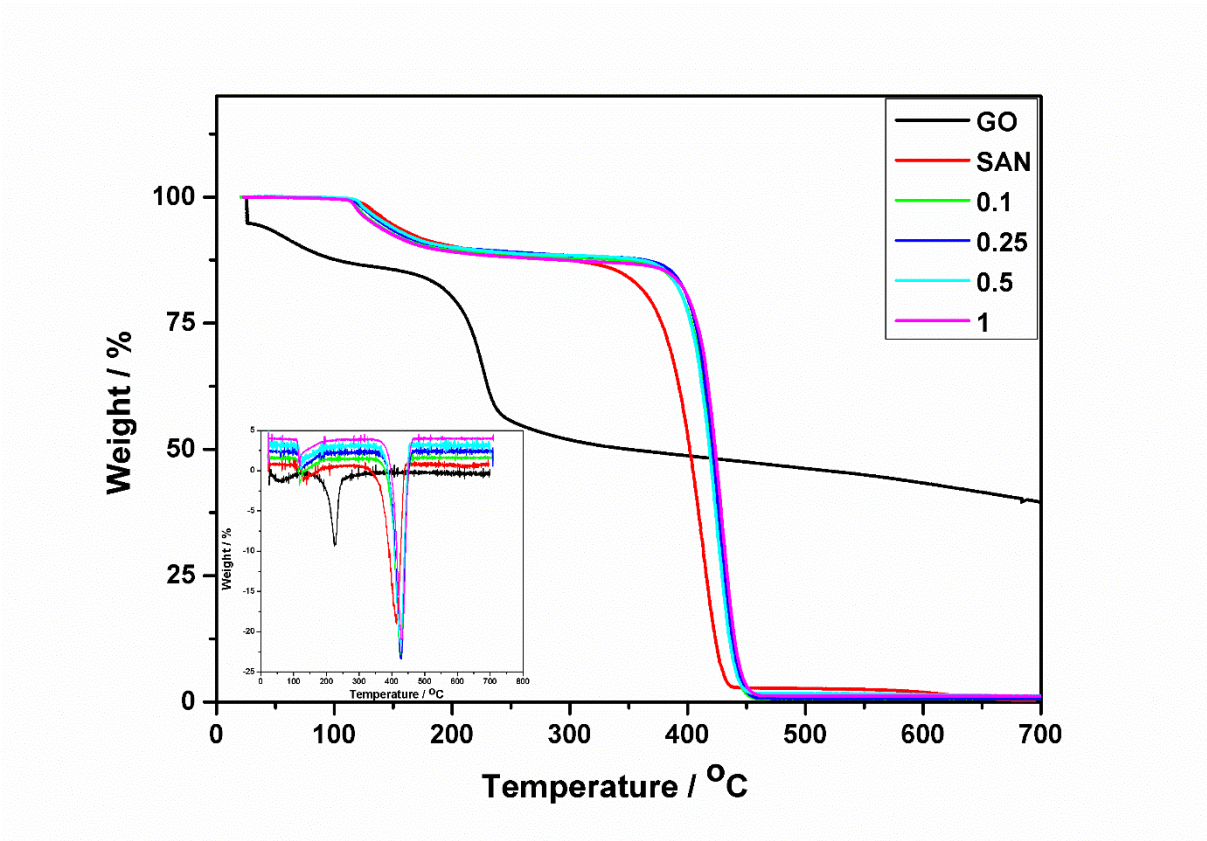

Figure 6.4. : TGA and DTG curves for GO, SAN and nanocomposites.

For the GO curve, the weightlessness can be seen at around 100 ^{o}C which can be ascribed to the elimination of bound moisture at this temperature.

A mass loss can also be noticed below 100 ^{o}C which is ascribed to the removal of adsorbed water. The emission of CO and CO_2 gases can be observed at around 224 ^{o}C which is the thermal degradation temperature for the current sample and this is in the second platform of the thermal behaviour of GO. The final stage of the GO thermal behaviour suggested the remaining amount of the GO after heating up to 700 ^{o}C was about 40%.

This result can be attributed to the removal of a large amount of oxygen functionalities from the GO nanosheet that promoted GO oxidation (Tang *et al*. 2012 ; Liu *et al*. 2016). (Qiu *et al*. 2015) confirmed that the maximum weight loss of the GO used in their study occurred at 200 ^{o}C and a char yield of 53% was obtained at 700 ^{o}C. These findings are quite close to the results achieved in the current study. For pure SAN and nanocomposites, it can be seen that there are several stages of weight loss starting at approximately 125 ^{o}C and ending at 700 ^{o}C.

This corresponds to the degradation of the reinforcing agent followed by structural degradation of the polymer matrix (Wang *et al*. 2005). The degradation of neat SAN occurred in the range of ~ (350-500) ^{o}C is due to the main chain pyrolysis and emission of acrylonitrile (Mainil *et al*. 2010). The $T_{d\ max}$ for the neat SAN was 413.4 ^{o}C which compares very well with the result obtained by (Cai *et al*. 2007). The addition of GO nanosheets to the polymer led to an improvement in thermal stability as the maximum thermal degradation temperature $T_{d\ max}$ shifted higher. The char residue is another indication of thermal performance of the nanocomposites (Cai *et al*. 2007). However, the early decomposition temperature for all the nanocomposites may be due to the thermal instability of GO incorporated in the polymer. (Chu *et al*. 2004) came up with the same explanation for the early decomposition for SAN nanocomposites as the reinforcing agent they had used was considered to be thermally unstable. In addition, the higher T_{dmax} for the nanocomposites compared with the virgin polymer suggests a good dispersion and compatibility of the GO nanosheets with the matrix.

(Mainil *et al*. 2010) drew the same conclusion regarding the thermal stability improvement for their nanocomposites when they reinforced SAN with clay. Table 6.3. shows the $T_{d\ max}$ and char yield for GO, SAN and nanocomposites obtained here.

Table 6.3. : Thermal degradation temperature and char for GO, SAN and nanocomposites.

Sample	**$T_{d\ max}$ / ºC**	**Char at 700 ºC / %**
GO	224.8	40
SAN	413.4	0.32
SAN/GO 0.1 wt.%	425.6	0.60
SAN/GO 0.25 wt.%	427.7	0.69
SAN/GO 0.5 wt.%	425.1	1.17
SAN/GO 1 wt.%	431.6	1.13

6.3.4.2. DSC

Figure 6.5 shows the T_g values of SAN and its nanocomposites obtained by DSC. The Tg for pure SAN in the current study was 107.8 ºC and this was higher for greater weight fraction of incorporated GO. A similar value for the T_g of pure SAN was reported by (Arsac *et al*. 2000) which was 107.6 ºC.

The group compared the T_g value of SAN with that of one of its counterparts which was PS. The T_g for SAN as a randomly copolymer was found to be higher than that of homopolymer PS due to interchain attraction, chain stiffness, and the presence of polar groups of nitriles which might raise T_g compared with the non-polar groups with equivalent size. (Wang *et al*. 2005) showed that T_g was higher as the weight fraction of clay nanoparticles increased compared with neat SAN. The same group attributed the increase of T_g values in the nanocomposites to the restricted movement of the confined polymer chains in the gallery of the incorporated nanoparticles.

This implies that the motion of polymer segments was retarded by the GO nanosheets, and the dispersion of nanosheets in the matrix was affected the values of T_g. The random dispersion of the nanosheets in the matrix led to the enhancement of T_g values compared with the pure polymer.

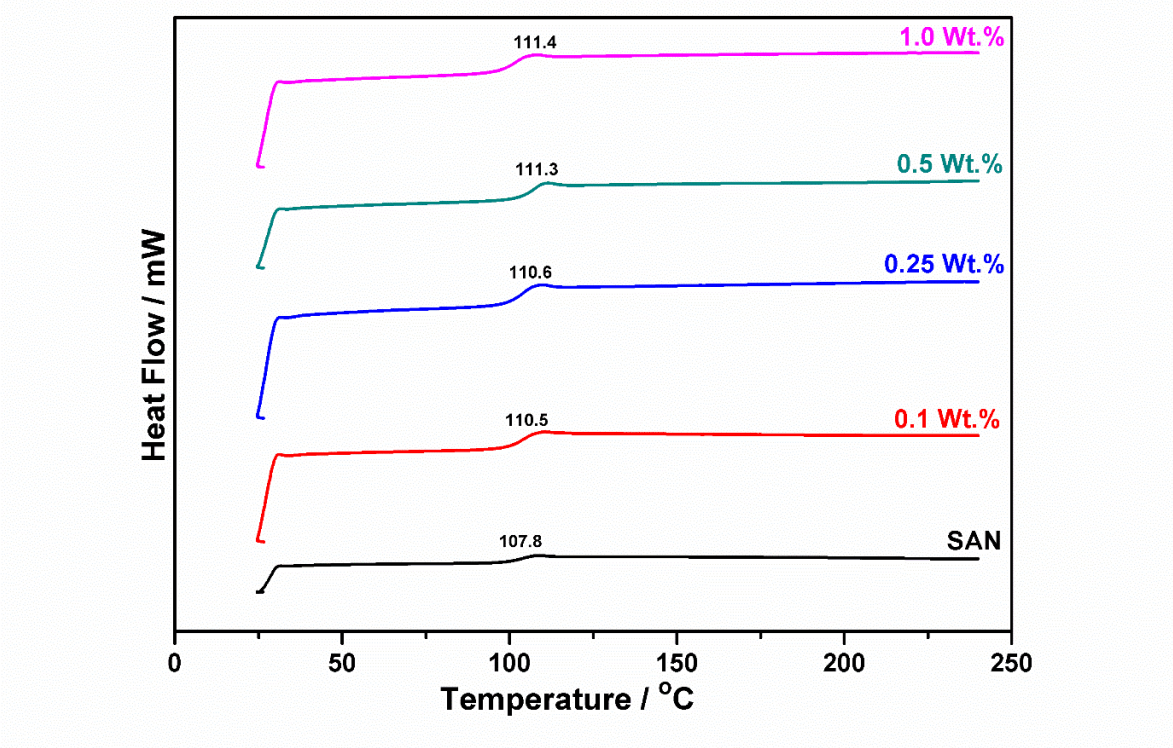

Figure 6.5. : T_g values obtained by DSC for SAN and its nanocomposites.

6.3.4.3. DMA

Figure 6.6.(a) shows the thermomechanical behaviour for SAN and its nanocomposites and Table 6.4 gives the storage modulus values for them.

Table 6.4. : Storage modulus for SAN and its nanocomposites.

Sample	Storage Modulus at 30 ºC / GPa
SAN	2.44
SAN/GO 0.1 wt.%	2.58
SAN/GO 0.25 wt.%	3.13
SAN/GO 0.5 wt.%	3.65
SAN/GO 1.0 wt.%	3.90

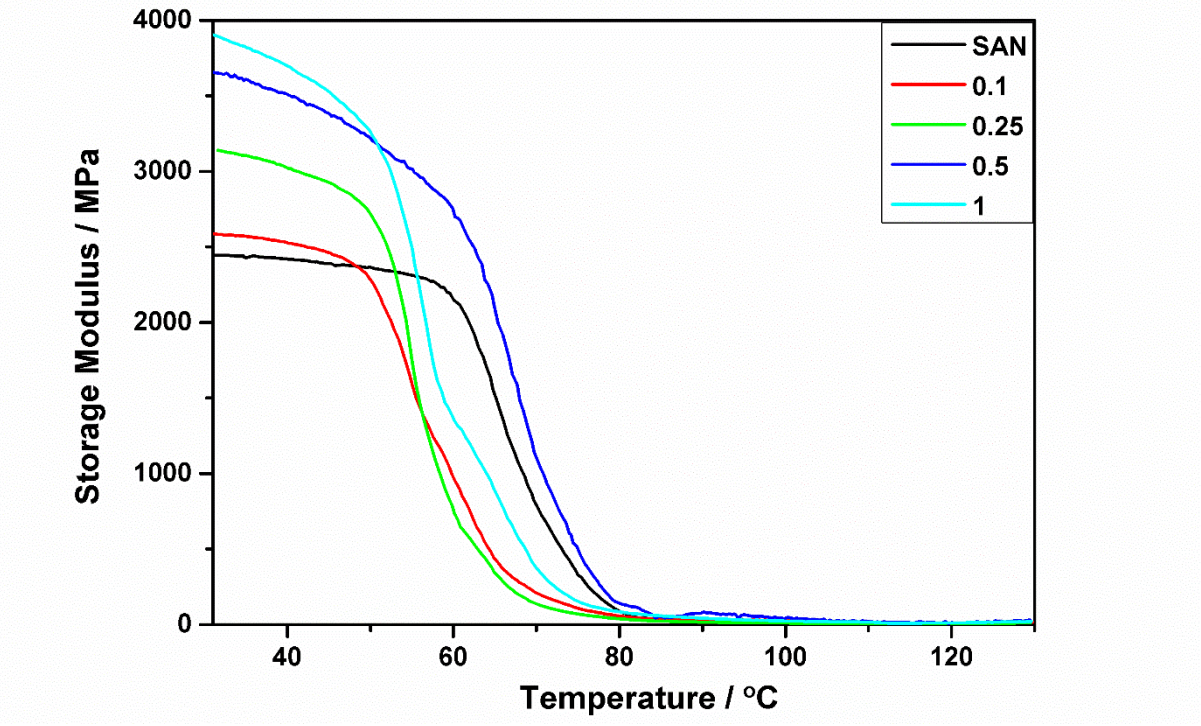

Figure 6.6. (a). : Thermomechanical behaviour represented by storage modulus for SAN and its nanocomposites.

The storage modulus for nanocomposites was significantly increased compared with the neat polymer. The measured storage modulus for SAN was 2.44 GPa which is close to that achieved by (Vu *et al*. 2016). These workers reported a considerable improvement in the value of the storage modulus for SAN nanocomposites reinforced with sulfonated reduced graphene oxide SRGO (0.5 and 1.0) wt. % compared with pure SAN.

A small amount of GO led to a significant improvement in the thermomechanical properties due to the large interfacial area, and high aspect ratio for the GO nanosheets. (Cai *et al*. 2007) reported a significant improvement in the storage modulus for SAN reinforced with 5.0 wt. % of clay at 30 ^{o}C which was the starting temperature for testing the thermomechanical behaviour in the current study. The justification for this is the incomplete relaxation caused by jamming which was led to solid-like behaviour resulting in an improvement in the value of the storage modulus. The solid-like behaviour can be attributed to the formation of physical networks. Another reason for the improvement of storage modulus values of the nanocomposites is the well-dispersed nanosheets in the matrix.

It was expected that chemical compatibility of GO with SAN would have resulted in a better reinforcement effect, and good interfacial adhesion (Cai *et al*. 2007; Mainil *et al*. 2010; Jeddi *et al*. 2017) and this was confirmed in the measured storage modulus values of the current study. Figure 6.6. (b) shows the improvement in thermomechanical behaviour (storage modulus) with the increase of GO weight fraction for SAN nanocomposites.

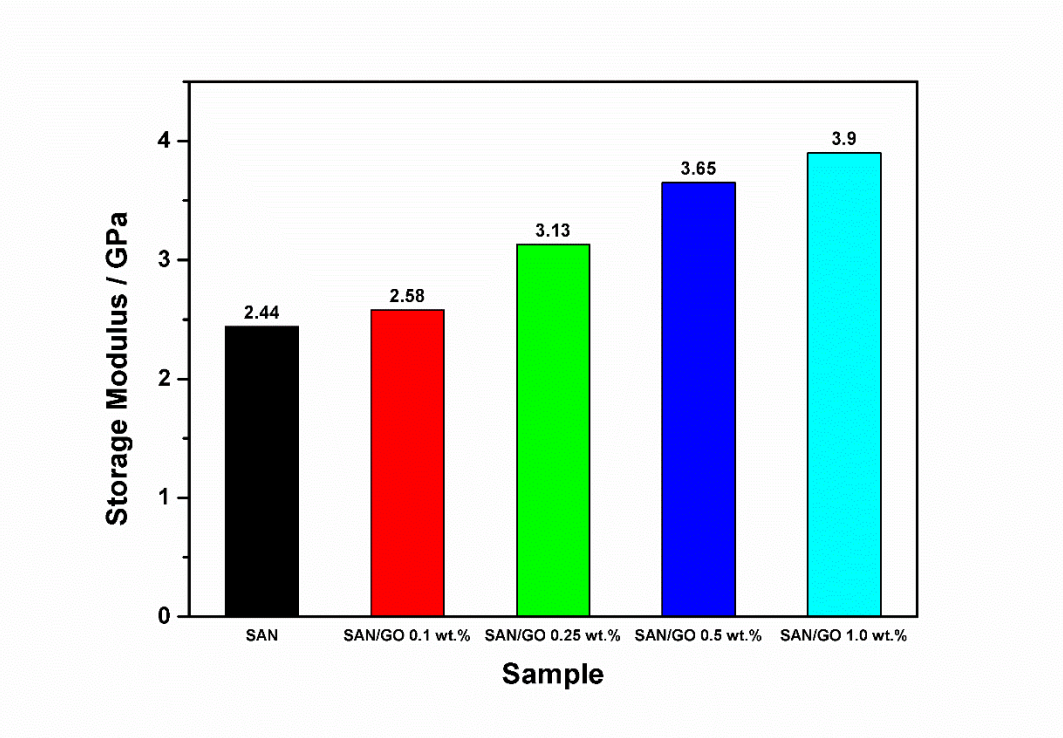

Figure 6.6. (b). : The improvement of storage modulus with the increase of GO weight fraction for SAN nanocomposites.

Figure 6.7. shows a summary about the thermal behaviour (T_d and Tg) for SAN and its nanocomposites. AS GO weight fraction increased, the thermal behaviour is improved.

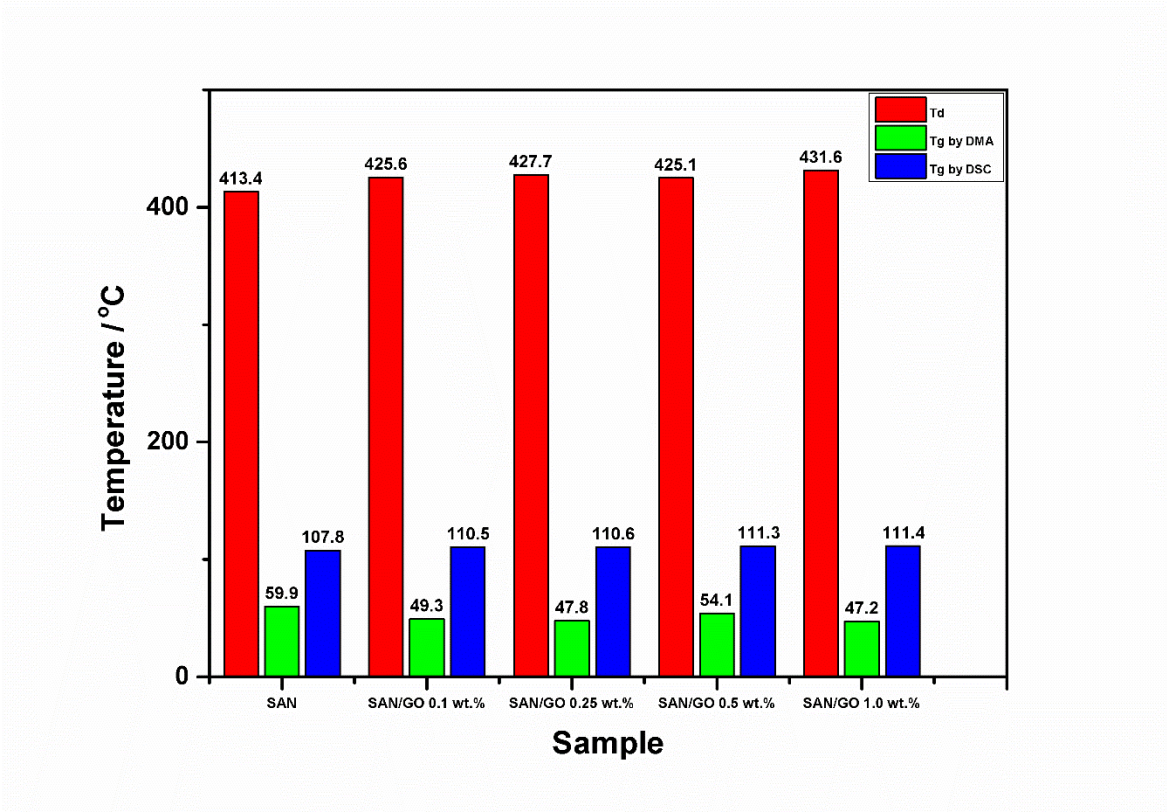

Figure 6.7. : Summary of thermal properties for SAN and its nanocomposites.

6.3.5. Mechanical properties

Figure 6.8. (a) shows the mechanical properties for SAN and its nanocomposites and Table 6.5. gives the values for each parameter. Figure 6.8. (b) shows the improvement of the Young's modulus and tensile strength for SAN nanocomposites compared to the neat SAN.

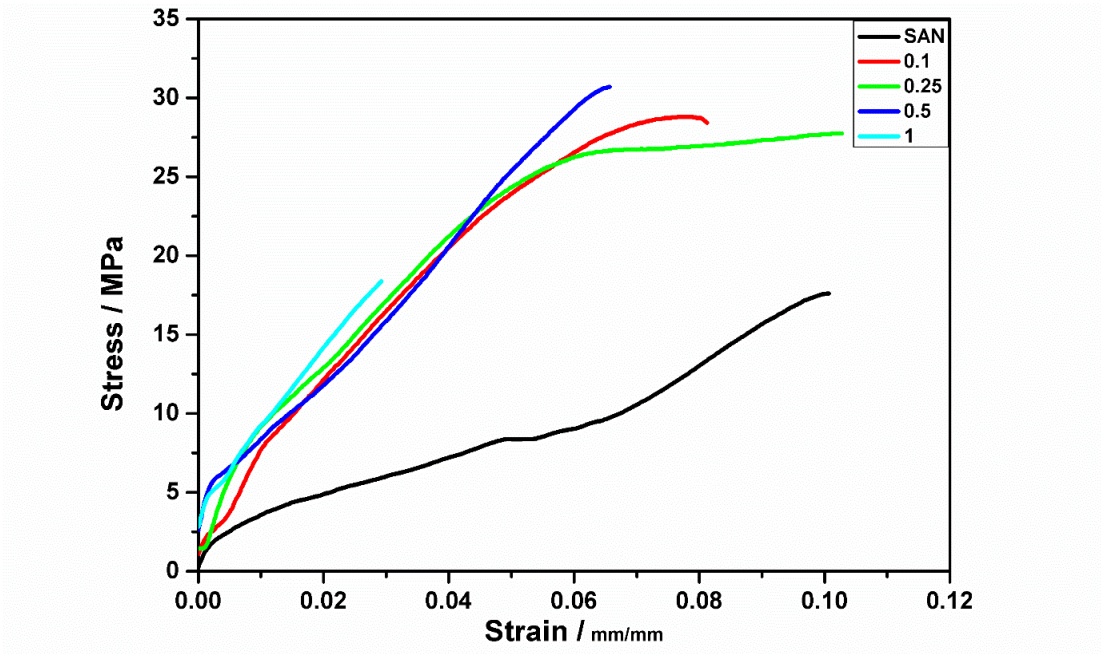

Figure 6.8. (a). : Young's modulus and tensile strength curves for SAN and nanocomposites.

Table 6.5. : Mechanical properties for SAN and its nanocomposites.

Sample	Young's Modulus / MPa	Tensile strength / MPa	Elongation at break / mm	Toughness / $MJ.m^{-3}$
SAN	538.89 ± 20.34	17.60 ± 14.31	0.097 ± 0.003	1.80 ± 1.30
SAN/GO 0.1 wt.%	668.06 ± 3.06	28.09 ± 1.91	0.086 ± 0.007	1.53 ± 0.77
SAN/GO 0.25 wt.%	770.94 ± 59.40	27.06 ± 0.93	0.092 ± 0.010	1.81 ± 0.26
SAN/GO 0.5 wt.%	933.05 ± 63.49	28.59 ± 0.45	0.067 ± 0.002	0.99 ± 0.02
SAN/GO 1.0 wt.%	1116.4 ± 30.12	15.57 ± 29.33	0.047 ± 0.025	1.21 ± 1.35

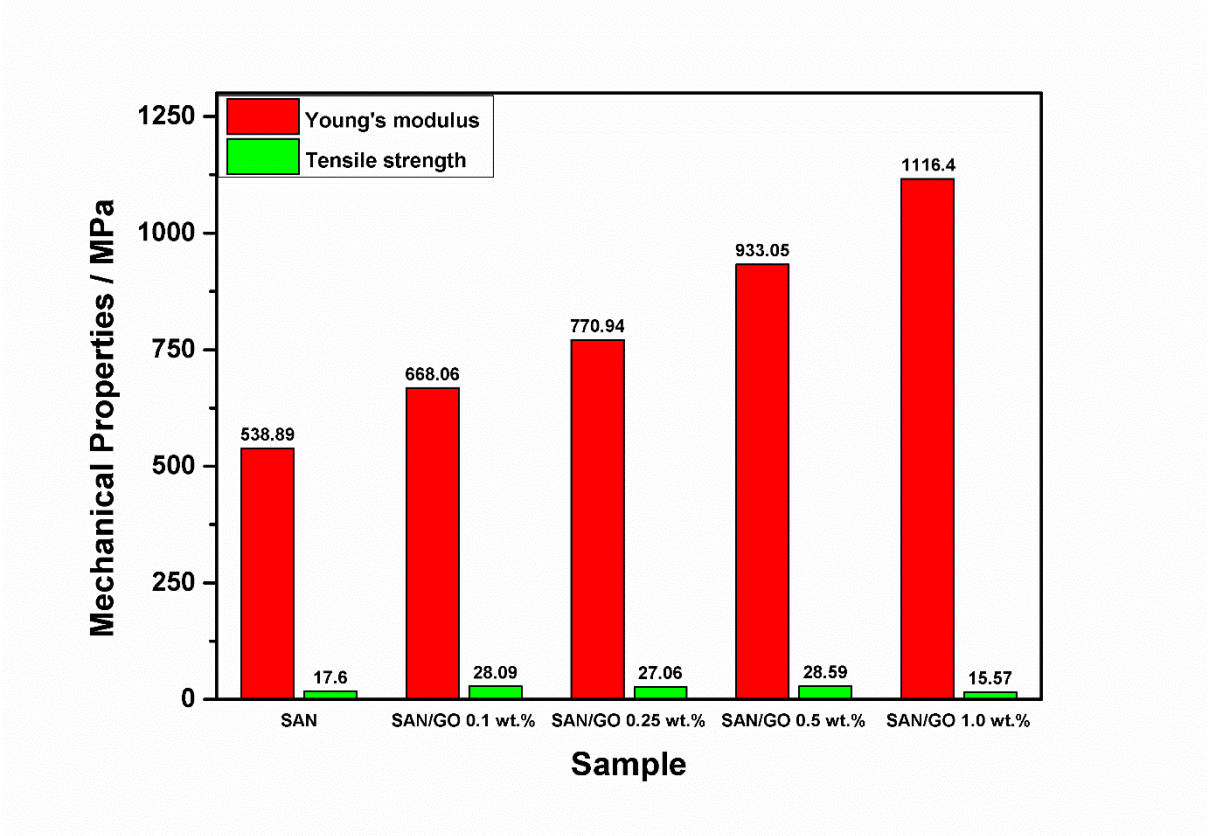

Figure 6.8. (b). : The improvement of mechanical properties for SAN/GO nanocomposites compared to the pure SAN. Data points per sample represent an average based on 2 repeats.

The graph of stress-strain curves and the table show the considerable increase in Young's modulus with the increase in weight fraction of the incorporated GO in SAN.

Nanocomposites have exhibited a higher Young's modulus values compared with the neat polymer. This improvement can be attributed to the improved dispersion of the GO nanosheets in the matrix.

(Stretz *et al*. 2005) observed an increase in Young's modulus for SAN reinforced with 3.2 wt. % montmorillonite MMT, and they ascribed this improvement to the high aspect ratio and good orientation for the platelets.

(Choi and Ryu, 2010) reported an improvement in Young's modulus values for SAN reinforced with MWCNT, and they ascribed this improvement to the better dispersion of the nanotubes in the polymer matrix.

However, the values of tensile strength were increased for all the nanocomposites compared with pure SAN except the last sample reinforced with a higher weight fraction of GO (1.0 wt. %). The tensile strength for the latter sample was the lowest even from the neat polymer. The aggregation of nanosheets as shown in the SEM image, apart from the poor interfacial interaction, might be the main reason for deterioration. (Bourbigot *et al*. 2004) reported a substantial improvement in Young's modulus for the SAN nanocomposites.

The neat polymer reinforced with clay but the values of tensile strength decreased for all the nanocomposites, and the neat polymer gave the highest value of tensile strength. The samples break in a brittle manner due to small aggregations of nanoparticles in the matrix. The behaviour of the nanocomposite of SAN/GO 1.0 wt. % in the current study is quite similar to that confirmed by (Choi and Ryu, 2010). Moreover, (Wissert *et al*. 2010) reported a higher Young's modulus for SAN reinforced with graphite and chemically reduced graphite oxide as compared with neat SAN, but they agreed with the same approach of other authors as the tensile strength values of nanocomposites were lower than that reported for pure SAN.

Generally speaking, the incorporation of reinforcing agents at the nanoscale with SAN led to an improvement in Young's modulus values and a regression in tensile strength values. The quality of interfacial interaction, the dispersion of the nanofillers and the nature of load transfer from matrix to fillers are the most important reasons behind the trend of results of mechanical performance obtained in the current study and confirmed in the literature.

6.4. Conclusion

This study can consolidate the understanding of the performance of SAN reinforced with GO as the latter was narrowly used to reinforce the former despite that fact that they are promising nanofillers and they were successfully incorporated in a range of polymers. The results showed that the low loadings of GO incorporated in SAN participated efficiently in the performance improvement for the majority of properties tested in the current study. The fairly dispersion of the nano-fillers in the matrix played an efficient role in that improvement. It is expected that the promising co-polymer which was being reinforced with the promising nanofillers produce a wide array of applications in different disciplines and daily life aspects.

The novelty in this chapter represented by preparing nanocomposites of SAN reinforced with very low weight fractions of GO and investigating the structure and different properties of the resultant nanocomposites beside the neat polymer. The studies of SAN/GO nanocomposites are few and the majority of previous studies focused on reinforcing SAN with clay, CNT, rGO, and graphite sheets.

Chapter 7

7.1. General discussion and conclusions

This thesis investigates the structure-property relationship of polymer graphene nanocomposites. The selected polymers in this work is PS and one of its counterparts SAN. The reasons for selecting these materials were low cost, ease in processability, and amorphousness. Furthermore, given these materials in their pristine form, are in effect an industry standard, any novel work added in performance terms from preparing nanocomposites with them, would provide a more rapid route to deployment in these industrial applications and other new ones.

The amorphousness of polymers offers the opportunity for investigations of nanoscale reinforcements at very low loadings, because these polymers are mechanically weaker than semi-crystalline polymers. Moreover, some semi-crystalline polymers require more complex procedures to prepare them as nanocomposite materials.

Semi-crystalline polymers such as PP require high temperatures to be dissolved, stronger organic solvents for processing that have higher boiling points and poorer volatility, and in most cases these polymers as nanocomposite materials require additional processing techniques such as extrusion, injection moulding, and hot pressing. Many researchers have confirmed the relatively poorer dispersion of nanoparticles in different polymer matrices when these processing techniques are used. Indeed, in-situ polymerization, and solution blending are regarded as the preferred methods for preparing nanocomposites that provide a homogenous distribution of nanoparticles in the matrix.

Below are the main conclusions from the work described in this thesis and this is followed by some recommendations on possible future directions for this research.

1- In the current thesis, a solution blending approach was selected for its ease of use in preparing nanocomposites and versatile solvent THF was selected for preparing the PS and SAN nanocomposites. This solvent dissolved the pellets of the selected polymers, and it is readily used to obtain a stable suspension of GO as detailed in chapter two of the literature review. The pellets of PS and SAN dissolve within a couple of hours resulting in clear solutions. In contrast whilst the solvent DMF is amongst the best for obtaining stable suspension of GO, it is far from ideal for dissolving PS pellets often resulting in problems due to gel formation in the glassware where the process is carrying out. This issue was verified experimentally in the current study, in confirmation with the published literature, and THF was found to have a long term stability as a co-solvent for PS, SAN, and GO. It should be mentioned that the dialysis bags contributed efficiently in pH improvement for graphite oxide compared to the pH value obtained by using the common way of washing by using the centrifuge. A higher pH value means better adsorption for the polymer in nanosheets galleries.

2- Experimental investigations were carried out on mixing PS/THF and GO/THF with the aim of improving the dispersion of GO nanosheets in polymers matrices. To this end direct mixing was conducted by magnetic stirring. Also a combination of other dispersion techniques of bath sonication and shear mixing are adopted to enhance the distribution of GO nanosheets in PS and SAN matrices. At the beginning of this study, a specific weight fraction of 0.5 wt. % often used in structural applications was incorporated into the PS matrix. Magnetic stirring was applied for 1.5 h followed by bath sonication and shear mixing for different periods of time, and experiments were carried out on the effect of varying of these timings. Finally, polymer films are obtained by casting the suspension of all the samples (nanocomposites and the neat polymer) onto glass substrate petri-dishes.

3- The neutral mixing time (half an hour and 1 h using bath sonication and shear mixing respectively) gives better results compared with the longer mixing times (1 h and a couple of hours using bath sonication and shear mixing respectively) as evidenced by images of SEM, TEM, and DMA measurements.
In contrast however the longer mixing time did show a better performance in tests such as TGA, DSC and the mechanical properties, but this difference in performance, however was not sufficient to justify adopting the longer time of mixing for preparing the nanocomposites described in the other chapters due to other trade-offs in the nanocomposite quality. For example, a longer processing time duration leads to a loss and deterioration in the integrity of the nanosheets which has a negative impact on the performance of the nanocomposites. Nevertheless, all the results of the mechanical, thermal and thermomechanical properties obtained for the nanocomposites are improvements on that of the neat polymer. SEM and TEM measurements described in this thesis on the GO nanosheets confirmed a wrinkled morphology, and spectral results using FTIR confirmed the presence of the main peaks of PS, GO and evidence of the interaction between them in specific regions. Importantly, for practical purposes, the neutral time of mixing is the adopted approach to prepare the nanocomposites in the other chapters.

4- Liquid phase exfoliation was used to precipitate a few drops of GO solution over a glass substrate for obtaining images of the GO nanosheets by AFM. With this technique clear nanosheets with a thickness varies from (0.7-1.1) nm and lateral size varies from 863 nm to 1.2 μm were obtained.

5- Different low weight fractions of GO at (0.01, 0.05, 0.1, 0.25, and 1.0) wt. %. Were incorporated into PS and the resultant nanocomposites were characterised in terms of their spectral, chemical, morphological, thermal, mechanical, and thermomechanical properties. Solutions of PS/THF and GO/THF were prepared by solution blending involving the neutral mixing time for bath sonication and shear mixing preceded by an hour and a half of magnetic stirring. Observations were made of the main infrared peaks of GO, graphite oxide, graphite and PS using FTIR. As the concentration of GO is very low, the peaks in the PS/GO nanocomposites are the same as that in PS.

   In addition, the peaks of the GO in these nanocomposites were in the same position as the peaks of pure GO with the addition of some weak shoulders confirming the interaction between the polymer and the nanomaterial. The results of Raman spectroscopy for PS and its nanocomposites were also very similar for the same reason. Measurements were also carried out on the Raman spectrum of graphite and GO and the results showed the peaks of D and G bands for graphite and the new positions of these peaks for the GO acquired due to the oxidation process. Results are consistent with the published literature.

6- Measurement of XRD in these materials indicated differences in structure between graphite and GO. These differences were identified in the sharpness of the peaks, their positions, and interlayer spacing between them which indicated a successful oxidation process. The main peaks of PS confirmed the amorphous structure of the polymer, but no prominent peaks for GO could be found for the nanocomposites which confirmed the random dispersion of the nanosheets in the matrix, and the dilution of the GO peaks by the amorphous peaks of PS.

7- Images obtained using optical microscopy provided evidence of a homogenous distribution of GO nanosheets in the nanocomposites' matrix. Further imaging using SEM on cryogenically fractured surfaces showed a uniform fracture surface for pure PS and a quite rough fracture surface for nanocomposite. This suggested the nanosheets were homogenously distributed within a few locations of the nanosheets aggregate. The difference in morphology between the polymer and the nanocomposites was further evidenced from TEM images. In brief, all the microscopic techniques confirmed the random dispersion of the nanosheets in the matrix structure.

8- The thermomechanical properties of nanocomposites were characterised using DMA and the storage modulus and hence the rigidity exhibited a consistent increase for an increase of GO loading compared with the pristine polymer. Data on the thermal properties of nanocomposites was acquired using DSC and TGA techniques. The results showed that a slight increase in T_g and Td for increasing GO weight fraction. All measurements of T_g and Td were higher than the neat polymer thereby indicating an improvement in thermal performance due to the homogenous distribution of GO in the polymer matrix.

9- The nanomechanical behaviour of PS and GO was assessed by AFM and QNM after inducting a cryogenically fractured surface on the samples measured through the cryogenically fractured surface. Reduced Young's modulus at the nanoscale was determined using DMT in which contact mode was applied, after it had been imaged. The modulus for GO was found to be higher than in PS in all cases. The QNM measurement gave more accurate data on the modulus of the polymer, but errors appeared in measuring the modulus in GO due to the low spring constant.

10- GO was successfully reduced using a vacuum oven at very low exfoliating temperatures of (130, 165 and 200) ^{o}C for 24 h for each temperature. GO nanosheets like graphene were obtained, and successfully incorporated into PS with weight fractions of 1.0 wt. %. The extent of the reduction was confirmed with FTIR, XRD, Raman spectroscopy, TGA, and XPS.

11- The reduced forms of GO were found to have a beneficial effect on the performance of nanocomposites for all tested properties. The values of T_d, T_g, the storage modulus, and the mechanical properties improved more with increasing temperature of reduction. The aforementioned parameters were found to be higher than those obtained for PS/GO nanocomposites which means that the reduced forms of GO behaved as graphene-like materials. These forms were successfully reduced and improved the properties of the polymer matrix better than the pristine form of GO.

12- Different low weight fractions at (0.1, 0.25, 0.5 and 1.0) wt. % of GO were incorporated into SAN to study the different properties. All the mechanical, thermal, and thermomechanical properties for the nanocomposites performed better than the neat polymer. SAN and its nanocomposites were also found to be more stable and showed better mechanical, thermal, and thermomechanical performance compared with PS and its nanocomposites.

7.2. Future work

The following recommendations are proposed for future work in this field based on existing gaps in knowledge and ideas to progress the field.

1- Utilisation of in-situ polymerization in order to prepare PS/GO nanocomposites and investigate their different properties with reference to what has been achieved for these materials prepared by solution blending. A growing body in the literature referred to in-situ polymerization as a preferred approach to achieve a good dispersion of nano reinforcements in different polymer matrices compared with other relevant approaches.

2- Investigations on the effects of higher loadings of GO and rGO in PS and SAN matrices with regard to thermal and electrical conductivity performance. Drawing a conclusion about the electrical performance for the nanocomposites required high loadings of GO compared to very low loadings employed in the current research.

3- Exploring of different types of nanofillers that can be mixed with PS such as CNTs, clay and expandable graphite with studying different properties. The successful employment for these different nanoscale reinforcements will give a comprehensive conceive about which kind of nano reinforcement is better than the others for different properties of the nanocomposites.

4- Investigations of the properties of nanocomposites in other PS counterparts such as HIPS and ABS with reinforcing them with low loadings of GO. These materials have better mechanical and thermal properties compared to PS and reinforcing them with low loadings of GO will contribute to employ them in wide range of applications besides obtaining a good comparison about their performance compared to the PS nanocomposites.

5- A study of the effects of polymer crystallinity on the properties of nanocomposites. Of particular interest is the employment of semi-crystalline forms of PS, such as a-tactic PS and syndiotactic sPS by reinforcing them with low loadings of GO, and studying their properties. The GO and other nano reinforcement might work as a nucleating agent that affect the polymer crystallinity. This will consequently affect the mechanical and thermal properties which is so important to investigate.

6- A deeper investigation of the nanomechanical behaviour of the interphase is of interest of many authors. Studies would be used on the use of QNM and band excitation AFM. Acquiring an in depth knowledge about the interphase will lead to understand the mechanism of effective load transfer. In addition, the understanding of the characteristics of this region is the key to prepare advanced PGNs.

7- Investigations on more environmentally friendly ‘green’ approaches for reducing GO, for example with vitamins and natural reductants. The potential applications for the nanocomposites that are being incorporated with reduced forms of GO obtained by this green approach are electrodes, supercapacitors, and sensors.

7.2.1. Conferences

The abstracts for the participations where the oral presentations presented were published in the proceedings of these conferences.

Name of Conference	Participation	The title of presentation or poster	Date
University of Sheffield Engineering Symposium USES 2015	Poster and oral presentation (Abstract published)	Preparation and properties of polymer graphene nanocomposites	24/06/2015
5th annual postgraduate symposium of Nanotechnology, The University of Birmingham	Attendance		14/12/2015
Nanotech. France, Paris 2016	Oral presentation (Abstract published)	Studying the effect of dispersion technique and processing conditions on the structure and properties of polystyrene/graphene oxide nanocomposites	1/06/2016

7.2.2. Papers in preparation

1- The effect of different periods of mixing time using different dispersion techniques on the structure and properties of polystyrene/graphene oxide nanocomposites.

2- Studying the properties and the nanomechanical behaviour of Polystyrene/Graphene Oxide nanocomposites using very low loadings of graphene oxide.

3- Studying the properties of Polystyrene /thermally reduced graphene oxide nanocomposites using vacuum oven at low temperatures.

4- Properties of polystyrene –co – acrylonitrile /graphene oxide nanocomposites.

Bibliography

Alhassan, S.M. et al., 2013. Preparation and thermal properties of graphene oxide/main chain benzoxazine polymer. *European Polymer Journal*, 49(12), pp.3825–3833.

Alsharaeh, E.H., Othman, A.A. & Aldosari, M.A., 2014. Microwave irradiation effect on the dispersion and thermal stability of RGO nanosheets within a polystyrene matrix. *Materials*, 7(7), pp.5212–5224.

Ammar, A. et al., 2015. Influence of graphene oxide on mechanical, morphological, barrier, and electrical properties of polymer membranes. *Arabian Journal of Chemistry*, pp.1–13.

Araby, S. et al., 2014. Electrically and thermally conductive elastomer/graphene nanocomposites by solution mixing. *Polymer (United Kingdom)*, 55(1), pp.201–210.

Arsac et al., 2000. Rheological Characterization of styrene acrylonitrile copolymers. *Applied polymer Science*, 77, pp.1316–1321.

Asif, M. et al., 2016. Synthesis of a highly efficient 3D graphene–CNT–MnO 2 –PANI nanocomposite as a binder free electrode material for supercapacitors. *Phys. Chem. Chem. Phys.*, 18(38), pp.26854–26864.

Ayán-Varela, M. et al., 2014. A quantitative analysis of the dispersion behavior of reduced graphene oxide in solvents. *Carbon*, 75, pp.390–400.

Basu et al., 2013. Dielectric, electrical and rheological characterization of graphene filled Polystyrene nanocomposites. *Polymer composite*, pp.2082–2093.

Beach, E.R. et al., 2002. Pull-off force measurements between rough surfaces by atomic force microscopy. *Journal of colloid and interface science*, 247(1), pp.84–99.

Beach, G., 2009. Dynamic Light Scattering Study of Polymer Chain Dimensions Objectives : , pp.1–8.

Bhattacharya, M., 2016. Polymer nanocomposites-A comparison between carbon nanotubes,

graphene, and clay as nanofillers. *Materials*, 9(262), pp.1–35.

Bhushan, B., 2005. Nanotribology and nanomechanics: An introduction. *Wear*, 259, pp.1507–1531.

Bird, R.J., Rooney, G. & Mann, J., 1971. The fracture of polystyrene: some observations on strength and cracking phenomena. *Polymer*, 12(12), pp.742–759.

Birowska et al., 2011. Van Der Waals Density Functionals for Graphene Layers and Graphite. *Acta Physica Polonica a*, 120(5), pp.845–848.

Bkakri, R. et al., 2015. Degree of phase separation effects on the charge transfer properties of P3HT:Graphene nanocomposites. *Journal of Luminescence*, 161, pp.264–270.

Bonnell, 2001. *Scanning probe microscopy and spectroscopy* 2nd Editio., Canada: John Wiley and Sons.

Bourbigot, S. et al., 2004. Solid state NMR characterization and flammability of styrene-acrylonitrile copolymer montmorillonite nanocomposite. *Polymer*, 45(22), pp.7627–7638.

Butt, H.J., Cappella, B. & Kappl, M., 2005. Force measurements with the atomic force microscope: Technique, interpretation and applications. *Surface Science Reports*, 59(1–6), pp.1–152.

Cai, D. et al., 2012. High performance polyurethane/functionalized graphene nanocomposites with improved mechanical and thermal properties. *Composites Science and Technology*, 72(6), pp.702–707.

Cai et al., 2007a. Morphology, Thermal and Mechanical Properties of Poly (Styrene-Acrylonitrile) (SAN)/Clay Nanocomposites from Organic-Modified Montmorillonite. *Polymer-Plastics Technology and Engineering*, 46, pp.541–548.

Cai et al., 2007b. Preparation and characterization of poly (styrene-acrylonitrile) (SAN)/clay

nanocomposites by melt intercalation. *Journal of Materials Science*, 42(14), pp.5524–5533.

Cano, M. et al., 2013. Improving the mechanical properties of graphene oxide based materials by covalent attachment of polymer chains. *Carbon*, 52, pp.363–371.

Cappella, B. & Dietler, G., 1999. *Force-distance curves by atomic force microscopy*,

Chandrasekaran, S., Seidel, C. & Schulte, K., 2013. Preparation and characterization of graphite nano-platelet (GNP)/epoxy nano-composite: Mechanical, electrical and thermal properties. *European Polymer Journal*, 49(12), pp.3878–3888.

Chang, H. & Wu, H., 2013. Graphene-based nanocomposites: preparation, functionalization, and energy and environmental applications. *Energy & Environmental Science*, 6(12), pp.3483–3507.

Chee, W.K. et al., 2015. Nanocomposites of graphene/polymers: a review. *RSC Adv.*, 5(83), pp.68014–68051.

Chen, C. et al., 2013. Electric field induced orientation-selective unzipping of zigzag carbon nanotubes upon oxidation. *Physical chemistry chemical physics : PCCP*, 15(17), pp.6431–6436.

Chen, C. et al., 2014. Theoretical simulation of the reduction of graphene oxide by lithium naphthalenide. *Physical Chemistry Chemical Physics*, 16(20), pp.12858–12864.

Chen, H. et al., 2007. Effect of dispersion method on tribological properties of carbon nanotube reinforced epoxy resin composites. *Polymer Testing*, 26(3), pp.351–360.

Chen, Y. et al., 2015. Enhanced electromagnetic interference shielding efficiency of polystyrene/graphene composites with magnetic Fe3O4 nanoparticles. *Carbon*, 82(C), pp.67–76.

Chen et al., 2013. Graphene and its derivatives for the development of solar cells,

photoelectrochemical, and photocatalytic applications. *Energy & Environmental Science*, 6(5), pp.1362–1387.

Chen et al., 2011. High performance supercapacitors based on reduced graphene oxide in aqueous and ionic liquid electrolytes. *Carbon*, 49(2), pp.573–580.

Chen et al., 2010a. Preparation of graphene by the rapid and mild thermal reduction of graphene oxide induced by microwaves. *Carbon*, 48(4), pp.1146–1152.

Chen et al., 2017. Super-high thermal conductivity of polyamide-6/graphene-graphene oxide composites through in situ polymerization. *High Performance Polymers*, 29(5), pp.585–594.

Da Chen et al, 2012. Graphene Oxide : Preparation , Functionalization , and Electrochemical Applications. *Chemical Reviews*, 112, pp.6027–6053.

Chen, Yan, L. & Bangal, P.R., 2010b. Chemical Reduction of Graphene Oxide to Graphene by Sulfur-Containing Compounds.pdf. *J.Phys. Chem. C*, 114(47), pp.19885–19890.

Chizhik, S.A. et al., 1998. Micromechanical properties of elastic polymeric materials as probed by scanning force microscopy. *American Chemical Society, Polymer Preprints, Division of Polymer Chemistry*, 14(2), pp.2606–2609.

Choi and Ryu, 2010. Enhancement of dispersion of carbon nanotube and physical properties of PSAN / MWCNT nanocomposite via surface initiated ATRP. *Applied polymer Science*, 116, pp.2930–2936.

Chu, L.-L. et al., 2004. Styrene-acrylonitrile (SAN) layered silicate nanocomposites prepared by melt compounding. *Polymer*, 45(12), pp.4051–4061.

Chua, C.K. & Pumera, M., 2016. The reduction of graphene oxide with hydrazine: elucidating its reductive capability based on a reaction-model approach. *Chemical Communications*, 52(1), pp.72–75.

Cleveland, J.P. et al., 1998. Energy dissipation in tapping-mode atomic force microscopy. *Applied Physics Letters*, 72(20), pp.2613–2615.

Clifford, C. a & Seah, M.P., 2009. Improved methods and uncertainty analysis in the calibration of the spring constant of an atomic force microscope cantilever using static experimental methods. *Measurement Science and Technology*, 20(12), pp.125501–125511.

Clifford, C. a & Seah, M.P., 2005. The determination of atomic force microscope cantilever spring constants via dimensional methods for nanomechanical analysis. *Nanotechnology*, 16(9), pp.1666–1680.

Coates, J., 2000. Interpretation of Infrared Spectra , A Practical Approach Interpretation of Infrared Spectra , A Practical Approach. In *Encyclopedia of Analytical Chemistry*. Chichester: John Wiley and Sons, pp. 10815–10837.

Compton, O.C. & Nguyen, S.T., 2010. Graphene oxide, highly reduced graphene oxide, and graphene: Versatile building blocks for carbon-based materials. *Small*, 6(6), pp.711–723.

Cosmoiu, I. et al., 2016. Influence of Filler Dispersion on the Mechanical Properties of Nanocomposites. *Materials Today: Proceedings*, 3(4), pp.953–958.

Cromer, B.M. et al., 2015. In-situ polymerization of isotactic polypropylene-nanographite nanocomposites. *Polymer (United Kingdom)*, 80, pp.275–281.

Das, T.K. & Prusty, S., 2013. Graphene-Based Polymer Composites and Their Applications. *Polymer-Plastics Technology and Engineering*, 52(4), pp.319–331.

Dawkins, 1976. Thermodynamic Interpretation. *Journal of polymer science*, 14, pp.569–571.

Derjaguin, B. V, Muller, V.M. & Toporov, Y.U.P., 1975. Effect of contact deformation on the adhesion of particles. *Journal of colloid and interface science*, 53(2), pp.314–326.

Dhand, V. et al., 2013. A Comprehensive Review of Graphene Nanocomposites : Research

Status and Trends. *Journal of Nanomaterials*, 2013, pp.1–15.

Dharmaraj, P. et al., 2014. Selective area growth of Bernal bilayer epitaxial graphene on 4H-SiC (0001) substrate by electron-beam irradiation. *Applied Physics Letters*, 105, pp.1–6.

Ding, P. et al., 2015. Anisotropic thermal conductive properties of hot-pressed polystyrene/graphene composites in the through-plane and in-plane directions. *Composites Science and Technology*, 109, pp.25–31.

Domke, J. & Radmacher, M., 1998. Measuring the elastic properties of thin polymer films with the atomic force microscope. *Langmuir*, 14(12), pp.3320–3325.

Drewniak, S. et al., 2016. Studies of Reduced Graphene Oxide and Graphite Oxide in the Aspect of Their Possible Application in Gas Sensors. *Sensors (Basel, Switzerland)*, 16(103), p.16.

Dreyer et al., 2010. The chemistry of graphene oxide. *Chemical Society reviews*, 39, pp.228–240.

E.L.Wolf, 2014. Practical productions of graphene, supply and cost. In *Applications of Graphene*. Springer, pp. 19–38.

Earl & Nancy Boysen, 2011. *Nanotechnology for dummies* 2nd ed., USA: Wiley Publishing, Inc.

Eaton and West, 2010. *Atomic force microscopy, e book*, Oxford: Oxford University Press.

Economopoulos, S.P. & Tagmatarchis, N., 2013. Chemical functionalization of exfoliated graphene. *Chemistry - A European Journal*, 19(39), pp.12930–12936.

Eda, G. & Chhowalla, M., 2010a. Chemically derived graphene oxide: Towards large-area thin-film electronics and optoelectronics. *Advanced Materials*, 22(22), pp.2392–2415.

Eda, G. & Chhowalla, M., 2010b. Chemically derived graphene oxide: towards large-area

thin-film electronics and optoelectronics. *Advanced materials (Deerfield Beach, Fla.)*, 22(22), pp.2392–2415.

Eda, G. & Chhowalla, M., 2009. Graphene-based Composite Thin Films for Electronics136. *Nano Letters*, 9(2), pp.814–818.

Edwards, R.S. & Coleman, K.S., 2013. Graphene synthesis: relationship to applications. *Nanoscale*, 5(1), pp.38–51.

El-Khodary, S. a. et al., 2014. Preparation and Characterization of Microwave Reduced Graphite Oxide for High-Performance Supercapacitors. *Electrochimica Acta*, 150, pp.269–278.

Eswaraiah, V., Balasubramaniam, K. & Ramaprabhu, S., 2011. Functionalized Graphene Reinforced Thermoplastic Nanocomposites as Strain sensors in Structural Health Monitoring. *J Mater Chem*, 21, pp.12626–12628.

Fan et al., 2013. Fabrication of electrically conductive graphene/polystyrene composites via a combination of latex and layer-by-layer assembly approaches. *Journal of Materials Research*, 28(4), pp.611–619.

Fornes, T.. et al., 2001. Nylon 6 nanocomposites: the effect of matrix molecular weight. *Polymer*, 42(25), pp.09929–09940.

Fu et al., 2013. Evaluation and Characterization of Reduced Graphene Oxide Nanosheets as Anode Materials for Lithium-Ion Batteries. *Int. J. Electrochem. Sci*, 8, pp.6269–6280.

Gao, C. et al., 2014. Graphene networks with low percolation threshold in abs nanocomposites: Selective localization and electrical and rheological properties. *ACS Applied Materials and Interfaces*, 6(15), pp.12252–12260.

Gay, 2015. *Composite materials* Third Edit., USA: CRC Press.

Geim and Novoselov, 2007. The rise of graphene. *Nature Mater.*, 6(3), pp.183–191.

Gengler, R.Y.N., Spyrou, K. & Rudolf, P., 2010. A roadmap to high quality chemically prepared graphene. *Journal of Physics D: Applied Physics*, 43(37), pp.1–20.

Giannelis, E., 1996. Polymer layered Silicate Nanocomposites. *Advanced materials*, 8(1), pp.29–35.

Glover, A.J. et al., 2011. In situ reduction of graphene oxide in polymers. *Macromolecules*, 44(24), pp.9821–9829.

Goumri, M. et al., 2017. Synthesis and characterization of nanocomposites films with graphene oxide and reduced graphene oxide nanosheets. *Chinese Journal of Physics*, 55(2), pp.412–422.

Grigorescu, R.M. et al., 2016. Mechanical and dielectric properties of SEBS modified by graphite inclusion and composite interface. *Journal of Physics and Chemistry of Solids*, 89, pp.97–106.

Gudarzi, M.M. & Sharif, F., 2011. Self assembly of graphene oxide at the liquid–liquid interface: A new route to the fabrication of graphene based composites. *Soft Matter*, 7(7), pp.3432–3440.

Guo, S. & Dong, S., 2011. Graphene nanosheet: synthesis, molecular engineering, thin film, hybrids, and energy and analytical applications. *Chemical Society reviews*, 40(5), pp.2644–2672.

Gupta, M.L. et al., 2013. The effect of mixing methods on the dispersion of carbon nanotubes during the solvent-free processing of multiwalled carbon nanotube/epoxy composites. *Journal of Polymer Science, Part B: Polymer Physics*, 51(6), pp.410–420.

Han, Y. et al., 2013. Preparation and properties of polystyrene nanocomposites with graphite oxide and graphene as flame retardants. *Journal of Materials Science*, 48(12), pp.4214–4222.

Han, Y. et al., 2016. Preparation of thermally reduced graphene oxide and the influence of its reduction temperature on the thermal, mechanical, flame retardant performances of PS nanocomposites. *Composites Part A*, 84(A), pp.336–343.

Harsini, I. et al., 2017. Polymer nanocomposites processed via self-assembly through introduction of nanoparticles, nanosheets, and nanofibers. *Journal of Materials Science*, 52(4), pp.1969–1980.

Hasan, M. & Lee, M., 2014. Enhancement of the thermo-mechanical properties and efficacy of mixing technique in the preparation of graphene/PVC nanocomposites compared to carbon nanotubes/PVC. *Progress in Natural Science: Materials International*, 24(6), pp.579–587.

Hassan, M. et al., 2013. High-yield aqueous phase exfoliation of graphene for facile nanocomposite synthesis via emulsion polymerization. *Journal of colloid and interface science*, 410, pp.43–51.

Heo et al., 2012. ABS nanocomposite films based on functionalized graphene sheets. *Journal of Applied Polymer Science*, 124(7), pp.4663–4670.

Hernandez, Y. et al., 2010. Measurement of multicomponent solubility parameters for graphene facilitates solvent discovery. *Langmuir*, 26(5), pp.3208–3213.

Hirata, M. et al., 2004. Thin-film particles of graphite oxide 1: High-yield synthesis and flexibility of the particles. *Carbon*, 42(14), pp.2929–2937.

Hontoria-Lucas, C. et al., 1995. Study of oxygen-containing groups in a series of graphite oxides: Physical and chemical characterization. *Carbon*, 33(11), pp.1585–1592.

Hossain, M.E. et al., 2015. Effect of Dispersion Conditions on the Thermal and Mechanical Properties of Carbon Nanofiber–Polyester Nanocomposites. *Journal of Engineering Materials and Technology*, 137(3), pp.1–9.

Hu, H. et al., 2010. Preparation and properties of graphene nanosheets-polystyrene nanocomposites via in situ emulsion polymerization. *Chemical Physics Letters*, 484(4–6), pp.247–253.

Hu, K. et al., 2014. Graphene-polymer nanocomposites for structural and functional applications. *Progress in Polymer Science*, pp.1–39.

Huang, X. et al., 2012. Graphene-based composites. *Chemical Society Reviews*, 41(2), pp.666–686.

Hummers, W.S. & Offeman, R.E., 1958. Preparation of Graphitic Oxide. *Journal of the American Chemical Society*, 80(6), pp.1339–1339.

Ionita, M. et al., 2014. Improving the thermal and mechanical properties of polysulfone by incorporation of graphene oxide. *Composites Part B: Engineering*, 59, pp.133–139.

Iqbal, M.Z. et al., 2016. Processable conductive graphene/polyethylene nanocomposites: Effects of graphene dispersion and polyethylene blending with oxidized polyethylene on rheology and microstructure. *Polymer (United Kingdom)*, 98, pp.143–155.

Jang, B.N. & Wilkie, C.A., 2005. The effects of clay on the thermal degradation behavior of poly(styrene-co-acrylonitirile). *Polymer*, 46(23), pp.9702–9713.

Jarusuwannapoom, T. et al., 2005. Effect of solvents on electro-spinnability of polystyrene solutions and morphological appearance of resulting electrospun polystyrene fibers. *European Polymer Journal*, 41(3), pp.409–421.

Jeddi, J. et al., 2017. Morphology, microstructure and rheological properties of SAN (styrene-acrylonitrile)/EPDM (ethylene-propylene-diene monomer) nanocomposites: Investigating the role of organoclay type and order of mixing. *Materials Chemistry and Physics*, 187, pp.191–202.

Jia, B. & Zou, L., 2012. Graphene nanosheets reduced by a multi-step process as high-

performance electrode material for capacitive deionisation. *Carbon*, 50(6), pp.2315–2321.

Jiang, H. et al., 2014. Facile fabrication of poly (tetrafluoroethylene)/graphene nanocomposite via electrostatic self-assembly approach. *Composites Science and Technology*, 103, pp.28–35.

John Masters & Joseph Au ed., 1987. Fractography of modern engineering materials: Composites and metals. In Philadelphia: American Society of Testing and Materials ASTM.

Johnson, D.W., Dobson, B.P. & Coleman, K.S., 2015. A manufacturing perspective on graphene dispersions. *Current Opinion in Colloid and Interface Science*, 20(5–6), pp.367–382.

Ju, H.M. et al., 2010. Structures of thermally and chemically reduced graphene. *Materials Letters*, 64(3), pp.357–360.

Justin, R. & Chen, B., 2014. Body temperature reduction of graphene oxide through chitosan functionalisation and its application in drug delivery. *Materials Science and Engineering C*, 34(1), pp.50–53.

Kang, S.H. et al., 2013. Mechanical properties of free-standing graphene oxide. *Diamond and Related Materials*, 38, pp.73–78.

Karak, N., 2009. Fundamentals of polymers: raw materials to finish products. , p.290.

Kattimuttathu et al., 2015. Synthesis, characterization and optical properties of graphene oxide polystyrene nanocomposites. *Polym.Adv.Technol*, 26, pp.214–222.

Kim, S. & Ryu, C.Y., 2015. Mechanical properties of poly(styrene-co-acrylonitrile) nanocomposites containing organically modified layered double hydroxides. *Polymers for Advanced Technologies*, 26(12), pp.1537–1543.

Kim et al., 2010. Graphene/polymer nanocomposites. *Macromolecules*, 43(16), pp.6515–6530.

Konios, D. et al., 2014. Dispersion behaviour of graphene oxide and reduced graphene oxide. *Journal of Colloid and Interface Science*, 430, pp.108–112.

Krishnamoorthy, K. et al., 2013. The chemical and structural analysis of graphene oxide with different degrees of oxidation. *Carbon*, 53, pp.38–49.

Kuila, T. et al., 2013. Recent advances in the efficient reduction of graphene oxide and its application as energy storage electrode materials. *Nanoscale*, 5(1), pp.52–71.

Kuilla, T. et al., 2010. Recent advances in graphene based polymer composites. *Progress in Polymer Science*, 35(11), pp.1350–1375.

Lago, E. et al., 2016. Solution blending preparation of polycarbonate/graphene composite: boosting the mechanical and electrical properties. *RSC Adv.*, 6(100), pp.97931–97940.

Lan and Pinnavaia, 1994. Clay-Reinforced Epoxy. , 6(21), pp.2216–2219.

Layek, R.K. & Nandi, A.K., 2013. A review on synthesis and properties of polymer functionalized graphene. *Polymer (United Kingdom)*, 54(19), pp.5087–5103.

Lee, C. et al., 2008. Measurement of the Elastic Properties and Intrinsic Strength of Monolayer Graphene. *Science*, 321, pp.385–388.

Lee, W. et al., 2013. Simultaneous enhancement of mechanical, electrical and thermal properties of graphene oxide paper by embedding dopamine. *Carbon*, 65, pp.296–304.

Lerf, A. et al., 1998. Structure of Graphite Oxide Revisited. *Journal of Physical Chemistry B*, 102(23), pp.4477–4482.

Leszczynska, A. et al., 2007. Polymer / montmorillonite nanocomposites with improved thermal Part II : Thermal stability of montmorillonite nanocomposites based on different

polymeric matrixes. *Thermochim Acta*, 453(2), pp.75–96.

Li et al., 2013a. The role of functional groups on graphene oxide in epoxy nanocomposites. *Polymer*, 54(21), pp.5821–5829.

Li, Z. et al., 2015. Improved synthesis of fluffy and wrinkled reduced graphene oxide for energy storage application. *Vacuum*, 117, pp.35–39.

Li and Wang, 2008. *Introduction to micromechanics and nanomechanics*, Singapore: World Scientific.

Li et al., 2013b. The effect of the ultrasonication pre-treatment of graphene oxide (GO) on the mechanical properties of GO/polyvinyl alcohol composites. *Carbon*, 55, pp.321–327.

Liebscher, M. et al., 2013. A morphological study on the dispersion and selective localization behavior of graphene nanoplatelets in immiscible polymer blends of PC and SAN. *Polymer (United Kingdom)*, 54(21), pp.5875–5882.

Lim et al., 2003. Dispersion quality and rheological property of polymer clay NC ultrasonication effect by Lim et al.2003.pdf. , 9(1), pp.51–57.

Lin, L.Y. & Kim, D.E., 2012. Measurement of the elastic modulus of polymeric films using an AFM with a steel micro-spherical probe tip. *Polymer Testing*, 31(7), pp.926–930.

Liu, L. et al., 2012. Mechanical properties of graphene oxides. *Nanoscale*, 4(19), pp.5910–5916.

Liu, W.K. et al., 2004. *An introduction to computational nanomechanics and materials*,

Liu, Y. et al., 2014. Manganese dioxide nanosheet arrays grown on graphene oxide as an advanced electrode material for supercapacitors. *Electrochimica Acta*, 117, pp.528–533.

Liu, Y. et al., 2016. Polystyrene/graphene oxide nanocomposites synthesized via Pickering polymerization. *Progress in Organic Coatings*, 99, pp.23–31.

Loh, K.P. et al., 2010. The chemistry of graphene. *Journal of Materials Chemistry*, 20(12), pp.2277–2289.

Loryuenyong, V. et al., 2013. Preparation and Characterization of Reduced Graphene Oxide Sheets via Water-Based Exfoliation and Reduction Methods. , 2013, pp.1–5.

Ma, H.-L. et al., 2012. Functionalization and reduction of graphene oxide with p -phenylene diamine for electrically conductive and thermally stable polystyrene Composites. *ACS Applied Materials & Interfaces*, 4, pp.1948–1953.

Ma, Q. et al., 2013. A rapid and easy approach for the reduction of graphene oxide by formamidinesulfinic acid. *Carbon*, 54, pp.36–41.

Maheshkumar et al., 2014. Research updates on Graphene oxide based polymeric nanocomposites. *Polymer composites*, pp.1–14.

Mainil et al., 2010. Morphology and properties of SAN-clay nanocomposites prepared principally by water-assisted extrusion. *Polymer engineering and science*, pp.10–21.

Malas, A. & Das, C.K., 2015. Effect of graphene oxide on the physical, mechanical and thermo-mechanical properties of neoprene and chlorosulfonated polyethylene vulcanizates. *Composites Part B: Engineering*, 79, pp.639–648.

Marcano et al., 2010. Improved Synthesis of Graphene Oxide. *ACS Nano*, 4(8), pp.4806–4814.

Martínez-Tong, D.E. et al., 2014. Quantitative mapping of mechanical properties in polylactic acid/natural rubber/organoclay bionanocomposites as revealed by nanoindentation with atomic force microscopy. *Composites Science and Technology*, 104, pp.34–39.

Van Melick, H.G.H., Govaert, L.E. & Meijer, H.E.H., 2003. Prediction of brittle-to-ductile transitions in polystyrene. *Polymer*, 44(2), pp.457–465.

Menard, K.P. & Bilyeu, B.W., 2000. *Dynamic Mechanical Analysis of Polymers and*

Rubbers,

Meyer et al., 2007. The structure of suspended graphene sheets. *Surface Science Reports*, 4, pp.1–14.

Ming et al., 2013. Humidity-dependant compression properties of graphene oxide foams prepared by freeze-drying technique. *Micro & Nano Letters*, 8(2), pp.66–67.

Mittal, G. et al., 2015. A review on carbon nanotubes and graphene as fillers in reinforced polymer nanocomposites. *Journal of Industrial and Engineering Chemistry*, 21, pp.11–25.

Mkhoyan, K.A. et al., 2009. Atomic and Electronic Structure of Graphene-Oxide. *Nano Letters*, 9(3), pp.1058–1063.

Modulation, F., 2003. *Force Measurements*,

Mohan, V.B. et al., 2015. Characterisation of reduced graphene oxide: Effects of reduction variables on electrical conductivity. *Materials Science and Engineering B*, 193(B), pp.49–60.

Moore, 1967. *An introduction to plymer chemistry* 2nd Impres., London: University of London Press Ltd.

Mori and Barth, 1999. *Size Exclusion Chromatography*, Germany: Springer.

Muda et al., 2017. Fundamental study of reduction graphene oxide by sodium borohydride for gas sensor application. *AIP Conference Proceedings*, pp.1–7.

Muller, V.M., Derjaguin, B. V. & Toporov, Y.P., 1983. On two methods of calculation of the force of sticking of an elastic sphere to a rigid plane. *Colloids and Surfaces*, 7(3), pp.251–259.

Namitha, L.K. et al., 2013. Effect of micro- and nano-fillers on the properties of silicone

rubber-alumina flexible microwave substrate. *Ceramics International*, 39(6), pp.7077–7087.

Nielsen & Landel, 1994. *Mechanical properties of polymers and composites* 2nd editio., New York: Marcel Dekker Incorporation.

Okada, A. & Usuki, A., 1995. The chemistry of polymer-clay hybrids. *Materials Science and Engineering: C*, 3(2), pp.109–115.

Olabisi, O., 1997. *Handbook of thermoplastics*, USA: Marcel Dekker Incorporation.

De Oliveira, H.P., Sydlik, S.A. & Swager, T.M., 2013. Supercapacitors from free-standing polypyrrole/graphene nanocomposites. *Journal of Physical Chemistry C*, 117(20), pp.10270–10276.

Panaitescu, D.M. et al., 2012. Morphological investigation of PP/nanosilica composites containing SEBS. *Polymer Testing*, 31(2), pp.355–365.

Panaitescu, D.M., Frone, A.N. & Nicolae, C., 2013. Micro- and nano-mechanical characterization of polyamide 11 and its composites containing cellulose nanofibers. *European Polymer Journal*, 49(12), pp.3857–3866.

Pandey, J.K. et al., 2005. An overview on the degradability of polymer nanocomposites. *Polymer Degradation and Stability*, 88(2), pp.234–250.

Panwar, V. et al., 2017. Fabrication of conducting composite sheets using cost-effective graphite flakes and amorphous styrene acrylonitrile for enhanced thermistor, dielectric, and electromagnetic interference shielding properties. *Materials Chemistry and Physics*, 193, pp.329–338.

Panwar, V. & Mehra, R.M., 2008. Study of electrical and dielectric properties of styrene-acrylonitrile/graphite sheets composites. *European Polymer Journal*, 44(7), pp.2367–2375.

Papageorgiou, D.G., Kinloch, I.A. & Young, R.J., 2017. Mechanical Properties of Graphene and Graphene-based Nanocomposites. *Progress in Materials Science*, 90, pp.75–127.

Paredes, J.I. et al., 2008. Graphene oxide dispersions in organic solvents. *Langmuir*, 24(19), pp.10560–10564.

Park, S. et al., 2011. Hydrazine-reduction of graphite- and graphene oxide. *Carbon*, 49(9), pp.3019–3023.

Park, W. et al., 2014. Electrical and thermal conductivities of reduced graphene oxide/polystyrene composites. *Applied Physics Letters*, 104(11), pp.1–4.

Park et al., 2009. Colloidal Suspensions of Highly Reduced Graphene Oxide in a Wide Variety of Organic Solvents. *Nano Lett.*, 9(4), pp.1593–1597.

Paul, D.R. & Robeson, L.M., 2008. Polymer nanotechnology: Nanocomposites. *Polymer*, 49(15), pp.3187–3204.

Pawar, S.P., Gandi, M. & Bose, S., 2016. High performance electromagnetic wave absorbers derived from PC/SAN blends containing multiwall carbon nanotubes and Fe 3 O 4 decorated onto graphene oxide sheets. *RSC Adv.*, 6(44), pp.37633–37645.

Pei, S. & Cheng, H.M., 2012. The reduction of graphene oxide. *Carbon*, 50(9), pp.3210–3228.

Peponi, L. et al., 2014. Processing of nanostructured polymers and advanced polymeric based nanocomposites. *Materials Science and Engineering R: Reports*, 85, pp.1–46.

Pham et al., 2011. Superior conductive polystyrene – chemically converted graphene nanocomposite. *Journal of Materials Chemistry*, 21(30), pp.11312–11316.

Potts et al., 2011. Graphene-based polymer nanocomposites. *Polymer*, 52(1), pp.5–25.

Pour & Ghaemy, 2016. Polymer grafted graphene oxide: For improved dispersion in epoxy

resin and enhancement of mechanical properties of nanocomposite. *Composites Science and Technology*, 136, pp.145–157.

Prolongo, S.G. et al., 2008. Effects of dispersion techniques of carbon nanofibers on the thermo-physical properties of epoxy nanocomposites. *Composites Science and Technology*, 68(13), pp.2722–2730.

Pumera, M., 2010. Graphene-based nanomaterials and their electrochemistry. *Chemical Society reviews*, 39(11), pp.4146–4157.

Qian, T. et al., 2013. Gold nanoparticles coated polystyrene/reduced graphite oxide microspheres with improved dispersibility and electrical conductivity for dopamine detection. *Colloids and Surfaces B: Biointerfaces*, 112, pp.310–314.

Qiu et al., 2015a. Functionalized graphene sheets filled isotactic polypropylene nanocomposites. *Composites Part B: Engineering*, 71, pp.175–183.

Qiu, Y. et al., 2016. Thermoplastic polyester elastomer nanocomposites filled with graphene: Mechanical and viscoelastic properties. *Composites Science and Technology*, 132, pp.108–115.

Qiu et al., 2015b. Effect of functionalized graphene oxide with organophosphorus oligomer on the thermal and mechanical properties and fire safety of polystyrene. *Industrial and Engineering Chemistry Research*, 54(13), pp.3309–3319.

Rafiee, M. a. et al., 2009. Enhanced mechanical properties of nanocomposites at low graphene content. *ACS Nano*, 3(12), pp.3884–3890.

Rajender, N. & Suresh, K.I., 2016. Surface-Initiated Atom Transfer Radical Polymerization (SI-ATRP) from Graphene Oxide: Effect of Functionalized Graphene Sheet (FGS) on the Synthesis and Material Properties of PMMA Nanocomposites. *Macromolecular Materials and Engineering*, 301(1), pp.81–92.

Ren et al., 2011. Improved properties of highly oriented graphene polymer nanocomposites. *Applied polymer Science*, 121, pp.3167–3174.

Rountree et al., 2016. Graphene reflux: improving the yield of liquid-exfoliated nanosheets through repeated separation techniques. *Nanotechnology*, 27(50), pp.1–6.

Ryder, 1971. *The elements of Fractography*, London: Technical editing and reproduction Ltd.

Salavagione et al., 2011. Graphene-based polymer nanocomposites. In *Physics and applications of graphene*. pp. 1–14.

Saravanan, N. et al., 2014. Graphene and modified graphene-based polymer nanocomposites - A review. *Journal of Reinforced Plastics and Composites*, 33(12), pp.1158–1170.

Schiers and Priddy, 2003. *Polystyrene and styrenic copolymers*, England: John Wiley and Sons.

Shah, R. et al., 2015. Progression from Graphene and Graphene Oxide to High Performance Polymer-Based Nanocomposite: A Review. *Polymer-Plastics Technology and Engineering*, 54(2), pp.173–183.

Shen, J. et al., 2009. Fast and facile preparation of graphene oxide and reduced graphene oxide nanoplatelets. *Chemistry of Materials*, 21(15), pp.3514–3520.

Sheng, X. et al., 2015. In situ thermal reduction of graphene nanosheets based poly(methyl methacrylate) nanocomposites with effective reinforcements. *Industrial and Engineering Chemistry Research*, 54(2), pp.649–658.

De Silva, K.K.H. et al., 2017. Chemical reduction of graphene oxide using green reductants. *Carbon*, 119, pp.190–199.

Silvestre, J., Silvestre, N. & De Brito, J., 2016. Polymer nanocomposites for structural applications: Recent trends and new perspectives. *Mechanics of Advanced Materials and Structures*, 23(11), pp.1263–1277.

Singh, K., Ohlan, A. & Dhawan, S.K., 2012. *Polymer-Graphene Nanocomposites : Preparation , Characterization , Properties , and Applications*,

Singh, R., Barman, P.B. & Sharma, D., 2016. Enhanced thermal properties of highly monodispersed ZnO nanoparticle/poly(styrene-co-acrylonitrile) nanocomposite. *Polymer Science - Series B*, 58(4), pp.439–448.

Singh, V. et al., 2011. Graphene based materials: Past, present and future. *Progress in Materials Science*, 56(8), pp.1178–1271.

Smolyakov, G. et al., 2016. AFM PeakForce QNM mode: Evidencing nanometre-scale mechanical properties of chitin-silica hybrid nanocomposites. *Carbohydrate Polymers*, 151, pp.373–380.

Sperling, L., 1992. *Introduction to physical polymer science* 2nd ed., Canada: John Wiley and Sons.

Srivastava, R.K. et al., 2011. The strain sensing and thermal-mechanical behavior of flexible multi-walled carbon nanotube/polystyrene composite films. *Carbon*, 49(12), pp.3928–3936.

Stankovich, S. et al., 2007. Synthesis of graphene-based nanosheets via chemical reduction of exfoliated graphite oxide. *Carbon*, 45(7), pp.1558–1565.

Stille, 1966. *Introduction to polymer chemistry* 2nd printi., John Wiley and Sons.

Stretz, H.A., Paul, D.R. & Cassidy, P.E., 2005. Poly(styrene-co-acrylonitrile)/montmorillonite organoclay mixtures: A model system for ABS nanocomposites. *Polymer*, 46(11), pp.3818–3830.

Sun, X. et al., 2013. Developing polymer composite materials: Carbon nanotubes or graphene? *Advanced Materials*, 25(37), pp.5153–5176.

Suresh, D. et al., 2015. Clove extract mediated facile green reduction of graphene oxide, its

dye elimination and antioxidant properties. *Materials Letters*, 142, pp.4–6.

Szabo et al., 2006. Evolution of surface functional groups in a series of progressively oxidized graphite oxides. *Chemistry of Materials*, 18(11), pp.2740–2749.

T.K., B.S. et al., 2014. Microwave exfoliated reduced graphene oxide epoxy nanocomposites for high performance applications. *Polymer*, 55(16), pp.3614–3627.

Tang, L.C. et al., 2014. Creep and recovery of polystyrene composites filled with graphene additives. *Composites Science and Technology*, 91, pp.63–70.

Tang et al., 2012a. General route to graphene with liquid-like behavior by non-covalent modification. *Soft Matter*, 8(35), pp.9214–9220.

Tang et al., 2012b. Highly efficient synthesis of graphene nanocomposites. *Nano Letters*, 12(1), pp.84–90.

Tang et al., 2012c. Highly Efficient Synthesis of Graphene Nanocomposites. *Nano Letters*, 12, pp.84–90.

Teach and Kiessling, 1960. *Polystyrene*, New York: Reinhold publishing corporation.

Terrones, M. et al., 2011. Interphases in graphene polymer-based nanocomposites: Achievements and challenges. *Advanced Materials*, 23(44), pp.5302–5310.

Thakur, S. & Karak, N., 2015. Alternative methods and nature-based reagents for the reduction of graphene oxide: A review. *Carbon*, 94, pp.224–242.

Thio, B.J.R. & Meredith, J.C., 2007. Measurement of polyamide and polystyrene adhesion with coated-tip atomic force microscopy. *Journal of Colloid and Interface Science*, 314(1), pp.52–62.

Thostenson, E.T. & Chou, T.W., 2006. Processing-structure-multi-functional property relationship in carbon nanotube/epoxy composites. *Carbon*, 44(14), pp.3022–3029.

Tian, N. et al., 2015. The nanomechanical behavior of a graphite nanoplatelet/polycarbonate nanocomposite. *Polymer Testing*, 47, pp.87–91.

Tjong, 2006a. Structural and mechanical properties of polymer nanocomposites. *Materials Science and Engineering R: Reports*, 53(3–4), pp.73–197.

Tjong, 2006b. Structural and mechanical properties of polymer nanocomposites. *Materials Science and Engineering R: Reports*, 53(3–4), pp.73–197.

Toselli et al., 2015. In situ thermal reduction of graphene oxide forming epoxy nanocomposites and their dielectric properties. *Polymer composite*, pp.294–301.

Traina, M. & Pegoretti, A., 2012. In situ reduction of graphene oxide dispersed in a polymer matrix. *Journal of Nanoparticle Research*, 14(4).

Tripathi, S.N. et al., 2013. Electrical and mechanical properties of PMMA/reduced graphene oxide nanocomposites prepared via in situ polymerization. *Journal of Materials Science*, 48(18), pp.6223–6232.

Tseng, I.H. et al., 2013. Enhanced thermal conductivity and dimensional stability of flexible polyimide nanocomposite film by addition of functionalized graphene oxide. *Polymer International*, 62(5), pp.827–835.

Tu, N.D.K. et al., 2015. Remarkable Conversion between n- and p-Type Reduced Graphene Oxide on Varying the Thermal Annealing Temperature. *Chemistry of Materials*, 27(21), pp.7362–7369.

Tu, Z. et al., 2014. Controllable growth of 1-7 layers of graphene by chemical vapour deposition. *Carbon*, 73, pp.252–258.

Turi, E.A., 1997. Measurement of the Glass Transition Temperature Using Dynamic Mechanical Analysis. In *Thermal characterization of polymeric materials*. New York, p. 1997.

Vaia, R.A. & Maguire, J.F., 2007. Polymer nanocomposites with prescribed morphology: Going beyond nanoparticle-filled polymers. *Chemistry of Materials*, 19(11), pp.2736–2751.

Veeco, 2005. *Nanoindentation and Nanoscratching with SPMs*, Santa Barbara.

Verdejo, R. et al., 2011a. Graphene filled polymer nanocomposites. *Journal of Materials Chemistry*, 21(10), p.3301.

Verdejo, R. et al., 2011b. Graphene filled polymer nanocomposites. *Journal of Materials Chemistry*, 21(10), pp.3301–3310.

Vu et al., 2016. Effect of reduced graphene oxide functionalization by sulfanilic acid on the mechanical properties of PSAN/reduced graphene oxide composites. *Polymers composites*, pp.44–50.

Vukoje, I.D. et al., 2014. Characterization of silver/polystyrene nanocomposites prepared by in situ bulk radical polymerization. *Materials Research Bulletin*, 49, pp.434–439.

Wan & Chen, 2012. Reinforcement and interphase of polymer/graphene oxide nanocomposites. *Journal of Materials Chemistry*, 22(8), pp.3637–3646.

Wang, C. et al., 2008. Polystyrene-acrylonitrile-CNTs nanocomposites preparations and tribological behavior research. *Wear*, 265(11–12), pp.1923–1926.

Wang, H.W., Chang, K.C. & Chu, H.C., 2005. Effect of clay on the properties of poly(styrene-co-acrylonitrile)-clay nanocomposites. *Polymer International*, 54(1), pp.114–119.

Wang, X. et al., 2016. Mechanical properties of polymer composites reinforced by functionalized graphene prepared via direct exfoliation of graphite flakes in styrene. *RSC Advances*, 6, pp.112486–112492.

Wissert, R. et al., 2010. Graphene nanocomposites prepared from blends of polymer latex

with chemically reduced graphite oxide dispersions. *Macromolecular Materials and Engineering*, 295(12), pp.1107–1115.

Wollbrink, A. et al., 2017. Improved hydrogen selectivity of Surface Modified Graphite (SMG) membranes: Permeation experiments and characterisation by micro-Raman spectroscopy and XPS. *Journal of Membrane Science*, 528(December 2016), pp.316–325.

Wu, N. et al., 2012a. Synthesis of network reduced graphene oxide in polystyrene matrix by a two-step reduction method for superior conductivity of the composite. *Journal of Materials Chemistry*, 22, pp.17254–17261. Available at: http://xlink.rsc.org/?DOI=c2jm33114d.

Wu, N. et al., 2012b. Synthesis of network reduced graphene oxide in polystyrene matrix by a two-step reduction method for superior conductivity of the composite. *Journal of Materials Chemistry*, 22, pp.17254–17261.

Wu, X. et al., 2014. Synergetic reduction of graphene oxide by sodium hydroxide and microwave irritation. *Micro & Nano Letters*, 9(11), pp.804–806.

Xing, M. et al., 2010. Adhesion force studies of nanofibers and nanoparticles. *Langmuir*, 26(14), pp.11809–11814.

Xu, C. et al., 2013. Can in situ thermal reduction be a green and efficient way in the fabrication of electrically conductive polymer/reduced graphene oxide nanocomposites? *Composites Part A*, 53(A), pp.24–33.

Xu, C. et al., 2015. Fabrication and characteristics of reduced graphene oxide produced with different green reductants. *PLoS ONE*, 10(12), pp.1–15.

Xu, J., Wang, Y. & Hu, S., 2017. Nanocomposites of graphene and graphene oxides: Synthesis, molecular functionalization and application in electrochemical sensors and

biosensors. A review. *Microchimica Acta*, 184(1), pp.1–44.

Yadav, S.K. & Cho, J.W., 2013. Functionalized graphene nanoplatelets for enhanced mechanical and thermal properties of polyurethane nanocomposites. *Applied Surface Science*, 266, pp.360–367.

Yan, X. et al., 2012. A Raman Spectroscopy Study on Single-Wall Carbon Nanotube / Polystyrene Nanocomposites : Mechanical Compression Transferred from the Polymer to Single-Wall Carbon Nanotubes. *Journal of Physical Chemistry C*, 116, pp.17897–17903.

Yang, J. et al., 2013. Preparation of polystyrene/graphene oxide composites and their supercritical carbon dioxide foaming. *Journal of Polymer Research*, 20(173), pp.1–9.

Yasmin et al., 2006a. Processing of expanded graphite reinforced polymer nanocomposites. *Composites Science and Technology*, 66(9), pp.1182–1189.

Yasmin, Luo, J.J. & Daniel, I.M., 2006b. Processing of expanded graphite reinforced polymer nanocomposites. *Composites Science and Technology*, 66(9), pp.1182–1189.

Yin, G. et al., 2013. Preparation of graphene oxide coated polystyrene microspheres by Pickering emulsion polymerization. *Journal of colloid and interface science*, 394, pp.192–198.

Yongchao & Samulski, 2008. Synthesis of Water Soluble Graphene. *Nano Letters*, 8(6), pp.1679–1682.

Yoshioka, A. & Tashiro, K., 2004. Solvent effect on the glass transition temperature of syndiotactic polystyrene viewed from time-resolved measurements of infrared spectra at the various temperatures and its simulation by molecular dynamics calculation. *Macromolecules*, 37(2), pp.467–472.

Young, R.J. et al., 2012. The mechanics of graphene nanocomposites: A review. *Composites*

Science and Technology, 72(12), pp.1459–1476.

Young, R.J. & Lovell, P.A., 1990. *Introduction to Polymers, 2 nd ed,* CRC.

Young, T.J. et al., 2011. The use of the PeakForce quantitative nanomechanical mapping AFM-based method for high-resolution Young's modulus measurement of polymers. *Measurement Science and Technology*, 22(12), pp.1–6.

Yu, Y.-H. et al., 2014. High-performance polystyrene/graphene-based nanocomposites with excellent anti-corrosion properties. *Polym. Chem.*, 5(2), pp.535–550.

Yuan, M. et al., 2014. High performance solid polymer electrolyte with graphene oxide nanosheets. *RSC Adv.*, 4(Cv), pp.59637–59642.

Zeng, Q., Yu, A. & Lu, G., 2008. Multiscale modeling and simulation of polymer nanocomposites. *Progress in Polymer Science*, 33, pp.191–269.

Zhang, H. Bin et al., 2010. Electrically conductive polyethylene terephthalate/graphene nanocomposites prepared by melt compounding. *Polymer*, 51(5), pp.1191–1196.

Zhang, J. et al., 2006. Styrenic polymer nanocomposites based on an oligomerically-modified clay with high inorganic content. *Polymer Degradation and Stability*, 91(11), pp.2665–2674.

Zhang, X. et al., 2014. Graphene nanosheets synthesis via chemical reduction of graphene oxide using sodium acetate trihydrate solution. *Synthetic Metals*, 193, pp.132–138.

Zhang et al., 2017. Grafting of polystyrene onto reduced graphene oxide by emulsion polymerization for dielectric polymer composites: High dielectric constant and low dielectric loss tuned by varied grafting amount of polystyrene. *European Polymer Journal*, 94(111), pp.196–207.

Zhang et al., 2015. Recent advances in the synthesis and applications of azo initiators. *Polym. Chem.*, 42(6), pp.6107–6124.

Zhang et al., 2011a. Vacuum-assisted synthesis of graphene from thermal exfoliation and reduction of graphite oxide. *Journal of Materials Chemistry*, 21(14), pp.5392–5397.

Zhang, Liu, Y.D. & Choi, H.J., 2011b. Graphene oxide coated core-shell structured polystyrene microspheres and their electrorheological characteristics under applied electric field. *Journal of Materials Chemistry*, 21(19), pp.6916–6921.

Zhao, X. et al., 2010. Enhanced mechanical properties of graphene-based polyvinyl alcohol composites. *Macromolecules*, 43(5), pp.2357–2363.

Zhu, Y. et al., 2010. Graphene and graphene oxide: Synthesis, properties, and applications. *Advanced Materials*, 22(35), pp.3906–3924.

Zhu, Y., Gianola, D. & Zhu, T., 2016. Editorial for the focus issue on Nanomechanics in Extreme Mechanics Letters. *Extreme Mechanics Letters*, 8, pp.125–126.

Zilg, C., Mülhaupt, R. & Finter, J., 1999. Morphology and toughness/stiffness balance of nanocomposites based upon anhydride-cured epoxy resins and layered silicates. *Macromolecular Chemistry and Physics*, 200(3), pp.661–670.

Zunjarrao, S.C., Sriraman, R. & Singh, R.P., 2006. Effect of processing parameters and clay volume fraction on the mechanical properties of epoxy-clay nanocomposites. *Journal of Materials Science*, 41(8), pp.2219–2228.

Appendices

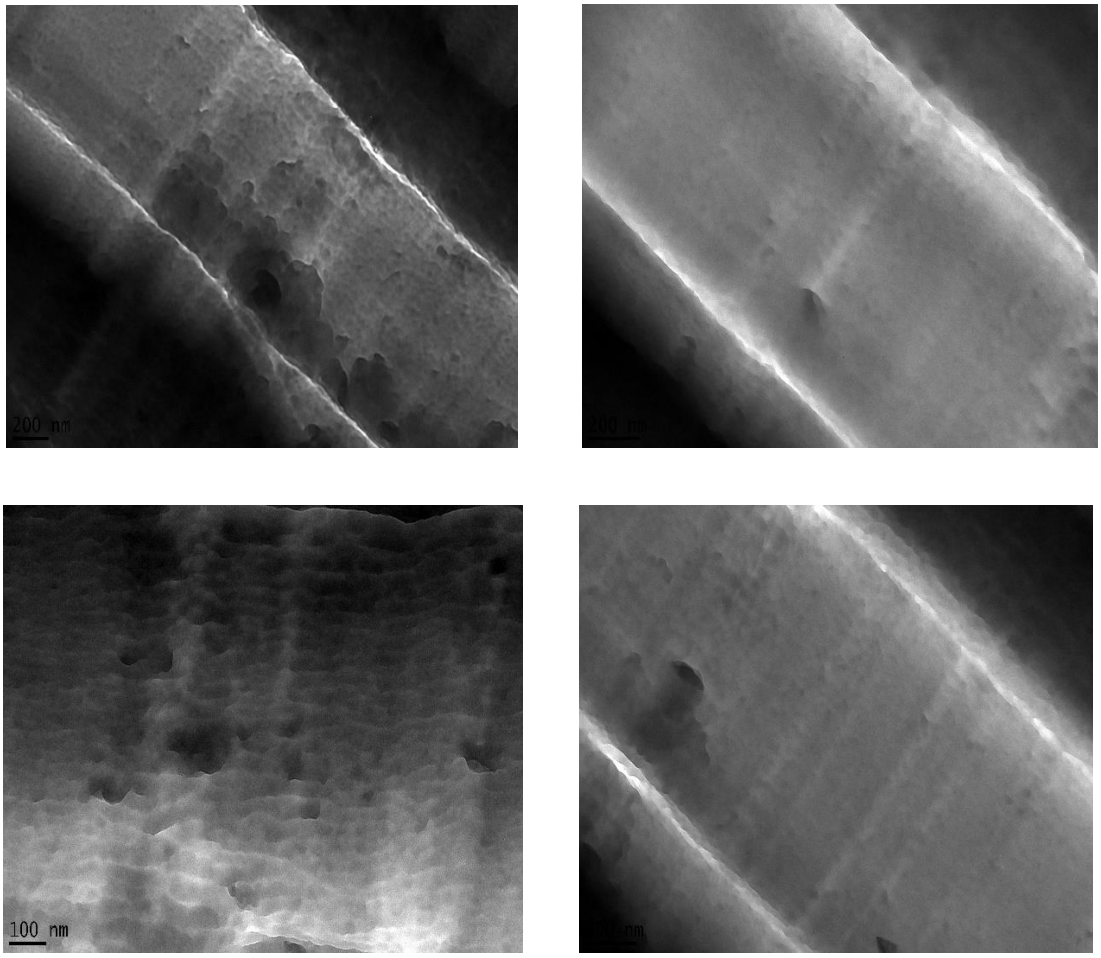

Appendix 1. : TEM images for PS/GO 0.5 wt. %

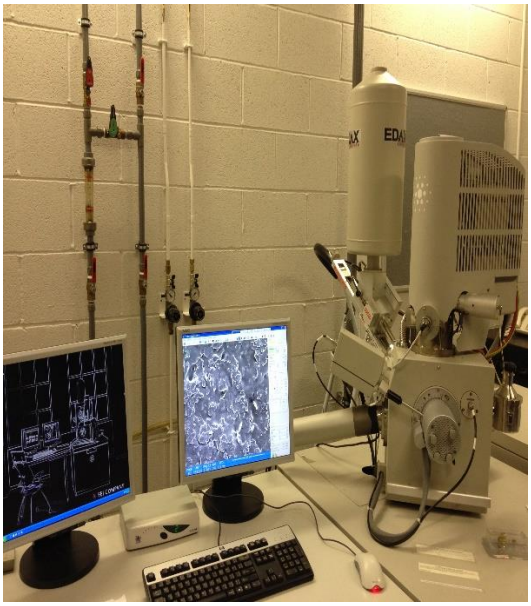

Appendix 2. : Some techniques employed in the current work. The top couple of images show AFM and SEM respectively. The bottom couple of images show extensometer and QNM respectively.

Appendix 3. : Table shows the specifications of the used dumbbell in the current research.

BS ISO 137: Type 2, 2005	
Test length (mm)	20 ± 0.5
Overall length (mm)	75
Width of ends (mm)	12.5 ± 1
Length of narrow portion (mm)	25 ± 1
Width of narrow portion (mm)	4 ± 0.1
Transition radius outside (mm)	8 ± 0.5
Transition radius inside (mm)	12.5 ± 1

Appendix 4. : Table of FTIR bands for the materials characterized by this technique in this work with their references.

Wavenumber / cm^{-1}	**Type of bond**	**Reference**
3500	O-H stretching vibration of hydroxyl groups (GO)	(Ming et al. 2013)
1730 – 1706	C=O carbonyl and carboxylic acid groups (GO)	(Ming et al. 2013)
1625	C=C Unoxidized graphitic domain (GO)	(Yin et al. 2013)
1465 – 1340	C-H bending vibration (GO)	(Ming et al. 2013)
1300 – 1000	C-O stretching vibration of epoxy groups (GO)	(Ming et al. 2013)
1387	O-H deformations in C-OH group (GO)	(Wu et al. 2012b)
3100 - 2800	C-H stretching vibration of the aromatic ring and aliphatic chain (PS)	(Vukoje et al. 2014)
2920 - 2849	Asymmetric and symmetric stretching vibration of CH2 respectively (PS)	(Han et al. 2013)
1492 - 1452	C-C stretching vibration of benzene ring (PS)	(Yin et al. 2013)
753 - 695	C-H out of plane bending vibration of the benzene ring (PS)	(Han et al. 2013)
1095 - 803	The range of the possible interaction between PS and GO. The type of interaction is Π-Π stacking	(Yin et al. 2013) (Han et al. 2013)
1370	Interaction between PS and GO	(Wan & Chen, 2012)
1610	Possible interaction between PS and rGO	(Alsharaeh et al. 2014)
3000 - 3700	C-OH stretching vibrations of the hydroxyl groups (graphite oxide)	(Drewniak et al. 2016) (Hontoria-Lucas et al. 1995)
1620	C=C skeletal vibration of non-oxidized graphite	(Drewniak et al. 2016)
_____	Graphite	(Kattimuttathu et al. 2015)
750 - 700	Monosubstituted benzene peaks (SAN)	(Wang et al. 2005)
1600 – 1500 – 1450	Aromatic C=C group (SAN)	(Wang et al. 2005)
2240	-C≡N stretching of AN group (SAN)	(Wang et al. 2005)
3200 - 2900	Aromatic C-H vibration (SAN)	(Wang et al. 2005)
1100	Possible interaction between SAN and GO	(Wang et al. 2005)

Appendix 5. : Table of Raman spectra bands for the materials characterized by this technique in this work with their references.

Raman shift / cm^{-1}	**Band type**	**Reference**
1575	G band related to E_{2g} phonons by SP^2 carbon atoms and caused by in phase vibrations of the graphitic lattice (graphite).	(Ma et al. 2013) (Liu et al. 2016) (Mohan et al. 2015) (Krishnamoorthy et al. 2013)
1350	D band associated with the breathing mode k point photons of A_{1g} symmetry. It is caused by bond length disorder, bond angle disorder, and other reasons (graphite).	(Ma et al. 2013) (Liu et al. 2016) (Mohan et al. 2015) (Krishnamoorthy et al. 2013)
2700	2D peak associated with the number of graphene layers and caused by double resonance transitions resulting in the production of two photons with opposite momentum (graphite).	(Eda & Chhowalla, 2010)
1589	G band shifting in accordance to the oxidation process (GO)	(Krishnamoorthy et al. 2013)
1357	D band shifting in accordance to the formation of disorder and defects (GO)	(Krishnamoorthy et al. 2013)
3025 – 2900	Aromatic and aliphatic C-H vibration (PS)	(Yan et al. 2012)
800	C-C vibration (PS)	(Yan et al. 2012)
1600	C=C vibration (PS)	(Yan et al. 2012)
1000	Aromatic carbon ring	(Yan et al. 2012)
1353	D band new peaks' position for rGOs due to defects formation after performing the process of reduction	(Chen et al. 2010)

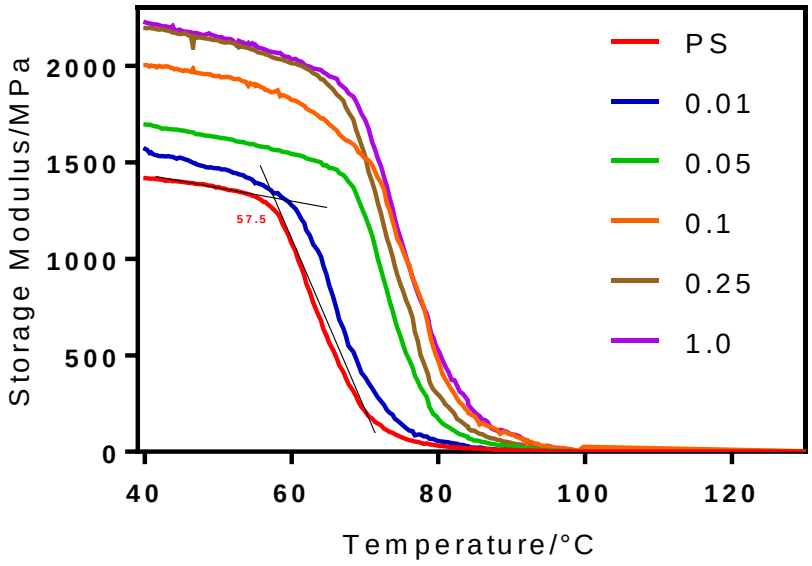

Appendix 6. : Finding Tg from storage modulus curve. The method was shown for one curve only and adopted for all other curves in all the experimental chapters in the thesis.